RELATION OF THE ADHESION OF PLASMA SPRAYED COATINGS TO THE PROCESS PARAMETERS SIZE, VELOCITY AND HEAT CONTENT OF THE SPRAY PARTICLES

J.M. HOUBEN
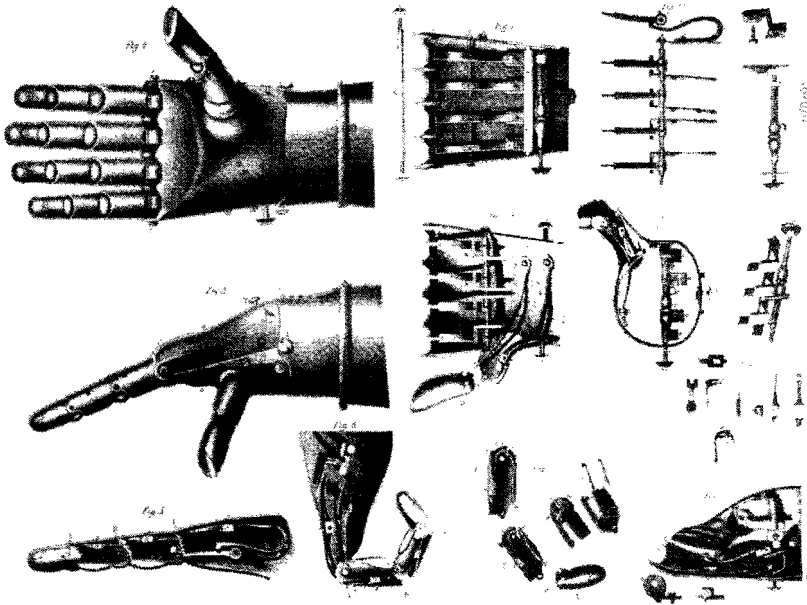
The iron hand of the brave german
knight Götz von Berlichingen~1535.

Mutantur tempora, quae homines sentiunt non mutantur:
A manu ferrea Godefridi, equitis Berlichingensis, ad artem
plasmatis spargendi.

RELATION OF THE ADHESION OF PLASMA SPRAYED COATINGS
TO THE PROCESS PARAMETERS
SIZE, VELOCITY AND HEAT CONTENT
OF THE SPRAY PARTICLES

RELATION OF THE ADHESION OF PLASMA SPRAYED COATINGS
TO THE PROCESS PARAMETERS
SIZE, VELOCITY AND HEAT CONTENT
OF THE SPRAY PARTICLES

PROEFSCHRIFT

ter verkrijging van de graad van doctor aan de
Technische Universiteit Eindhoven, op gezag van
de rector magnificus, Prof. ir. M. Tels, voor een
commissie aangewezen door het College van
Decanen in het openbaar te verdedigen op
vrijdag 9 december 1988 te 16.00 uur.

door

JOHAN MARTIN HOUBEN

geboren te Oirsbeek

Dit proefschrift is goedgekeurd
door de promotoren:

1^e promotor: Prof. dr. ir. J.A. Klostermann
2^e promotor: Prof. dr. R. Metselaar

Aan Johanna, Tim, Rita, Max en Inez

CONTENTS   page

0   GENERAL INTRODUCTION

This thesis is dedicated to the technology of plasma spraying which is a method to apply coatings to a substrate. All thermal spray techniques, and plasma spraying is one of them, use the thermal and kinetic energy of a combustion flame or an electric arc discharge to accelerate and to heat solid powdered material which is to be projected onto a substrate. In this way machine parts (or constructions) can be improved regarding their surface properties, since very often a machine part fails due to surface attacks such as fatigue, wear, erosion, corrosion, oxidation or a combination of some of these phenomena. A coating also may be applied to insulate or to conduct heat and electricity. At last, thermal spray techniques are employed to produce free standing bodies, mostly made of refractory or ceramic materials. Plasma spraying is a technique where an inert, or partly inert gas is heated by a controlled arc discharge to such a temperature level ($\geq$ 10.000 K) that partly ionisation of the gas occurs. This gas has a very high enthalpy and is called a plasma, the fourth state of matter. The plasma generating device is called a plasma torch.

Apart from the high energy content an arc plasma for thermal spraying is characterized by it's relatively high torch — outflow velocity ($\geq$ 200 ms^{-1}). The plasma leaves the torch as a jet stream with an effective diameter of approximately 5 mm and a length around 45 mm. Powdered material, size 5 — 100 μm, is injected side — on into the plasma jet which accelerates and heats the powder. The energy transfer from the plasma to the spray particles consists of a thermal part and a kinetic part. Both energies are strongly coupled. If the control setting of the torch is changed, the heat content and the velocity of the particles change simultaneously, which makes the tracing of optimum spray conditions for the achievement of pre — set coating proporties rather elaborate, if

1

possible. The built up of a plasma sprayed coating can be reduced to the many fold repeated process of interaction of one single particle with the substrate as far as the adhesion to the substrate is concerned.

The subject of this thesis is the investigation of the relation between the input parameters velocity, size and heat content of a spray particle and the morphology of the spread particle. Subsequently, the relation between the morphology and the adhesion will be determined in order to find the optimum combination of the spray parameters with regards to the adhesion strength. The individual influence of heat content and particle velocity can be determined by the application of a rotating substrate support. Four polished substrates are fixed at the perimeter of a disk shaped substrate holder. The disk is mounted on the shaft of a grinding device, which permits the application of rotational speeds up to 24.000 revolutions per minute. With a disk diameter of 100 mm, the rotation velocity of the substrate amounts up to 125 ms^{-1}. This velocity can be added to or subtracted from the standard flight velocity of a particle with a pre – set heat content. So, the impact velocity can be varied over rather a wide range, independent of the standard heat content. The third main input parameter is the particle size. It can be fixed within a narrow range by sieving. In this way it is possible to determine experimentally the particle morphologies and the related adhesion strengths as a function of the impact velocity or as a function of the heat content.

To back up these experiments, the thermal energy transfer of the particle to the substrate will be described. Subsequently, a collision theory elucidates the mechanical and thermodynamical effects which are coherent with a shock compression and the relaxation after the shock wave. The splash models, emanating from this theory, will be experimentally tested on the basis of photographic pictures of spread particles and their cross sections.

Finally adhesion tests will be carried out to determine the specific strength level of particular morphologies. The final aim of the whole work is to find the optimum combination of the three input parameters in order to design a new generation of plasma spray equipment with sufficient control over these parameters.

CHAPTER 1.   INTRODUCTION TO PLASMA SPRAYING.

1.1.   Macro characterisation of the plasma spray process.

(Note: In this thesis the decimal comma is used in stead of the decimal point.)
For scientific purposes plasma spraying can be described appropriately as a
connected energy transmission process, starting with the energy transfer from an
electric potential field to the plasma gas, proceeding with the energy transfer from
the plasma to the material particles which are to build up the coating and
concluding with the energy transfer from the particles to the substrate.
Fig. 1.1. is a schematic drawing of plasma spraying as it will be considered in this
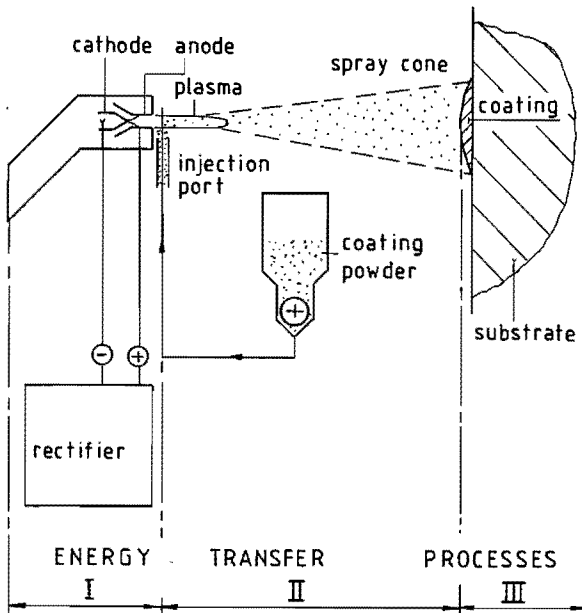
Fig. 1.1:   Plasma spraying schematically represented as a sequence of three
              energy transfer processes.

4

thesis. The successive three processes have in common that the energy exchange consists of a simultaneously occurring thermal and kinetic part. Regarding the thermal part, a macroscopic energy balance can be set up.

A typical one reads:

— Rectifier energy supplied to the torch : 42,0

— Cooling water losses 66% : −27,7

— Remaining enthalpy of the exhausting plasma: 14,3

— Losses due to convection and radiation to the

surrounding atmosphere : −13,3

— Net energy stored in the spray particles: 1,0 kw

The energy efficiency of this spray operation:

$$\eta = \frac{\text{Net energy stored in the spray particles}}{\text{Rectifier energy supplied to the torch}} \times 100\% =$$

$$= \frac{1,0}{42,0} \times 100\% \cong 2,4\%$$

The low energy efficiency may be considered as one of the characteristics of plasma spraying. It causes a low heat flow density through the substrate surface. To emphasize this feature it will be compared to a typical macroscopic thermal energy balance occurring with CO_2 welding and handwelding with a covered electrode.

On the basis of these data the heat flow densities through the substrate surface can be calculated. For the welding processes, the heat flow density is:

$$q''_w = \frac{\text{efficiency} \times \text{current} \times \text{voltage} \times \text{time}}{\text{traverse speed} \times \text{weld width} \times \text{time}}$$

5

For plasma spraying, the heat flow density reads:

$$q''_{pl} = \frac{\text{deposit mass flow rate} \times \text{heat content of the particles}}{\text{traverse speed} \times \text{weld width} \times \text{time}}$$

Table 1: Processvariables for CO_2-welding, handwelding with covered electrode and plasma spraying [1].

Variable	Unit	CO_2 welding	Hand-welding	Plasma-spraying
Deposit mass flow rate	$g \, min^{-1}$	42	40	40
current	ampere	200	200	400
voltage	volt	25	25	40
traverse speed	mms^{-1}	5,5	3,6	40
weld/spray width	mm	11,5	10	25
heat content of the spray particles	$kJ \, kg^{-1}$	–	–	1500

Assuming the welding energy efficiency 80% and substituting the data of table 1, it turns out.

For CO_2 welding:

$$q''_{w-CO_2} = \frac{0,8 \times 200 \times 25 \times 1}{5,5 \times 11,5 \times 1} \cong 63 \, \frac{J}{mm^2}$$

for handwelding:

$$q''_{w-hand} = \frac{0,8 \times 200 \times 25 \times 1}{3,6 \times 10 \times 1} \cong 111 \, \frac{J}{mm^2}$$

6

for plasma spraying:

$$q_{pl}^{"} = \frac{\frac{40}{60} \times 1500}{40 \times 25 \times 1} = 1 \frac{J}{mm^2}$$

Roughly one may say that the heat flow density with plasma spraying amounts 1% of the standard welding heat flow density. The fairly low heat flow rate involved with plasma spraying is the second characteristic that should be mentioned here.

From fig. 1.1 it is evident that a free standing distance between the plasma torch and the substrate is maintained. The plasma flame itself is not in contact with the surface to avoid heating up of the substrate, where in welding processes the heat of the welding arc is directed to the surface for the very reason of heating, thus creating the weld pool.

So, in plasma spraying the coating particles are thrown on their own energybasis and this is so because an excessive heating of the substrate material would generally cause severe damage to the coating due to the widely differing thermal dilatation of the coating and the substrate material, mostly inherent to a spray operation. The free standing distance is a third characteristic of plasma spraying implying a low heat transfer rate from the plasma to the surface. A plasma spray coating is built up by discrete particles without a weld pool. This phenomenon should be understood well in order to give judgement about the coating properties and their service performance. For this reason a standard plasma spray operation of e.g. Mo onto a steel substrate will be considered in detail [1]. On the basis of this consideration some interesting and possibly important insights may be gained.

The spray operation: Mo onto steel; spray rate $m = 40$ g min^{-1}; mean particle size $d_p = 50$ μm; specific mass $\rho_{mo} = 10200$ kgm^{-3}. With these data the

7

average number of injected particles can be calculated: $N_1 = 10^6$ particles per second (ps^{-1}). Some more data: The torche's traverse speed $v = 40$ mms^{-1}, the spray width $w = 25$ mm. Finally, let the splashed particle have a lamella diameter $D = 125$ μm. Now the following process properties can be determined:

The average number of lamella on top of each other after one pass of the torch: N_2

N_1 parts per second are injected into the plasma. Assume that all of them stick to the substrate. Then N_1 [ps^{-1}] produce a total spray surface per unit time

$$A_p = N_1 \times \frac{\pi}{4} D^2 \qquad (1.1)$$

$$= 10^6 \times \frac{\pi}{4} \times 0,125^2 = 12.271 \quad [mm^2 s^{-1}]$$

The covered substrate area per unit time

$$A_s = v \times w \times 1 \qquad (1.2)$$

$$= 40 \times 25 \times 1 = 1000 \; [mm^2 s^{-1}]$$

Note: 1 stands for 1 second in order to maintain proper dimensions.

The average number of lamellae on top of each other

$$N_2 = \frac{A_p}{A_s} = \frac{N_1 \times \frac{\pi}{4} D^2}{v \times w \times 1} \qquad (1.3)$$

$$= \frac{12271}{1000} \cong 12$$

In other words: a one pass coating is formed by 12 lamellae on top of each other. Fig 1.2 visualizes the above mentioned data and calculations. Before carrying on with the determination of spray process properties, a simplification has to be made to keep the calculations formally correct. Assume the perpendicular
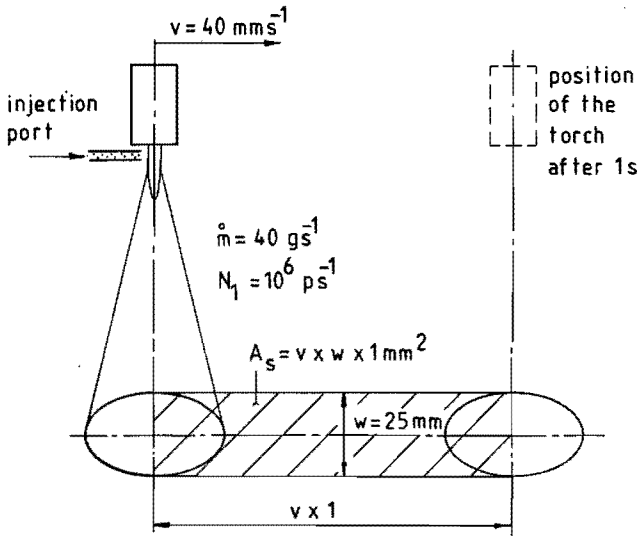
Fig. 1.2:   Data for a standard plasma spray operation.

section through the spray cone to be square shaped instead of circular and
maintain the same section area, see fig. 1.3 then, it holds:

$$\frac{\pi}{4}w^2 = w_*^2 \text{ or } w_* = \frac{1}{2} w \sqrt{\pi} \cong 0{,}9 \text{ w} \qquad (1.4)$$

circular transverse   square
section of the   section with
spray cone   same area
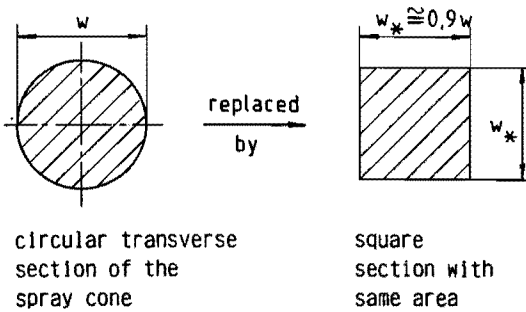
Fig. 1.3:   Definition of w_*.

9

The definition of w_* enables us to make the following calculations formally right and simple without being bothered by second order geometrical effects conjugated with the circular geometry of a transverse section.

The deposition time is the time period during which a surface element is exposed to the bombardment with particles, see fig. 1.4
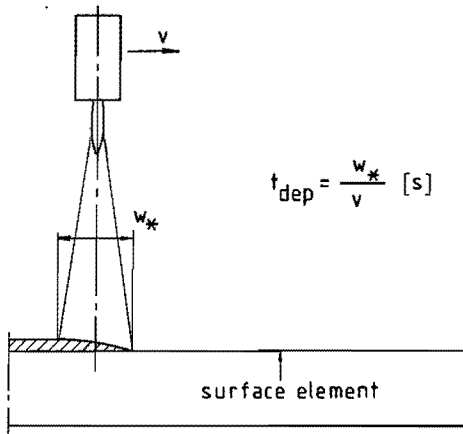
$$t_{dep} = \frac{w_*}{v} \quad [s]$$

Fig. 1.4:   Definition of the deposition time t_{dep}.

$$t_{dep} = \frac{w_*}{v} \, [s] \qquad (1.5)$$

The intensity of the bombardment is

$$n = \frac{N_1}{w_*^2} \, [ps^{-1}m^{-2}] \qquad (1.6)$$

Thus, the surface receives per unit area

$$\acute{N}_2 = t_{dep} \cdot n = \frac{w_*}{v} \times \frac{N_1}{w_*^2} = \frac{N_1}{v \cdot w_*} \, [pm^{-2}] \qquad (1.7)$$

10

can also be defined in another way.

N_2 equals the number of lamellae on top of each other: $N_2 = \dfrac{A_p}{A_s}$,

multiplied with the number of lamellae needed to cover one unit area: $\dfrac{1}{\frac{\pi}{4} D^2}$

hence: $\dot{N}_2 = \dfrac{A_p}{A_s} \cdot \dfrac{1}{\frac{\pi}{4} D^2}$ (1.8)

using e.q. (1.3) and (1.4)

$$\dot{N}_2 = \frac{N_1 \cdot \frac{\pi}{4} D^2}{v \cdot w \cdot 1} \cdot \frac{1}{\frac{\pi}{4} D^2} = \frac{N_1}{v \cdot w_*} \; [p \cdot m^{-2}]$$

(1.8a)

eq. (1.7) and (1.8a) are identical, thus elucidating and backing the validity of the deposition time concept for a surface element.

The time elapse between the collision of two particles belonging to the ith and the $i + 1^{th}$ lamella plane: t_w

The waiting time, t_w, can now be expressed in the foregoing terms.

The deposition time for N_2 lamella planes is given in eq. (1.5): $t_{dep} = \dfrac{w_*}{v}$;

t_{dep} also equals the number of lamellae on top of each other multiplied with the waiting time between the collission of two particles:

$$t_{dep} = t_w \times N_2$$ (1.9).

equating (1.5) and (1.9) yields:

$\dfrac{w_*}{v} = t_w \times N_2$ and for the waiting time:

11

$$t_w = \frac{w_*}{v \times N_2} \qquad (1.10)$$

Numerically:

$$t_w = \frac{0,9 \times 25}{40 \times 12} \cong 0,047 \ [s]$$

The solidification time for a 50 μm Mo particle on a steel substrate is determined by [2b,2c], see also eq. 1.33:

$$t_{sol} = \frac{X^2}{4 p^2 a} \qquad (1.11)$$

where   X = lamella thickness

p = constant

a = thermal diffusivity of Mo

numerically: X = 7 μm; p = 0,582 for Mo on steel and

$a_{Mo} = 5,61 \cdot 10^{-5} \ [m^2 s^{-1}]$.

Inserting these figures in eq. (1.11) yields:

$$t_{sol} \cong 6,5 \cdot 10^{-7} \ [s]$$

The ratio $\theta \quad = \dfrac{t_w}{t_{sol}}$ $\qquad (1.12)$

$$= \frac{0,047}{6,5 \cdot 10^{-7}} = 7,2 \cdot 10^4$$

indicates that the waiting time in between two collisions of particles onto each other is by far longer than the time needed for the solidification. The conclusion can be drawn that a splashing particle will not likely meet a liquid surface. Thus, under normal conditions for spraying a weld pool does not exist.

<u>The virtual flight distance of two particles in the same trajectory: S_v.</u>

S_v is the distance between two particles in the same trajectory and this distance can be calculated by multiplying the waiting time, t_w, with the flight velocity, U_p, of the particles. Assume this last one to be 50 $[\text{ms}^{-1}]$. With $t_w = 0,047$ [s]

$$S_v = U_p \cdot t_w \qquad (1.13)$$

$$= 50 \cdot 0,047 = 2,35 \; [\text{m}].$$

The required flight distance between two particles in the same trajectory in order to meet a liquid foregoing particle should not be longer than:

$$S_L \leq U_p \cdot t_{sol} \qquad (1.14)$$

$$= 50 \cdot 6,5 \cdot 10^{-7} = 3,25 \cdot 10^{-5} \; [\text{m}]$$

or $\quad S_L \leq 32 \; \mu\text{m}.$

From the calculation of S_v and S_L it is evident, as is from the ratio θ, e.q. (1.12), that a particle will not likely meet a liquid foregoing one.

<u>The number of simultaneously solidifying particles per unit area.</u>

During the solidification of one particle, there will arrive at the surface

$$N_3 = t_{sol} \times N_1 \qquad (1.15)$$

$$= 6,5 \cdot 10^{-7} \cdot 10^6 = 0,65 \text{ particles}$$

These particles are spread over the surface area, A_0.

$$A_o = \frac{\pi}{4} \cdot w^2 \qquad (1.16)$$

So, per unit area there will arrive durring the solidification of one particle

$$N_4 = \frac{1}{A_0} \cdot N_3 \qquad (1.17)$$

Substituting all length parameters in mm:

$$N_4 = \frac{10^6}{\frac{\pi}{4} \cdot 25^2} \cdot 0{,}65 = 1324 \; [\text{pm}^{-2}].$$

These N_4 particles will start to solidify simultaneously. So, once more, the conclusion can be drawn that there will not likely be a great interaction between solidifying particles.

1.2   Micro characterization of the thermal interaction between a single plasma spray particle and the substrate.

As seen in the foregoing section, a thermally sprayed coating is built up particle by particle, each having its own individual interaction with the substrate surface. This interaction can be split up into a thermal part and a kinetic — dynamic part. Before starting with the actual theme of this thesis, which is the kinetic — dynamical interaction, first the thermal phenomena in the contact zone between spray particle and substrate will be depicted. When this done, it will be clear that many of the mechanical collision effects can be described without taking into account a great deal of the thermal effects. The theoretical considerations of the following section will be applied to the practical cases of Mo and AISI–316 steel on Fe. The numerical calculations hold for these two systems. The thermal interaction has been discussed, [2a, 2b, 2c], assuming that the particles take a disk shape during solidification from the very first moment of contact with the substrate. (Mind that the working formula's as presented in [2b] are partly misprinted). Further assumptions to be made are:

—   Absence of diffusion or heatbarriers in the interface.

—   Heat transfer takes place only by conduction.

—   The thermophysical properties are not temperature dependent.

- The Mo disk has a uniform temperature, equalling the melting temperature T_m.

- Supercooling or pressure dependent phenomena are absent in the contact area.

- Melting effects of the substrate material are to be neglected even if melting obviously will take place.

Basically the mathematical background is given by Neumann and Schwartz and can befound in ref. [3].

Fig. 1.5 defines the coordinate system to be used.
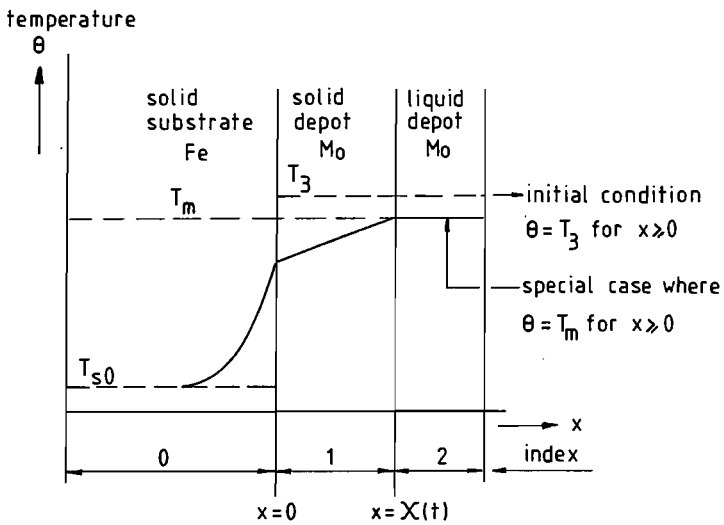
x=0 marks the position of the substrate
x=X(t) marks the position of the surface of
separation between the solid and liquid phases
of the spraymaterial

Fig. 1.5:   Coordinate system for heat transfer from disk to substrate.

15

The initial conditions:

Suppose the region $x > 0$ to be initially liquid at uniform temperature T_3 and the region $x < 0$ to be initially solid at the uniform temperature T_{s0}. The formulation of these conditions is:

$$x < 0 : \quad \theta_0 = T_{s0} \text{ for } t = 0$$

$$x > 0 : \quad \theta_2 = T_3 \text{ for } t = 0$$

A simplified special case will be considered:

$$x > 0 : \quad \theta_2 = T_3 = T_m = \text{melting temperature.}$$

The heat conduction equations:

$$x \leq 0 \quad : \quad \frac{\partial^2 \theta_0}{\partial x^2} - \frac{1}{a_0} \cdot \frac{\partial \theta_0}{\partial t} = 0$$

$$(1.18)$$

$$0 \leq x \leq X(t) \quad : \quad \frac{\partial^2 \theta_1}{\partial x^2} - \frac{1}{a_1} \cdot \frac{\partial \theta_1}{\partial t} = 0$$

$$(1.19)$$

$$x \geq X(t) \quad : \quad \frac{\partial^2 \theta_2}{\partial x^2} - \frac{1}{a_2} \cdot \frac{\partial \theta_2}{\partial t} = 0$$

$$(1.20)$$

For the special case where $\theta_2 = T_3 = T_m$

e.q. (1.20) falls due.

The boundary conditions:

$$\theta_0 = T_{s0} \text{ as } x \rightarrow -\infty \qquad (1.21)$$

$$\theta_0 = \theta_1 \text{ as } x = 0 \qquad (1.22)$$

16

$$\lambda_0 \frac{\partial \theta_0}{\partial x} = \lambda_1 \frac{\partial \theta_1}{\partial x} \quad \text{as} \ x = 0 \tag{1.23}$$

$$\lambda_1 \frac{\partial \theta_1}{\partial x} - \lambda_2 \frac{\partial \theta_2}{\partial x} = L\rho \frac{dX}{dt} \quad \text{as} \ x = X(t) \tag{1.24}$$

$$\theta_1 = \theta_2 \quad \text{as} \ x = X(t) \tag{1.25}$$

For the special case where $\theta_2 = T_3 = T_m$ eq. (1.24) simplifies to :

$$\lambda 1 \frac{\partial \theta_1}{\partial x} = L\rho \frac{dX}{dt} \quad \text{as} \ x = X(t) \tag{1.24a}$$

and eq. (1.25) changes into:

$$\theta_1 = \theta_2 = T_m \quad \text{as} \ x \geq X(t) \tag{1.25a}$$

Particular solutions to the equations:

SOLUTION 1 : For the substrate.

$$\text{ASSUME} \ \theta_0 = T_{s0} + \alpha \left(1 + \text{erf} \frac{x}{\sqrt{4a_0 t}}\right) \tag{1.26}$$

where α is a constant to be determined. Solution (1.26) satisfies eq. (1.18) and

because $\theta_0 \rightarrow T_{s0}$ as $x \rightarrow -\infty$, also satisfies condition (1.21)

SOLUTION 2: For the solid depot.

$$\text{ASSUME} \ \theta_1 = T_{s0} + \beta + \gamma \, \text{erf} \frac{x}{\sqrt{4a_1 t}} \tag{1.27}$$

where β and γ are constants.

Solution (1.27) satisfies eq. (1.19) and also satisfies condition (1.22) if $\beta = \alpha$

because $\theta_0 = \theta_1$ as $x = 0$.

Eq. (1.27) now can be written as:

$$\theta_1 = T_{s0} + \alpha + \gamma \, \text{erf} \frac{x}{\sqrt{4a_1 t}} \tag{1.27a}$$

17

and this solution still has to satisfy condition (1.23).

The connection between α and γ can be determined as follows: find expressions for $\dfrac{\partial \theta_0}{\partial x}$ and $\dfrac{\partial \theta_1}{\partial x}$ by differentiating the eq. (1.26) and (1.27) and substitute the result into condition (1.23).

$$\frac{\partial \theta_0}{\partial x} = \alpha \frac{\partial}{\partial x} \, \text{erf} \, \frac{x}{\sqrt{4a_0 t}} = \alpha \cdot \frac{2}{\sqrt{\pi}} \cdot e^{-x^2/4a_0 t} \cdot \frac{1}{\sqrt{4a_0 t}}$$

$$\frac{\partial \theta_0}{\partial x} = \frac{\alpha}{\sqrt{\pi a_0 t}} \cdot e^{-x^2/4a_0 t} \tag{1.28}$$

For $x = 0$:

$$\left(\frac{\partial \theta_0}{\partial x} \right)_{x \, = \, 0} = \frac{\alpha}{\sqrt{\pi a_0 t}} \tag{1.29}$$

$$\frac{\partial \theta_1}{\partial x} = \gamma \frac{\partial}{\partial x} \, \text{erf} \, \frac{x}{\sqrt{4a_1 t}} = \frac{\gamma}{\sqrt{\pi a_1 t}} \cdot e^{-x^2/4a_1 t}$$

$$\tag{1.30}$$

For $x = 0$:

$$\left(\frac{\partial \theta_1}{\partial x} \right)_{x \, = \, 0} = \frac{\gamma}{\sqrt{\pi a_1 t}} \tag{1.31}$$

Substitution of eq. (1.29) and (1.31) into eq. (1.23) gives:

$$\lambda_0 \frac{\alpha}{\sqrt{\pi a_0 t}} = \lambda_1 \frac{\gamma}{\sqrt{\pi a_1 t}}$$

Introducing $B = \dfrac{\alpha}{\gamma}$ and using the definition for the thermal diffusivity $a = \dfrac{\lambda}{\rho c}$, this relation can be written as:

$$B = \frac{\alpha}{\gamma} = \frac{\sqrt{\lambda_1 \rho_1 c_1}}{\sqrt{\lambda_0 \rho_0 c_0}} \qquad (1.32)$$

So, if B is chosen according to eq. (1.32) the conditon (1.23) will be satisfied.

Using (1.32), eq. (1.27a) may be expressed as:

$$\theta_1 = T_{s0} + \gamma \left(\frac{\alpha}{\gamma} + \mathrm{erf} \, \frac{x}{\sqrt{4 a_1 t}} \right) \qquad \text{or:}$$

$$\theta_1 = T_{s0} + \gamma \left(B + \mathrm{erf} \, \frac{x}{\sqrt{4 a_1 t}} \right) \qquad (1.26b)$$

Overlooking the equations it can be established that the solutions (1.26) and (1.27) are appropriate for the equations (1.18) and (1.19) and the conditions (1.21), (1.22) and (1.23) are satisfied. For the special case where $\theta_2 = T_3 = T_m$ the remaining boundary conditions are (1.24a) and (1.25a) The condition (1.25a) requires $\theta_1 = \theta_2 = T_m$ as $x \geq X(t)$. Using eq. (1.27b) at $x = X(t)$, condition (1.25a) gives:

$$\gamma \left(B + \mathrm{erf} \, \frac{X}{\sqrt{4 a_1 t}} \right) = T_m - T_{s0} \qquad (1.33)$$

Since this equation has to be valid for all values of the time, X must be proportional to $\sqrt{t}$, which is Neumann's assumption:

$$X = p \sqrt{4 a_1 t} \qquad (1.34)$$

where p is a numerical constant to be determined from the remaining condition (1.24a).

Using (1.30) for $x = X(t)$, condition (1.24a) gives:

$$\lambda_1 \cdot \frac{\gamma}{\sqrt{\pi a_1 t}} \cdot e^{-X^2/4a_1 t} = L \cdot \rho \cdot \frac{dX}{dt} \tag{1.35}$$

This equation is in fact the energy balance at the solidification front.

From (1.34) follows:

$$\frac{dX}{dt} = p \sqrt{\frac{a_1}{t}} \tag{1.36}$$

Substitution of (1.36) into (1.35) yields:

$$\lambda_1 \cdot \frac{\gamma}{\sqrt{4a_1 t}} \cdot e^{-X^2/4a_1 t} = L \cdot \rho \cdot p \cdot \sqrt{\frac{a_1}{t}} \tag{1.37}$$

From (1.33) and (1.34) follows:

$$\gamma = \frac{T_m - T_{s0}}{B + erf \dfrac{X}{4a_1 t}} = \frac{T_m - T_{s0}}{B + erf\, p} \tag{1.38}$$

Inserting (1.38) and (1.34) into (1.37) yields:

$$\lambda_1 \frac{T_m - T_{s0}}{B + erf\, p} \cdot \frac{1}{\sqrt{\pi a_1 t}} \cdot e^{-p^2 \cdot 4a_1 t/4a_1 t} = L \cdot \rho \cdot p \sqrt{\frac{a_1}{t}}$$

Suppose that the density of the liquid equals the density of the solidified material,

then $\rho = p_1$ and the last equation can be rewritten as:

$$\lambda_1 \frac{T_m - T_{s0}}{B + erf\, p} \cdot \frac{1}{\sqrt{\pi a_1 t}} \cdot \frac{1}{\sqrt{\dfrac{a_1}{t}}} = L \cdot \rho_1 \cdot p \cdot e^{p^2}$$

Finally:

$$(B + erf\, p)\ pe^{p^2} = \frac{C_1\,(T_m - T_{s0})}{L\,\sqrt{\pi}} \tag{1.39}$$

20

Recapitulation:

Eq. (1.26) : $\theta_0 = T_{s0} + \alpha \left(1 + \text{erf}\, \dfrac{x}{\sqrt{4a_0 t}}\right)$

is the temperature profile in the substrate.

Eq. (1.27b): $\theta_1 = T_{s0} = \gamma \left(B + \text{erf}\, \dfrac{x}{\sqrt{4a_1 t}}\right)$

is the temperature profile in the solid depot.

Eq. (1.32): $B = \dfrac{\alpha}{\gamma} = \dfrac{\sqrt{\lambda_1 \rho_1 c_1}}{\sqrt{\lambda_0 \rho_0 c_0}}$ $= \text{constant}$

Eq. (1.34): $X = p\sqrt{4a_1 t}$

is the location of the surface of separation between the solid

and the liquid phases of the depot material.

Eq. (1.38): $\gamma = \dfrac{T_m - T_{s0}}{B + \text{erf}\; p};$ $= \text{constant}$

Eq. (1.39): $(B + \text{erf}\; p)\, p e^{p^2} = \dfrac{C_1\,(T_m - T_{s0})}{L\,.\;\sqrt{\pi}}$ is a

relation to determine the constant p emanating from the

energy balance at the solidification front.

From (1.32) follows: $\alpha = \gamma B.$, using eq. (1.38) gives:

$$\alpha = \dfrac{B.\,(T_m - T_{s0})}{B + \text{erf}\; p} \qquad (1.40)$$

Inserting (1.40) into (1.26) gives the real substrate temperature profile:

$$\theta_0 = T_{s0} + \dfrac{B\,(T_m - T_{s0})}{B + \text{erf}\; p} \cdot \left(1 + \text{erf}\, \dfrac{x}{\sqrt{4a_0 t}}\right)$$

$$(1.41)$$

21

Inserting (1.38) into (1.27b) gives the solid depot temperature profile:

$$\theta_1 = T_{s0} + \frac{T_m - T_{s0}}{B + \mathrm{erf}\ p} \cdot (B + \mathrm{erf}\frac{x}{\sqrt{4a_1 t}}) \qquad (1.42)$$

Rewriting (1.41) and (1.42) yields the formulations for the temperature profiles:

$$\frac{\theta_0 - T_{s0}}{T_m - T_{s0}} = \frac{B}{B + \mathrm{erf}\ p} \cdot (1 + \mathrm{erf}\frac{X}{\sqrt{4a_0 t}}) \qquad (1.41a)$$

$$\frac{\theta_1 - T_{s0}}{T_m - T_{s0}} = \frac{1}{B + \mathrm{erf}\ p} \cdot (B + \mathrm{erf}\frac{x}{\sqrt{4a_1 t}}) \qquad (142a)$$

Eq. (1.41a) and (1.42a) are purely analytical and strictly hold for two $\frac{1}{2}\infty$ bodies. Nevertheless the formula's also describe exactly the temperature history of a disk shaped depot of limited thickness and of the substrate during the solidification. So if the time under consideration is restricted to $t \leq t_{sol}$, the equations hold fully under the registered assumptions.

From eq. (1.34) follows:

$$t = \frac{X^2}{4a_1\ p^2} \qquad (1.34a)$$

and since X in this equation gives the position of the solidification front, the equation may be read as:

$$t_{sol} = \frac{X^2}{4a_1\ p^2} \qquad (1.34b)$$

where t_{sol} is the solidification time for a lamella with thickness X.

In order to calculate the solidification time and the actual temperature profiles according to eq. (1.41a) and (1.42a) some numerical values of thermophysical properties must be introduced, see table 2, Iron is taken as substrate material and $T_{s0} = 20C$.

Table 2: Numerical values of some thermophysical quantities.

Quantity	Fe	Mo	AISI–316	Unit
λ	75	146	18	$Js^{-1}m^{-1}K^{-1}$
ρ	7870	10200	7670	kgm^{-3}
$C=C_p$	460	255	489	$Jkg^{-1}K^{-1}$
a	$2,07 \cdot 10^{-5}$	$5,61 \cdot 10^{-5}$	$4,8 \cdot 10^{-6}$	$m^2 s^{-1}$
T_m	1536	2610	1375–1400	C
L	$272 \cdot 10^3$	$288 \cdot 10^3$	$297 \cdot 10^3$	Jkg^{-1}
$\sqrt{\lambda \rho c}$	16478	19478	8217	$Jm^{-2}K^{-1}s^{-\frac{1}{2}}$
$\dfrac{C \ (T_m - T_{s0})^*}{L \ \sqrt{\pi}}$	1,4464	1,2938	1,2707	[–]
T_{s0}	20			C
		Mo on Fe	AISI–316 on Fe	[–]
B		1,1826	0,4987	[–]
$(B + erf \ p) \ pe^{p^2}$		1,2938	1,2703	[–]
p		0,5487	0,6835	[–]
$p.e^{p^2}$		0,7415	1,0905	[–]
erf p		0,5622	0,6662	[–]
$\sqrt{\dfrac{a_1}{a_0}}$		1,6463	0,4815	[–]

$$^* \text{ e.g. for Fe: } \frac{C \ (T_m - T_{s0})}{L \ \sqrt{\pi}} = \frac{460 \ (1536 + 273 - 293)}{272 \cdot 10^3 \ \sqrt{\pi}} = 1,4464$$

The solidification time is proportional to the square of the disk thickness X, thus demonstrating that the particle size has a strong influence on the processes in the interface with the substrate during solidification. On the basis of eq. (1.34a) the solidification time for increasing lamella thicknesses and for two different materials, Mo and steel AISI–316, will be determined to gain a real impression about the order of time length that plays a role in solidification processes, see table 3 and fig 1.6.
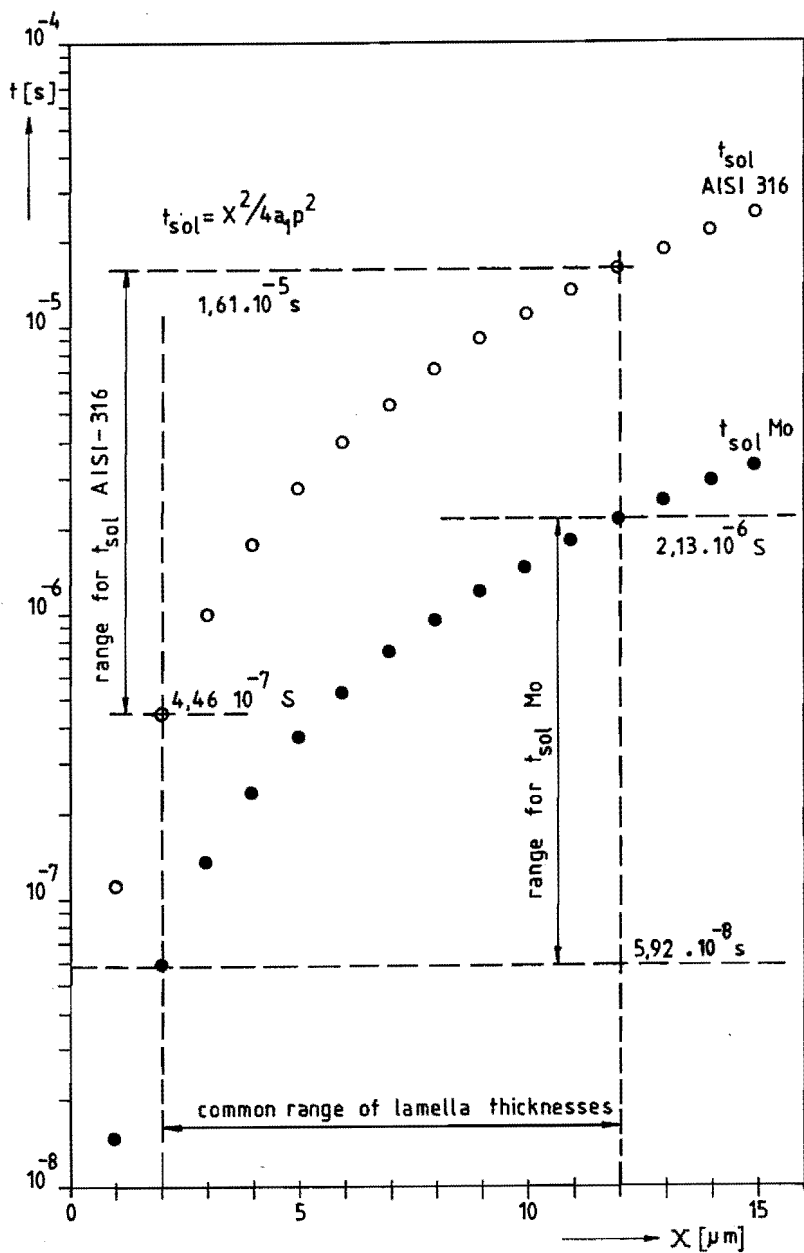
Fig. 1.6: Solidification time on a Fe substrate for Mo and AISI – 316 as a function of lamella thickness.

24

Table 3: Solidification time on an Fe substrate as a function of the lamella thickness for Mo and AISI–316.

| X μm | $t_{sol} = X^2/4a_1 \, p^2$ [s]. (eq. 1.34a) | |
	Mo on Fe	AISI–316 on Fe
1	$1,48 \cdot 10^{-8}$	$1,11 \cdot 10^{-7}$
2	$5,92 \cdot 10^{-8}$	$4,46 \cdot 10^{-7}$
3	$1,33 \cdot 10^{-7}$	$1,00 \cdot 10^{-6}$
4	$2,37 \cdot 10^{-7}$	$1,78 \cdot 10^{-6}$
5	$3,70 \cdot 10^{-7}$	$2,79 \cdot 10^{-6}$
6	$5,33 \cdot 10^{-7}$	$4,01 \cdot 10^{-6}$
7	$7,25 \cdot 10^{-7}$	$5,46 \cdot 10^{-6}$
8	$9,47 \cdot 10^{-7}$	$7,14 \cdot 10^{-6}$
9	$1,20 \cdot 10^{-6}$	$9,03 \cdot 10^{-6}$
10	$1,48 \cdot 10^{-6}$	$1,11 \cdot 10^{-5}$
11	$1,79 \cdot 10^{-6}$	$1,35 \cdot 10^{-5}$
12	$2,13 \cdot 10^{-6}$	$1,61 \cdot 10^{-5}$
13	$2,50 \cdot 10^{-6}$	$1,88 \cdot 10^{-5}$
14	$2,90 \cdot 10^{-6}$	$2,18 \cdot 10^{-5}$
15	$3,33 \cdot 10^{-6}$	$2,51 \cdot 10^{-5}$

(left margin, vertical: COMMON RANGE)

Acommon range of lamella thicknesses that occur is 2 –12 μm. From these figures it appears that the lower thermal conductivity of AISI–316 causes longer solidification times. As an average holds:

$$\frac{t_{sol} \text{ AISI–316}}{t_{sol} \text{ Mo}} \cong 7,55$$

Further more it is clear that very short solidification times only occur for extreme small particles. To keep in mind, a 7 μm thick lamella of Mo has a $t_{sol} = 7,25.10^{-7}$s and the same lamella of AISI–316 has a $t_{sol} = 5,46.10^{-6}$s.

To gain some insight in the heat transfer to the surface due to one single lamella the temperature profiles in depot and substrate can be calculated just after the solidification of the lamella is completed. The procedure is the following one.

From eq. (1.34b) follows:

$$\sqrt{t_{sol}} = \frac{X}{p \sqrt{4a_1}} \qquad (1.43)$$

Inserting (1.43) into eq. (1.41a) and (1.42a) gives the temp. profiles as a function of the lamella thickness at the time $t = t_{sol}$.

SUBSTRATE:

$$\frac{\theta_0 - T_{s0}}{T_m - T_{s0}} = \frac{B}{B + \text{erf } p} (1 + \text{erf } \frac{x}{\sqrt{4a_0}} \cdot \frac{p \sqrt{4a_1}}{X})$$

So, the substrate temperature profile after solidification is:

$$\frac{\theta_0 - T_{s0}}{T_m - T_{s0}} = \frac{B}{B + \text{erf } p} (1 + \text{erf } \frac{x}{X} p \sqrt{\frac{a_1}{a_0}}) \qquad (1.44)$$

DEPOT:

$$\frac{\theta_1 - T_{s0}}{T_m - T_{s0}} = \frac{1}{B + \text{erf } p} (B + \text{erf } \frac{x}{\sqrt{4a_1}} \cdot \frac{p \sqrt{4a_1}}{X})$$

The depot profile after solidification is:

$$\frac{\theta_1 - T_{s0}}{T_m - T_{s0}} = \frac{1}{B + \text{erf } p} (B + \text{erf } \frac{x}{X} p) \qquad (1.45)$$

The actual temperature curves will now be calculated for a thin lamella having a thickness $X = 2$ μm and a thick lamella with $X = 12$ μm. They will be determined for both materials, Mo and AISI–316 on Fe. The numerical values are taken from

or based on table 2. The calculations are listed in appendix 1 – profile 1 to 8. The results are visualized in fig. 1.7. From the graphs of fig 1.7 distinct differences appear regarding the thermal interaction between Mo and AISI–316 with Fe. The most remarkable items are:

– Mo, having a high melting temperature causes melting of the substrate while the AISI–316 contact temperature remains far below the melting point of Fe.

– A thin lamella and a thick one of the same material exhibit the same contact temperature.

– The occurrance of a steep temperature gradient for Mo and a moderate one for AISI–316, see table 4.

Table 4: Average gradients after solidification for $12\mu m \leq x \leq X = 12 \ \mu m$.

gra-dient	Mo	on Fe	AISI–316	on Fe
$\dfrac{d\theta}{dx}$	$\dfrac{2610-1775,5}{12\cdot10^{-6}} =$	$\dfrac{1775,5-373,3}{12\cdot10^{-6}} =$	$\dfrac{1115-488,7}{12\cdot10^{-6}} =$	$\dfrac{488,7-320,9}{12\cdot10^{-6}}$
$\dfrac{deg}{m}$	$69,5\cdot10^{6}$	$116,9\cdot10^{6}$	$52,2\cdot10^{6}$	$14,0\cdot10^{6}$

The penetration of the latent heat after solidifcation extends over a substrate depth roughly equaling twice the lamella thickness. Thermal stresses are proportional to the temperature gradient, thus a thin lamella will suffer more than a thick one from the induced stress.

27
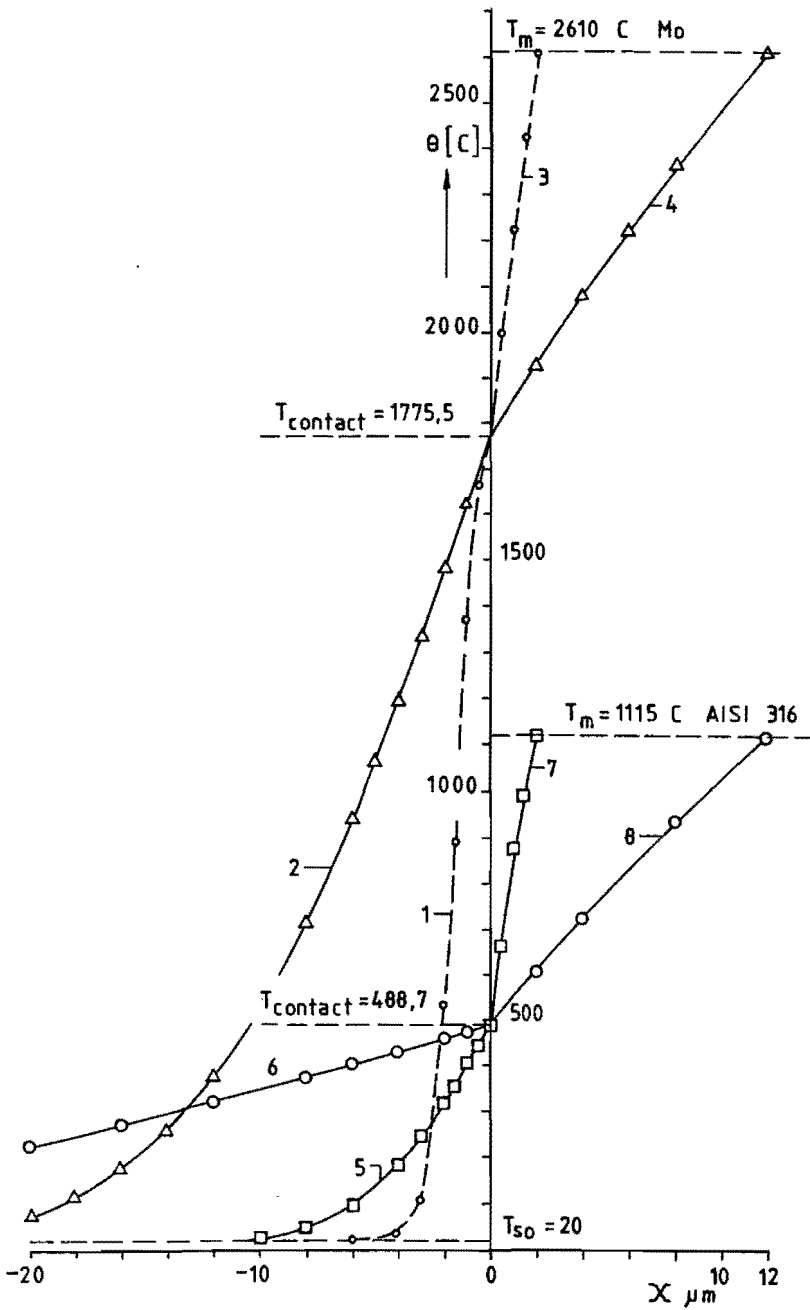
Fig. 1.7: Temperature profiles right after the solidification of a thin (2 μm and a thick (12 μm) lamella of Mo and AISI $-$ 316 steel on Fe.

28

Especially table 4 shows that the gradient in the Fe substrate is larger than the gradient in the Mo deposit and, on the other hand, the gradient in the Fe substrate is smaller than the gradient in the AISI–316 steel. Both phenomena can be explained on the basis of the property B, the ratio of the contact conductivities of the spray– and the substrate material. For Mo on Fe, $B = 1,1826$ and for AISI–316 on Fe, $B = 0,4987$. The high value for B in the first combination is representing a system where the latent heat is set free fastly. To earry this heat away, the substrate has to adopt a steep gradient. When B is rather low, as is the case in the second combination, the latent heat is set free slowly and a moderate gradient within the substrate is sufficiently effective for the necessary heat conduction. To close this section an important question is put forward: how does the thermal interaction influence the adhesion between spray and substrate material? Fig 1.7 represents $\theta_0 = \theta_0 (x_1 t)$ on a micronscale. For the estimation of diffusion effects which possibly may occur in the contact area, it is necessary to g further into detail. The temperature–time field very close to the contact surface has to be considered on an Ångstrom scale as will be done in the next section.

1.3   Material transport across the interface between spray material and
       substrate.

The low contact temperature inherent to the combination AISI–316 on Fe climinates large scale interdiffusion between these components. On the other hand, Mo on Fe causes very high contact temperatures, even exceeding the melting point of Fe. Therefore, this system will be examined closer. A basic assumption in this discussion is that melting of the substrate is ignored. This implies that only diffusion in solid Fe takes place, thus stating a lower limit to the diffusion effects than can be expected.

Heywegen [4] gives full details about the diffusion of Mo into Fe. Van Loo [5] and Heywegen report that the diffusion of Mo into Fe is by far more important than the reverse one which justifies the next simplification: only diffusion of Mo into Fe will be taken into account. The phase diagram Mo–Fe [6], see fig 1.8, shows an
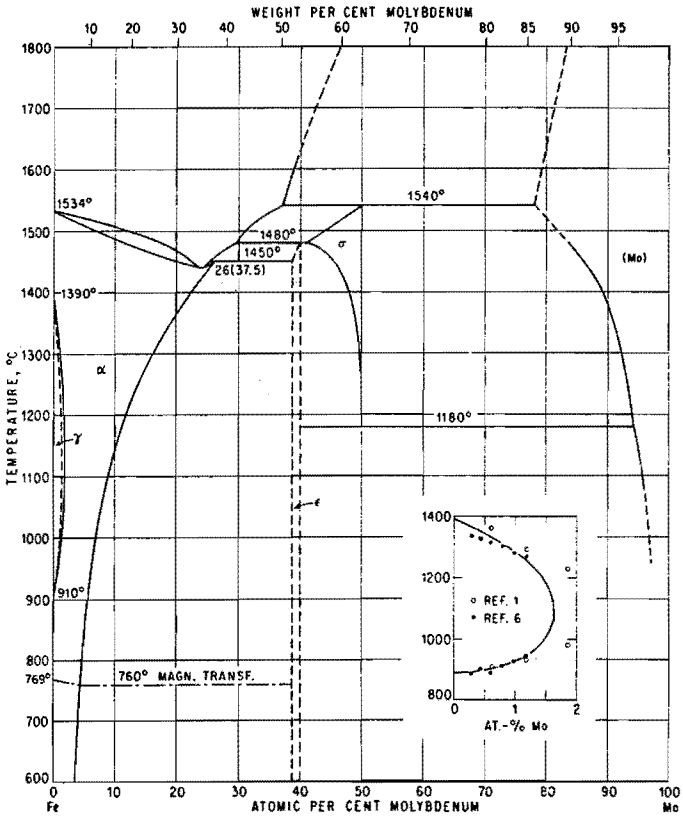
Fig. 1.8:   Phase diagram Fe – Mo, [6].

α–solid solution of Mo in Fe, containing 2,71 ^{W}/o Mo at 1100 C. For T > 1390 C the Mo content of α–Fe runs from zero to more than 30 ^{W}/o. The formation of α solid solution may guarantee a good bond between Mo and Fe. Suppose that the

30

bulk diffusion laws and data which were determined or used in [4] also hold for

the spray situation, then for the development of α solid solution can be written:

$$x_\alpha^2 = k\,t \qquad (1.46)$$

which is the parabolic growth law for diffusion, where:

x_α = penetration of α solid solution into the substrate.

k = penetration "constant" depending on the temperature.

Penetration constant k as a function of the temperature θ, taken from figure 8.3,

ref. [4]:

θ [C]	1000	1200	1400[*]	1600[*]	1775,5[*]
$k\left[\dfrac{m^2}{s}\right]$	3.10^{-13}	$7,5.10^{-12}$	$5,5.10^{-11}$	3.10^{-10}	$1,7.10^{-9}$

The [*] marked values are obtained by extrapolation.

The α solid solution penetration into the substrat can now be calculated as a

function of time. Mind that the temperature is supposed to be constant during the

variation of time. See table 5 and fig 1.9.

<u>Table 5</u>: Values for $x_\alpha = \sqrt{kt}$; x_α in 10^{-10}m $\hat{=}$ 1 Å

θ_0 [c]	$\begin{array}{c}t\\ \text{[s]}\end{array}$ 10^{-9}	10^{-8}	10^{-7}	10^{-6}	10^{-5}
1000	0,17	0,54	1,73	5,47	17,3
1200	0,86	2,73	8,66	27,3	86,6
1400	2,34	7,41	23,4	74,1	234
1600	5,47	17,3	54,7	173	547
1775,5	13,0	41,2	130	412	1303
Symbol	in	fig.	1.9		
	●	⊙	□	△	▽
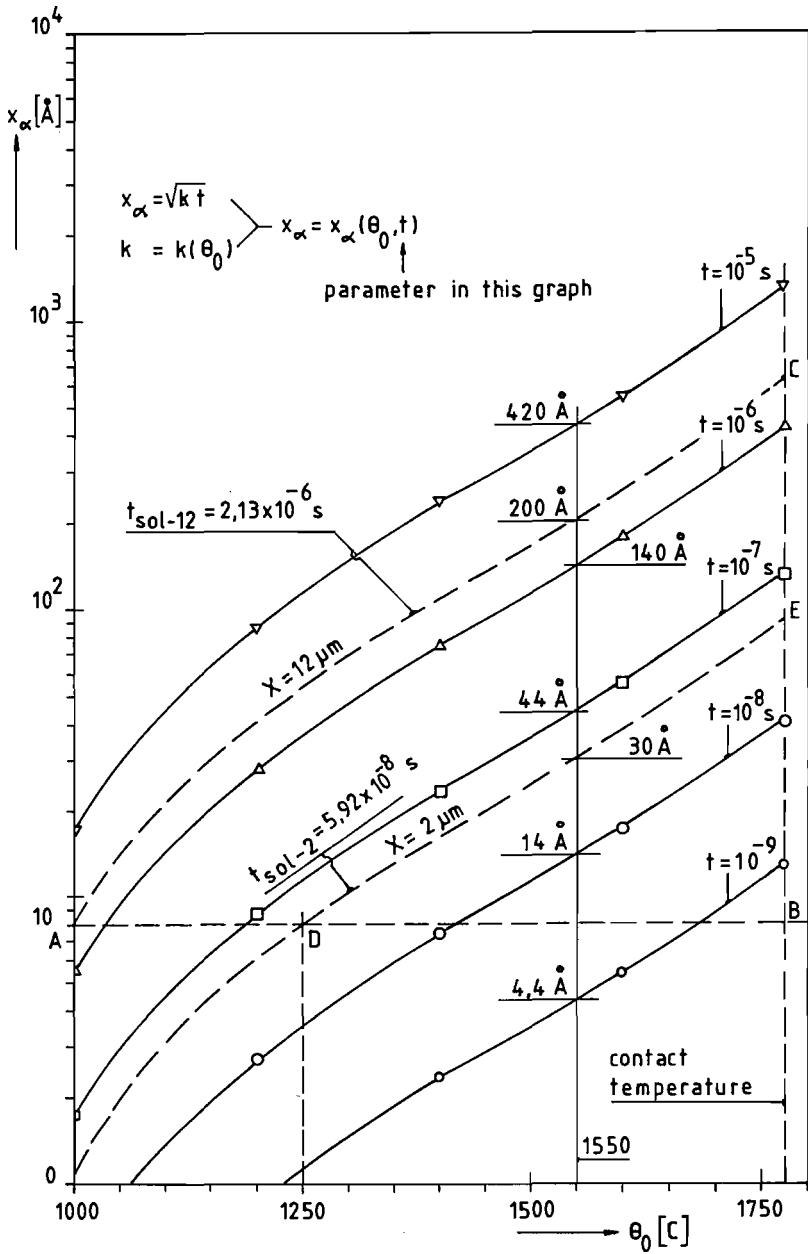
Fig. 1.9:   Penetration of α − solid solution into the substrate.

The time temperature conditions above the dotted line in table 5 do not permit large scale diffusion effects. Below that line the conditions are such that diffusion over a penetration range from 8,66 − 1303 Å can take place, which means that the α solid solution abridges at least 3 atomic distances. The figures of table 5 are visualized in fig 1.9 where the time is taken as the parameter. If an 8 Å deep diffusion zone is chosen as the arbitrary lower limit for real diffusion, then the dotted line AB in fig. 1.9 marks this boundary. The vertical line at the contact temperature 1775,5 C is supposed to be the temperature limit for the estimation of diffusion effects in the system under consideration. The question now arises what time limit should be taken into account for the estimation of diffusion. To answer this queston the temperature profiles $\theta_0 = \theta_0$ (x,t) will be determined on sub−micron scale for x <u>during</u> the solidification of one lamella of Mo. The time variation for the calculation of the profiles will run from 10^{-9} to 10^{-5} [s], thus including the solidification times for a thick lamella $(t_{sol-12} = 2{,}13 \cdot 10^{-6}$ [s]) and for a thin one $(t_{sol-2} = 5{,}92 \cdot 10^{-8}$ [s]). See appendi 2, profiles 1 to 6. The results are firstly compiled in fig 1.10 where the depth x below the surface is taken as parameter. Fig 1.10 shows that a temperature rise to e.g. 1000 C occurs to a depth of 1000 Å in the very short time of $t_1 = 10^{-9}$[s] while the same temperature rise to the depths of 5000 Å and 10.000 Å takes $t_2 = 2{,}6 \cdot 10^{-8}$[s] and $t_3 = 1{,}1 \cdot 10^{-7}$[s] respectively. In order to overlook the heat penetration as function of time, the figures of appendix 2 can also be grouped according to fig. 1.11 where $\theta_0 = \theta_0$ (x,t) is given with t as parameter. From fig. 1.9 and 1.11 the following data regarding heat pentration and the penetration of α solid solution can be read easily, see table 6.
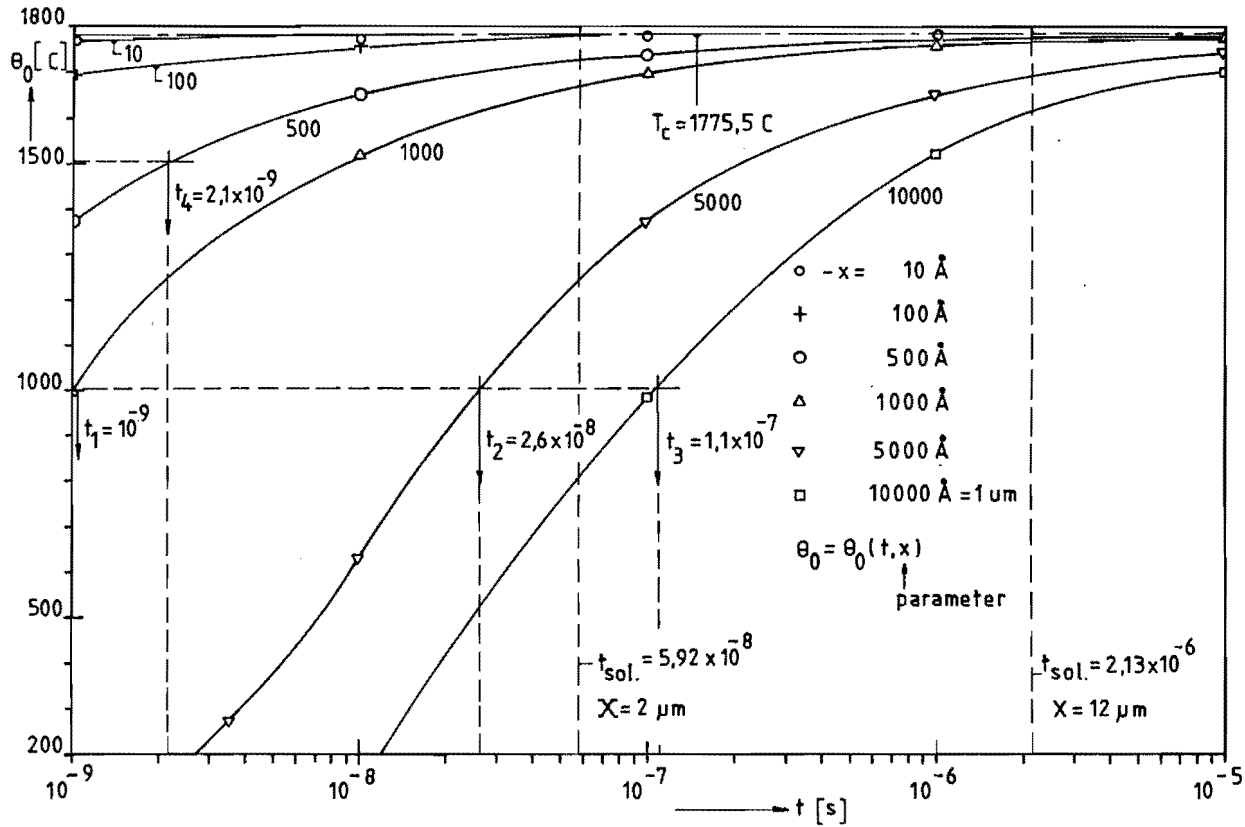
Fig. 1.10: Temperature profiles near to the contact surface as a function of time: Mo on Fe.
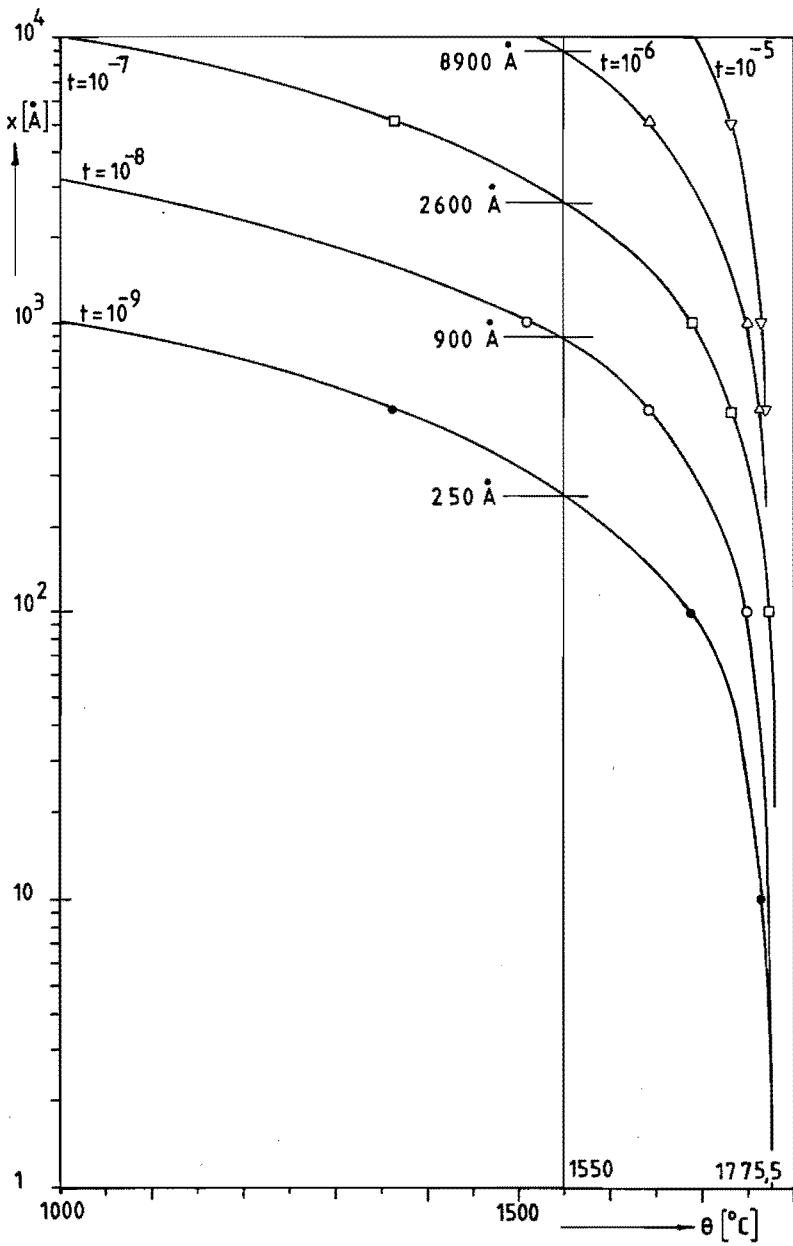
Fig. 1.11: Penetration of heat.

35

Table 6: Penetration of heat and α solid solution into the substrate at a constant temperature of 1550 C.

T	θ_0	x	x_α	x_α/x
[s]	[C]	[Å]	[Å]	[--]
10^{-9}	1550	250	4,4	0,0176
10^{-8}	1550	900	14	0,0155
10^{-7}	1550	2600	44	0,0169
10^{-6}	1550	8900	140	0,0157
10^{-5}	1550	25570*	420	0,0164

N.B. The * marked value for x has been calculated from the averaged value $\dfrac{x_\alpha}{x} = 0{,}0164$ which holds for the time elapse from 10^{-9}–10^{-6} [s]. It is not surprising that the factor x_α/x has more or less the same value because heat and material penetration do obey analogous diffusion laws. The main conclusion that can be drawn form table 6 is that the temperature profile $\theta = 1550$ C is well ahead of the materialdiffusion profile. There is no objection against adopting a constant substrate temperature of 1550 C close to the surface in order to estimate the lower limit of the really occurring diffusion layer thickness. The timeperiod during which this temperature is maintained is t_{sol}, thus answering the open question about the time limit for diffusion. After inserting in fig. 1.9 the dotted inclined lines AC and DE for $t = t_{sol-12} = 2{,}13 \cdot 10^{-6}$ [s] and $t = t_{sol-2} = 5{,}92 \cdot 10^{-8}$ [s] respectively, the estimated diffusion layer thickness right after solidification is 30 Å for a thin lamella and 200 Å for a thick lamella of Mo. These data are based on the assumption that only solid material diffusion takes place. In fact the substrate will first melt over a certain depth during the solidification.

The heat absorbtion connected with the melting of the substrate is not included in the mathematical equations (1.18) to (1.25a). Concluding this section: melting of the substrate over a certain depth − 1μm? − and diffusion of Mo over a distance ranging from 30 Å to 200 Å is likely to occur. The time elapse during which solidification takes place is t_{sol}. However, the substrate undergoes physical and chemical changes in a shorter period of time, overall characterized by table 6. It is likely that a metallurgical bond comes into existence between Mo en Fe−or comparable systems − due to thermal interaction of the spraymaterial and the substrate. Allsop e.a. [7] reported allready in 1961 about the existence of a 1 μm thick interfacial layer between Fe and Mo spray material, while in [8] details are given about the formation of reaction interfaces between Mo and Fe at elevated heat flow rates through the substrate surface. Steffens e.a. [9] describe the Niobium−steel interface sprayed under inert condition. The micro analysis of the interfacial area reveals a 10 to 13 μm thick intermediate zone which is also attributed to the thermal interaction. The remarkable thing now is that interfacial layer thicknesses exceeding 1 μm are not likely to occur during a standard plasma spray operation. Nevertheless they are determined by micro analysis by several authors which brings us to the background of this thesis.

1.4   Background of this thesis.

As elucidated in the foregoing sections, thermal interaction plays a part in the adhesion phenomena between coating and substrate. If the substrate is converted to liquid heavy interdiffussion will occur and a good bond is assured. If diffusion into a solid substrate takes place, only very restricted diffusion patterns are to be expected, if any. It is common practice to roughen the surface by grit blasting, thus creating an ancre ground which mechanically locks the coating material.

37

Nevertheless bonding also can be created on a polished surface even with moderately heated particles. This thesis deals with the investigation of the kinetic–dynamic interaction part of spray material with the substrate. It is expected that some of the bonding phenomena occuring when spraying moderately heated particles can be understood.

CHAPTER 2   COLLISION THEORY.

2.1   Introduction.

In a first round a theory will be depicted regarding the collision of a spherical

particle onto a smooth and rigid substrate, see ref. [10]. A rigid substrate does not

take part in the energy absorbtion mechanisms during the collision; it does either

vibrate neither erode. Heat withdrawal from the particle will be considered apart

from the other collision phenomena. The spherical particle may be solid or liquid,

it's main property is to be initially spherical. The theory is in first instance

applied to the arbitrary chosen spray material aluminium. Such a numerical

application illustrates the theory and helps to identify weak places within the

theory. The aim of this first round theory is to give a qualitative description of

the collision phenomena which cause the final shape of the spread particle. In a

second round of the theory the aim is to find out whether the deformation

processes taking place during the collision, adds to the adhesion of the spray

particle. The collision model will exist of two main parts: a thermodynamical part

and a dynamical part.

2.2   Thermodynamical aspects of the collision of a spherical spray

             particle onto a rigid, smooth surface.

2.2.1   Compression.

The very abrupt stop which a particle undergoes during the collision gives rise to

the formation of shock waves in the particle material as well as in the substrate.

From ballistic research it is known that material under high pressure looses its

typical relationship between either elastic or plastic stress and the strain. The stress – strain relation which rules the high pressure deformation during a collision is called the hydrostat or Hugoniot curve. An introduction to his matter is given in ref. [11] where Zukas describes a one dimensional approach related to the dilatation of material only. In such a shock wave regime high pressures are generated which can lead to considerable changes in densitiy of the material. As long as no lateral deformation due to plastic flow of the material occurs, the one dimensional shock approach implying an uniaxial strain situation holds fully. The following derivation of the shock wave equations can basically be found in [11]. Consider a plate of compressible material that suddenly undergoes a pressure P_1 at one face. The pressure pulse propagates at velocity U_s in the material initially at pressure P_0. The applied pressure P_1 compresses the material, initially at the density P_0, to the density P_1 and accelerates simultaneously the compressed material to a velocity U_p. Fig 2.1 depicts the situation under consideration. Under influence of the pressure P_1, material initally at location AA has moved to
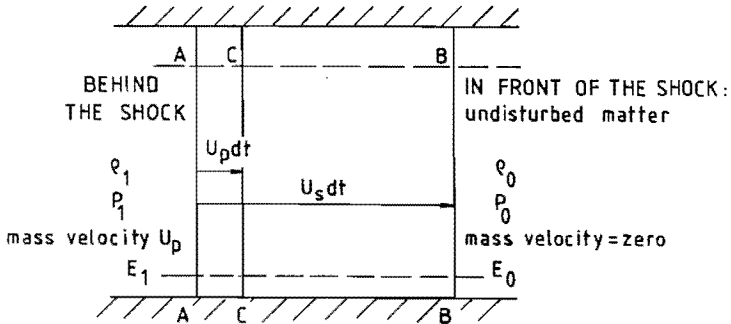
Fig. 2.1:   Progress of a plane shock wave, [11]. Uniaxial strain situation, no lateral displacements.

40

CC after dt while the shock front has moved to BB. The conservation laws for mass, momentum and energy now can be applied across the shock wave.

Conservation of mass:

The matter initially within the space AABB has been forced by the shock wave into the space CCBB. Per unit cross–sectional area the initial mass of the control volume was $\rho_0\, U_s$ dt and after the shock the same mass is $\rho_1\, (U_s - U_p)$ dt, which leads to:

$$\rho_0\, U_s = \rho_1\, (U_s - U_p); \qquad\qquad (2.1)$$

rewritten in terms of specific volume V:

$$V_1 U_s = V_0\, (U_s - U_p) \qquad\qquad (2.1a)$$

where $V = \dfrac{1}{\rho}$

Conservation of momentum:

The mass $\rho_0 U_s dt$ is accelerated in the time dt to the velocity U_p by the force $P_1 - P_0$. Newton's law applied to this mass gives:

$$P_1 - P_0 = \frac{\rho_0\, U_s\, dt\, U_p}{dt} \qquad ; \qquad \text{or:}$$

$$P_1 - P_0 = \rho_0\, U_s\, U_p \qquad\qquad (2.2)$$

41

Conservation of energy:

The work done by the shock wave equals the sum of the increase in both kinetic and internal energy of the system. The work done is $P_1 U_p$ dt. The mass $\rho_0 U_s$ dt is brought to a velocity U_p, so the increase in kinetic energy is: $\frac{1}{2}\rho_0 U_s$ dt U_p^2. The specific internal energy changes from E_0 to E_1, thus:

$$P_1 U_p \, dt = \frac{1}{2}\rho_0 U_s U_p^2 \, dt + \rho_0 U_s \, dt \, (E_1 - E_0)$$

or:

$$P_1 U_p = \frac{1}{2}\rho_0 U_s U_p^2 + \rho_0 U_s (E_1 - E_0) \qquad (2.3)$$

From (2.1) follows: $U_p = \dfrac{\rho_1 - \rho_0}{\rho_1} U_s \qquad (2.1b)$

Substitution of (2.1b) into (2.2) yields an equation for the shock velocity:

$$U_s^2 = \frac{\rho_1}{\rho_0} \left(\frac{P_1 - P_0}{\rho_1 - \rho_0} \right) \qquad (2.4)$$

or:

$$U_s^2 = \frac{1}{\rho_0^2} \left(\frac{P_1 - P_0}{V_0 - V_1} \right) \qquad (2.4a)$$

Substitution of (2.4) into (2.1b) gives:

$$U_p = \frac{\rho_1 - \rho_0}{\rho_1} \left(\frac{\rho_1}{\rho_0} \cdot \frac{P_1 - P_0}{\rho_1 - \rho_0} \right)^{\frac{1}{2}} \qquad (2.5)$$

Substitution of (2.4) and (2.5) into eq. (2.3) yields the Rankine –Hugoniot equation:

$$E_1 - E_0 = \frac{1}{2}(P_1 + P_0) \left(\frac{1}{\rho_0} - \frac{1}{\rho_1} \right) \qquad (2.6)$$

$$= \frac{1}{2}(P_1 + P_0)(V_0 - V_1) \qquad (2.6a)$$

42

Survey of equations and parameters: Three conservation equations contain 8
parameters:

Parameter	1	2	3	4	5	6	7	8
	E_1	ρ_1	P_1	U_s	U_p	E_0	ρ_0	P_0

Generally the parameters 6,7 and 8 are known. In the domain of high pressure
physics parameter 4 and 5 can be measured. Then, there are available 3 equations
to determine the unknown parameters 1, 2 and 3, which are the material
properties right after the pass of the shock wave front. In the domain of thermal
spraying parameter 5 $\stackrel{\frown}{=} U_p$ equals the spray particle velocity and is considered to
be known. Parameter 4 $\stackrel{\frown}{=} U_s$ only can be determined by properly equipped
laboratories, for the time being it is an unknown property. Now there are three
ways to solve the system:

first: Find a theoretical formulation for U_s and add this equation to the
            three conservation laws. Then, with 4 independent equations, E_1,
            ρ_1, P_1 and U_s can be determined.

second: Find a theoretical expression for E_1 to state the fourth required
            equation.

third: The Rankine – Hugoniot curve or simply the Hugoniot, relatess all
            pressure – density states of a material under shock load. Some of
            the Hugoniots $\stackrel{\frown}{=} P = f \left(\dfrac{V}{V_0} \right)$ curves have been determined by
            ballistic laboratories and will be presented at a later phase of this
            thesis.

The first way to solve the equations can be deduced from Zukas [11] and Zwikker [12]. Zukas states:

$$U_s = a + bUp \qquad (2.7)$$

where the constant a represents the longitudinal wave velocity in an extended medium and b is related to the Grüneisen, parameter Γ. In appendix 3 eq. (2.7) is worked out. Two expressions have been derived, which basically should give the same value for U_s.

$$U_s = (\frac{K + \frac{4}{3} G}{\rho_0})^{\frac{1}{2}} + (\frac{1}{2} + \frac{\alpha K}{2 \rho_0 C_v}) U_p \qquad (2.7a)$$

and:

$$U_s = (\frac{E}{\rho_0})^{\frac{1}{2}} (\frac{1 - \nu}{(1 + \nu)(1 - 2\nu)})^{\frac{1}{2}} + (\frac{1}{2} + \frac{\alpha E}{6(1 - 2\nu) \rho_0 C_v}) U_p \qquad (2.7b)$$

(Mind: C_v acc. to $(A_3.14a)$).

These lengthy equations can be written in a more convenient form by inserting the numerical values for the material properties.

Table 7: Material data for the calculation of U_s; $T_0 = 298$ K.

Quantity	Al	Fe	Mo	Unit
ρ_0	2700	7870	10200	kgm^{-3}
ν	0,34	0,28	0,35	[-]
E	$7 \cdot 10^{10}$	$21,3 \cdot 10^{10}$	$30,05 \cdot 10^{10}$	Nm^{-2}
$\beta = \frac{1}{3}\alpha$	$26 \cdot 10^{-6}$	$12,0 \cdot 10^{-6}$	$6,5 \cdot 10^{-6}$	K^{-1}
C_p	900	460	255	$J kg^{-1} K^{-1}$
K	$7,219 \cdot 10^{10}$	$16,833 \cdot 10^{10}$	$27,458 \cdot 10^{10}$	Nm^{-2}
G	$2,63 \cdot 10^{10}$	$8,31 \cdot 10^{10}$	$11,57 \cdot 10^{10}$	Nm^{-2}
C_v	852	452	252	$Jkg^{-1}K^{-1}$

44

Within this thesis eq.(2.7b) will be used only. It reduces to eq. (2.7b.1) when the proper material data are inserted.

For Al: $U_s = 6317 + 1,74\, U_p$ }

For Fe: $U_s = 5882 + 1,32\, U_p$ }   (2.7b.1)

For Mo: $U_s = 6876 + 1,77\, U_p$ }

The shock related material properties can be determined now in the following order,

SOLUTION SCHEME 1:

1.   Take eq. (2.7b) to calculate U_s as a function of the input parameter U_p.

2.   Substitute U_s into eq. (2.4). Then with eq. (2.5) two equations are available to calculate P_H an ρ_1.

3.   Take eq. (2.6) and calculate ΔE

Mind that the equation system does not provide means to determine shock material temperatures.

The second way to solve the equations makes use of a theory published by Duvall and Zwolinski [14, 15], which permits the calculation of ΔT, the increase in temperature during the pass of the shock front. D and Z introduce an equation of state for pressurized material:

$$P = f(V) + T \cdot g(V),\qquad\qquad (2.8)$$

indicating that the pressure increase during the occurance of shock compression, generally consists of a part $f(V)$ and a part $T \cdot g(V)$. Notice that now another parameter, namely the temperature T, has turned up in the system of equations. This implies the necessity of finding an extra consistent equation in order to solve the system of equations. Duvall [15] introduced without further explanation:

$$E = \int_0^T C_V dt + \int_{V_0}^V \left\{ T\left(\frac{\partial P}{\partial T}\right)_V - P \right\} dV \text{ which can be converted into:}$$

45

$$E_1 - E_0 = C_v (T_1 - T_0) + \int_{V_1}^{V_0} f(V)\, dV \tag{2.9}$$

See appendix 4 for an elucidation of (2.9). The Hugoniot pressure $\equiv$ shock pressure may be expressed interms of eq. (2.8) as:

$$P_1 = P_H (V1) = f(V1) + T_1 g(V1) \tag{2.10}$$

where: T_1 is the Hugoniot temperature $\equiv$ the shock temperature.

For an isothermal compression holds:

$$P_i (V_1) = f(V_1) + T_0 g(V_1) \tag{2.11}$$

where: T_0 is the initial temperature.

Subtracting (2.11) from (2.10) yields after rewriting:

$$T_1 - T_0 = \frac{P_H (V_1) - P_i (V_1)}{g(V_1)} \tag{2.12}$$

Equating (2.6a) and (2.9) gives:

$$C_v (T_1 - T_0) + \int_{V_1}^{V_0} f(V)\, dV = \tfrac{1}{2}(P_1 + P_0)(V_0 - V_1) \tag{2.13}$$

Substitution of (2.12) into (2.13) and setting

$P_1 = P_H (V_1) \equiv P_H$ and $P_i(V_1) \equiv P_i$ gives:

$$C_v \cdot \frac{P_H - P_i}{g(V_1)} + \int_{V_1}^{V_0} f(V)\, dV = \tfrac{1}{2} P_H (V_0 - V_1) + \tfrac{1}{2} P_0 (V_0 - V_1) \tag{2.14}$$

State by definition:

$$\int_{V_1}^{V_0} f(V)\, dV \equiv F(V_1) \tag{2.15}$$

and set $P_0 = 0$, then eq. (2.14) may be written as:

$$C_v \cdot \frac{P_H - P_i}{g \ (V_1)} + F \ (V_1) = \frac{1}{2} P_H \ (V_0 - V_1) \qquad (2.14a)$$

from which follows the relation between the Hugoniot pressure and the isothermal

pressure.

$$P_H = \frac{P_i - \dfrac{F \ (V_1) \ \cdot \ g \ (V_1)}{C_v}}{1 - \dfrac{(V_0 - V_1) \ \cdot \ g \ (V_1)}{2 \ C_v}} \qquad (2.16)$$

The generalized form of the equation of state, (2.8) encompasses the undefined

functions f(V) and g(V). To identify these expressions, the Murnaghan [14, 15]

equation of state will be introduced:

$$P = \frac{K}{s} [(\frac{\rho}{\rho_0})^s - 1] + (\rho T - \rho_0 T_0) \frac{\alpha \ K}{\rho_0} \qquad (2.17)$$

where: $K =$ Bulk modules $= -V_0 \ (\dfrac{\partial P}{\partial V})_T$

$\alpha =$ Coefficient of thermal expansion

$=$ 3 x linear expansion coefficient

$=$ 3β

$s =$ a parameter which Duvall has taken from data originated

by Bridgman [17], see table 8.

*   Appendix 3 gives a formula for the bulk modulus which relates K to E

and ν: $K = \dfrac{E}{3 \ (1-2\nu)}$.

Table 8: Parameters for the Murnaghan equation of state after Duvall [14, 15] and Bridgman [17]; values determined at 298 K.

Material	K Nm^{-2}	s [–]	α K^{-1}	ρ_0 $Kg\ m^{-3}$
Al[*]	$7{,}219 \cdot 10^{10}$	4,2674	$78 \cdot 10^{-6}$	2700
Cu	$13{,}755 \cdot 10^{10}$	4,6098	$51 \cdot 10^{-6}$	8890
Fe[*]	$16{,}833 \cdot 10^{10}$	3,6996	$36 \cdot 10^{-6}$	7870
Pb	$4{,}134 \cdot 10^{10}$	5,1263	$90 \cdot 10^{-6}$	11340
Sn	$5{,}601 \cdot 10^{10}$	1,6028	$69 \cdot 10^{-6}$	7300
Mg	$4{,}155 \cdot 10^{10}$	2,0406	$78 \cdot 10^{-6}$	1740
U	$9{,}769 \cdot 10^{10}$	9,3360	$51 \cdot 10^{-6}$	18700

Application of this formula (see table 7 for numerical values of ν and E) yields,

For Al: $\quad K_{Al} = 7{,}29.10^{10} \ Nm^{-2}$

For Fe: $\quad K_{Fe} = 16{,}136.10^{10} \ Nm^{-2}$

thus illustrating the qualitative character of all in this thesis involved numerical calculations.

Equating both equations of state (2.8) and (2.17), defines f(V) and g(V):

$$f(V) = \frac{K}{s} \left\{ \left(\frac{\rho}{\rho_0}\right)^s - 1 \right\} - \alpha K T_0 \qquad (2.18)$$

$$g(V) = \frac{\rho}{\rho_0} \ \alpha K \qquad (2.19)$$

For an isothermal compression to the density ρ_1 at the temperature T_0, eq. (2.17) gives the isothermal pressure:

$$P_i = \frac{K}{s} \left\{ \left(\frac{\rho_1}{\rho_0}\right)^s - 1 \right\} + \alpha K T_0 \left(\frac{\rho_1}{\rho_0} - 1\right) \qquad (2.20)$$

In eq. (2.16) now remains as undefined property $F(V_1)$.

$$F(V_1) \equiv \int_{V_1}^{V_0} f(V) \ dV \qquad (2.15)$$

48

and with (2.18):

$$F(V_1) = \int_{V_1}^{V_0} \left[\frac{K}{s}\left\{\left(\frac{\rho}{\rho_0}\right)^s - 1\right\} - \alpha KT_0\right] dV \qquad (2.21)$$

The result of the integration is:

$$F(V_1) = \frac{1}{\rho_0}\left[\frac{K}{s(s-1)}\left\{\left(\frac{\rho_1}{\rho_0}\right)^{s-1} - 1\right\} - \left(\frac{K}{s} + \alpha KT_0\right)\left(1 - \frac{\rho_0}{\rho_1}\right)\right]$$
$$(2.22)$$

NB: Eq. (2.22) differs form that given by Duvall [15] the factor $\frac{1}{\rho_0}$, obviously a

misprint in [15]. A recapitulation of all equations developed thus far, leads to the

conclusion that all shock related material properties can be determined in the

following order:

SOLUTION SCHEME 2:

1. Take eq. (2.22) to calculate $F(V_1)$

   with $\frac{\rho_0}{\rho_1}$ as input parameter and s as a known quantity.

2. Take eq. (2.20) to calculate P_i

3. Take eq. (2.19) to calculate $g(V_1)$

4. Take eq. (2.16) to calculate P_H

5. Take eq. (2.6) to calculate ΔE

6. Take eq. (2.9) to calculate ΔT

7. Take eq. (2.4) to calculate U_s

8. Take eq. (2.5) to calculate U_p

NB: 1 — The only variable that must be inserted into the equations system

is ρ_1. If once the variable ρ_1, or preferably the input variable $\frac{\rho_0}{\rho_1}$, has

been chosen, all shock related properties can be determined

consistently according to the given scheme.

49

2 − Remind that $P_0 = 0$ in the eq. (2.4), (2.5) and (2.6) and that $P_H = P_1$.

3 − The theory makes use of the Murnaghan equation of state and this equation is based on the Bridgman parameter s. If for an arbitrary material, s is unknown the whole theory can not be applied. For such cases another solution philosophy must be developed. One possibility is to use experimentally determined data, different from s, as input parameter.

This leads to the third way to solve the equations.

In ballistic laboratories the loci of related P_H and $\dfrac{V_1}{V_0} = \dfrac{\rho_0}{\rho_1}$ points have been determined. In other words the Hugoniot curves for a series of materials are known from experiment. Rice, Mcqueen and Walsh [18] produce for 27 materials the Hugoniot curves $P_H = P_H \left(\dfrac{\rho_0}{\rho_1}\right)$ and give for 25 materials the analytical fittings of the Hugoniot data from the graphical relations in the form

$P = A\mu + B\mu^2 + C\mu^3$ where $\mu = \dfrac{\rho_1}{\rho_0} - 1$. A,B and C are coefficients given in table 9, ref. [18].

Nineteen analytically fit Hugoniot curves are added to this thesis as fig. 2.2.1 − 2.2.5. The original Hugoniot curve for Fe is added for the sake of completeness, see fig. (2.2.6)

The shock related material properties can now be determined in the following order.

Table 9: Analytical fits of Hugoniot Curves, $P = A\mu + B\mu^2 + C\mu^3$, with pressure in Kilobars [18]; $\mu = \dfrac{\rho_1}{\rho_0} - 1$

Metal	A	B	C
Beryllium	1182	1382	0
Cadmium	479	1087	2829
Chromium	2070	2236	7029
Cobalt	1954	3889	1728
Copper	1407	2871	2335
Gold	1727	5267	0
Lead	417	1159	1010
Magnesium	370	540	186
Molybdenum	2686	4243	733
Nickel	1963	3750	0
Silver	1088	2687	2520
Thorium	572	646	855
Tin	432	878	1935
Titanium	990	1168	1246
Zinc	662	1577	1242
24St aluminum	765	1659	428
Brass	1037	2177	3275
Indium	496	1163	0
Niobium	1658	2786	0
Palladium	1744	3801	15230
Platinum	2760	7260	0
Rhodium	2842	6452	0
Tantalum	1790	3023	0
Thallium	317	938	1485
Zirconium	934	720	0

Fig. 2.2.1: *FIT HUGONIOT CURVES* Be; Cr; Cu; Pb.

□ Be   + Cr   ◇ Cu   △ Pb
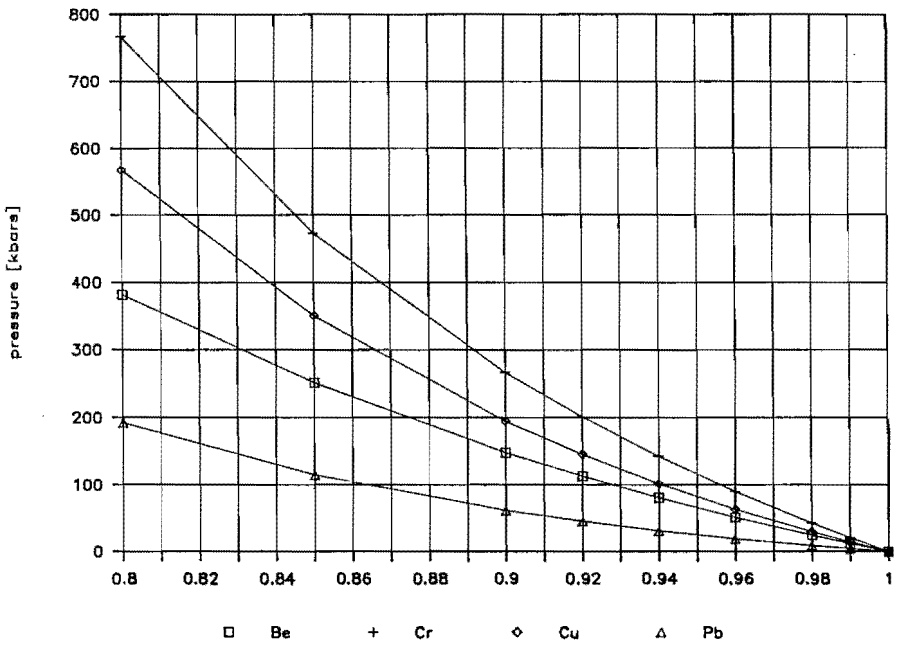
Fig. 2.2.2: *FIT HUGONIOT CURVES* Au; Sn; Ti; Zn.

□ Au   + Sn   ◇ Ti   △ Zn

52
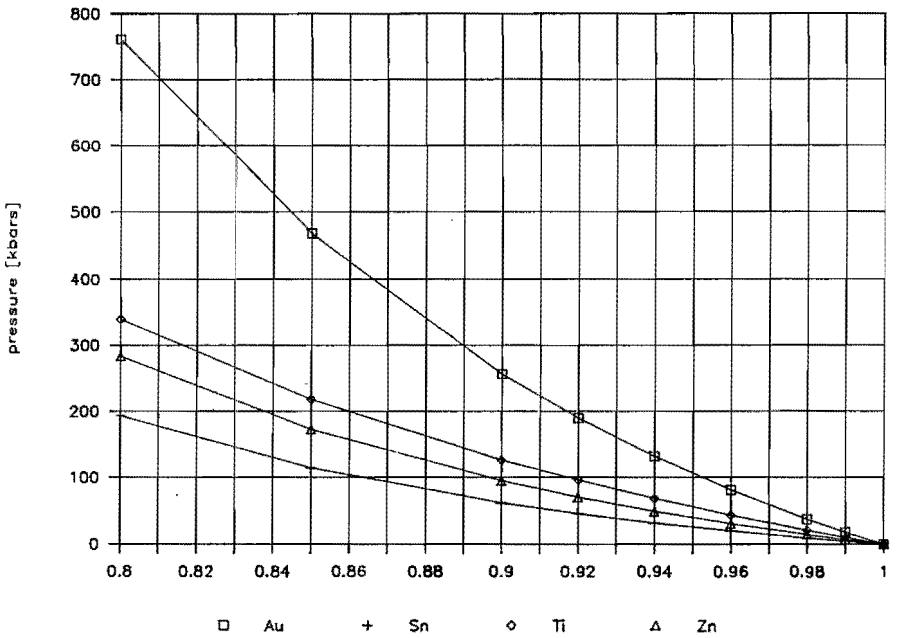
Fig. 2.2.3: *FIT HUGONIOT CURVES* Co; Mg; Mo; Ag.
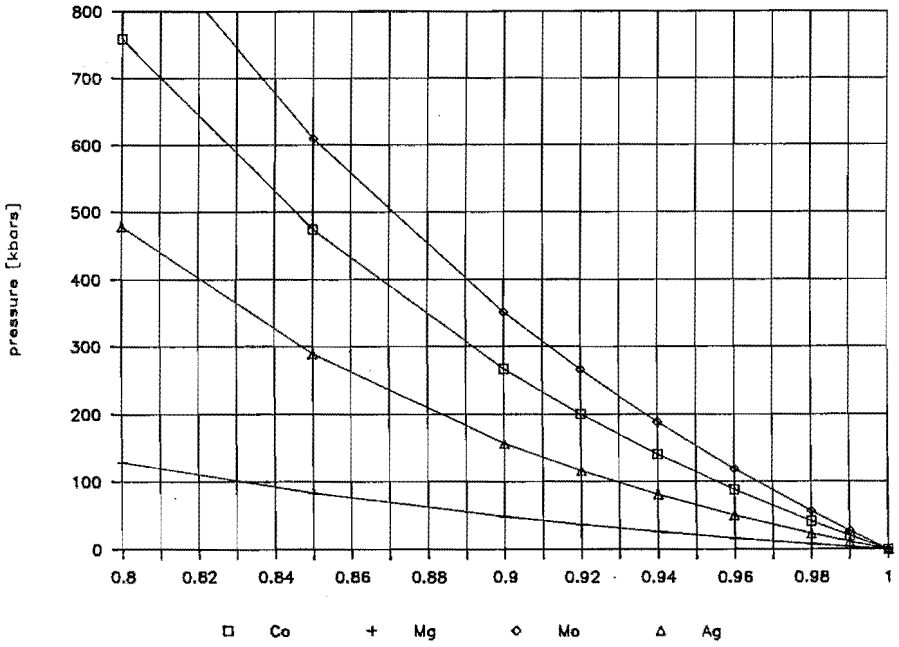
Fig. 2.2.4: *FIT HUGONIOT CURVES* Nb; Ta; Zr.

53
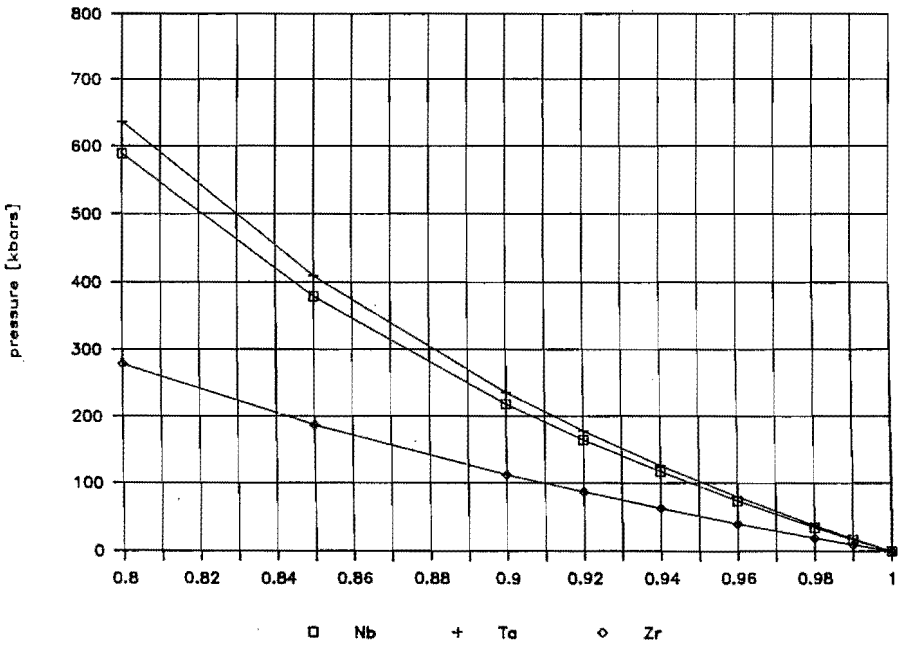
FIT HUGONIOT CURVES Ni; Al; Brass; In.
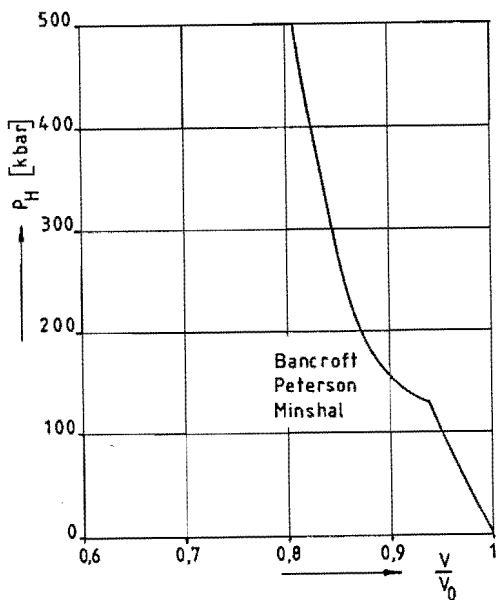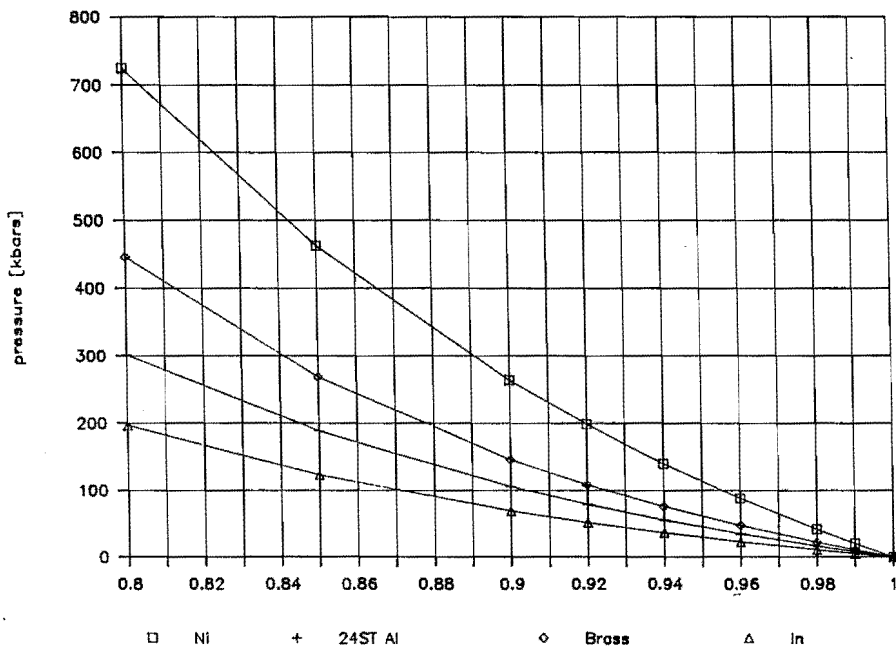
Fig. 2.2.6:   Hugoniot curve for Armco iron. V/Vo [18].

54

SOLUTION SCHEME 3:

1. Take P_H and ρ_1 from the Hugoniot curves.

2. Take eq. (2.4) to calculate U_s

3. Take eq. (2.5) to calculate U_p

4. Take eq. (2.6) to calculate ΔE

5. Take eq. (2.19) to calculate $g(V_1)$

6. Take eq. (2.16) and eliminate P_i with eq. (2.20) and $F(V_1)$ with eq. (2.22). Thus, one equation remains with s as unknown quantity. Calculate s.

7. Take eq. (2.22) to calculate $F(V_1)$

8. Take eq. (2.9) to calculate ΔT.

The third way to solve the eqautions opens for many important spray materials those mentioned in fig. 2.2.1 – 2.2.2 – the possibility of a theoretical analysis of shock phenomena during spraying. Nevertheless a great deal of interesting materials such as oxides and ceramics can not be analysed before spraying, just because the parameter s is unknown or the Hugoniot curve is not yet determined. At this moment it is worth while to consider the first solution scheme once more, taking also into account the equations which have been developed to determine the shock temperature and which were not yet used at the moment of first consideration of solution scheme 1. The shock related material properties can now be determined in the following order.

EXTENDED SOLUTION SCHEME 1:

1. Take eq. (2.7b) to calculate U_s as a function of U_p, which is considered to be a known input parameter.

2. Substitute U_s into eq. (2.4), then with eq. (2.5) there are two equations and two variables, P_H and ρ_1. P_H and ρ_1 can bedetermined.

3. Take eq. (2.6) and calculate ΔE.

4. Take eq. (2.19) and calculate $g(V_1)$

5. Take eq. (2.16) eliminate P_i with eq. (2.20) and eliminate $F(V_1)$ with eq. (2.22). Thus one equation remains with s as unknown property. Calculate s.

6. Take eq. (2.22) and calculate $F(V_1)$.

7. Take eq. (2.9) and calculate ΔT.

It turns out that the equation system now can be solved, purely theoretically. Experiments to measure e.g. U_s, s, ρ_1 or P_H are not necessary. The system holds for any material obeying the adopted equation of state. This is certainly an attractive basis for a first round analysis of the occurring shock phenomena. Apart form that the theoretical basis is a good introduction to a realistic experimental approach. Recapitulation: The set of equations, developed so far permits the determination of the shock relevant properties ΔE, ΔT and U_s as a function of U_p.

2.2.2 Relaxation.

The previous section dealt with compression during a shock load. In this section the relaxation after the shock front will be considered in order to determine the remaining temperature. During the shock loading the material is heated up and during the relaxation it cools down. If the final temperature after the pass of the shock exceeds the temperature just before the shock loading, one may say that kinetic energy of the moving material has been transferred to thermal energy. For thermal spray processes, especially for those working at high particle velocities, it is important to gain insight in the energy conversion since it can determine widely the wanted optimum combination of particle size, velocity and temperature. In order to be able to calculate the temperature after relaxation a few other equations are required. Fig. 2.3 depicts a P–V cycle of shock loading and
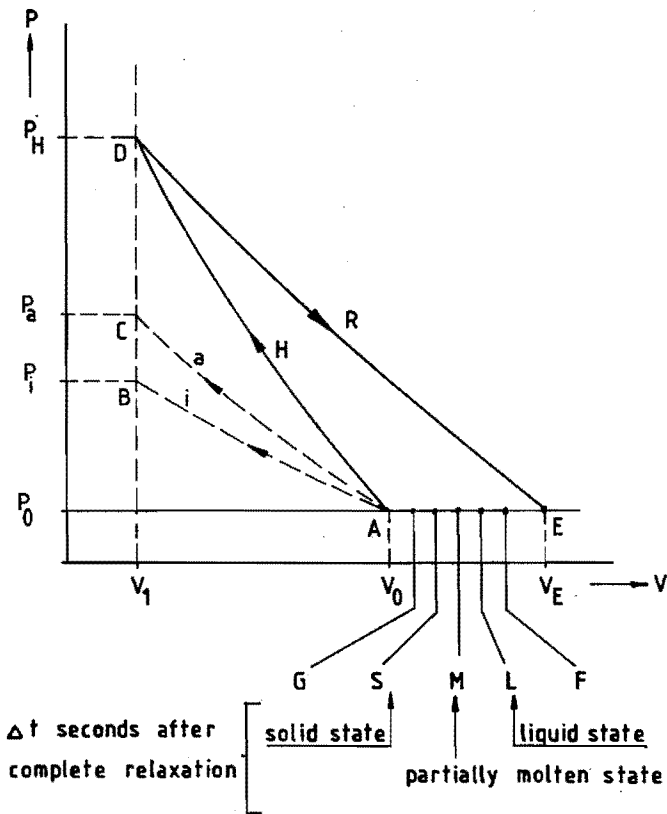
Fig. 2.3:   P − V diagram.

relaxation. This figure plays an important part in understanding the derivation of the new set of equations. A carefull description of all points and lines will facilitate the procedure of deduction.

The curves: H ≙ Hugoniot

a ≙ adiabate

i ≙ isotherm

R ≙ Relaxation adiabate

57

The points:

A $(V_0, T_0, S_0, E_0, P_0) \widehat{=}$ starting point

B $(V_1, T_0, S_B, E_B, P_i)$ marks the end of an isothermal compression

C $(V_1, T_c, S_c = S_A = S_0, E_c, P_a)$ marks the end of an adiabatic compression

D $(V_1, T_D, S_D, E_1, P_1 = P_H)$ marks the end of the shock compression

E $(V_E > V_0, T_E, S_E = S_D, E_E, P_0)$ marks the non equilibrated relaxed state or the equilibrium final state if no phase changes occur during the shock and the relaxation.

G $(V_G, T_G, S_G, E_G, P_0)$ marks a final state at a temperature below the melting point.

S $(V_s, T_M, S_s, E_s, P_0)$ marks the ultimate possible state of solid material $\widehat{=}$ start of melting.

L $(V_L, T_M, S_M, E_M, P_0)$ marks a completely molten state.

M $(V_M, T_M, S_M, E_M, P_0)$ marks a partial molten state.

F $(V_F > V_0, T_F, S_F, E_F, P_0)$ marks generally the equilibrium final state. F may be located in between A and E.

Two basic rules, which both can be inferred from the first and second law of thermodynamics, will be applied in the following reasoning. These rules are for a change of state, at constant volume:

$$(S_2 - S_1)_V = C_v \ln \frac{T_2}{T_1} \qquad (2.23)$$

at constant pressure:

$$(S_2 - S_1)_P = C_p \ln \frac{T_2}{T_1} \qquad (2.24)$$

where $S \widehat{=}$ entropy.

The set of equations developed in section 2.2.1 permits to determine T_D, the shock state temperature. With eq. (2.23), this temperature is related to T_C, since

the path from C to D vice versa represents a change of state at constant volume. So, the application of rule (2.23) leads to:

$$S_D - S_C = S_V \ln \frac{T_D}{T_C} \tag{2.25}$$

with $S_C = S_0 = 0$

$$S_D = C_V \ln \frac{T_D}{T_C} \tag{2.25a}$$

Eq. (2.25a) encompasses two unknow variables: the entropy in the shock state, S_D, and the adiabatic compression temperature, T_C. The entropy $S_C = S_A = S_0$ because AC represents an adiabatic, read isentropic, change. The entropy S_0 is arbitrarily set zero (so S_D to be read as ΔS_D etc.). The first step in determining S_D and T_C is to find a solution for T_C, as follows: The entropy change along the isotherm AB is given by:

$$S_B - S_A = \int_{V_0}^{V_1} g(V) \, dV \quad = \int_{V_0}^{V_1} \frac{\rho}{\rho_0} \alpha K \, dV$$

$$= \frac{\alpha K}{\rho_0} \ln \frac{V_1}{V_0} \tag{2.26}$$

See appendix 5 for the derivation of (2.26). With $S_A = S_0 = 0$:

$$S_B = \frac{\alpha K}{\rho_0} \ln \frac{V_1}{V_0} \tag{2.26a}$$

$\dfrac{V_1}{V_0} = \dfrac{\rho_0}{\rho_1}$ is either an input parameter or can be calculated as shown in the foregoing section, thus S_B is fixed.

Application of (2.23) on the path BC yields:

$$S_C - S_B = C_v \ln \frac{T_C}{T_0} \qquad (2.27)$$

with $S_C = S_0 = 0$:

$$-S_B = C_v \ln \frac{T_C}{T_0} \qquad (2.27a)$$

from which follows:

$$T_C = T_0 \exp \frac{-S_B}{C_v} \qquad (2.28)$$

Substitution of (2.28) into (2.25a) with $S_C = S_0 = 0$ yields:

$$S_D = C_v \ln \frac{T_D}{T_0 \exp . \dfrac{-S_B}{C_v}} \qquad (2.29)$$

Elimination of S_B from (2.26a) and (2.27a) gives:

$$\frac{-\alpha K}{\rho_0} \ln \frac{V_1}{V_0} = C_v \ln \frac{T_C}{T_0} \text{ from which follows:}$$

$$T_C = T_0 \exp . \frac{-\alpha K \ln \dfrac{V_1}{V_0}}{\rho_0 . C_v} \qquad (2.30)$$

Eq. (2.30) is apart from (2.28) another equation to determine T_C, the adiabatic compression temperature. Consider eq. (2.25a) once again.

60

If $T_D = T_C$ then $S_D = 0$. In words: as long as the shock temperature T_D equals the adiabatic temperature T_C, the entropy of the shock state will not increase. If this is the case, the permanent equilibrium temperature after relaxation will be T_0. The shock does not contribute to a conversion of kinetic energy to thermal energy. The temperature after relaxation, T_E, can be derived from the applicatio of rule (2.24) to the change from A to E, thus:

$$S_E - S_A = C_p \ln \frac{T_E}{T_A} \text{ with } S_A = S_0 = 0:$$

$$S_E = C_p \ln \frac{T_E}{T_A} \qquad (2.31)$$

If the relaxation is adiabatic and isentropic, then $S_E = S_D$; with (2.31)

$$C_p \ln \frac{T_E}{T_A} = S_D; \text{ with } T_A = T_0:$$

$$T_E = T_0 \exp. \frac{S_D}{C_p} \qquad (2.32)$$

Mind that T_E acc. to (2.32) is based on an assumed isentropic change of state along the path DE. A phase change during the relaxation invalidates eq. (2.32). If phase changes take place right after the relaxation, eq. (2.32) remains true. An important question rises now. During the compression the temperature has increased to T_D. Does melting occur? If melting occurs, what is the final state or final temperature of the material? To answer these questions, the phenomenon of melting under high pressure needs a closer examination.

The governing equation is given by Clapeyron, ref. [16], pg 177:

$$\frac{dp}{dt} = \frac{\Delta H \text{ melt, m}}{T_f \quad \Delta V \text{ melt, m}} \qquad (2.33)$$

where ΔH melt, m = molar enthalpy of fusion

ΔV melt, m = molar volume change on melting

T_f = Temperature at which melting occurs

Note that $\dfrac{\Delta H \text{ melt, m}}{T_f}$, is the molar entropy of melting.

Integration of (2.33) gives the equation of the solid − liquid equilibrium phase line:

$$P = P^* + \frac{\Delta H \text{ melt, m}}{\Delta V \text{ melt, m}} \ln \frac{T_f}{T^*} \qquad (2.34)$$

where P^* and T^* are the pressure and temperature on a fixed point of the line, e.g. the melting temperature at standard pressure,

$$P^* = 10^5 \text{ Nm}^{-2} \text{ and } T^* = T_M.$$

A numerical illustration might elucidate the abstract formulas. For this reason eq (2.34) will be worked out for the arbitrarily chosen material Al. The relevant numerical quantities for Al are: Volume growth on melting ~ 6%, ref. [20], so, ΔV melt = 0,06 V_{T_M}, where V_{T_M} = Volume at T_M = 933K.

$$V_{933} = V_{298} (1 + \alpha \Delta T) = 3,38 \cdot 10^{-4} \text{ m}^3 \text{ kg}^{-1}$$

$$\Delta V \text{ melt} = 0,06 V_{933} = 2,332 \cdot 10^{-5} \text{ m}^3 \text{kg}^{-1}$$

The latent heat $\hat{=}$ enthalpy of fusion is:

$$L = 387 \cdot 592 \text{ J kg}^{-1}, \text{ ref. [21]}.$$

62

Substitution of these values into eq. (2.34) yields:

$$P = 10^5 + \frac{387.592}{2,332.10^{-5}} \ln \frac{T_f}{T_M} \quad ,$$

or:

$$P = 10^5 + 1,662.10^{10} \ln \frac{T_f}{T_M} \tag{2.35}$$

Eq. (2.35) is worked out numerically in table 10a and visualized in fig. 2.4. Next, on the basis of fig. 2.4, table 10b is determined. The reason for the choice of the temperature intervals as presented in table 10b will be justified later.
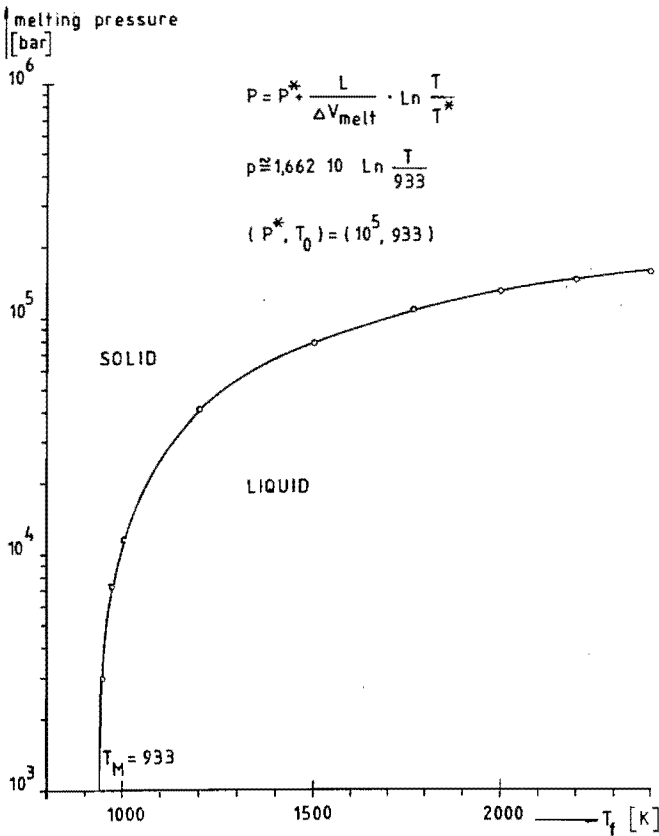
Fig. 2.4:   Melting temp. of Al as a function of pressure.

From table 10 it may be concluded that the melting temperature increase due to the pressure rise amounts some 7 degrees per 1000 bar. A provisional conclusion could be that an initially liquified particle, partially can be converted into a solid during the collision. Probably this will be an amorphous solid, because the material has the entropy of a liquid at the moment that the shock wave passes by and causes the pressure increase in an extremely short time delay. It all depends on the magnitude of pressure increase which occurs during the collision.

From (2.35) follows for the melting temperature under increased pressure:

$$T_f = T_M \exp \frac{P_H}{1,662 \cdot 10^{10}} \qquad (2.36)$$

Table 10a: Melting temperature of Al as a function of pressure.

T_f	P	
[K]	[Nm^{-2}]	[bar]
933	$1 \cdot 10^5$	1
1000	$1,15 \cdot 10^9$	$1,15 \cdot 10^4$
1200	$4,18 \cdot 10^9$	$4,18 \cdot 10^4$
1500	$7,89 \cdot 10^9$	$7,89 \cdot 10^4$
2000	$1,27 \cdot 10^{10}$	$1,27 \cdot 10^5$
2200	$1,43 \cdot 10^{10}$	$1,43 \cdot 10^5$
2400	$1,57 \cdot 10^{10}$	$1,57 \cdot 10^5$
2600	$1,70 \cdot 10^{10}$	$1,70 \cdot 10^5$

If $T_D \leq T_f$, then melting does not occur during the compression. As will be shown the compression by shock takes actually place in the solid region of the phase diagram. This implies also for the relaxation process that no melting occurs during the pressure release.

Table 10b: Calculation of mean values $\overline{\Delta T/\Delta P}$ for successive temperature intervals.

ΔT	990–933 = 57	1070–990 = 80	1220–1070 = 150	1400–1220 = 180	K
ΔP	9,5	10,5	25,0	22,0	kbar
$\dfrac{\overline{\Delta T}}{\Delta P}$	6,0	7,6	6,0	8,2	$\dfrac{K}{kbar}$

Purely theoretical a pressure smaller than 1 bar can arise due to dynamical effects if the situation of uniaxial strain is maintained during the relaxation. As will be shown in the next section, the uniaxial strain situation during the compression will turn over in a plain strain situation when relaxation starts. For this reason it is further assumed that no melting occurs during the pressure release phase of the material. When the decompression along the line DE has been finished, the entropy in the pseudo – final state E equals the entropy in the shock state and the pseudo – final temperature T_E can be calculated according to eq. (2.32). If T_E surmounts T_M, the decompressed material will start to melt. The actual criterion which governs the melt phenomenon is the magnitude of the shock entropy $S_D = S_E$. If $S_D = S_E > S_{M_S}$ then melting of the decompressed material sets in. Note that S_{M_S} is the maximum solid state entropy at pressure P_0 as indicated in the description of the $P - V$, diagram. If melting occurs it will take place at the pressure P_0 and the governing rule that relates the entropy states between point A and any other point of the horizontal line at pressure P_0 is given in eq. (2.24). Application of this rule to the points A and S produces the lower entropy boundary for melting = the maximum entropy for a solid state

65

$$S_S - S_A = C_p \ln \frac{T_M}{T_A} \qquad (2.37)$$

with S_A = arbitrarily zero and $T_A = T_0$ = the spray particle temperature;

$$S_S = C_p \ln \frac{T_M}{T_0} \qquad (2.37a)$$

The upper entropy boundary for melting is:

$$S_L = S_S + \frac{L}{T_M} \qquad (2.38)$$

where L = latent heat. A partially molten final state is characterized by the entropy:

$$S_M = S_S + \frac{\phi L}{T_M} \qquad (2.39)$$

where $0 \leq \phi \leq 1$ denotes the melting degree.

$$\phi = (S_M - S_S) \frac{T_M}{L} \qquad (2.39a)$$

follows directly from (2.39). Mind that $S_M = S_E = S_D$.

The entropy S_0 of a super − heated state $\hat{=}$ liquid at the temperature $T_0 > T_M$ is:

$$S_0 = S_L + C_p \ln \frac{T_0}{T_M} \qquad (2.40)$$

The entropy of a liquid at temperature $T_F > T_0$ is:

$$S_F = S_0 + C_{P_L} \ln \frac{T_F}{T_0} \qquad (2.40a)$$

with $C_{P_L} \cong C_{P_S} = C_p$ and S_0 arbitrarily set zero:

$$\frac{S_F}{C_p} = \ln \frac{T_F}{T_0}, \text{ from which follows directly:}$$

$$T_F = T_0 \exp. \frac{S_F}{C_p} \tag{2.40b}$$

Mind that in the case of shock loading $S_F = S_D = S_E$ = the entropy produced during the shock. T_F is the temperature which the liquid adopts after relaxation. Note further that eq. (2.40b) is identical to eq. (2.32). A solid final state has the entropy:

$$S_S = C_p \ln \frac{T_G}{T_0} \tag{2.41}$$

from which follows directly:

$$T_G = T_0 \exp. \frac{S_G}{C_p} \tag{2.41a}$$

If the shock entropy $S_D = S_E > S_L$, then use eq. (2.40).

If $S_S < S_D = S_E < S_L$, then use eq. (2.39).

If $S_D = S_E < S_E$, then use eq. (2.41)

2.2.3   Final energy balance.

The formulation of the energy balance for a material that will undergo a shock load depends on its phase – state. Three main cases will be distinguished.

1.   A solid material that hits the surface at a temperature T_0 and is heated up, due to collision phenomena, to the temperature $T_G < T_M$.

2.   A solid material, initially at temperature T_0 which partly melts due to the collision.

3.   A liquified material, initially at temperature T_0 which is heated up tot the temperature T_F.

The macro–energy balances are for.

<u>Case 1:</u>

$$E_0 + \frac{1}{2} U_p^2 = W_0 \tag{2.42}$$

where: E_0 denotes the specific internal energy before the start of the collision.

$\frac{1}{2} U_p^2$ is the kinetic energy before the collision.

W_0 is the total energy of the material right before the collision starts.

The internal energy is practically equal to the enthalpy so:

$$E_0 = \int_{298}^{T_0} C_{p_s} \, dT \tag{2.43}$$

where C_{p_s} denotes the specific heat capacity at constant pressure of the solid material. Substitution of (2.43) into (2.42) gives the energy balance before the collision:

$$\int_{298}^{T_0} C_{p_s} \, dT + \frac{1}{2} U_p^2 = W_0 \tag{2.44}$$

After the relaxation, the balance reads:

$$\int_{298}^{T_0} C_{p_s} \, dT + \frac{1}{2} U_p^2 = \Delta E_{pot} + E_1 = W_0 \tag{2.45}$$

where:

$$\Delta E_{pot} = \frac{1}{2} U_p^2 - \Delta E_{th} \tag{2.46}$$

and:

$$\Delta E_{th} = \int_{T_0}^{T_G} C_{p_s} \, dT = C_p \, (T_G - T_0) \tag{2.47}$$

In words: ΔE_{th} is the kinetic energy which is converted to thermal energy due to shock phenomena. ΔE_{pot} is the remaining kinetic energy, transformed to potential energy and available for creation of the final morphology of the spray particle.

$$E_1 = \int_{298}^{T_G} C_{P_S}\, dT \qquad (2.48)$$

is the specific internal energy after relaxation. Check: Substitution of (2.48), (2.47) and (2.46) into (2.45) satisfies (2.45).

Case 2:

The energy balance right before the collison is given by eq. (2.42). After relaxation, the balance reads like (2.45) where:

$$E_1 = \int_{298}^{T_M} C_{P_S}\, dT + \phi L \qquad (2.49)$$

(with ϕ = melting degree and L = Latent heat)

$$\Delta E_{pot} = \tfrac{1}{2} U_p^2 - \Delta E_{th} \qquad (2.46)$$

and

$$\Delta E_{th} = \int_{T_0}^{T_M} C_{P_S}\, dT + \phi L = C_p (T_M - T_0) + \phi L \qquad (2.50)$$

Check: substitution of (2.50), (2,46) and (2.49) into (2.45), satisfies (2.45).

Case 3:

The energy balance before the collision is given by eq. (2.42). After relaxation the balance is like (2.45) where:

$$E_1 = \int_{298}^{T_M} C_{P_S}\, dT + \phi L + \int_{T_M}^{T_F} C_{P_L}\, dT \qquad (2.51)$$

($C_{P_L} = C_p$ for liquid material)

$$E_0 = \int_{298}^{T_M} C_{P_S}\, dT + \phi L + \int_{T_M}^{T_0} C_{P_L}\, dT \qquad (2.52)$$

$$\Delta E_{pot} = \tfrac{1}{2} U_p^2 - \Delta E_{th} \qquad (2.46)$$

and

$$\Delta E_{th} = \int_{T_0}^{T_F} C_{P_L}\, dT = C_p (T_F - T_0) \qquad (2.53)$$

69

Check: Substitution of (2.53), (2.46) and (2.51) into (2.45) statifies (2.45)

Note: The energy balance has been set up to identify two portions of energy, ΔE_{th} and ΔE_{pot}. A complete survey of all equations required for the calculation of shock – relevant quantities may be of great help for the set up of the calculation program.

SURVEY OF EQUATIONS REGARDING COMPRESSION

Nr.   Eq

1 $\qquad U_s^2 = \dfrac{\rho_1}{\rho_0} \left(\dfrac{P_1 - P_0}{\rho_1 - \rho_0} \right)$ (2.4)

2 $\qquad U_p = \dfrac{\rho_1 - \rho_0}{\rho_1} \left(\dfrac{\rho_1}{\rho_0} \cdot \dfrac{P_1 - P_0}{\rho_1 - \rho_0} \right)^{\frac{1}{2}}$ (2.5)

3 $\qquad \Delta E = E_1 - E_0 = \frac{1}{2}(P_1 + P_0)\left(\dfrac{1}{\rho_0} - \dfrac{1}{\rho_1} \right)$ (2.6)

4 $\qquad U_s = \left(\dfrac{E}{\rho_0} \right)^{\frac{1}{2}} \cdot \left(\dfrac{1 - \nu}{(1+\nu)(1-2\nu)} \right)^{\frac{1}{2}} \left(\dfrac{1}{2} + \dfrac{\alpha E}{6(1-2\nu)\,\rho_0 C_v} \right)$

(2.7b)

5 $\qquad \Delta E = E_1 - E_0 = C_v(T_1 - T_0) + \displaystyle\int_{V_1}^{V_0} f(V)\, dV$

(2.9)

$\qquad\qquad\qquad\quad = C_v(T_1 - T_0) + F(V_1)$ (2.9a)

70

6    $$P_H = \dfrac{P_i - \dfrac{F(V_1) \cdot g(V_1)}{C_v}}{1 - \dfrac{(V_0 - V_1) \cdot g(V_1)}{2\,C_v}}$$ (2.16)

7    $$g(V_1) = \frac{\rho_1}{\rho_0}\,\alpha K$$ (2.19)

8    $$P_i = \frac{K}{s}\left\{\left(\frac{\rho_1}{\rho_0}\right)^s - 1\right\} + \alpha KT_0\left(\frac{\rho_1}{\rho_0} - 1\right)$$ (2.20)

9    $$F(V_1) = \frac{1}{\rho_0}\left[\frac{K}{s\,(s-1)}\left\{\left(\frac{\rho_1}{\rho_0}\right)^{s-1} - 1\right\} - \left(\frac{K}{s} + \alpha KT_0\right)\left(1 - \frac{\rho_0}{\rho_1}\right)\right]$$

   (2.22)

mind: $P_1 \equiv P_H$

$P_0 = 0$

SURVEY OF EQUATIONS REGARDING RELAXATION.

Nr.

10    $$S_D = C_v \ln \frac{T_D}{T_C}$$ (2.25a)

11    $$S_B = \frac{\alpha K}{\rho_0} \ln \frac{V_1}{V_0}$$ (2.26a)

12     $T_C = T_0 \exp \dfrac{-S_B}{C_v}$ (2.28)

13     $T_E = T_0 \exp. \dfrac{S_D}{C_p}$ $(S_D = S_E)$ (2.32)

14     $S_S = C_p \ln \dfrac{T_M}{T_0}$ $(S_S = S_E)$ (2.37a)

15     $S_L = S_S + \dfrac{L}{T_M}$ (2.38)

16     $\phi = \dfrac{T_M}{L} (S_M - S_S)$ $(S_M = S_E)$ (2.39a)

17     $T_F = T_0 \exp. \dfrac{S_F}{C_p}$ $(S_F = S_E)$ (2.40b)

18     $T_G = T_0 \exp. \dfrac{S_G}{C_p}$ $(S_G = S_E)$ (2.41a)

19   If $S_D = S_E < S_S$:

$$\Delta E_{th} = \int_{T_0}^{T_S} C_{p_s} \, dT = C_p \, (T_G - T_0)$$ (2.47)

If $S_S < S_D = S_E < S_L$:

$$\Delta E_{th} = \int_{T_0}^{T_M} C_{p_s} dT + \phi L = C_p \, (T_M - T_0) + \phi L$$

$$(2.50)$$

If $S_D = S_E > S_L$:

$$\Delta E_{th} = \int_{T_0}^{T_F} C_{P_L} dT = C_P \, (T_F - T_O) \qquad (2.53)$$

20 $\qquad \Delta E_{pot} = \frac{1}{2} U_p^2 - \Delta E_{th}$ $\qquad\qquad\qquad$ (2.46)

The calculation of all shock parameters can now take place. For Al, the Murnagham parameter s is a known quantity which permits to chose for solution scheme 2 regarding the compression.

Input parameters: ρ_0, K, s, α, T_0, C_v, C_p, L, T_M, $\dfrac{\rho_0}{\rho_1}$

Step	Equation	Output
1	2.22	$F(V_1)$
2	2.20	P_i
3	2.19	$g(V_1)$
4	2.16	P_H
5	2.6	ΔE
6	2.9	$\Delta T; T_D$
7	2.4	U_s
8	2.5	$U_p; \frac{1}{2}U_p^2$
Relaxation:		
9	2.26a	S_B
10	2.28	T_C

11	2.25a	S_D
12	2.32	T_E
13	2.37a	S_S
14.	2.38	S_L
15.1	if $S_D = S_E < S_s$ (2.41a)	T_G
15.2	if $S_s < S_D = S_E < S_L$ (2.39a)	ϕ
15.3	if $S_D = S_E > S_L$ (2.40b)	T_F
16.1	2.47	$\Delta E_{th \cdot 1}$
16.2	2.50	$\Delta E_{th \cdot 2}$
16.3	2.53	$\Delta E_{th \cdot 3}$
17	2.46	ΔE_{pot}

Appendix 6 gives the detailed calculations of the quantities $F(V_1) \rightarrow S_L$. A characteristic selection of calculated data is summarized in table 11a, 11b and 11c. The computational results are visualized in figures 2.5 − 2.10. The discussion will take place on the basis of these figures. Fig. 2.5 shows the compression band of Al as a function of the spray particle velocity U_p. As will turn out, the energy conversion of kinetic energy into thermal energy starts at about $U_p = 240$ m/s. The compression than amounts $\rho_0/\rho_1 \cong 0,96$. The upper part of fig 2.5 shows the shock wave propagation velocity U_s as a function of U_p. The U_s lines are below the theoretical value as given by eq. (2.7b), thus demonstrating the qualitatieve character of all the calculations. Fig. 2.5 should give an overall impression about the thermal spray process for aluminium. Plasma spraying usually takes place in the region $U_p \leq 200 \frac{m}{s}$, while high velocity processes like Jet–Kote or D–Gun produce spray particles at velocities which usually exceed $300 \frac{m}{s}$. Note that also for $U_p < 240 \frac{m}{s}$ a considerable compression can take place.

Table 11a: Survey of shock related quantities for Al, $T_0 = 800$ K.

$\dfrac{\rho_0}{\rho_1}$		0,80	0,82	0,84	0,86	0,88	0,90
$F(V_1)$	$Nmkg^{-1}$	$4,711 \cdot 10^5$	$3,217 \cdot 10^5$	$2,027 \cdot 10^5$	$1,105 \cdot 10^5$	$4,207 \cdot 10^4$	$-5,384 \cdot 10^3$
P_i	Nm^{-2}	$2,804 \cdot 10^{10}$	$2,352 \cdot 10^{10}$	$1,954 \cdot 10^{10}$	$1,601 \cdot 10^{10}$	$1,288 \cdot 10^{10}$	$1,010 \cdot 10^{10}$
$g(V_1)$	$Jm^{-3}K^{-1}$	$7,038 \cdot 10^6$	$6,866 \cdot 10^6$	$6,703 \cdot 10^6$	$6,547 \cdot 10^6$	$6,398 \cdot 10^6$	$6,256 \cdot 10^6$
P_H	Nm^{-2}	$3,480 \cdot 10^{10}$	$2,862 \cdot 10^{10}$	$2,340 \cdot 10^{10}$	$1,893 \cdot 10^{10}$	$1,508 \cdot 10^{10}$	$1,174 \cdot 10^{10}$
ΔE	$J\,kg^{-1}$	$1,289 \cdot 10^6$	$9,541 \cdot 10^5$	$6,933 \cdot 10^5$	$4,910 \cdot 10^5$	$3,353 \cdot 10^5$	$2,174 \cdot 10^5$
ΔT	K	960	742	575	446	344	261
T_D	K	1760	1542	1375	1246	1144	1061
U_s	ms^{-1}	8028	7674	7360	7078	6824	6594
U_p	ms^{-1}	1605	1381	1177	990	818	659
S_B	$Jkg^{-1}K^{-1}$	$-465,3$	$-413,8$	$-363,6$	$-314,5$	$-266,5$	$-219,7$
T_C	K	1381	1300	1225	1157	1093	1035
$S_D = SE$	$Jkg^{-1}K^{-1}$	206,4	145,4	98,3	63,3	38,2	21,2
T_E	K	1006	940	892	858	834	819
S_S	$Jkg^{-1}K^{-1}$	138,4	138,4	138,4	138,4	138,4	138,4
S_L	$Jkg^{-1}K^{-1}$	553,8	553,8	553,8	553,8	553,8	553,8
100ϕ	%	16,3	1,68	0	0	0	0
T_F	K	no superheated liquid					
T_G	K	933	933	892	858	834	819
ΔE_{th}	Jkg^{-1}	$1,828 \cdot 10^5$	$1,262 \cdot 10^5$	$8,280 \cdot 10^4$	$5,220 \cdot 10^4$	$3,060 \cdot 10^4$	$1,710 \cdot 10^4$
$\frac{1}{2}U_p^2$	Jkg^{-1}	$1,288 \cdot 10^6$	$9,535 \cdot 10^5$	$6,926 \cdot 10^5$	$4,900 \cdot 10^5$	$3,345 \cdot 10^5$	$2,171 \cdot 10^5$
ΔE_{pot}	Jkg^{-1}	$1,105 \cdot 10^6$	$8,273 \cdot 10^5$	$6,098 \cdot 10^5$	$4,378 \cdot 10^5$	$3,039 \cdot 10^5$	$2,000 \cdot 10^5$

$\dfrac{\rho_0}{\rho_1}$		0,92	0,94	0,96	0,98	0,99	Equation
$F(V_1)$	$Nmkg^{-1}$	$-3{,}149 \cdot 10^4$	$-4{,}638 \cdot 10^4$	$-4{,}374 \cdot 10^4$	$-2{,}782 \cdot 10^4$	$-1{,}532 \cdot 10^4$	2.22
P_i	Nm^{-2}	$7{,}621 \cdot 10^9$	$5{,}399 \cdot 10^9$	$3{,}406 \cdot 10^9$	$1{,}615 \cdot 10^9$	$7{,}868 \cdot 10^8$	2.20
$g(V_1)$	$Jm^{-3}K^{-1}$	$6{,}120 \cdot 10^6$	$5{,}990 \cdot 10^6$	$5{,}865 \cdot 10^6$	$5{,}745 \cdot 10^6$	$5{,}687 \cdot 10^6$	2.19
P_H	Nm^{-2}	$8{,}803 \cdot 10^9$	$6{,}210 \cdot 10^9$	$3{,}907 \cdot 10^9$	$1{,}848 \cdot 10^9$	$9{,}002 \cdot 10^8$	2.16
ΔE	$J\,kg^{-1}$	$1{,}304 \cdot 10^5$	$6{,}900 \cdot 10^4$	$2{,}894 \cdot 10^4$	$6{,}847 \cdot 10^3$	$1{,}667 \cdot 10^3$	2.6
ΔT	K	193	135	85	40	19	2.9
T_D	K	993	935	885	840	819	2.9
U_s	ms^{-1}	6384	6191	6014	5851	5774	2.4
U_p	ms^{-1}	510	371	240	117	57	2.5
S_B	$Jkg^{-1}K^{-1}$	$-173{,}8$	$-129{,}0$	$-85{,}1$	$-42{,}1$	$-20{,}9$	2.26a
T_C	K	981	930	884	840	819	2.28
$S_D = SE$	$Jkg^{-1}K^{-1}$	10,4	4,2	1,2	0,14	0,01	2.25a
T_E	K	809	803	801	800	800	2.32
S_S	$Jkg^{-1}K^{-1}$	138,4	138,4	138,4	138,4	138,4	2.37a
S_L	$Jkg^{-1}K^{-1}$	553,8	553,8	553,8	553,8	553,8	2.38
100ϕ	%	0	0	0	0		2.39a
T_F	K						
T_G	K	809	804	801	800,12	800,008	2.41a
ΔE_{th}	Jkg^{-1}	$8{,}100 \cdot 10^3$	$2{,}700 \cdot 10^3$	900	108	7,2	2.47
$\tfrac{1}{2}U_p^{\,2}$	Jkg^{-1}	$1{,}300 \cdot 10^5$	$6{,}882 \cdot 10^4$	$2{,}880 \cdot 10^4$	6844	1624	2.5
ΔE_{pot}	Jkg^{-1}	$1{,}219 \cdot 10^5$	$6{,}612 \cdot 10^4$	$2{,}790 \cdot 10^4$	6736	1617	2.46

Table 11b: Survey of shock related quantities for Al, $T_0 = 933$ K $\hat{=} T_M$ Al.

$\dfrac{\rho_0}{\rho_1}$		0,80	0,82	0,84	0,86	0,88	0,90
$F(V_1)$	$Nmkg^{-1}$	$4,157 \cdot 10^5$	$2,718 \cdot 10^5$	$1,583 \cdot 10^5$	$7,170 \cdot 10^4$	$8,793 \cdot 10^3$	$-3,312 \cdot 10^4$
P_i	Nm^{-2}	$2,823 \cdot 10^{10}$	$2,369 \cdot 10^{10}$	$1,986 \cdot 10^{10}$	$1,613 \cdot 10^{10}$	$1,298 \cdot 10^{10}$	$1,018 \cdot 10^{10}$
$g(V_1)$	$Jm^{-3}K^{-1}$	$7,038 \cdot 10^6$	$6,866 \cdot 10^6$	$6,703 \cdot 10^6$	$6,547 \cdot 10^6$	$6,398 \cdot 10^6$	$6,256 \cdot 10^6$
P_H	Nm^{-2}	$3,573 \cdot 10^{10}$	$2,939 \cdot 10^{10}$	$2,404 \cdot 10^{10}$	$1,946 \cdot 10^{10}$	$1,551 \cdot 10^{10}$	$1,207 \cdot 10^{10}$
ΔE	$J\,kg^{-1}$	$1,323 \cdot 10^6$	$9,799 \cdot 10^5$	$7,123 \cdot 10^5$	$5,046 \cdot 10^5$	$3,447 \cdot 10^5$	$2,235 \cdot 10^5$
ΔT	K	1065	831	650	508	394	301
T_D	K	1998	1764	1583	1441	1327	1234
U_s	ms^{-1}	8135	7777	7460	7175	6919	6686
U_p	ms^{-1}	1627	1399	1193	1004	830	668
S_B	$Jkg^{-1}K^{-1}$	$-465,3$	$-413,8$	$-363,6$	$-314,5$	$-266,5$	$-219,7$
T_C	K	1610	1516	1429	1349	1275	1207
$S_D=SE$	$Jkg^{-1}K^{-1}$	183,6	128,9	86,9	55,8	33,7	18,6
T_E	K	1144	1076	1027	992	968	952
S_S	$Jkg^{-1}K^{-1}$	0	0	0	0	0	0
S_L	$Jkg^{-1}K^{-1}$	415,4	415,4	415,4	415,4	415,4	415,4
100ϕ	%	44,19	31,02	20,91	13,43	8,11	4,47
T_F	K	no superheated liquid					
$T=T_M$	K	933	933	933	933	933	933
ΔE_{th}	Jkg^{-1}	$1,712 \cdot 10^5$	$1,202 \cdot 10^5$	$8,107 \cdot 10^4$	$5,206 \cdot 10^4$	$3,144 \cdot 10^4$	$1,735 \cdot 10^4$
$\frac{1}{2}U_p^2$	Jkg^{-1}	$1,323 \cdot 10^6$	$9,786 \cdot 10^6$	$7,116 \cdot 10^5$	$5,040 \cdot 10^5$	$3,444 \cdot 10^5$	$2,231 \cdot 10^5$
ΔE_{pot}	Jkg^{-1}	$1,152 \cdot 10^6$	$8,583 \cdot 10^5$	$6,305 \cdot 10^5$	$4,519 \cdot 10^5$	$3,130 \cdot 10^5$	$2,057 \cdot 10^5$

Continuation table 11b

$\dfrac{\rho_0}{\rho_1}$		0,92	0,94	0,96	0,98	0,99	Equation
$F(V_1)$	$Nmkg^{-1}$	$-5,638 \cdot 10^4$	$-6,302 \cdot 10^4$	$-5,483 \cdot 10^4$	$-3,337 \cdot 10^4$	$-1,809 \cdot 10^4$	2.22
P_i	Nm^{-2}	$7,686 \cdot 10^9$	$5,447 \cdot 10^9$	$3,438 \cdot 10^9$	$1,630 \cdot 10^9$	$7,943 \cdot 10^8$	2.20
$g(V_1)$	$Jm^{-3}K^{-1}$	$6,120 \cdot 10^6$	$5,990 \cdot 10^6$	$5,865 \cdot 10^6$	$5,745 \cdot 10^6$	$5,687 \cdot 10^6$	2.19
P_H	Nm^{-2}	$9,054 \cdot 10^9$	$6,389 \cdot 10^9$	$4,020 \cdot 10^9$	$1,902 \cdot 10^9$	$9,266 \cdot 10^8$	2.16
ΔE	$J\,kg^{-1}$	$1,341 \cdot 10^5$	$7,099 \cdot 10^4$	$2,978 \cdot 10^4$	$7,048 \cdot 10^3$	$1,716 \cdot 10^3$	2.6
ΔT	K	223	157	99	47	23	2.9
T_D	K	1156	1090	1032	980	956	2.9
U_s	ms^{-1}	6474	6280	6101	5936	5858	2.4
U_p	ms^{-1}	517	376	244	118	58	2.5
S_B	$Jkg^{-1}K^{-1}$	$-173,8$	$-129,0$	$-85,1$	$-42,1$	$-20,9$	2.26a
T_C	K	1144	1085	1031	980	956	2.28
$S_D = SE$	$Jkg^{-1}K^{-1}$	9,1	3,7	1,0	0,12	0,01	2.25a
T_E	K	942	936	934	933	933	2.32
S_S	$Jkg^{-1}K^{-1}$	0	0	0	0	0	2.37a
S_L	$Jkg^{-1}K^{-1}$	415,4	415,4	415,4	415,4	415,4	2.38
100ϕ	%	2,19	0,89	0,24	0,028	0,002	2.39a
T_F	K						
$T=T_M$	K	933	933	933	933	933	
ΔE_{th}	Jkg^{-1}	$8,490 \cdot 10^3$	3452	933	112	9	2.50
$\frac{1}{2}U_p^2$	Jkg^{-1}	$1,336 \cdot 10^5$	$7,068 \cdot 10^4$	$2,976 \cdot 10^4$	6962	1682	2.5
ΔE_{pot}	Jkg^{-1}	$1,251 \cdot 10^5$	$6,723 \cdot 10^4$	$2,883 \cdot 10^4$	6850	1673	2.46

Table 11c: Survey of shock related quantities for Al, $T_0 = 1200$ K.

$\dfrac{\rho_0}{\rho_1}$		0,80	0,82	0,84	0,86	0,88	0,90
$F(V_1)$	$Nmkg^{-1}$	$2,338 \cdot 10^5$	$1,715 \cdot 10^5$	$6,923 \cdot 10^4$	$-6,247 \cdot 10^3$	$-5,802 \cdot 10^4$	$-8,880 \cdot 10^4$
P_1	Nm^{-2}	$2,624 \cdot 10^{10}$	$2,402 \cdot 10^{10}$	$1,996 \cdot 10^{10}$	$1,638 \cdot 10^{10}$	$1,319 \cdot 10^{10}$	$1,035 \cdot 10^{10}$
$g(V_1)$	$Jm^{-3}K^{-1}$	$6,951 \cdot 10^6$	$6,866 \cdot 10^6$	$6,703 \cdot 10^6$	$6,547 \cdot 10^6$	$6,398 \cdot 10^6$	$6,256 \cdot 10^6$
P_H	Nm^{-2}	$3,413 \cdot 10^{10}$	$3,095 \cdot 10^{10}$	$2,533 \cdot 10^{10}$	$2,051 \cdot 10^{10}$	$1.636 \cdot 10^{10}$	$1,273 \cdot 10^{10}$
ΔE	$J kg^{-1}$	$1,201 \cdot 10^6$	$1,031 \cdot 10^6$	$7,505 \cdot 10^5$	$5,319 \cdot 10^5$	$3,635 \cdot 10^5$	$2,359 \cdot 10^5$
ΔT	K	1135	1009	799	631	494	381
T_D	K	2335	2209	1999	1831	1694	1581
U_s	ms^{-1}	8157	7980	7657	7367	7106	6868
U_p	ms^{-1}	1549	1436	1225	1031	852	686
S_B	$Jkg^{-1}K^{-1}$	$-439,4$	$-413,8$	$-363,6$	$-314,5$	$-266,5$	$-219,7$
T_C	K	2009	1950	1838	1735	1640	1553
$S_D=SE$	$Jkg^{-1}K^{-1}$	127,7	106,3	71,4	45,7	27,5	15,2
T_E	K	1383	1350	1299	1262	1237	1220
S_S	$Jkg^{-1}K^{-1}$	–	–	–	–	–	–
S_L	$Jkg^{-1}K^{-1}$	–	–	–	–	–	–
100ϕ	%	100	100	100	100	100	100
T_F	K	1383	1350	1299	1262	1237	1220
T_G	K	–	–	–	–	–	–
ΔE_{th}	Jkg^{-1}	$1,646 \cdot 10^5$	$1,353 \cdot 10^5$	$8,917 \cdot 10^4$	$5,625 \cdot 10^4$	$3,350 \cdot 10^4$	$1,839 \cdot 10^4$
$\frac{1}{2}U_p^{\,2}$	Jkg^{-1}	$1,199 \cdot 10^6$	$1,031 \cdot 10^6$	$7,503 \cdot 10^5$	$5,314 \cdot 10^5$	$3,629 \cdot 10^5$	$2,352 \cdot 10^5$
ΔE_{pot}	Jkg^{-1}	$1,035 \cdot 10^6$	$8,956 \cdot 10^5$	$6,611 \cdot 10^5$	$4,752 \cdot 10^5$	$3,294 \cdot 10^5$	$2,169 \cdot 10^5$

$\dfrac{\rho_0}{\rho_1}$		0,92	0,94	0,96	0,98	0,99	Equation
$F(V_1)$	$Nmkg^{-1}$	$-1,009 \cdot 10^5$	$-9,643 \cdot 10^4$	$-7,711 \cdot 10^4$	$-4,451 \cdot 10^4$	$-2,366 \cdot 10^4$	2.22
P_i	Nm^{-2}	$7,816 \cdot 10^9$	$5,543 \cdot 10^9$	$3,500 \cdot 10^9$	$1,661 \cdot 10^9$	$8,095 \cdot 10^8$	2.20
$g(V_1)$	$Jm^{-3}K^{-1}$	$6,120 \cdot 10^6$	$5,990 \cdot 10^6$	$5,865 \cdot 10^6$	$5,745 \cdot 10^6$	$5,687 \cdot 10^6$	2.19
P_H	Nm^{-2}	$9,559 \cdot 10^9$	$6,748 \cdot 10^9$	$4,248 \cdot 10^9$	$2,011 \cdot 10^9$	$9,796 \cdot 10^8$	2.16
ΔE	$J\,kg^{-1}$	$1,416 \cdot 10^5$	$7,498 \cdot 10^4$	$3,146 \cdot 10^4$	$7,449 \cdot 10^3$	$1,814 \cdot 10^3$	2.6
ΔT	K	284	201	127	60	29	2.9
T_D	K	1484	1401	1327	1260	1229	2.9
U_s	ms^{-1}	6652	6454	6271	6103	6023	2.4
U_p	ms^{-1}	532	387	250	122	60	2.5
S_B	$Jkg^{-1}K^{-1}$	$-173,8$	$-129,0$	$-85,1$	$-42,1$	$-20,9$	2.26a
T_C	K	1471	1396	1326	1260	1229	2.28
$S_D = SE$	$Jkg^{-1}K^{-1}$	7,4	3,0	0,86	0,10	0,01	2.25a
T_E	K	1210	1204	1201,14	1200,13	1200,01	2.32
S_S	$Jkg^{-1}K^{-1}$	–	–	–	–	–	
S_L	$Jkg^{-1}K^{-1}$	–	–	–	–	–	
100ϕ	%	100	100	100	100	100	2.39a
T_F	K	1210	1204	1201,14	1200,13	1200,01	2.40b
$T = T_M$	K	–	–	–	–	–	
ΔE_{th}	Jkg^{-1}	$8,916 \cdot 10^3$	$3,606 \cdot 10^3$	1032	120	12	2.53
$\frac{1}{2}U_p^{\,2}$	Jkg^{-1}	$1,415 \cdot 10^5$	$7,488 \cdot 10^4$	$3,125 \cdot 10^4$	7442	1800	2.5
ΔE_{pot}	Jkg^{-1}	$1,325 \cdot 10^5$	$7,127 \cdot 10^4$	$3,021 \cdot 10^4$	7322	1788	2.46
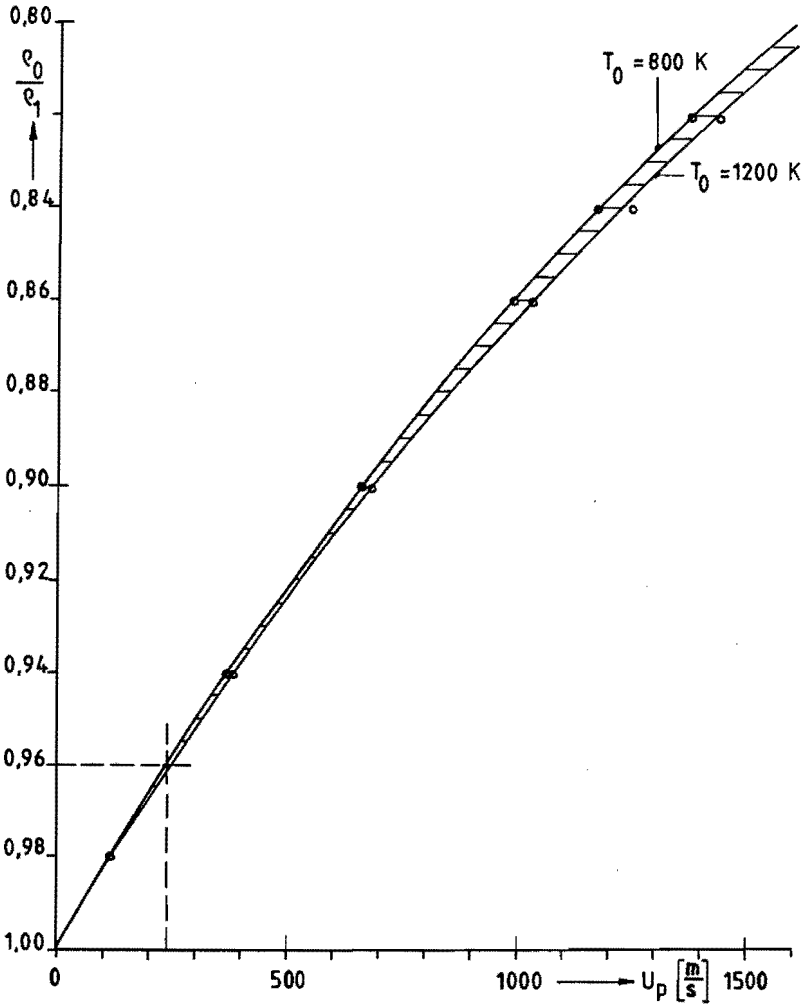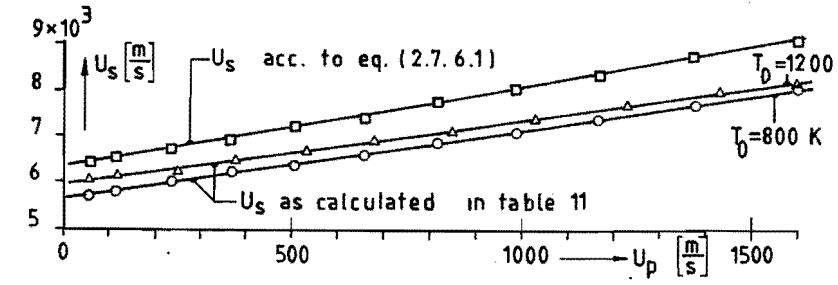
Fig. 2.5: Compression band and shock wave propagation velocity for Al.
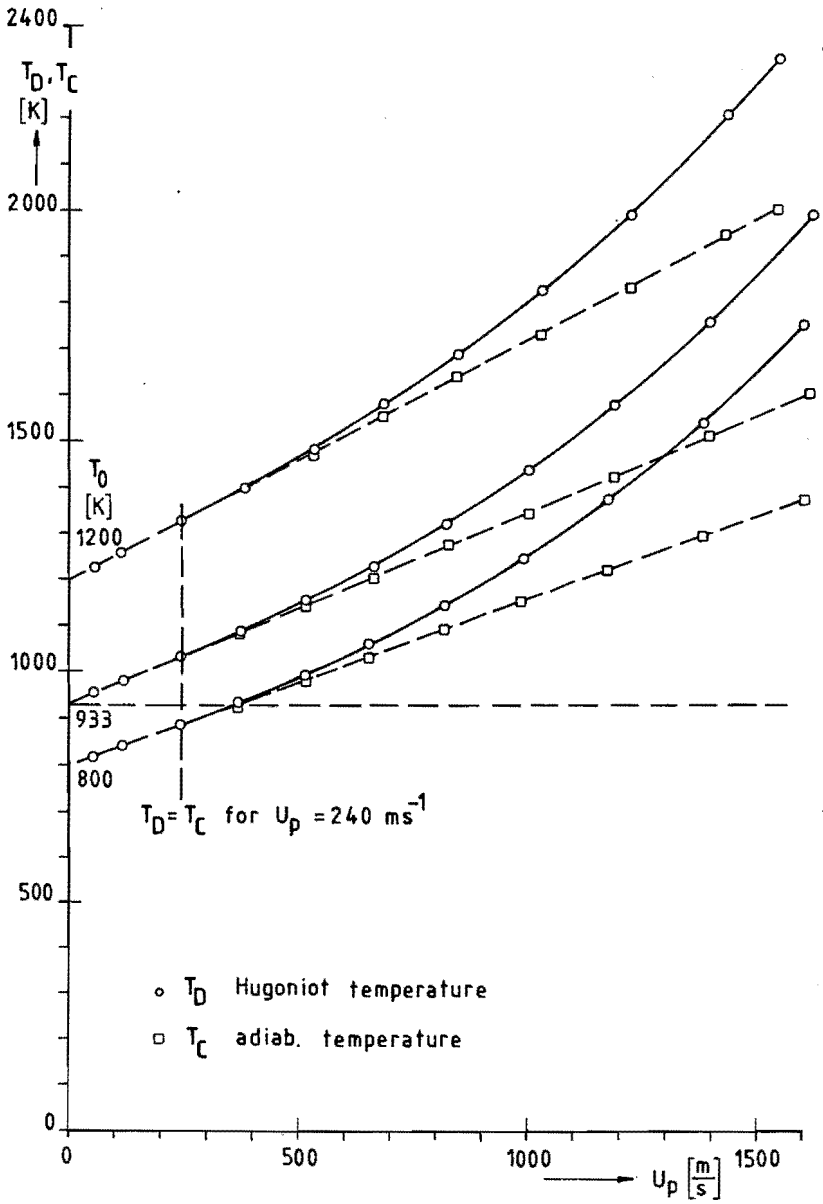
Fig. 2.6:   Compression temperatures for Al.
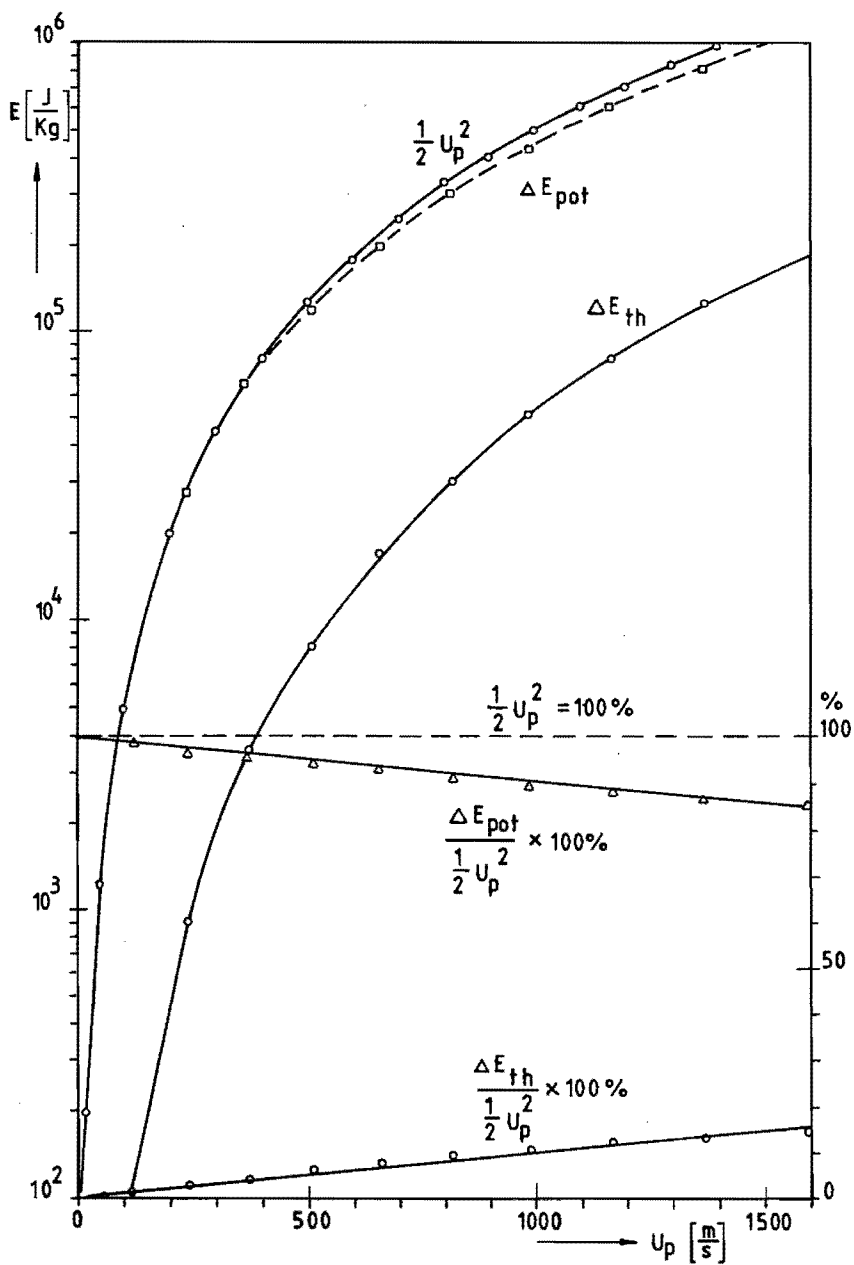
Fig. 2.7: Energy balance for Al, $T_0 = 800$ K.
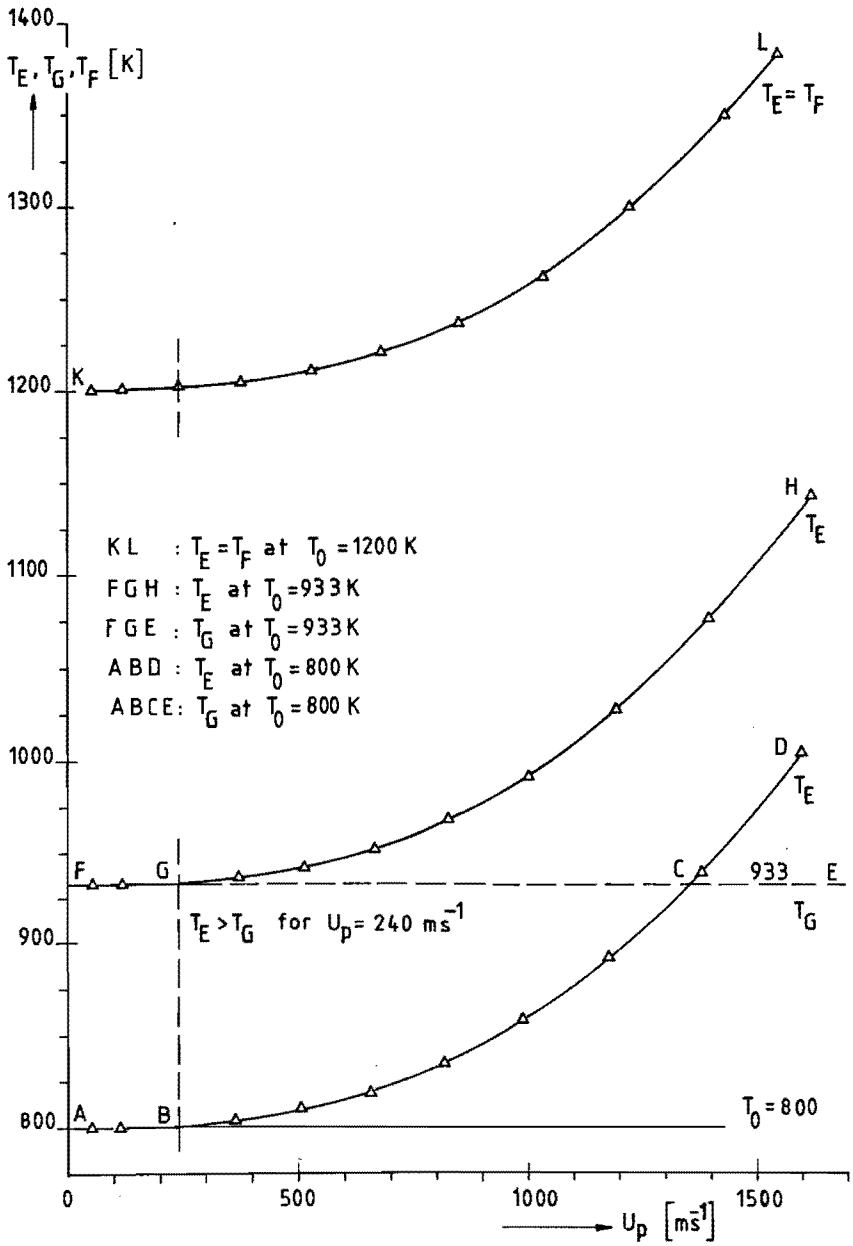
Fig. 2.8:   Relaxation temperatures for Al.

84
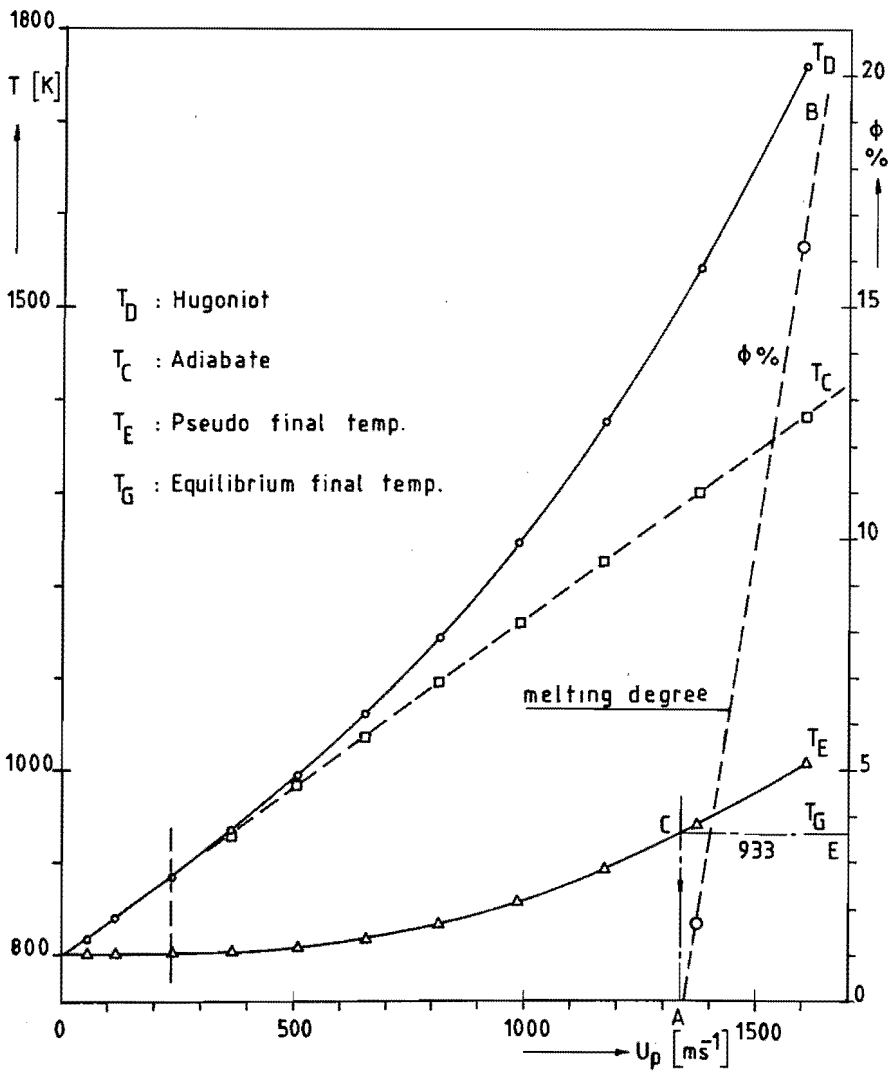
Fig. 2.9:   Melting degree and characteristic temperatures during compression and after relaxation.
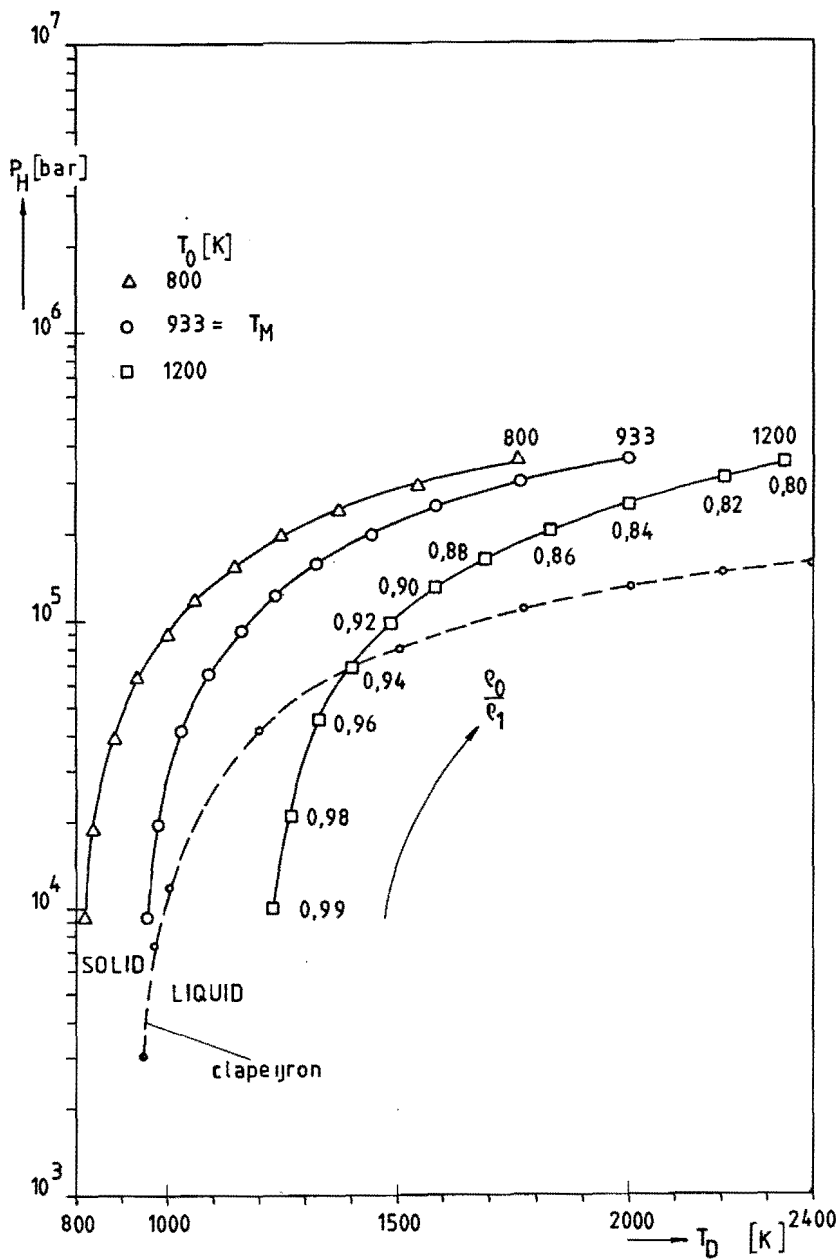
Fig. 2.10: Hugoniot pressure as a function of the shock compression temperature for Al.

Fig. 2.6 compiles the Hugoniot (T_D) and adiabatic (T_C) compression temperatures as a function of U_p. The T_D and T_C curves coincide for velocities up to $U_p = 240$ ms^{-1}; for $U_p > 240$ ms^{-1} T_D and T_C are divergent. According to eq. (2.25a), the shock entropy $S_D = 0$ for $T_D = T_C$, so for relatively weak shocks ($U_p < 240$ ms^{-1}) holds, that no conversion of kinetic to thermal energy takes place. With a standard plasma spray operation the spray particle velocities do not exceed 240 ms^{-1} and conversion of kinetic to thermal energy due to the collision is not to be expected. For an increased collision velocity this picture changes drastically, see also fig. 2.7, showing the energy balance. Sometimes in the literature the idea turns up that all kinetic energy will be directly converted to thermal energy. This idea must be rejected completely. Furthermore it is clear from fig. 2.6 that the temperature increase during the shock can amount two hundred degrees for weak shocks. Fig 2.8 compiles the relaxation temperatures for Al, initially heated to 800, 933 = T_M and 1200 K respectively. These curves also show the thermal effects that may be expected for $U_p > 240$ ms^{-1}. Curve KL represents both the non – equilibrium and the equilibrium final temperature for the case where the spray material is initially liquid. Curve FH represents the non equilibrium relaxed temperature and FGE the equilibrium final temperature for the case where the spray material is heated up to its melting point without being melted prior to the collision. The shock entropy production starts at a velocity of ~ 240 ms^{-1}. After relaxation this entropy is available for the liquefaction of the spray material. The temperature then remains T_M, which is represented by the straight line GE. Curve AD represents the non – equilibrium relaxation temperature for the case where the material initially is heated to a temperature below the melting point. The shock entropy production is first used to increase the temperature to the melting point, which is represented by point C, where the liquefaction starts and is continued along the straight line CE. Fig. 2.9 compiles

all characteristic temperature curves for both compression and relaxation for the case where $T_0 = 800$ K $< T_M = 933$ K. Curve T_D is the Hugoniot shock temperature. Curve TC is the adiabatic shock temperature; mind the point of coïncidence with T_D. Curve TE is the non − equilibrium relaxation temperature. The straight line CE marks the final equilibrium temperature equalling T_M. The straight line AB represents the melting degree ϕ in percent. The last figure regarding aluminium, fig. 2.10, compiles the relations between the Hugoniot temperatures and the Hugoniot pressures. Besides the equilibrium phase line indicating the boundary between the solid and the liquid phase according to Clapeyron has been drawn. (Fig. 2.4 shows this line previously). Now a remarkable conclusion can be drawn. Since the Clapeyron line intersects with the Hugoniot curves it can be expected that for moderate super heating temperatures liquified Al will be transformed to an amorphous solid during the compression phase of the collision. The relaxation will partly take place in the amorphous solid state. When the first (high) pressure release is over, the final release will come about in the liquid state of the material. A highly superheated liquid state of the material will not be changed into an amorphous solid, unless very high compression rates are applied. Consequently a highly super heated particle will spread as a liquid from the first begin of the collision. At this stage of the theory it is hard to imagine what differences will occur in the morphology of a moderately and a highly super heated particle. Experiments will have to clear this matter. The phenomenon of liquid − solid phase transformation occurring with Aluminium, gives rise to the question whether this symptom also appears for Molybdenum; a material with which many experiments have been carried out in the past decade [8, 10]. The final model on the spreading of a spray particle during the collision can be taken up after answering the question.

First the equilibrium solid − liquid phase line for Mo according to Clapeyron's

equation is calculated. The relevant data for Mo are:

$$P^* = 10^5 \text{ Nm}^{-2}; T^* = T_M = 2883K \qquad ;$$

$$\alpha = 19{,}5 \cdot 10^{-6} \text{ K}^{-1} \quad ; \quad \rho_0 = 10200 \text{ kg m}^{-3};$$

$$\Delta H \text{ melt, kg} = L = 288.10^3 \text{ Jkg}^{-1}$$

and the volume change on melting, ΔVmelt, is estimated 4% (no exact figure available) ref. [20a]. Substitution of these data into eq. (2.34) yields for Molybdenum:

$$P = 10^5 = 6{,}99.10^{10} \ln \frac{T_f}{2883} \tag{2.54}$$

See table 12a an 12b for a numerical evaluation of (2.54).

Table 12a: Melting temperature of Mo as a function of pressure.

Tf	P	
[K]	[Nm^{-2}]	[bar]
2883	$1 \cdot 10^5$	1
2900	$4{,}11 \cdot 10^8$	$4{,}11 \cdot 10^3$
3000	$2{,}78 \cdot 10^9$	$2{,}78 \cdot 10^4$
3100	$5{,}07 \cdot 10^9$	$5{,}07 \cdot 10^4$
3300	$9{,}44 \cdot 10^9$	$9{,}44 \cdot 10^4$
3500	$1{,}36 \cdot 10^{10}$	$1{,}36 \cdot 10^5$
4000	$2{,}29 \cdot 10^{10}$	$2{,}29 \cdot 10^5$
4500	$3{,}11 \cdot 10^{10}$	$3{,}11 \cdot 10^5$
5000	$3{,}85 \cdot 10^{10}$	$3{,}85 \cdot 10^5$

Table 12b: Calculation of mean values $\Delta T/\Delta P$ for successive temperature intervals.

ΔT	$3030-2883 =$ 147	$3190-3030 =$ 160	$3320-3190 =$ 130	$3490-3320 =$ 170	K
ΔP	35	32,5	32,5	50	kbar
$\dfrac{\Delta T}{\Delta P}$	4,2	4,9	4,0	3,4	$\dfrac{K}{kbar}$

From table 12 it may be concluded that the average increase in melting temperature for Mo amounts some 4 degrees per 1000 bar pressure increase. Compared to Al the temperature rise per 1000 bar is lower by a factor $4/7 = 0,57$. Once again a provisional conclusion can be that the Clapeyron curve wil intersect with the Hugoniot curves having the same consequenses for the stability of the liquid phase as described for Al.

The set of equations as given in the previous survey has to be solved in a different way than it has been done for Al. The Murnagham parameter s is for Mo an unknown quantity and must be determined prior to the solution of the equations in the following way. Calculate for a certain compression, e.g. $\dfrac{\rho_0}{\rho_1} = 0,8\, P_i$ (eq. 2.20) and $F(V_1)$ (eq. 2.22) as a function of s, where s is stepwise increased with eq. 0,0005. Substitute P_i and $F(V_1)$ into the right hand side of equation (2.16) and find by iteration the intersection with the Hugoniot pressure P_H, which can be found by application of the given Hugoniot fit curves for Mo, see table 9, at the same compression. In fact this way of solution fits solution scheme three. Once, the parameter s is known, solution scheme 2, as applied for Al can be used to determine all wanted quantities, see appendix 7.1 − 7.4. In table 13, a restricted selection of these data, regarding U_p, P_H, and T_D is compiled.
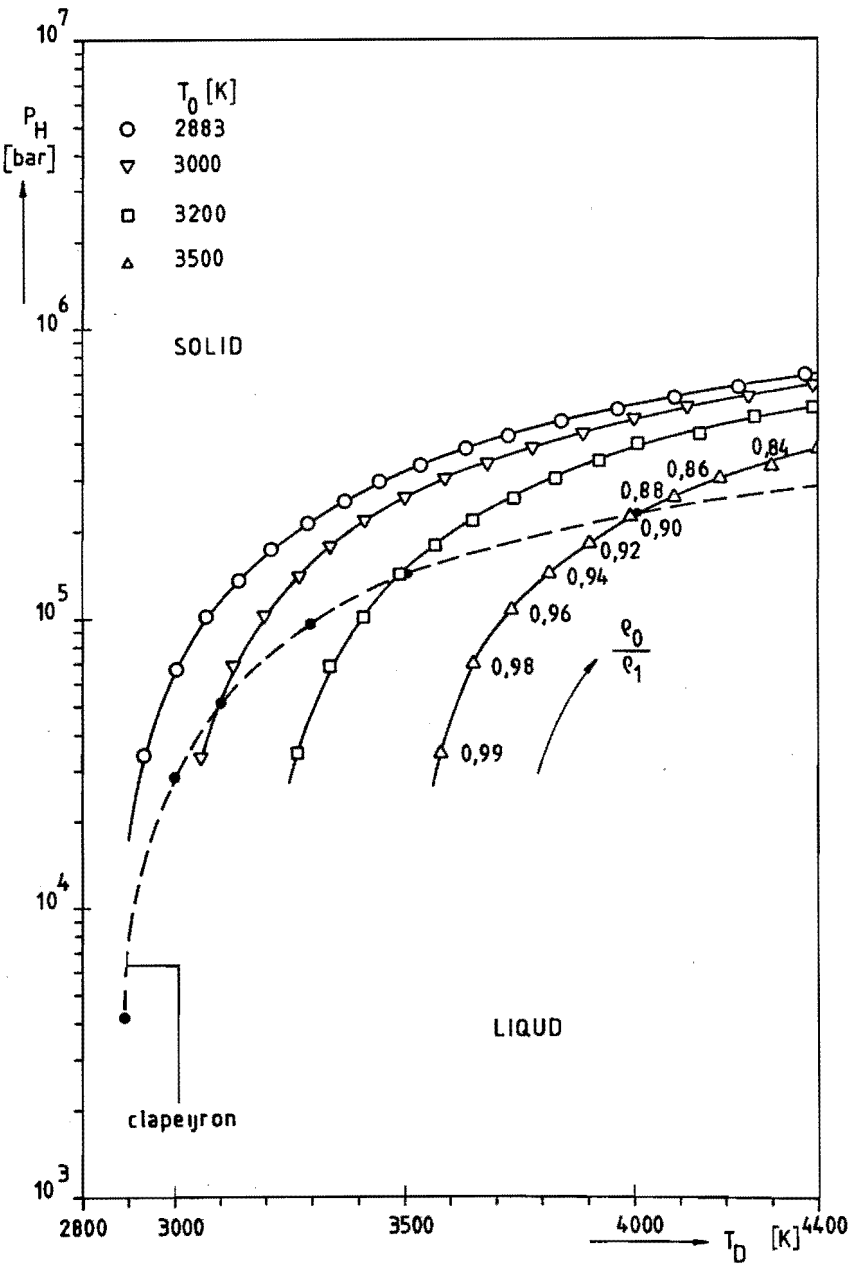
Fig. 2.11: Hugoniot pressure as a function of the shock compression temperature for Mo.

Table 13: Hugoniot Pressure versus compression Temperature for
Molybdenum T_D, T_0, T_M, [°K]; U_p [ms^{-1}]; P_H [Nm^{-2}].

T_0	2883 = T_M				3000	
$\dfrac{\rho_0}{\rho_1}$	U_p	P_H	T_D	U_p	P_H	T_D
0,80	1363	$9,48.10^{10}$	5132	1368	$9,54.10^{10}$	5323
0,81	1279	8,78	4916	1283	8,84	5101
0,82	1197	8,13	4719	1201	8,18	4899
0,83	1117	7,49	4540	1121	7,55	4716
0,84	1040	6,89	4377	1043	6,94	4547
0,85	964	6,32	4227	967	6,37	4393
0,86	890	5,78	4090	893	5,82	4251
0,87	818	5,26	3963	821	5,29	4120
0,88	748	4,76	3845	750	4,79	3999
0,89	679	4,27	3736	681	4,30	3886
0,90	611	3,81	3635	613	3,84	3781
0,91	545	3,37	3540	546	3,39	3682
0,92	480	2,94	3451	481	2,96	3590
0,93	416	2,53	3367	417	2,54	3503
0,94	353	2,13	3287	355	2,14	3421
0,95	292	1,74	3212	293	1,75	3342
0,96	232	1,37	3141	232	1,38	3268
0,97	172	1,01	3072	173	1,02	3197
0,98	114	$6,64.10^9$	3007	114	$6,68.10^9$	3129
0,99	56,6	$3,27.10^9$	2944	56,8	$3,29.10^9$	3063

T_0	3200			3500		
$\dfrac{\rho_0}{\rho_1}$	U_p	P_H	T_D	U_p	P_H	T_D
0,80	1376	$9,66.10^{10}$	5650	1388	$9,82.10^{10}$	6140
0,81	1291	8,95	5418	1302	9,10	5894
0,82	1208	8,27	5207	1218	8,41	5669
0,83	1127	7,63	5015	1137	7,76	5464
0,84	1049	7,02	4838	1058	7,14	5275
0,85	973	6,44	4676	981	6,55	5101
0,86	898	5,88	4527	906	5,98	4941
0,87	825	5,35	4389	832	5,44	4792
0,88	754	4,84	4261	760	4,92	4654
0,89	684	4,35	4142	690	4,42	4525
0,90	616	3,88	4030	621	3,94	4405
0,91	549	3,43	3926	554	3,48	4292
0,92	484	2,99	3828	488	3,04	4186
0,93	420	2,57	3736	423	2,61	4085
0,94	356	2,16	3648	359	2,20	3990
0,95	294	1,77	3565	297	1,80	3899
0,96	233	1,39	3486	235	1,42	3813
0,97	174	1,03	3410	175	1,04	3730
0,98	115	$6,75.10^9$	3337	115	$6,86.10^9$	3650
0,99	57,0	$3,27.10^9$	3267	57,5	$3,37.10^9$	3574

Fig. 2.11 visualizes the relation between P_H and T_D. Besides, the Clapeyron solid – liquid phase line has been drawn (on the basis of table 12). The foregoing provisional conclusion with regards to the possible intersection of Hugoniot pressure curves and the solid – liquid phase line, is now affirmed for the Hugoniot curves where the initial temperature is 3000, 3200 and 3500 K successively. From the position of the left hand curve, which holds for a solid material at melting temperature, it may be concluded that all Hugoniot curves for liquid have a position which implies an intersection with the Clapeyron line. Below the phase line those points are located which represent relatively weak shocks. For instance,

at $T_0 = 3000$ K: $\dfrac{\rho_0}{\rho_1} = 0{,}99$ and $0{,}98$ corresponding to collision velocities

$U_p = 56{,}8$ and 114 ms^{-1} successively;

at $T_0 = 3200$ K: $\dfrac{\rho_0}{\rho_1} = 0{,}99$; $0{,}98$ and $0{,}96$, corresponding to $U_p = 57{,}0$; 115 and

233 ms^{-1};

at $T_0 = 3500$ K: $\dfrac{\rho_0}{\rho_1} = 0{,}99$; $0{,}98$; $0{,}96$; $0{,}94$; $0{,}92$; and $0{,}90$, corresponding to U_p

$= 57{,}5$; 115; 235; 359; 488 and 621 ms^{-1}.

The collision velocities at which a liquid remains liquid increase with the initial temperature of the Molybdenum. In words: a slightly super heated Mo particle will be partly transformed to an amorphous solid, a more distinct super heated material will remain liquid. The behaviour of Mo does not differ greatly from that of Aluminium. According to this theory the spreading of a slightly superheated Mo particle must take place in an amorphous solid state and will not greatly differ from the spreading of an initially solid material slightly below melting temperature. This predicted phenomenon will be investigated experimentally. An amply super – heated Mo particle will spread completely in the liquid state. So, it

can be expected that a great difference exists in the spreaded morphology of an amply super – heated particle and a particle nearby the melting temperature. This theoretical predicted phenomenon will also be tested experimentally. The background of this thesis, as formulated in section 1.3 previously, can now be specified as an attempt to find a relation between the bond strength and the spreading phenomena occurring around the melting point and those, occurring in the superheated state. The model to be tested will now be extended to the domain of mechanical and kinematical effects which play an important role as will be depicted in the next section.

2.3   Mechanics of a colliding spherical particle.

The one dimensional approach regarding the deformation during the propagation of a shock wave implies a geometry as sketched in fig. 2.1. A spray particle mostly has a spherical shape when hitting the substrate. The question arises, what the consequences are for the validity of the previously desecribed shock theory. The main feature of that theory is the adoption of dilatation only, or in other words the appearance of a uniaxial strain situation during the propagation of the shock front. It will be shown that this basic assumption can be kept up right for the front position of the shock wave. The basic ideas for the critical deformation are adopted from Bowden and Field [22], authors who dealt with the collision of rain drops on a solid surface and the accompanying damage of that surface. In [10] the basic considerations of the following section can be found. The basic geometrical relations between a sphere's radius r and a segment's base line BB are sketched in fig. 2.12, where b is the height of a sphere cap and a is the radius of a circle with BB as diameter. When a spherically shaped spray material collides with a rigid target at a velocity U_p the situation after a time elapse of t

$$a^2 = 2rb - b^2$$

$$a = (2rb - b^2)^{\frac{1}{2}}$$
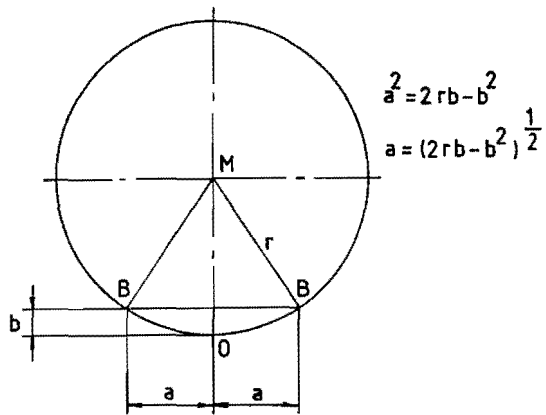
Fig. 2.12:   Geometrical relation between a sphere, a sphere segment and a
sphere cap.

seconds may be represented by fig. 2.13. The material initially within the volume
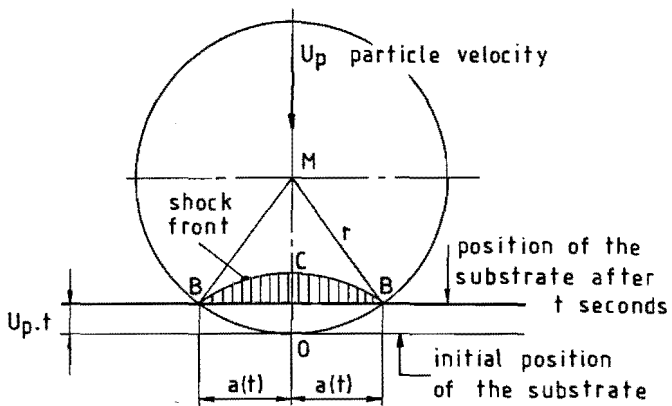
Fig. 2.13:   Scheme of a colliding spherical particle after t seconds.

BOB has been pressed together with the material within the volume BCB, where the line BCB marks the position of the shock wave front at the moment t. Analogous to fig. 2.12 it holds for the situation of fig 2.13:

$$a^2(t) = 2 \, r \, U_p \cdot t - (U_p \cdot t)^2 \qquad (2.55)$$

where a(t) represents the contact area radius at the time t. Differentiation of eq. (2.55) yields:

$$\dot{a}(t) = \frac{U_p \, (r - U_p \cdot t)}{\{2r \cdot U_p \cdot t - (U_p \cdot t)^2\}^{\frac{1}{2}}} = \frac{U_p \, (r - U_p \cdot t)}{a(t)}$$

$$(2.56)$$

where å(t) denotes the velocity at which the perimeter of the contact area moves outwards. Both quantities – a(t) and å(t) – have been computed as a function of time for two characteristic particles sizes: r = 5 μm and r = 25 μm, thus covering the size range from fine to middle – coarse. U_p has been taken into account as another parameter, varying from 50 to 800 ms^{-1}, thus covering practically all common thermal spray processes. Table 14 summarizes the calculated data; fig. 2.14 and 2.15 show the results which give rise to the following remarks:

– The perimeter velocity å(t) increases sharply with decreasing contact face radius. For the middle coarse particle size range, å(t) even touches the range of shock velicities.

– The initial collision phase, arbitrarily marked by a contact – radius of 1 μm, endures ~ $2 \cdot 10^{-9} \rightarrow 1,3 \cdot 10^{-10}$ seconds for a fine particle and $5 \cdot 10^{-10} \rightarrow 3 \cdot 10^{-11}$ seconds for a middle coarse particle.

The time elapse to reach a contact radius which is half the particle radius, is for a fine particle ~ 10^{-8}[s] and for a middle coarse particle ~ 5.10^{-8}[s]. The conclusion: the spreading velocity of a particle increases with it's size. The whole spreading process is about two orders of magnitude faster than the solidification, see table 3. On the one hand, this justifies the adiabatic conditions which were assumed in the

97
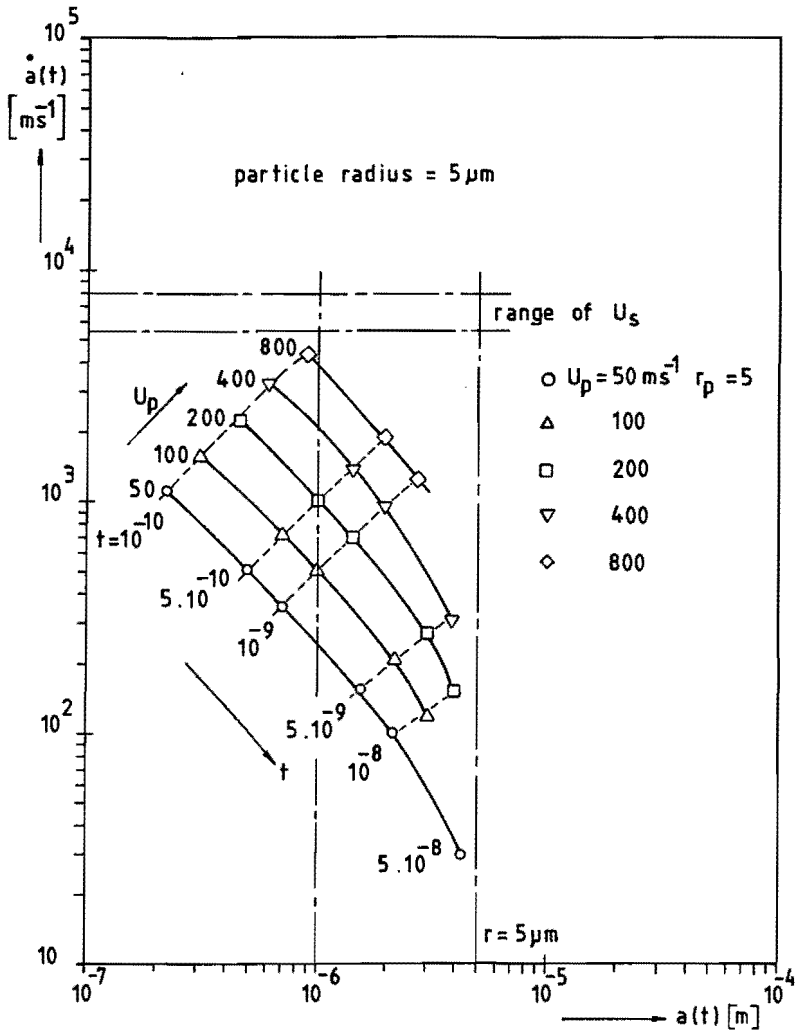
Fig. 2.14: Contact face perimeter velocity as a function of it's radius.
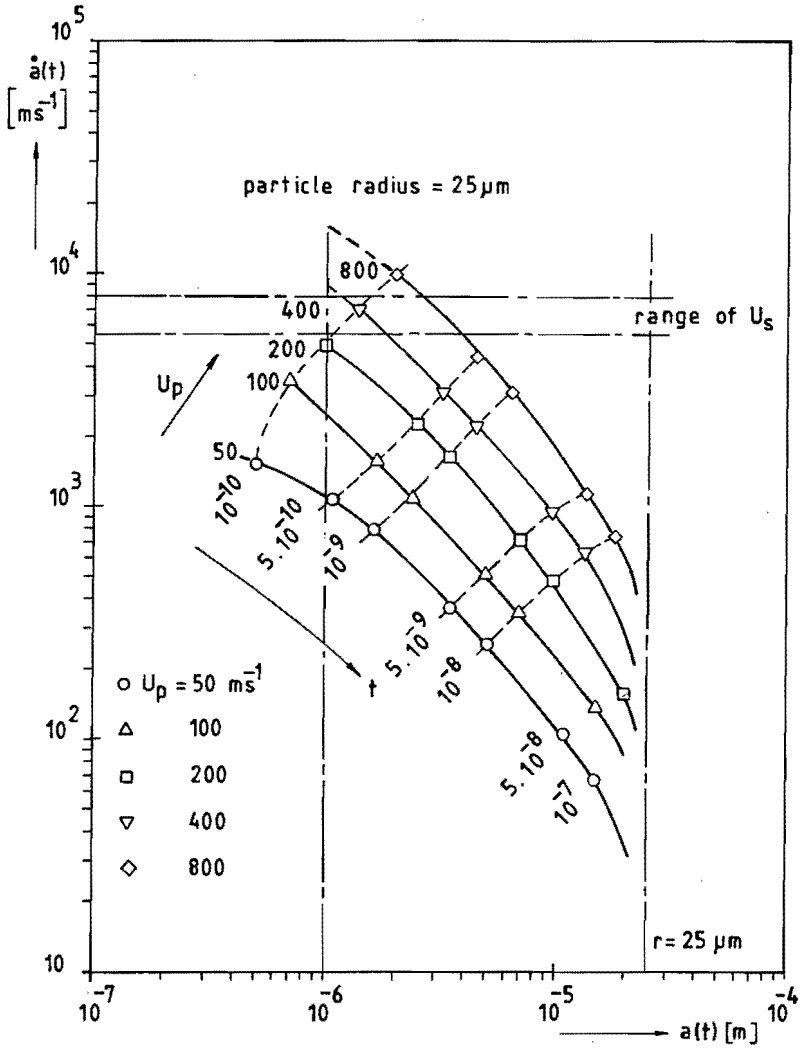
Fig. 2.15: Contact face perimeter velocity as a function of it's radius; r = 25 μm.

Table 14: Contact face radius, $a(t)$, and perimeter velocity, $\mathring{a}(t)$, as a function of U_p, t and the particle radius, r.

$[U_p, \mathring{a}_t] = ms^{-1}$; $[t] = s$; $[a(t)] = m$

Particle radius $r = 5\ \mu m$.

U_p	t	10^{-10}	5.10^{-10}	10^{-9}	5.10^{-9}	10^{-8}	5.10^{-8}	10^{-7}
50	$a(t)$	$2{,}23\cdot10^{-7}$	$4{,}99\cdot10^{-7}$	$7{,}05\cdot10^{-7}$	$1{,}56\cdot10^{-6}$	$2{,}18\cdot10^{-6}$	$4{,}33\cdot10^{-6}$	
	$\mathring{a}(t)$	$1{,}12\cdot10^{3}$	$4{,}98\cdot10^{2}$	$3{,}51\cdot10^{2}$	$1{,}52\cdot10^{2}$	$1{,}03\cdot10^{2}$	$2{,}88\cdot10^{1}$	
100	$a(t)$	$3{,}16\cdot10^{-7}$	$7{,}05\cdot10^{-7}$	$9{,}95\cdot10^{-7}$	$2{,}18\cdot10^{-6}$	$3\cdot10^{-6}$		
	$\mathring{a}(t)$	$1{,}58\cdot10^{3}$	$7{,}02\cdot10^{2}$	$4{,}92\cdot10^{2}$	$2{,}06\cdot10^{2}$	$1{,}33\cdot10^{2}$		
200	$a(t)$	$4{,}46\cdot10^{-7}$	$9{,}95\cdot10^{-7}$	$1{,}4\cdot10^{-6}$	$3\cdot10^{-6}$	$4\cdot10^{-6}$		
	$\mathring{a}(t)$	$2{,}23\cdot10^{3}$	$9{,}85\cdot10^{2}$	$6{,}86\cdot10^{2}$	$2{,}67\cdot10^{2}$	$1{,}5\cdot10^{2}$		
400	$a(t)$	$6{,}31\cdot10^{-7}$	$1{,}4\cdot10^{-6}$	$1{,}96\cdot10^{-6}$	$4\cdot10^{-6}$			
	$\mathring{a}(t)$	$3{,}14\cdot10^{3}$	$1{,}37\cdot10^{3}$	$9{,}39\cdot10^{2}$	$3\cdot10^{2}$			
800	$a(t)$	$8{,}91\cdot10^{-7}$	$1{,}96\cdot10^{-6}$	$2{,}71\cdot10^{-6}$	$4{,}89\cdot10^{-6}$			
	$\mathring{a}(t)$	$4{,}42\cdot10^{3}$	$1{,}88\cdot10^{3}$	$1{,}24\cdot10^{3}$	$1{,}63\cdot10^{2}$			

Particle radius $r = 25\mu m$

U_p		10^{-10}	5.10^{-10}	10^{-9}	5.10^{-9}	10^{-8}	5.10^{-8}	10^{-7}
50	$a(t)$	$4{,}99\cdot10^{-7}$	$1{,}12\cdot10^{-6}$	$1{,}58\cdot10^{-6}$	$3{,}52\cdot10^{-6}$	$4{,}97\cdot10^{-6}$	$1{,}09\cdot10^{-5}$	$1{,}5\cdot10^{-5}$
	$\mathring{a}(t)$	$2{,}49\cdot10^{3}$	$1{,}12\cdot10^{3}$	$7{,}89\cdot10^{2}$	$3{,}51\cdot10^{2}$	$2{,}46\cdot10^{2}$	$1{,}03\cdot10^{2}$	$6{,}67\cdot10^{1}$
100	$a(t)$	$7{,}07\cdot10^{-7}$	$1{,}58\cdot10^{-6}$	$2{,}23\cdot10^{-6}$	$4{,}97\cdot10^{-6}$	$7\cdot10^{-6}$	$1{,}5\cdot10^{-5}$	
	$\mathring{a}(t)$	$3{,}53\cdot10^{3}$	$1{,}58\cdot10^{3}$	$1{,}11\cdot10^{3}$	$4{,}92\cdot10^{2}$	$3{,}43\cdot10^{2}$	$1{,}33\cdot10^{2}$	
200	$a(t)$	$9{,}99\cdot10^{-7}$	$2{,}23\cdot10^{-6}$	$3{,}16\cdot10^{-6}$	$7\cdot10^{-6}$	$9{,}79\cdot10^{-6}$	$2\cdot10^{-5}$	
	$\mathring{a}(t)$	$4{,}99\cdot10^{3}$	$2{,}23\cdot10^{3}$	$1{,}57\cdot10^{3}$	$6{,}86\cdot10^{2}$	$4{,}69\cdot10^{2}$	$1{,}5\cdot10^{2}$	
400	$a(t)$	$1{,}41\cdot10^{-6}$	$3{,}15\cdot10^{-6}$	$4{,}45\cdot10^{-6}$	$9{,}79\cdot10^{-6}$	$1{,}35\cdot10^{-5}$	$2{,}45\cdot10^{-5}$	
	$\mathring{a}(t)$	$7{,}06\cdot10^{3}$	$3{,}14\cdot10^{3}$	$2{,}21\cdot10^{3}$	$9{,}39\cdot10^{2}$	$6{,}19\cdot10^{2}$	$8{,}16\cdot10^{1}$	
800	$a(t)$	$1{,}99\cdot10^{-6}$	$4{,}45\cdot10^{-6}$	$6{,}27\cdot10^{-6}$	$1{,}35\cdot10^{-5}$	$1{,}83\cdot10^{-5}$		
	$\mathring{a}(t)$	$9{,}97\cdot10^{3}$	$4{,}42\cdot10^{3}$	$3{,}08\cdot10^{3}$	$1{,}24\cdot.0^{3}$	$7{,}42\cdot10^{2}$		

100

foregoing section, on the other hand it may elucidate the existence of very thin, thermally instable layers, located in the contact area which were found by Safai and Herman [23]. S and H mention only the high solidification rate as the cause for the occurrance of the thin layers. This fact alone does not explain satisfactorily the existence of unstable thin films. They rather come into being by a fast cooling of highly compressed and consequently amorphous solid material. In ref. [22] Bowden and Field developed the initial concept of the critical contact radius for a liquid with curved profile. This concept is adopted here for a spherical particle, liquid or solid and will be elucidated in this part. An amplified model is shown in figures 2.16 and 2.17. In fig. 2.16 the propagation of wavelets, originating from the utmost frontside of the sphere, point O, is described. B is considered to be a surface location where a wavelet from O arrives simultaneously with the substrate. Then, from triangle OAB it appears that:

$$\overline{OB}^2 = \overline{OA}^2 + \overline{AB}^2 ,$$

expressed in terms of system parameters:

$$(U_s t)^2 = a(t)^2 + (U_p t)^2 \qquad (2.57)$$

Equating eq. (2.55) and eq. (2.57) yields:

$$t = \frac{2\ r U_p}{U_s^2} \qquad (2.58)$$

Also from triangle OAB appears:

$$\sin \varphi = \frac{U_p}{U_s} \qquad (2.59)$$

Eq. (2.58) defines the time needed for a wave front originating from O to reach point B, where point B basically represents the edge between the trapped contact surface BB and the free surface of the sphere. Fig. 2.16 contains more information. Consider the situation a time $\eta_1 t < t$ after the collision start. The

101
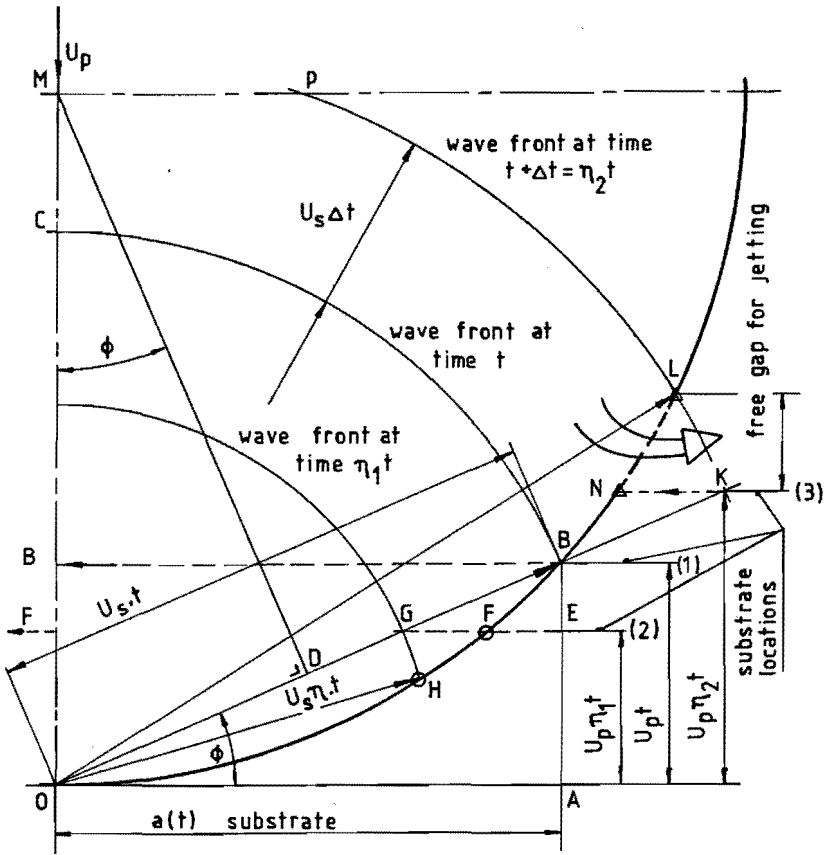
Fig. 2.16:   Position of wave fronts originating from 0; $0 < \eta_1 < 1$; $1 < \eta_2$.
B is a surface location where a wave from O arrives
simultaneously with the substrate. $\sin \phi = \dfrac{U_p}{U_s}$.

substrate has moved into location (2) and the wavelet that started in O, should
have reached point H of the surface if the material below the face FF were un—
deformed. Since the substrate has moved into position (2), the point H is a part of

the contact face between the particle and the substrate. Although location H will be under a high compressive stress, it will remain on its place by the equilibrium counter forces of the neighbour material. Consider the situation at $\eta_2 t > t$ later than the moment of collision begin. Then, the substrate moved into position (3) and the wavelet from O has reached point L of the surface. The gap NL forms a gate for the compressed material below the wave front line LP, through which the material escapes more or less parallel to the substrate. The potential energy ΔE_{pot}, as calculated in the foregoing section, is thus released and is used to give the spray material it's final spread shape.

A more rigorous discussion of the propagation of wave fronts will now be carried out on the basis of fig. 2.17, taking into account that wavelets originating from points along the surface OB arrive at B before the wave from O. Point B represents a surface location identical to point B in fig 2.16: B is a surface point where a wave from O arrives simultaneously with the substrate. Consider a wavelet, starting in point O_1, corresponding to position (1) of the substrate that has been reached after t_0 seconds. At the time t_1, the substrate has moved to position (2), and has abridged the distance

$U_p(t_1 - t_0)$. The wavelet from O_1 travelled in the same time over the distance $U_s(t_1 - t_0)$, implying that the wavelet and the substrate meet at point B_1. For triangle $O_1 A_1 B_1$ holds:

$$\sin \gamma = \frac{U_p}{U_s}$$ and with eq. (2.59) it turns out that $\phi = \gamma$. So, to any point O_1

between O and N along the surface curve belongs a point B_1, where the wave from O_1 and the substrate meet simultaneously. An infinitesimal time delay later than t_1, say t_2, the wave from O_1 overtakes the expanding perimeter of the contact face, thus creating a free gap, KL, through which the compressed material escapes laterally. The tangential point N marks the location where a wavelet
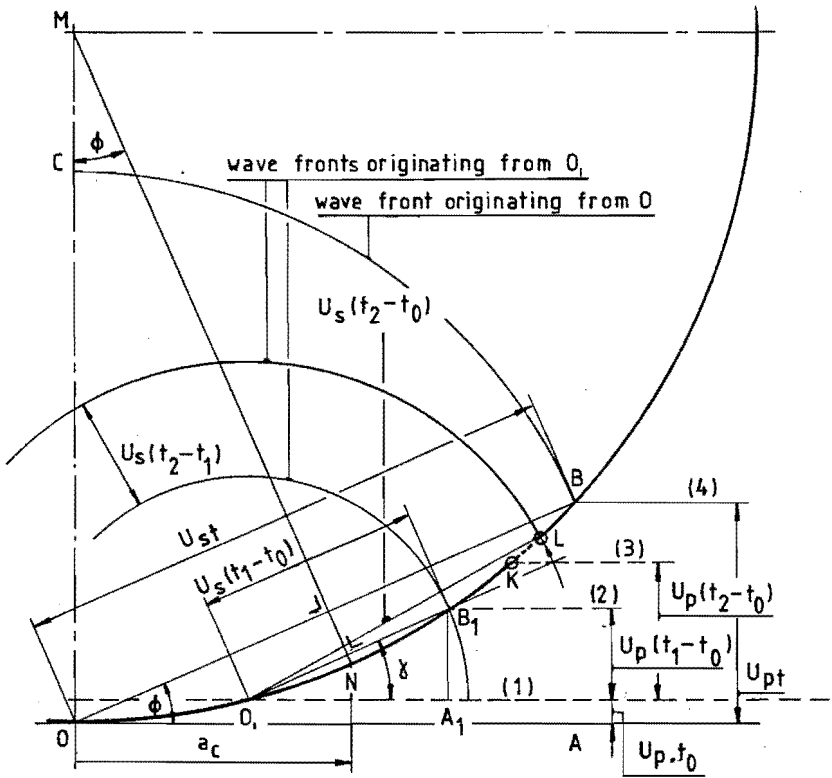
Fig. 2.17: Position of wave fronts originating from 0_1; $t > t_2 > t_1 > t_0$.
B is a surface location identical to the one in fig 2.16.
a_c = critical contact radius.

originating from N immediately reaches the free surface. N marks the critical

radius of the contact surface. Beyond N the compressed material starts it's

relaxation. The main features of fig. 2.17 are shown once again in fig 2.18 to

define the relation between the critical contact radius and the system parameters.

104

From this figure turns out that:

$$a_c = r \cdot \frac{U_p}{U_s} \qquad (2.60)$$

when the contact face radius a_c is overtaken, lateral outflow of the material will occur in order to escape from the pressurized zone below the wave front line. In addition to the critical radius, fig 2.18 shows another interesting feature. Triangle NQR is built up by the components
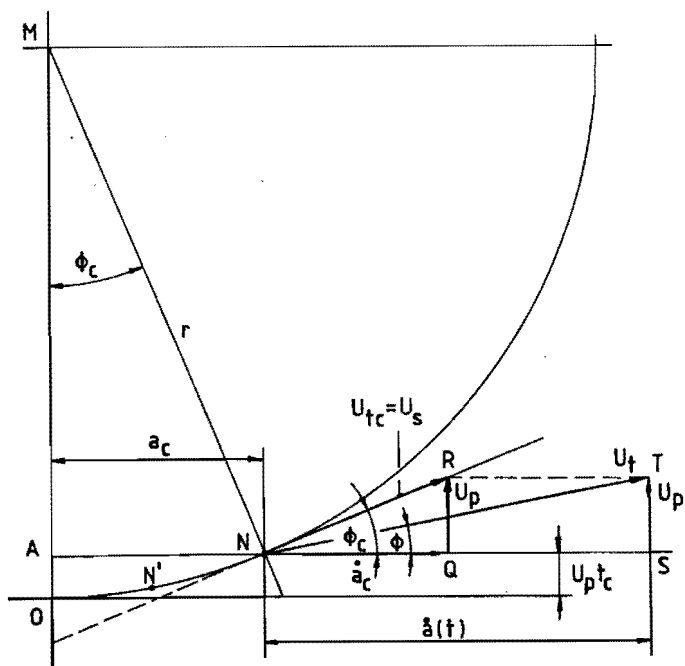
Fig. 2.18:   Definition of the critical contact radius $a_c \cong \overline{AN}$.

$$\sin \phi_c = \frac{\overline{AN}}{\overline{MN}} = \frac{a_c}{r} = \frac{U_p}{U_s}.$$

$\overline{NQ} = \mathring{a}_c$, $\overline{QR} = U_p$ and $\overline{NR} = U_{tc} = U_s$. The formal accuracy of this stated configuration can be proved as follows: For triangle NQR holds:

$$\tan \angle QNR = \tan \phi_c = \frac{U_p}{\mathring{a}_c} \tag{2.61}$$

from eq. (2.56) follows:

$$\mathring{a}_c = \frac{U_p \ (r - U_p \cdot t_c)}{a_c} \tag{2.56.1}$$

consequently:

$$\tan \phi_c = \frac{U_p}{U_p \ (r - U_p \cdot t_c)/a_c} = \frac{a_c}{r - U_p t_c} \tag{2.62}$$

This equation can be derived in another way, thus proving it's correctness: for triangle NAM (fig 2.18) holds:

$$\tan \angle AMN = \tan \phi_c = \frac{\overline{AN}}{\overline{AM}} = \frac{\overline{AN}}{\overline{OM} - \overline{OA}} = \frac{a_c}{r - U_p t_c}$$

which is exactly equation (2.62) q.e.d. For triangle QNR now holds:

$$\sin \phi_c = \frac{U_p}{U_{tc}} \text{ and on account of eq. (2.60)}$$

U_{tc} must equal U_s. The concept of the critical contact radius can now be described in words. For a surface location Ń along ON, where N denotes the critical radius location, the vector summation $\mathring{a}(t) + U_p$ equals U_t, the velocity at which the perimeter of the contact face moves tangentially to the sphere, see triangle NST fig. 2.18 (which in fact holds for a location Ń where $\phi \leq \phi_c$.) For the critical radius a_c, the spreading velocity $\mathring{a}(t) = \mathring{a}_c$ has decreased to such a level, that the vector summation with U_p equals U_s. The reduction of $\mathring{a}(t)$ with increasing contact radius has been described already in fig. 2.14 and 2.15. Once

106

the tangential velocity of the perimeter diminshed to U_s, any wave that starts from a surface location beyond the critical radius, will overtake immediately the contactface perimeter, thus creating a free gap for lateral jetting of the compressed material which has been trapped between the frontline of the shock waves and the substrate. Herewith, the physical meaning of the critical contact radius concept may be rounded off and clear.

The lengthy section 2.2 may now be justified too, because it permits to estimate the stored potential energy in the compression zone which is set free, on from the moment t_c. The time t_c marks the start of release waves into the compressed material and since the wave propagation speed in material under pressure exceeds the wave propagation speed for undisturbed material, it might be possible that the wave front is overhauled by a release wave that started at time t_c prior to the moment that the front wave reaches the upper boundary of the sphere. This phenomenon certainly will have to be subject of a deeper analysis in next future. The critical radius also determines the volumetric expansion of the pressurized zone at the moment that lateral outflow starts. Eq. (2.60) describes the influence of the particle size on the contact radius. Coarse particles will build up more potential energy than small particles will do at the same impact velocity. From ref. [24] and [25] it is worth while to mention that experimentally determined lateral flow velocities of water obey the law:

$$U_j = k \cdot U_p \qquad\qquad (2.63)$$

where k is a factor 3 approximately. This implies that the compressed material really will jet away laterally from the center of impact, even at low collision velocities. The time t_c marks also the moment when the uniaxial strain situation adopted as the theoretical basis of section 2.2 changes into a tri axial strain situation at the bottom side of the compressed zone. Finally the time t_c characterizes the duration of the time period for the thermodynamic effects which

107

take place in the contact zone with the substrate. T_c must be compared to the solidifiation time. It will be shown that the duration of the dynamical effects is so much shorter than the time span for the heat conduction, that both phenomena can be sonsidered separately without degradation of the theoretical basis.

A working expression for the critical time t_c can be derived as follows. Eq. (2.60) defines a_c. The radius as a function of time is given by eq. (2.55). When $t = t_c$, $a(t) = a_c$ and $å(t) = å_c$. Substitution of (2.60) into (2.55) yields:

$$\left(\frac{r \ U_p}{U_s}\right)^2 = 2 \ r \ U_p t_c - (U_p t_c)^2 . \tag{2.64}$$

Rewritten:

$$t_c^2 - \frac{2 \ r}{U_p} t_c + \left(\frac{r}{U_s}\right)^2 = 0 \tag{2.64a}$$

The roots of this equation are:

$$t_{c1} = \frac{r}{U_p} + \frac{r}{U_p} \sqrt{\frac{1 - U_p^2}{U_s^2}} \tag{2.65}$$

and:

$$t_{c2} = \frac{r}{U_p} - \frac{r}{U_p} \sqrt{\frac{1 - U_p^2}{U_s^2}} \tag{2.65a}$$

The deformation model prescribes $U_p t_c \leq r$ or $t_c \leq \dfrac{r}{U_p}$, so eq. (2.65a) is valid;

with $t_{c2} = t_c$:

$$t_c = \frac{r}{U_p} \left(1 - \sqrt{\frac{1 - U_p^2}{U_s^2}}\right) \tag{2.66}$$

Eq. (2.60) and (2.66) are expressions for the critical quantities a_c and t_c with eq. (2.7.b.1) for Mo, $U_s = 6876 + 1{,}77 \ U_p$, a numerical evaluation of a_c and t_c can be carried out, see table 15. The critical time varies from $2{,}6 \cdot 10^{-12}$ to $4{,}3 \cdot 10^{-10}$ seconds over a wide span of particle velocity and size.

108

Table 15: Critical radius, a_c, and critical time, t_c, as a function of r and U_p.

r μm	U_p	50	100	200	400	800	1600	ms^{-1}
5	a_c	$3{,}6\cdot10^{-8}$	$7{,}1\cdot10^{-8}$	$1{,}4\cdot10^{-8}$	$2{,}6\cdot10^{-7}$	$4{,}8\cdot10^{-7}$	$8{,}2\cdot10^{-7}$	m
	t_c	$2{,}6\cdot10^{-12}$	$5{,}0\cdot10^{-12}$	$9{,}6\cdot10^{-12}$	$1{,}7\cdot10^{-11}$	$2{,}9\cdot10^{-11}$	$4{,}3\cdot10^{-11}$	s
10	a_c	$7{,}2\cdot10^{-8}$	$1{,}4\cdot10^{-7}$	$2{,}8\cdot10^{-7}$	$5{,}3\cdot10^{-7}$	$9{,}6\cdot10^{-7}$	$1{,}6\cdot10^{-6}$	m
	t_c	$5{,}2\cdot10^{-12}$	$1{,}0\cdot10^{-11}$	$1{,}9\cdot10^{-11}$	$3{,}5\cdot10^{-11}$	$5{,}8\cdot10^{-11}$	$8{,}5\cdot10^{-11}$	s
20	a_c	$1{,}4\cdot10^{-7}$	$2{,}8\cdot10^{-7}$	$5{,}5\cdot10^{-7}$	$1{,}1\cdot10^{-6}$	$1{,}9\cdot10^{-6}$	$3{,}3\cdot10^{-6}$	m
	t_c	$1{,}0\cdot10^{-11}$	$2{,}0\cdot10^{-11}$	$3{,}8\cdot10^{-11}$	$7{,}0\cdot10^{-11}$	$1{,}2\cdot10^{-10}$	$1{,}7\cdot10^{-10}$	s
25	a_c	$1{,}8\cdot10^{-7}$	$3{,}5\cdot10^{-7}$	$6{,}9\cdot10^{-7}$	$1{,}3\cdot10^{-6}$	$2{,}4\cdot10^{-6}$	$4{,}1\cdot10^{-6}$	m
	t_c	$1{,}3\cdot10^{-11}$	$2{,}5\cdot10^{-11}$	$4{,}8\cdot10^{-11}$	$1{,}0\cdot10^{-10}$	$1{,}5\cdot10^{-10}$	$2{,}0\cdot10^{-10}$	s
30	a_c	$2{,}2\cdot10^{-7}$	$4{,}3\cdot10^{-7}$	$8{,}3\cdot10^{-7}$	$1{,}6\cdot10^{-6}$	$2{,}9\cdot10^{-6}$	$4{,}9\cdot10^{-6}$	m
	t_c	$1{,}5\cdot10^{-11}$	$3{,}0\cdot10^{-11}$	$5{,}7\cdot10^{-11}$	$1{,}0\cdot10^{-10}$	$1{,}7\cdot10^{-10}$	$2{,}6\cdot10^{-10}$	s
35	a_c	$2{,}5\cdot10^{-7}$	$5{,}0\cdot10^{-7}$	$9{,}7\cdot10^{-7}$	$1{,}8\cdot10^{-6}$	$3{,}4\cdot10^{-6}$	$5{,}8\cdot10^{-6}$	m
	t_c	$1{,}8\cdot10^{-11}$	$3{,}5\cdot10^{-11}$	$6{,}7\cdot10^{-11}$	$1{,}2\cdot10^{-10}$	$2{,}0\cdot10^{-10}$	$3{,}0\cdot10^{-10}$	s
40	a_c	$2{,}9\cdot10^{-7}$	$5{,}7\cdot10^{-7}$	$1{,}1\cdot10^{-6}$	$2{,}1\cdot10^{-6}$	$3{,}9\cdot10^{-6}$	$6{,}6\cdot10^{-6}$	m
	t_c	$2{,}1\cdot10^{-11}$	$4{,}0\cdot10^{-11}$	$7{,}6\cdot10^{-11}$	$1{,}4\cdot10^{-10}$	$2{,}3\cdot10^{-10}$	$3{,}4\cdot10^{-10}$	s
50	a_c	$3{,}6\cdot10^{-7}$	$7{,}1\cdot10^{-7}$	$1{,}4\cdot10^{-6}$	$2{,}6\cdot10^{-6}$	$4{,}8\cdot10^{-6}$	$8{,}2\cdot10^{-6}$	m
	t_c	$2{,}6\cdot10^{-11}$	$5{,}0\cdot10^{-11}$	$9{,}6\cdot10^{-11}$	$1{,}7\cdot10^{-10}$	$2{,}9\cdot10^{-10}$	$4{,}3\cdot10^{-10}$	s

A comparison with the solidification time for Mo on Fe leads to the conclusion that a separate describtion of dynamic and heat conduction phenomena is justified due to the short lasting dynamic effects. The a_c values have been compiled in fig. 2.19 which shows that the initial compression stage encompasses only a slight mass of the sphere. For impact velocities up to 100 ms^{-1} the critical contact radius is even limited to less than one micron for all size of particles.

109
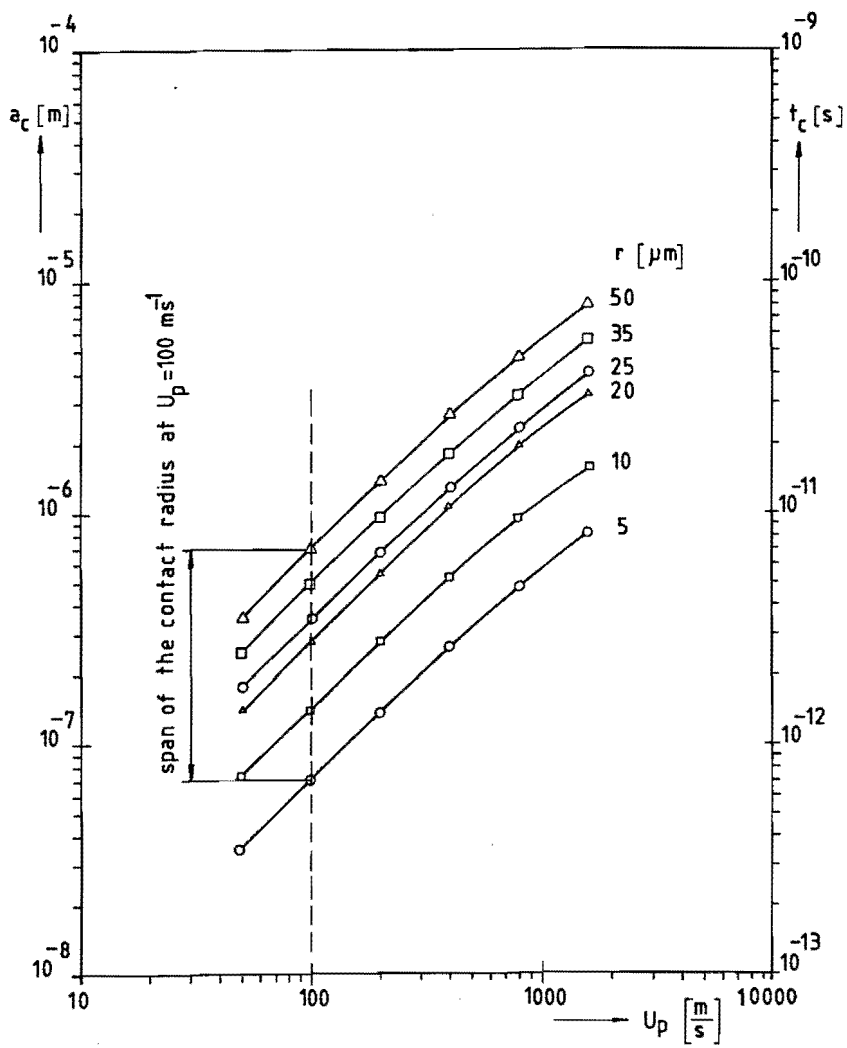
Fig. 2.19:   Critical radius and critical time for Mo.

This restricted amount of mass will be squeezed away laterally. At the same moment release waves will start moving towards the propelling shock front. The final collision model can be split up into two stages, see fig. 2.20 a and b.
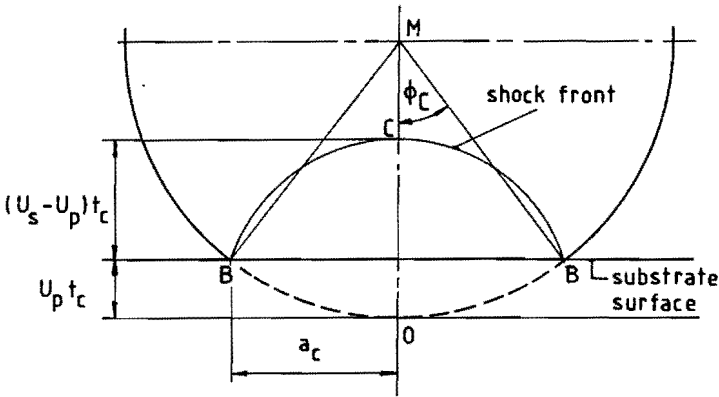
Fig. 2.20a: Initial stage of the collision.
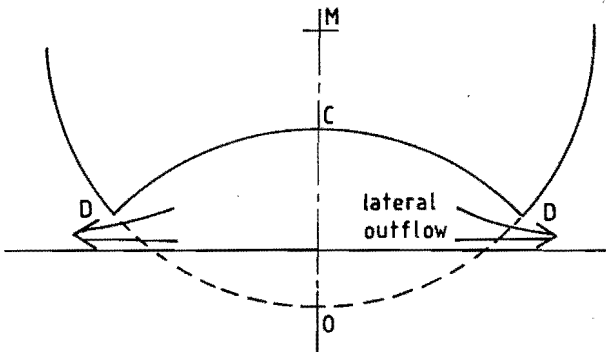
Fig. 2.20b: Post critical stage of the collision.

1.   An initial stage where material, primarily located within the volume OBB, is pressed together with the mass within volume BBC. In this stage no outflow occurs.

111

2.   A post – critical stage where the compressed material behind the shock
     wave laterally escapes from the pressurized zone and the spreading of the
     material actually takes place.

Apart from these two stages, another most important feature of the collision
model turned up from the thermodynamic calculations: a liquid can be
transformed into an amorphous solid by an exerted high pressure. If this is the
case, the lateral deformation process will be dammed by the shear forces of the
solid material. On the basis of the previous calculations, Al and Mo will spread
partially in a solid amorphous state, even if they are super heated It can be
foreseen that such a spread morphology has a more explosive character than that
occurring with an amorphous solid material. To conclude the theory chapter an
estimation will be made of the explosive potential that is built up during the first
stage of the collision. The volume encompassed by the shock wave, consists of two
parts: volume OBB $\hat{=} V_1$ and volume BBC $\hat{=} V_2$.

$$V_1 = \frac{\pi}{6} U_p t_c \{3a_c^2 + (U_p t_c)^2\} \tag{2.67}$$

$$V_2 = \frac{\pi}{6} (U_s - U_p) t_c \{3a_c^2 + (U_s - U_p)^2 t_c^2\} \tag{2.68}$$

Note: the shock front is assumed to be spherically shaped for an easy
approximation. Summation of eq. (2.67) and (2.68) produces the total shock
induced volume:

$$V_1 + V_2 = \frac{\pi}{2} a_c^2 U_s t_c + \frac{\pi}{6} (U_p t_c)^3 + \frac{\pi}{6} \{(U_s - U_p) t_c\}^3 \tag{2.69}$$

with a_c according to eq (2.60) and t_c according to (2.66) and disregarding the
terms with a third power of t_c, eq. (2.69) can be approximated by:

112

$$V_1 + V_2 \quad \cong \frac{\pi}{2} a_c^2 U_s t_c$$

$$= \frac{\pi}{2} r^3 \frac{U_p}{U_s} (1 - \sqrt{1 - \frac{U_p^2}{U_s^2}}$$

and with $M = \dfrac{U_p}{U_s}$

$$V_1 + V_2 \quad = \frac{\pi}{2} r^3 M (1 - \sqrt{1 - M^2} \qquad (2.70)$$

$$= \frac{\pi}{2} \cdot f(M) \cdot r^3 \qquad (2.70a)$$

where $f(M)$ is a growing function with increasing M. The potential energy contained within the volume $V_1 + V_2$ at the critical moment t_c is:

$$E_{pot_c} = \rho_0 (V_1 + V_2) \Delta E_{pot} \qquad (2.71)$$

which can be rewritten with (2.46) and (2.53):

$$E_{pot_c} = \frac{\pi}{2} \rho_0 f(M) r^3 [\tfrac{1}{2} U_p^2 - C_p (T_F - T_0)]$$

$$(2.72)$$

For weak shocks finally holds:

$$E_{pot_c} = \frac{\pi}{4} \rho_0 \cdot f(M) r^3 U_p^2 \qquad (2.73)$$

Eq. (2.73) gives a survey of the parameters which really matter regarding the spreading of a spherical particle. The size is of extreme importance. A big particle builds up more potential energy than a small one. Of course the impact velocity plays an important part too. The spread morphology of a big particle tends easier to an explosive character than will be the case with a small one. In fact a small one at moderate impact velocity, will not have an essential explosiv potential.

CHAPTER 3   EXPERIMENTS.

3.1   Introduction

The previous chapter describes the outlines of a thermo – dynamical and
mechanical model with regard to the spreading of a spherical particle on a rigid
substrate.
The main features of this model are:
1.   A two stage collision. During the first stage, kinetic energy is converted to
      potential energy, to be stored in the contact region with the substrate. In
      the second stage, first the stored potential energy is released and second, a
      continuous lateral outflow of compressed material will take place on the
      bottom side of the particle.
2.   A possible transformation of liquid to amorphous solid. An amorphous
      solid material will reduce the lateral outflow by shear forces, while a liquid
      can expand without being slowed down by strong counter acting forces.
It seems to be possible to test some aspects of the model by the application of a
high speed electronic camera which produces more than 10 million pictures per
second. Such a device is not available within the laboratory for thermal spraying.
Consequently an indirect check is adopted: microscopical examination of spread
particles.

3.2   First order of spread particle morphology.

A characteristic choice of Mo particle morphologies is shown in photo 1 to 9.
Generally the deposits may be distinguished in a pancake type and a flower type
deposit. The pancakes show cracks, the flower leaves have no fissures. Both types
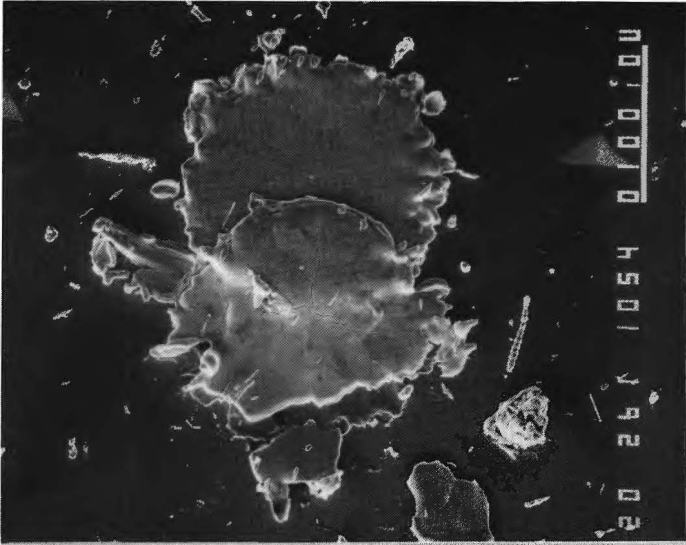
Photo 1: Two pancakes partly on top of each other; the deposit is cracked.

Photo 2: A SEM picture of one pancake with a typical corona around it.

Photo 5: Flower type deposits with and without corona.

Photo 4: A flower type deposit.

Photo 3: A pancake with a radially directed corona.

Photo 8: Pancake and flowerleaves within one particle. Mind that the central pancake deposit is cracked.
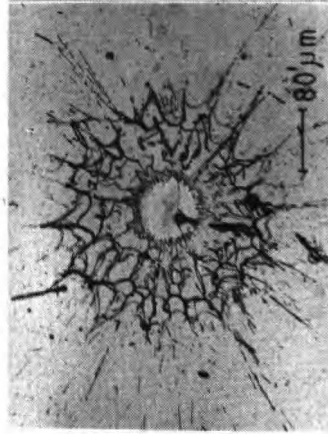
Photo 7: Typical appearance of a small particle.

116

Photo 6: SEM picture of a flower with corona.
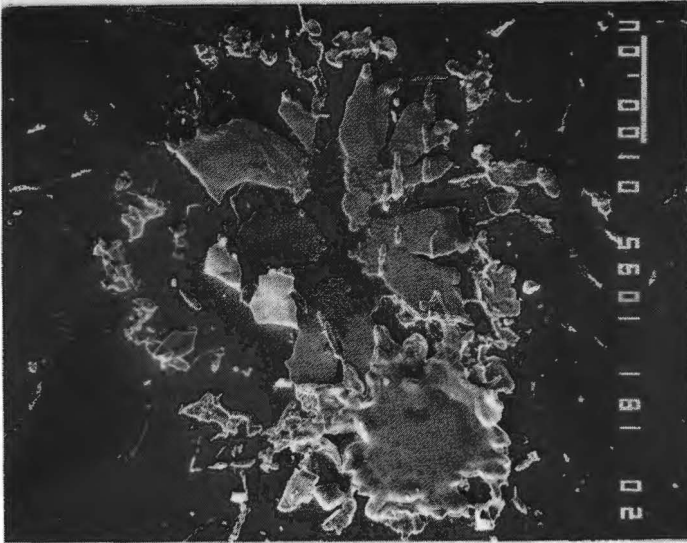
Photo 8: SEM picture of a pancake and a flower, overlapping each other.

117

can be accompanied by a corona around the central part of the deposit. The corona appears in three different forms sometimes overlapping each other. The first type exists of small upheavals, grouped as a chaplet around the central part at a certain distance from the outer boundary. The second type looks like a many times folded broken string, also enclosing at a certain distance the centrally located part of the deposit. The third type of corona exists of radially directed striations, emanating continuously from the center part; see fig. 3.1, 3.2 and 3.2a

more or less clean surface
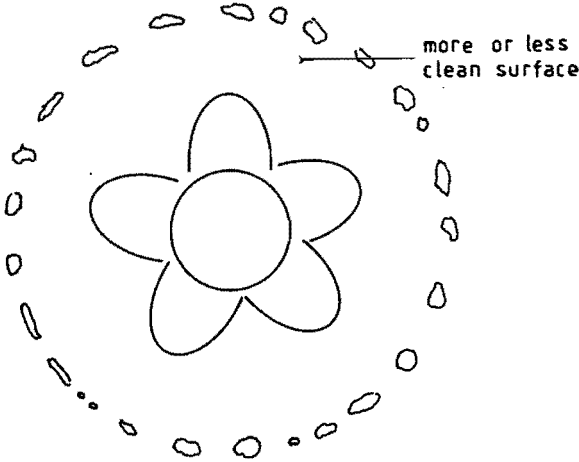
Fig. 3.1:   Corona of upheavels around the central part.

for a basic shetch of the corona types. A small particle always coexists with the string and the striation corona, while a coarse particle can be accompanied by all three types. A cut through a single particle perpendicula to the surface, reveals that the pancake type deposits are in good contact with the substrate while the flower leaves turn out to be free standing partially. The cracks in the pancake are due to the good contact with the substrate during the heat transfer from particle to substrate. The flower leaves on the other hand shrink partially without being
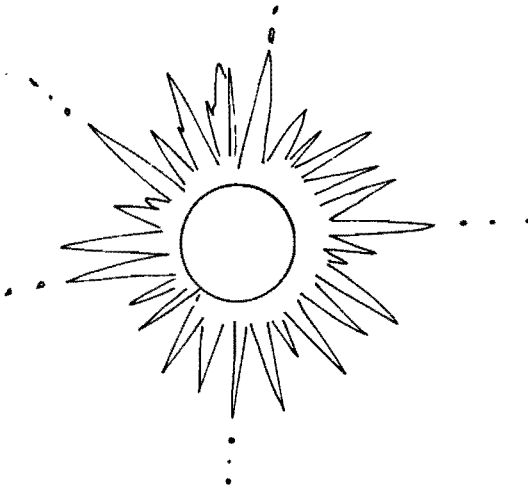
Fig. 3.2:   Radial type of corona adjacent to the central part.
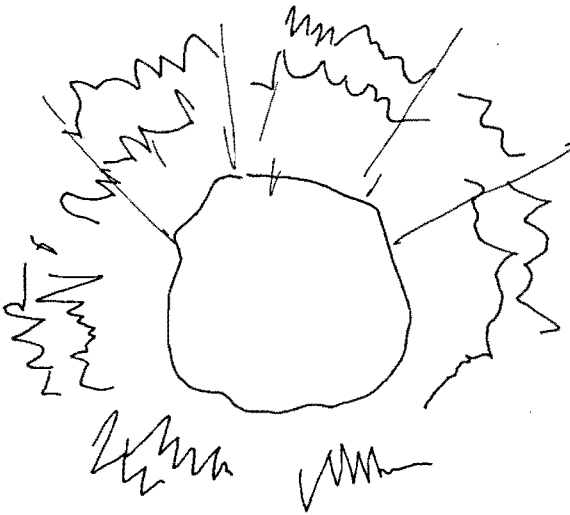
Fig. 3.2.a: String type corona.

119

hindered by contact forces. Therefore they are fissure free to a certain extent. A choice of characteristic metallographic cross sections is shown in photos 10, 11, 12, and 13, regarding flower types while photo 14 shows a typical pancake. Photo 13 especially demonstrates the corona in crossection on the right hand side. From an electron probe microanalysis it turns out that the chaplet shaped corona exists of both substrate and spray material. The substrate mostly is heavily deformed. The material has moved laterally from the center of impact. Overlooking many cuts through single particles the charateristic form of a pancake and a flower type deposit may be presented as in fig. 3.3 and 3.4. Especially the metallographic
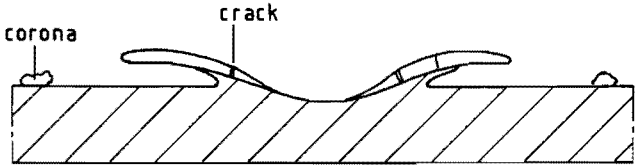
Fig. 3.4:   Scheme of a cut through a flower type deposit with corona.
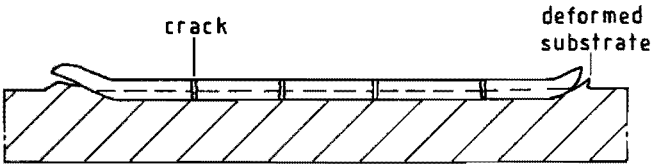
Fig. 3.3:   Scheme of a cut through a pancake deposit.

cross sections demonstrate one of the main features of the model: the lateral flow of material, occurring both for pancake and flower deposits. A rather interesting question turns up while observing a lot of splashes.

120

——— 18 um
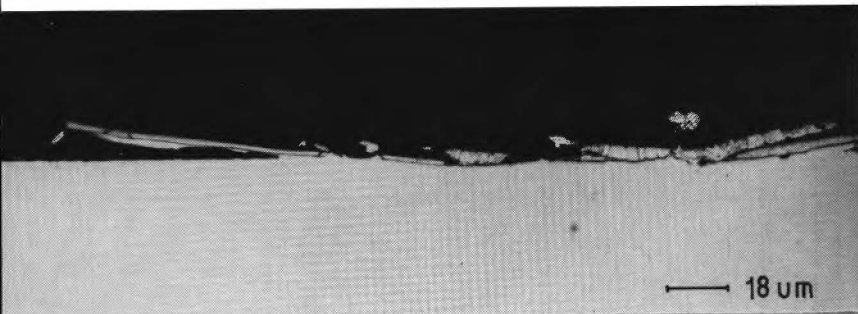
Photo 10: Cross section through flower type deposit; extreme
free standing leave.

——— 18 um
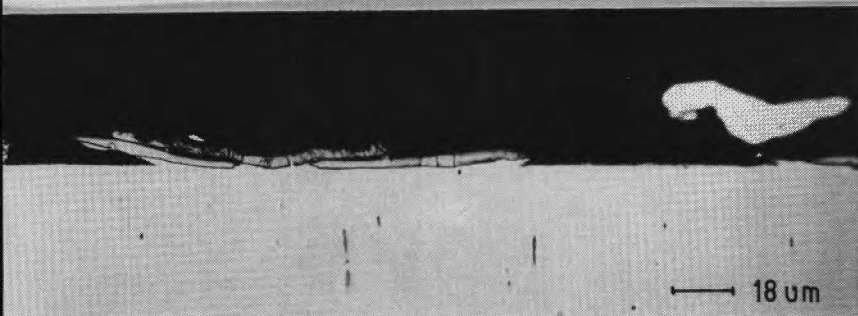
Photo 11: Overlapping flower and pancake.

——— 18 um
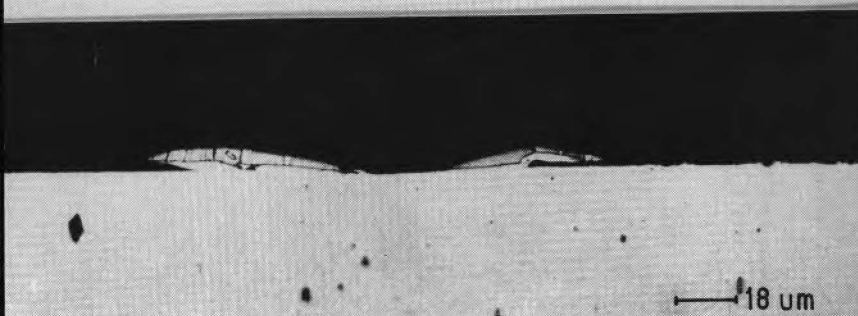
Photo 12: Spread particle without remaining spray material at
the center of impact.

Photo 13: Cut through a flower type deposit with distinct corona on the right hand side.
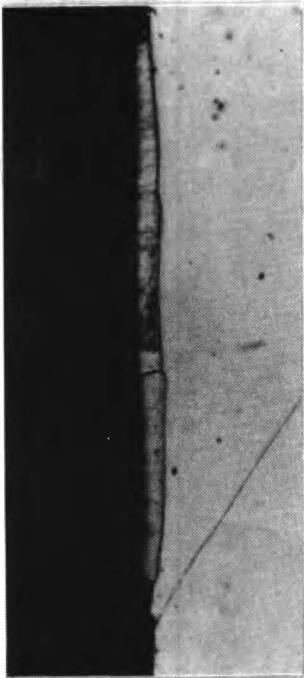
Photo 14: Typical pancake with fissures and good contact to the surface.
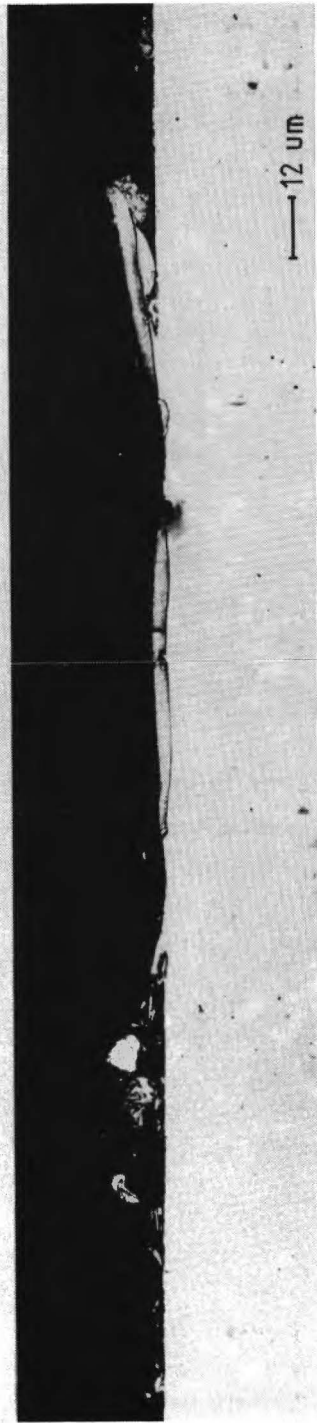
Photo 15: Cut through two interfering particles.

— 12 um

122

PHASE 1

liquid

solid

shock front

$t < t_c$ subcritical - no flow

PHASE 2

liquid

solid

produces

spray material

substrate

$t > t_c$ post critical - lateral flow

PHASE 3

spray gas

liquid

solid

liquid

corona of spray
and base
material

$\propto$
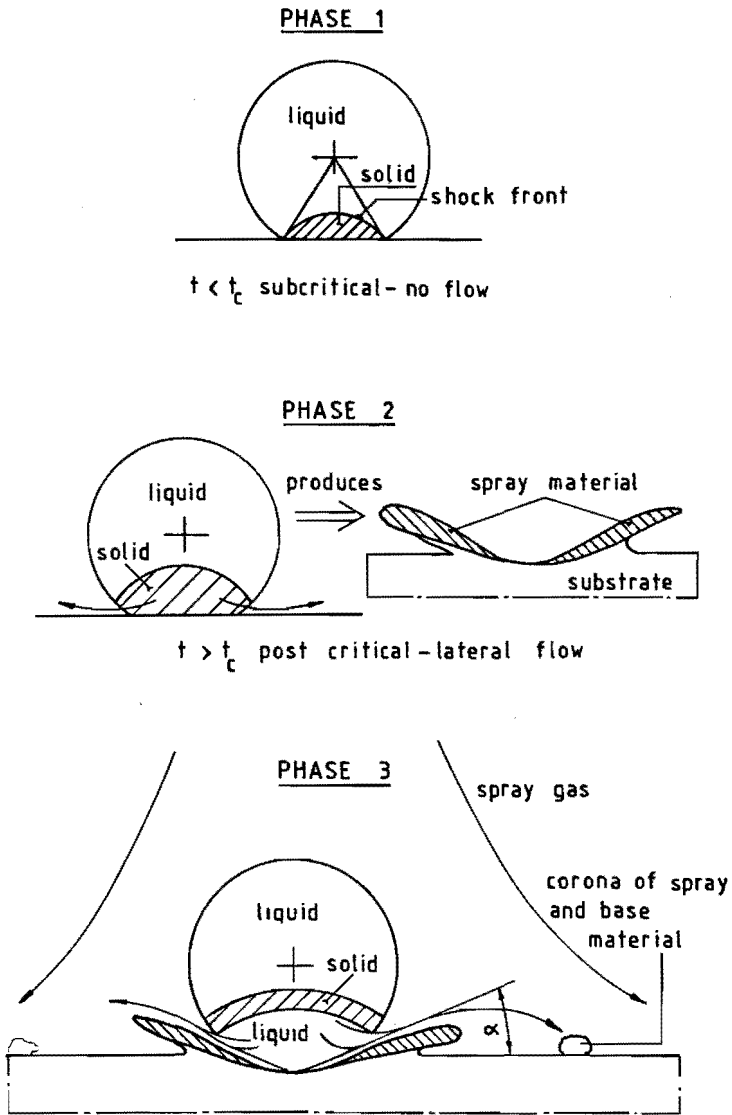
Fig. 3.5:   Final model for the spreading of a spray particle.

123

How do the corona's come into existence and how are they related to the described model for spreading? Apart from this question, the second main feature of the model, the possible transformation of liquid to an amorphous solid, should still be backed up by experiment. The following reasoning gives a combined answer to both issues, see fig. 3.5. In phase 1, the subcritical phase, compression takes place but no flow occurs. In phase 2, the postcritical one, the shock wave front opens a free gap in the surface of the sphere through which solid amorphous material is squeezed out laterally, causing a cavity in the substrate and causing the flower leaves. The release wave which accompanies the lateral outflow moves towards the shock wave front, relaxes the compressed solidified material, thus re transforming it into the liquid state. This liquid flows out sidewardly in good contact with the crater bottom and forms the corona of spray and substrate material. In fact the liquid jumps away from the surface over the inclined side border of the crater, but the spray gases smash the material onto the substrate once again. The same phenomenon of secondary adhesion has been observed in the case of very fine rebounding particles [26].

The folded string corona type, always accompanying a small particle and sometimes also coexisting with a coarse one, must be attributed to spreading of some material in a liquid state The radially directed striation corona must also be attributed to liquid or near liquid material flowing outwards over the surface of the central deposit.

At the end of this section it may be concluded that in first instance the experimentally found morphologies can be explained on the basis of the main features of the theoretical model. In a second round of experiments it will be tried to find a more specific relation between the three input parameters U_p, r and T_0 and the shape of the spread — material. Finally the mechanical properties of the various morphologies will be determined, if possible.

124

Prior to these intended actions very interesing details will be given regarding the build up of a sprayed coating.

3.2.1   How sprayed coatings are built up.

As has been depicted in the general introduction to the plasma spray process, a sprayed coating is built up particle by particle. This section gives some remarkable details on the interaction of particles with the substrate and with each other without using formula's. Photo 15 shows a section across two or three (not quite clear) interfering spread particles. On the right and the left hand side, impact craters are visible. In between them a pancake with fissures. On the right hand side the typical free standing flower leave, a heavily deformed substrate and corona material. The left side specifically shows the corona material. The section makes clear that zones where an excellent adhesion may be expected alternate with regions where heavily crushed material is present without a substantial bond to the substrate or even without any bond. The free gaps certainly will give rise to high stress intensities when the coating is loaded by a tensile force perpendicular to the surface. Photo 16 shows a section through two adjacent spread particles which have included a large zone of porosity in the centre of the picture. Photo 17 shows also such adjacent particles, but here the left one has filled up the free gap of the right hand sided one. This visual "repair" of binding faults occurs very often but it can not be expected to contribute essential to the strength of the coating in the as sprayed condition. For instance, photo 18 presents a well sprayed FeCrAlY coating [27] having a tensile strength of $70N \, mm^{-2}$. Although this strength may be considered as excellent for common practice, the nature of the fracture occuring in a tensile test is brittle. The apparent repair of binding faults due to the lateral movement of spreading

125
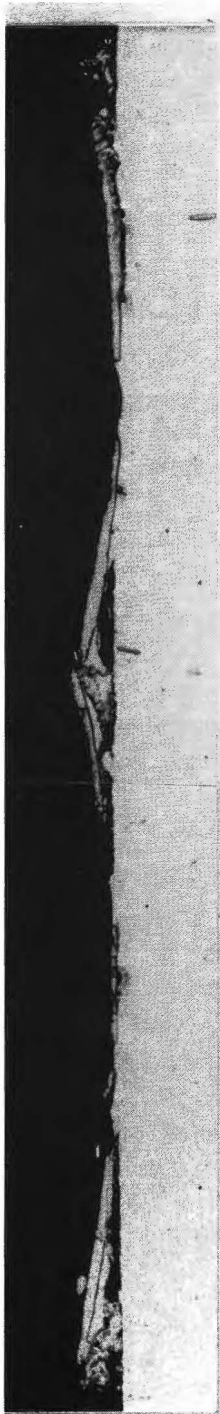
Photo 16: Cut through included porosity.
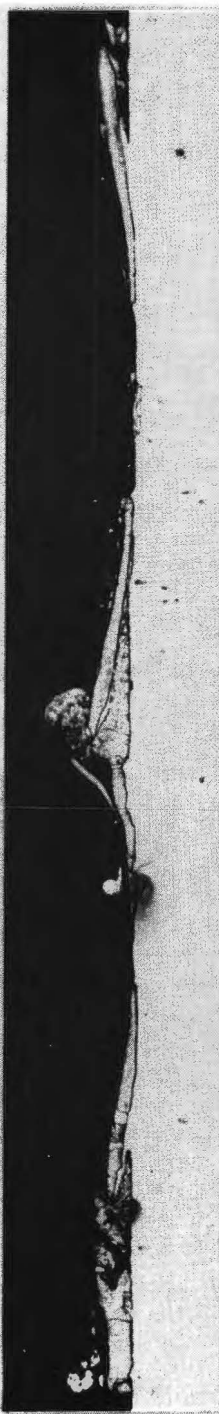
Photo 17: Cut through a free gap which has been filled up by the left particle.

Photo 19: Three particles on top of each other.

├──── 14 μm

126

material is very delusive for the judgement of mechanical properties. Photo 19 shows a cross section where three particles are deposited on top of each other and a fourth one has moved into the scene from the left. Especially the left hand side is most interesting to investigate. A schematic picture of the left side of this photograph is shown in fig. 3.6, including the description of some details.
An important feature which can be observed in the photo is enlarged and shown in photo 20: the wave pattern between particle 2 and the substrate and particle 1 and the substrate. Similar wave patterns can be found in the contact area of explosive – welded cladding material, where also a fast relative movement of the upper material with respect to the lower plate is the cause for a high strength bonding, see fig. 3.7 and ref. [25].
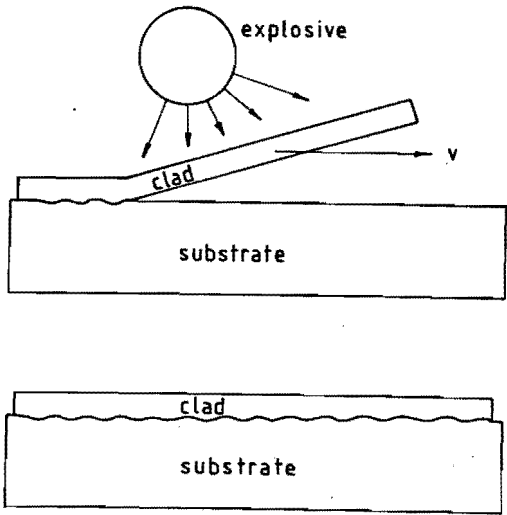
Fig. 3.7:   Explosive welding scheme.

On the other hand, the presence of oxide layers does affect the overall strength considerably.
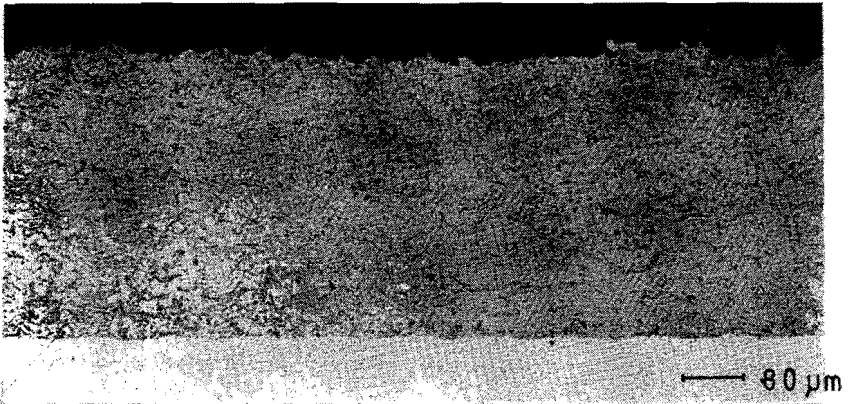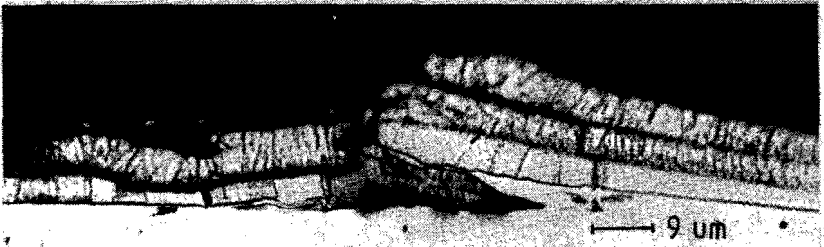
Photo 20: Enlarged part of photo 19 showing the wave pattern between particle and substrate.
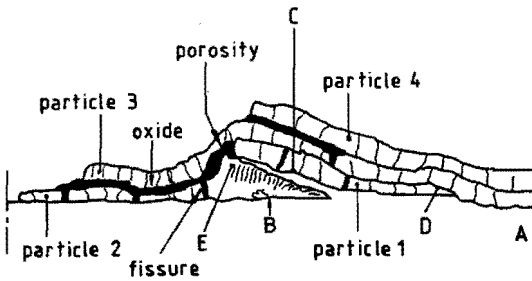
Fig. 3.6:   Schematic of the left side of photo 18.
A ≅ crater of impact.
B and C ≅ friction welds
D ≅ place where the eroding liquid after relaxation has cut off the priosly formed flower leave.
E ≅ place where particle 2, while moving to the right has been blocked bij the substrate and particle 1.

128

The photographs of this section may also contribute to the confirmation of the lateral flow model feature and give insight in the structure of a sprayed coating. To conclude this section, attention should be payed to the columnar structure of the spread particles at those places, where contact exists between the spray — and the basematerial or between the spraymaterial and a previously deposited particle. The crystals are obviously grown in a direction perpendicular to the substrate, VIZ in the direction of the heat flow during the solidification. This effect implies that the spreading of the particle took place prior to the heat transfer, a feature of the spreading model which has been described previously.

3.3   Second round categorization of spread particle morphology

3.3.1.   Experimental approach.

The morphologies as described in the previous section belong to unclassified Mo spray particles, having a rather wide $(22 - 75\mu m)$ size range, arbitrary velocities and undefined heat contents. In this section a more severe experimental scheme is set up in order to trace the relation between the morphology and the input parameters U_p, T_0 and r. Mind that T_0 stands for temperature but indirectly als for the heat content H. These three quantities do affect each other strongly and can not be controlled independently. A change of the operational control setting for the plasma torch implies a simultaneous change in heat and momentum transfer from the plasma to the particle, [2c]. The particle size is the only parameter which can be varied independently. For a scientific experiment regarding the influence of T_0 and U_p on the morphology of the spread material, it is necessary to find a way to vary also the velocity and the heat content independent from each other. The problem has been solved as follows.

Four polished pieces of the substrate material are mounted symmetrically in slots at the perimeter of a disk which is rotated by a grinding spindle up to 24.000 revolutions per minute, see fig. 3.8. The used disk has a diameter of 100 mm, so
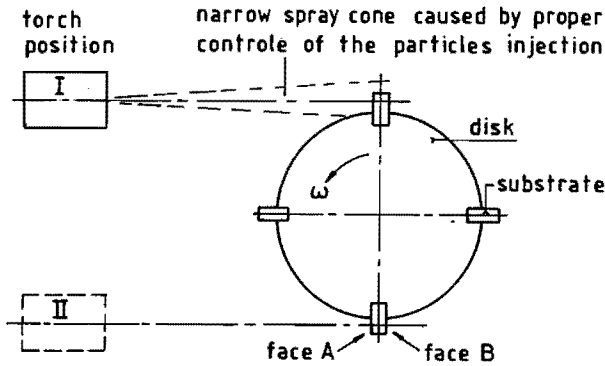
Fig. 3.8:   Experimental set up for the variation of the impact velocity U_p at constant heat content of the spray particles.

the impact velocity can be increased or diminished, depending on the torch position, with a velocity up to:

$$\Delta V = \omega \cdot r = \frac{24.000 \times 2\pi}{60} \cdot 50 \cdot 10^{-3} \cong 125 \text{ ms}^{-1}$$

The velocity variation can take place step wise or continuously. Now for a definite heat content, a wide range of impact velocities can be applied in order to trace the velocity influence on the morphology on one hand and the influence of the heat content on the other hand. The heat content, H, of the particles can be drawn as a function of the temperature. Basically such a picture looks like fig. 3.9. Position 1 indicates that the particle has been heated up near the melting point but it still is a solid. Position 2 marks a liquid state just above the melting point and positions 3 and 4 are representing a superheated liquid.

130
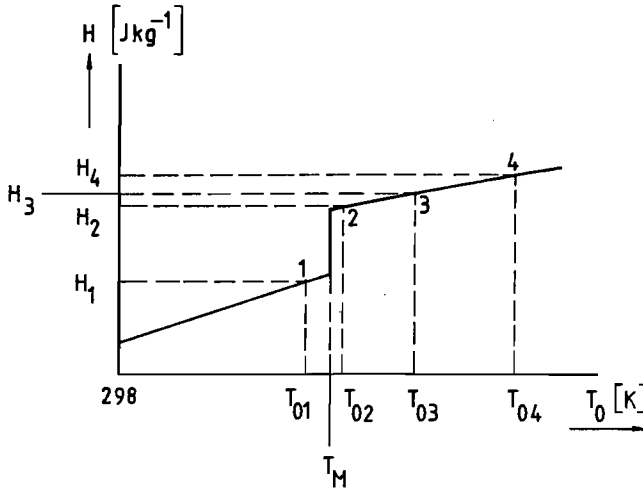
Fig. 3.9:   Basic form of a heat content as a function of the particle temperature. Identification of experiments with several heat contents.

The torch can be operated in such a way that particles with a heat content according to position 1 to 4 can be produced. Each heat content is related to a basic impact velocity subsequently denoted by U_{p1}, U_{p2}, U_{p3} and U_{p4}. This basic velocity can be varied by ΔV upwards and downwards. The last direction even offers means to determine the average basic velocity. Imagine the torch to be located in position II, fig 3.8. As long as the perimeter speed of the disk, ΔV, is less than the basic velocity U_p, the particles will stick on face A of the substrate specimen. If the perimeter speed exceeds the basic velocity, the particles will be caught on face B. The disk acts like a fly swapper in that case. The moment that the relative velocity is approximately zero can be observed visually. This velocity measurement works simply and accurately but is rather elaborate and therefore powder consuming. For this reason in first instance, a photographic way for the determination of the basic velocity U_p has been applied.

131

Table 18: Identification of performed experiments

MAT./SIZE		Molybdenum / 53–63 µm						
HEAT CONT.		−ΔV		$\overline{U}_p$	+ΔV			
H1		23	48	73	98	123	148	IMPACT VELOCITY m/s
code	Mo	7	6	1	2	3	4	S.P.*
	Mo	17	16	11	12	13	14	C.*
H2		27	52	77	102	127	152	IMPACT VELOCITY
code	Mo	27	26	21	22	23	24	S.P.
	Mo	37	36	31	32	33	34	C.
H3				79				IMPACT VELOCITY
code	Mo	57		41		53		S.P.
	Mo			51				C.
MAT/SIZE		AISI–316 /63–75 µm						
H1		U*−50	U*−25	U*	U*+25	U*+50	U*+75	IMPACT VELOCITY
code	A316	7	6	1	2	3	4	S.P.
	A316	17	16	11	12	13	14	C.
H2		34	59	84	109	134	159	IMPACT VELOCITY
code	A316	27	26	21	22	23	24	S.P.
	A316	37	36	31	32	33	34	C.
H3				U*				IMPACT VELOCITY
code	A316			41				S.P.
	A316			51				C.
MAT./SIZE		Aluminium / 53–75 µm						
H2				U*				IMPACT VELOCITY
code	Al			21				S.P.
	Al			31				C.
H3				U*				IMPACT VELOCITY
code	Al			41				S.P.
	Al			51				C.
H4				U*				IMPACT VELOCITY
code	Al			61				S.P.
	Al			71				C.

Note: U* means undetermined velocity

* S.P. = Single particles

* C. = Coating

132

The method will be described in one of the following sections, as will be the case with the heat content measurement.

The experimental results are listed in table 18.

The added or subtracted support velocity ΔV is known by measurement. Most of the experiments are performed on 4 polished substrate specimen, to be used either for metallographic or mechanical examination. Per heat content, the first series of test specimen is made to study the splash of single particles. The second series is intended to produce a coating with a thickness of approximately 0,1 mm.

Horizontally arranged experiments of table 18 permit the comparison of the results on the basis of a varying impact velocity and a constant heat content. The vertical arranged ones give insight in the influence of the heat content at the same velocity.

For a correct performance of the experiments it is required to determine the heat content and the velocity of the spray particles. The third input parameter, the size of the particle, can be fixed within a rather narrow range by sieving.

3.3.2   Determination of the particles' heat content, subsequently the temperature at the moment of impact.

The heat content of adhering spray particles can be measured by the following procedure, see fig. 3.10, [8]. An isolated steel strip, (size 14x3x120 mm) is placed in the centreline of the passing spray cone. The supplied heat causes a temperature rize. The heat capacity of the steel strip is a known quantity, thus the heat transfer can be determined. If first the plasma torch is passed by without
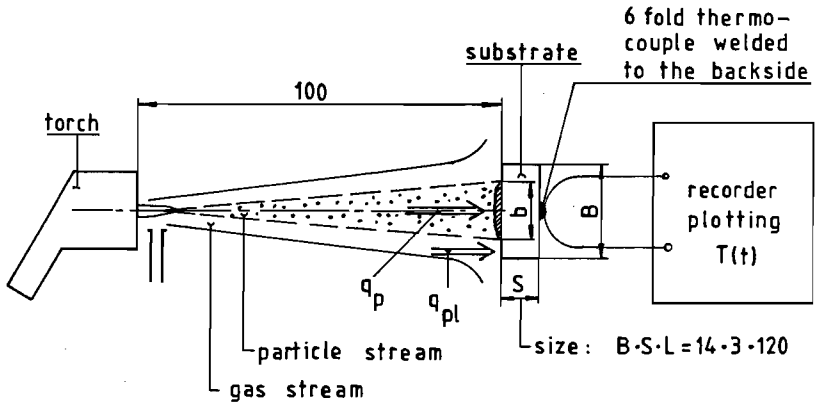
Fig. 3.10:   Schematic set up for heat transfer determination.

spraying particles, the heat transfer to the strip is caused by the plasma gases alone:

$$q_{pl}^{(1)} = m_s \cdot C_s \cdot \Delta T^{(1)} + q_l^{(1)} \tag{3.1}$$

where:

$q_{pl}^{(1)}$ $\hat{=}$ heat absorbed from the plasma

C_s $\hat{=}$ specific heat of the steel strip

m_s $\hat{=}$ mass of the steel strip

$\Delta T^{(1)}$ $\hat{=}$ temperature rise of the steel strip due to the plasme heat

$q_l^{(1)}$ $\hat{=}$ heat loss from the strip to the surrounding during the heat

          supply period

(1)   refers to a pass of the torch without spraying particles.

If next a spray operation is carried out, the total heat absorbed by the strip is extracted from the plasma and from the particles.

134

For the sum of both thermal energies can be written:

$$q_{sum} = q_{pl}^{(2)} + q_p =$$

$$= m_s C_s \Delta T^{(2)} + m_p C_p \Delta T^{(2)} + q_l^{(2)}$$

$$(3.2)$$

where:

$\Delta T^{(2)}$ $\hat{=}$ temperature rise due to the heat supply by plasma plus particles.

m_p $\hat{=}$ mass of the deposit

C_p $\hat{=}$ mean specific heat of the spray material over the temperature range $\Delta T^{(2)}$

$q_l^{(2)}$ $\hat{=}$ heat loss from the test piece during the second pass of the torch.

(2)   refers to a pass of the torch while spraying particles.

The test piece is kept in it's place by four steel needles, thus restricting the heat loss to a negligable quantity, so:

$$q_l^{(1)} = q_l^{(2)} = 0 \qquad\qquad (3.3)$$

Since the net thermal energy stored in the spray particles only amounts a few percent of the gas enthalpy, it can be assumed that the plasma gases deliver the same quantity of heat to the substrate in both cases (1) and (2), then:

$$q_{pl}^{(1)} = q_{pl}^{(2)} \qquad\qquad (3.4)$$

Using (3.3) and (3.4) while subtracting eq. (3.1) from (3.2) yields:

$$q_p = m_s C_s (\Delta T^{(2)} - \Delta T^{(1)}) + m_p C_p \Delta T^{(2)} \qquad (3.5)$$

an equation which determines the heat transfer due to the particles only.

If H is the specific heat content of the particles, then for q_p can bewritten also:

$$q_p = m_p \cdot H \qquad\qquad (3.6)$$

135

Equating (3.5) and (3.6) yields:

$$H = \frac{m_s C_s}{m_p}(\Delta T^{(2)} - \Delta T^{(1)}) + C_p \Delta T^{(2)} \qquad (3.7)$$

Eq. (3.7) relates the wanted specific heat content of the spray particles to measurable quantities. Another expression for H is:

$$H = \int_{T_s}^{T_M} C_{ps}dT + L + \int_{T_M}^{T_0} C_{pL}dT \qquad (3.8)$$

where:

T_s = surrounding temperature

T_M = melting temperature of the spray material

C_{ps} = specific heat of the spray material in solid state; C_{ps} is a function of the temperature.

L = latent heat of melting

T_0 = temperature of the spray particle at the moment of impact

C_{pL} = specific heat of the spray material in the liquid state.

The integration of eq. (3.8) can be carried out if C_{ps} and C_{pL} are known quantities as functions of the temperature. Assume $C_{pL} = C_{ps}$ for $T = T_M$; C_{ps} can be found in the literature [28]; C_p curves for Mo — AISI–316 and Al are presented in fig. 3.11. Integration of these curves according to eq. (3.8) yields the heat content curves of fig. 3.12. Now two equations for H are available, eq. (3.7) and (3.8). Equating them yields the temperature T_0 of the spray particle. Actually the measured heat content according to (3.7) is inserted in the curve of fig. (3.12) and the temperature can be read directly in this last figure.

The method can be applied reliably for well adhering spray material. The procedure becomes inaccurate when to many particles rebound from the surface. In that case, heat without the adequate mass is transferred and the resulting values for the heat content are too high.

136
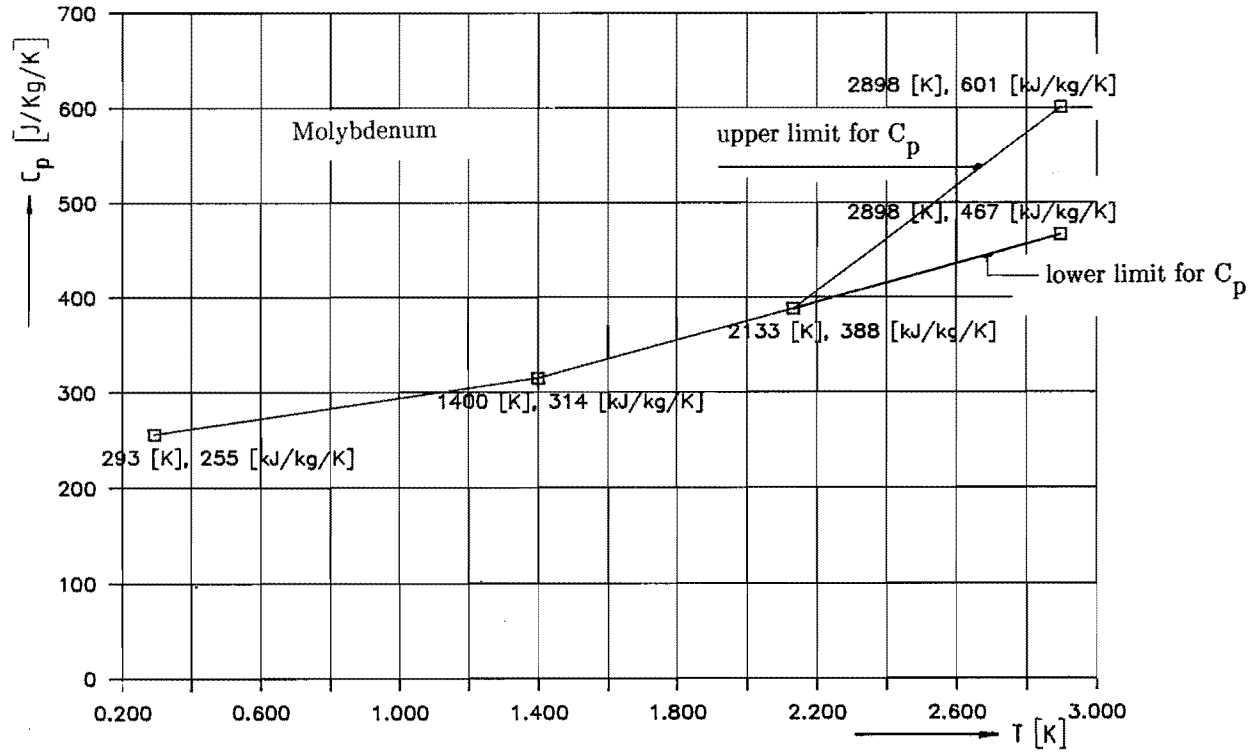
Fig. 3.11a: C_p versus T for Molybdenum [28].
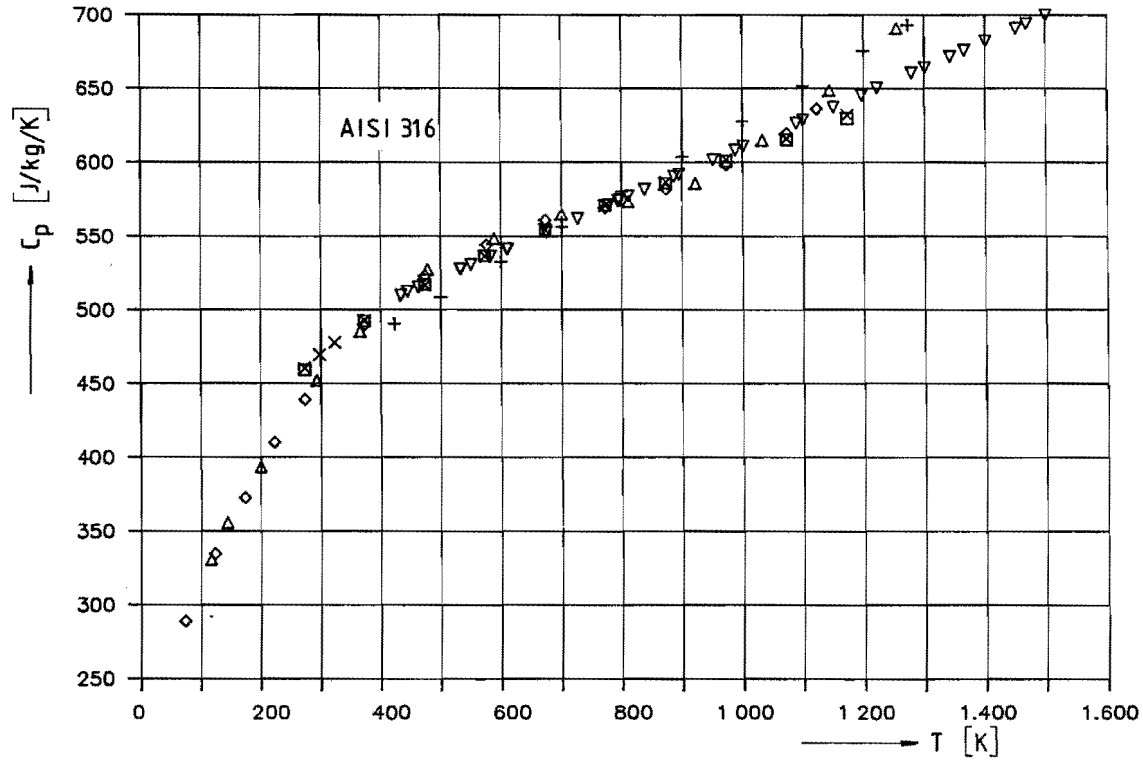
Fig. 3.11b: C_p versus T for AlSl − 316 [28].
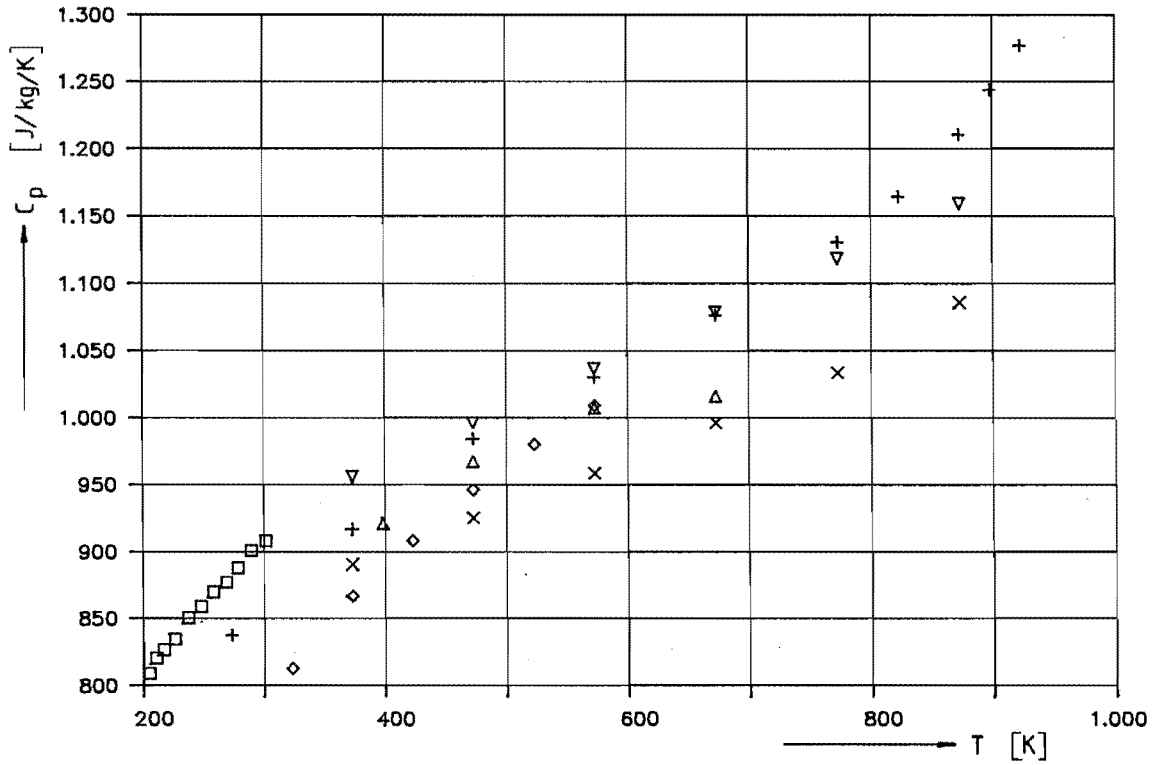
Fig. 3.11c: C_p versus T for Aluminium [28].
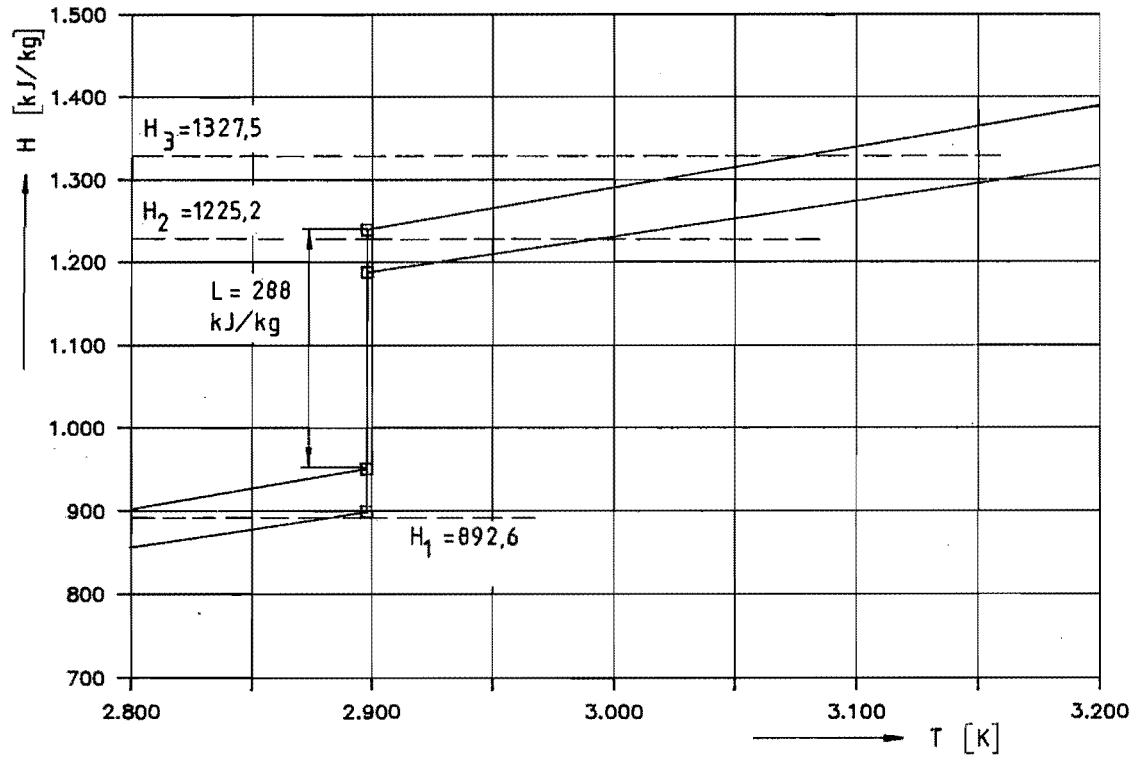
Fig. 3.12a: H versus T for Molybdenum, as can be achieved by integration of fig 3.11a.
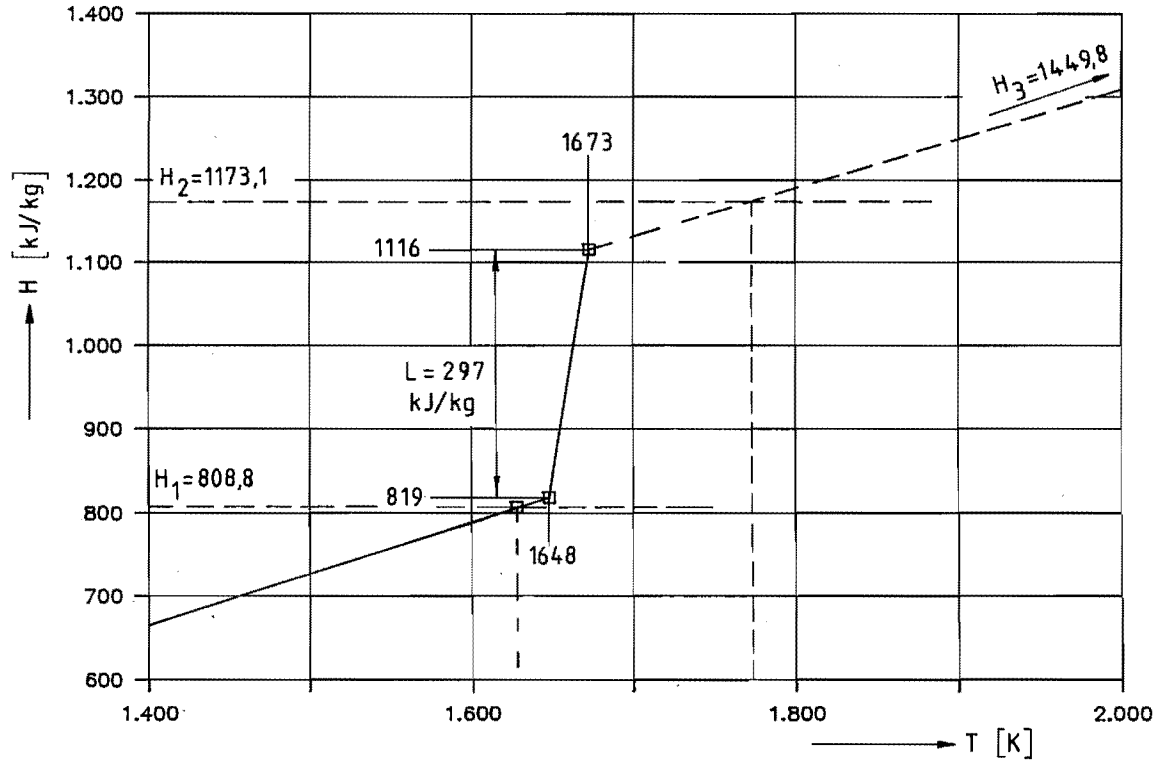
Fig. 3.12b: H versus T for AlSl − 316 (L according to [30]).
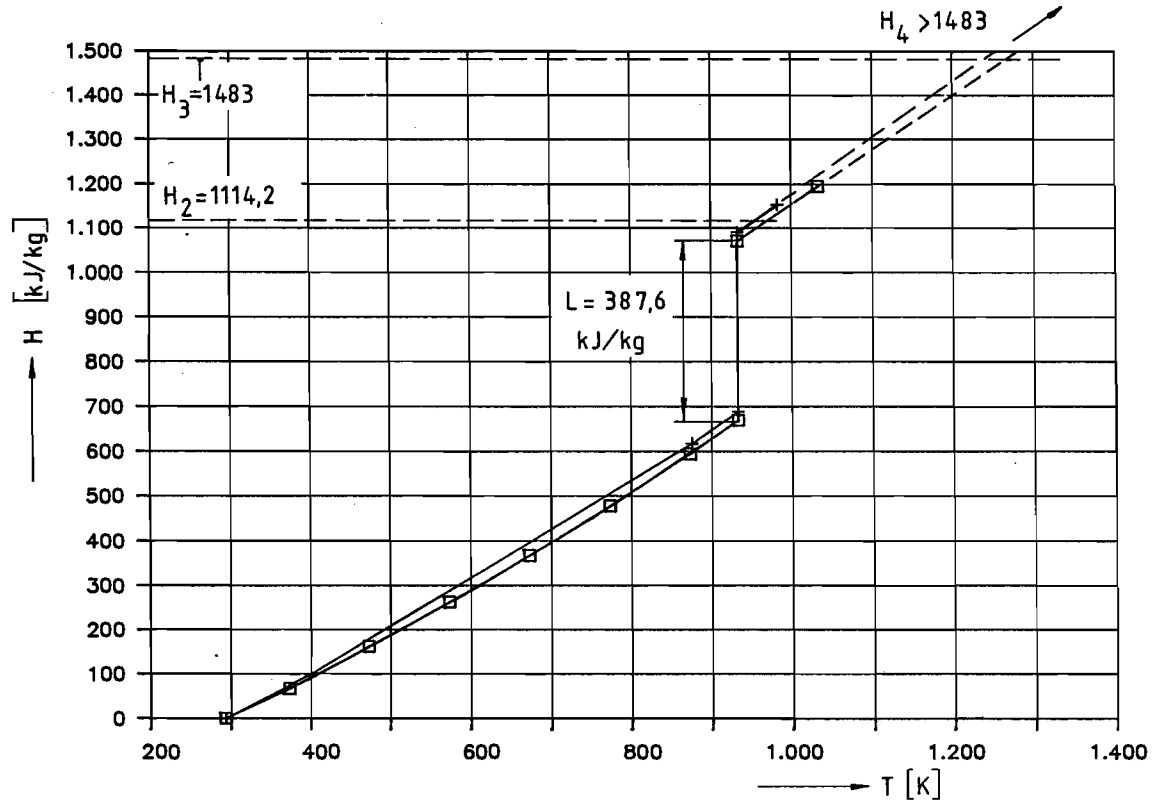
Fig. 3.12c: H versus T for Aluminium.

Another inaccuracy is to be ascribed to the various data for C_p, see fig. 3.11a for Mo; C_p is know with a maximum uncertainty of $\pm$ 30 J kg^{-1}K^{-1}. Therefore the C_p curve of fig. 3.11a is integrated both over the lower values and the upper ones, thus deriving two lines for the specific enthalpy of a Mo spray particle. As a result the accuracy of the temperature of a Mo spray particle is not very great, while on the basis of the heat content more or less can be assured that a particle has an unmolten state, a molten state or a super heated state. The C_p values for AISI–316 and Al do not vary as much as for Mo, thus increasing the accuracy of the method. Table 16 contains the main spray conditions for the achievement of the heat content as given in the right hand columm.

143

Spray Material	Powder size [μm]	Nozzle diam. [mm]	Current [A]	Primary Gas Argon		Secondary Gas Hydrogen		Heat content H kj kg^{-1}	Location in fig. 3.9
				scales	Nl min^{-1}	scales	Nl min^{-1}		
Mo	53–63	7	400	150	72	4	1,8	892,6	H1
		7	450	100	50	5	2,4	1225,2	H2
		7	600	100	50	15	8,1	1327,5	H3
AISI–316	63–75	7	450	200	92	4	1,8	808,8	H1
		8	400	150	72	5	2,4	1173,1	H2
		7	500	100	50	15	8,1	1449,8	H3
Al	53–75	7	500	150	72	3	1,1	1114,2	H2
		7	500	100	50	15	8,1	1483,0	H3
		7	700	100	50	15	8,1	≫1483	H4

Table 16: Plasma spray conditions and heat contents of the particles.

3.3.3 Estimation of the velocity of the particles

A photographic method is used [29] which comes down to taking pictures of the same particle at very distinct time intervals. The irradiated film length is a direct measure for the travelled distance of the particle during a distinct time elapse. Thus, the velocity may be calculated from the calibrated, irradiated film length and the time.

Two phenomena affect the applicability of this method. First, the overlapping irradiation of particles does not always permit to trace one single particle. Second, the radiation of poorly heated particles e.g. corresponding to location 1 in fig. 3.9 is too weak to be determined by standard photographic procedures. The final impact velocity is the sum of the basic velocity and the velocity at which the substrate is moved as described before.

Table 17: Estimation of the particles base velocity.

Spray material	Heat content acc. to the location in fig. 3.9	Base velocity U_p ms^{-1}	$\overline{U_p}$ ms^{-1}
Mo	H1	69–77	73
	H2	88–89–70–61	77
	H3	92–97–96–99–92	79
AISI–316	H1	Too weak radiation	–
	H2	78–79–86–99–89–73	84
	H3	83–87–73–118–111–77	92
Al	H2	Too weak radiation	–
	H3	to be determined	–
	H4	photographically	–

145

The substrate velocity, to be added to or subtracted from the basic velocity, is a well known quantity by electronic measurement of the revolution speed of the rotating disk which serves as a support for the test pieces. In table 17, the estimated basic velocities are given for the spray conditions as listed in table 16 previously. Overlooking the performed experiments at this moment, table 18 can be drawn up.

3.3.4.   Experimental results regarding the morphology.

Overlooking so many spread particles as have been examined, it is hardly possible to produce a complete photographic picture of all morphologies which come across. Therefore only a selection will be shown that describes the reproducible experiments. It must be kept in mind that plasma spray particles, although belonging to the same population as regards size, heat content and velocity, may differ greatly. Nevertheless it will be possible to sketch the main features of the relation between the input parameters and the morphology.

FIRST MATERIAL: MOLYBDENUM.

Photo 21 gives an overview of spread Mo particles, sprayed with a heat content H1, which is projected just below melting point. The pictures are arranged in an array of increasing impact velocities according to table 18. Photo 22 contains an overview of four cross sections.
The spread particles form pancakes over the whole range of spray velocities. Any particle has a radial or a string corona. As will be described on the basis of splashed stainless steel particles. These two corona types are closely related regarding their origin. Here it can be mentioned, that the material which forms

146

Mo—1

Mo—4

Mo—6

Mo—3

Photo 21 / B1 / Mo—7

Mo—2

4.7 μm

147

Mo – 1

Mo – 2

Mo – 3

Mo – 4 ⊢——⊣ 14 μm Photo 22 / H1

148
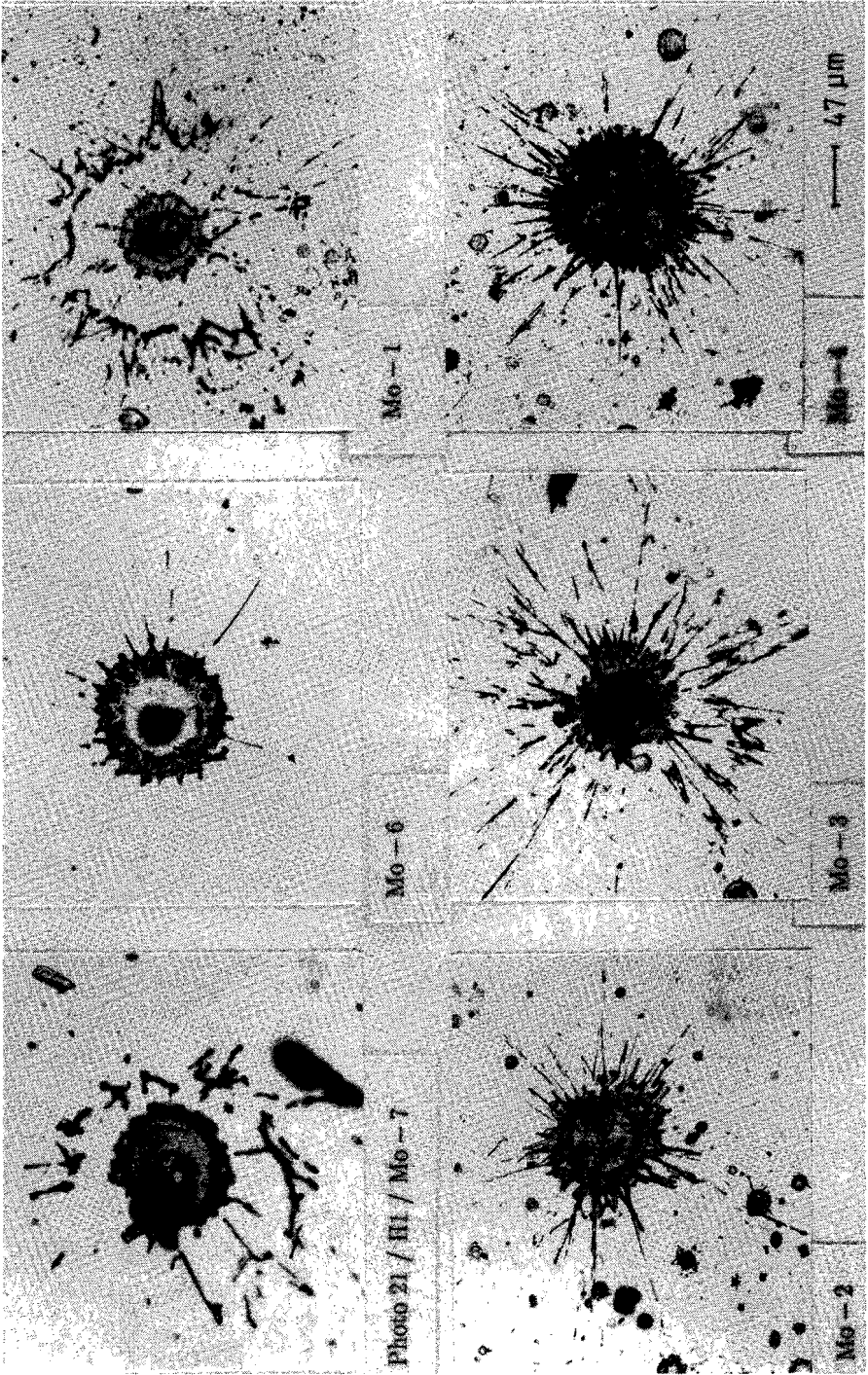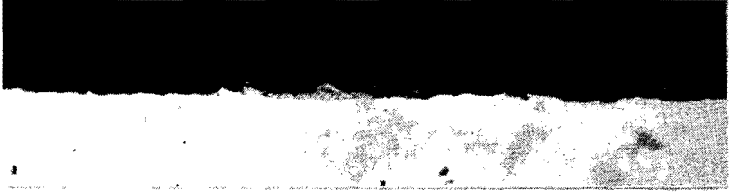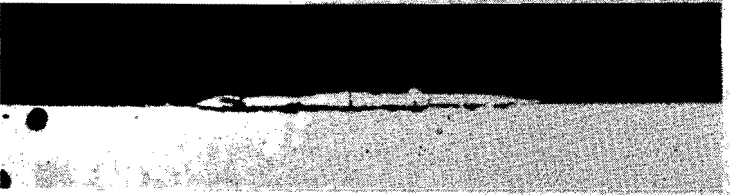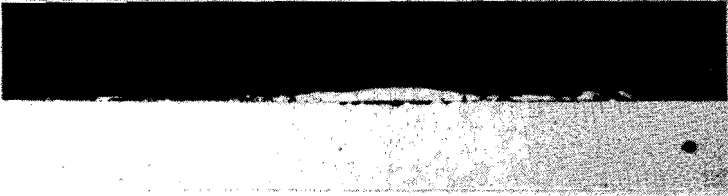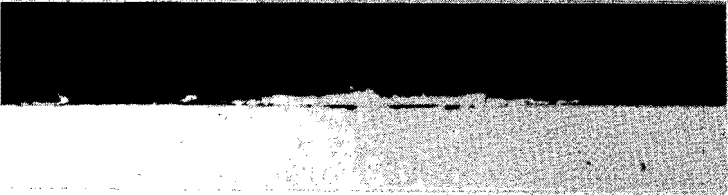
the radial or string corona, comes from the surface of the spray particle, probably in a liquid state. Note that previously it was assumed that the radial and string corona material is squeezed out of the contact region between particle and substrate. So the model has to be corrected in accordance with the experimental findings. The particles flatten with increasing velocities as shown schematically in fig. 3.13. The contact with the surface is excellent; diffusion of Fe into Mo can be
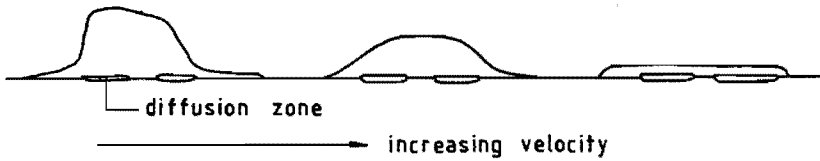
Fig. 3.13:   Cross sections of spread Mo with heat content H1.

observed. The next series of photographic pictures photo 23 and 24, describes the morphology of particles with a heat content H2, projected just above the melting point. Again the pictures are arranged according to the experimental scheme of table 18.

For the low velocity domain the morphology is to be typified as a pancake with diffusion zones over the whole contact area.

For the realm of increased velocity the shape of the cross sections changes drastically as is sketched in fig. 3.14.
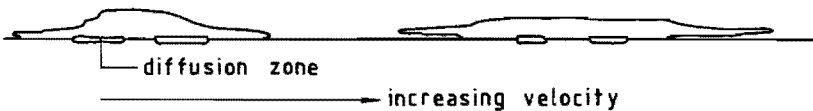
Fig. 3.14:   Cross sections of spread Mo − 22 with heat content H2.

149

Mo — 21

Mo — 24

45 μm
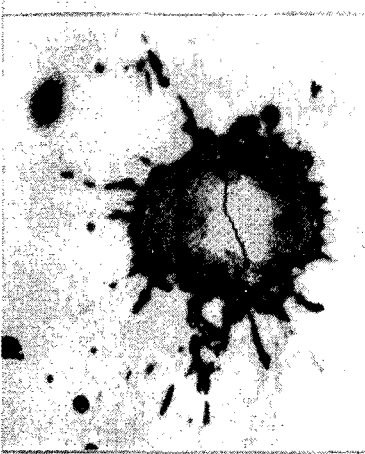
Mo — 26

Mo — 23

Photo 23 / H2 / Mo — 27

Mo — 22

Mo – 27

Mo – 26

├─── 13 μm

Mo – 21

Mo – 22

Mo – 23

├─── 22 μm

Photo 24 / H2 /

Mo – 24

151
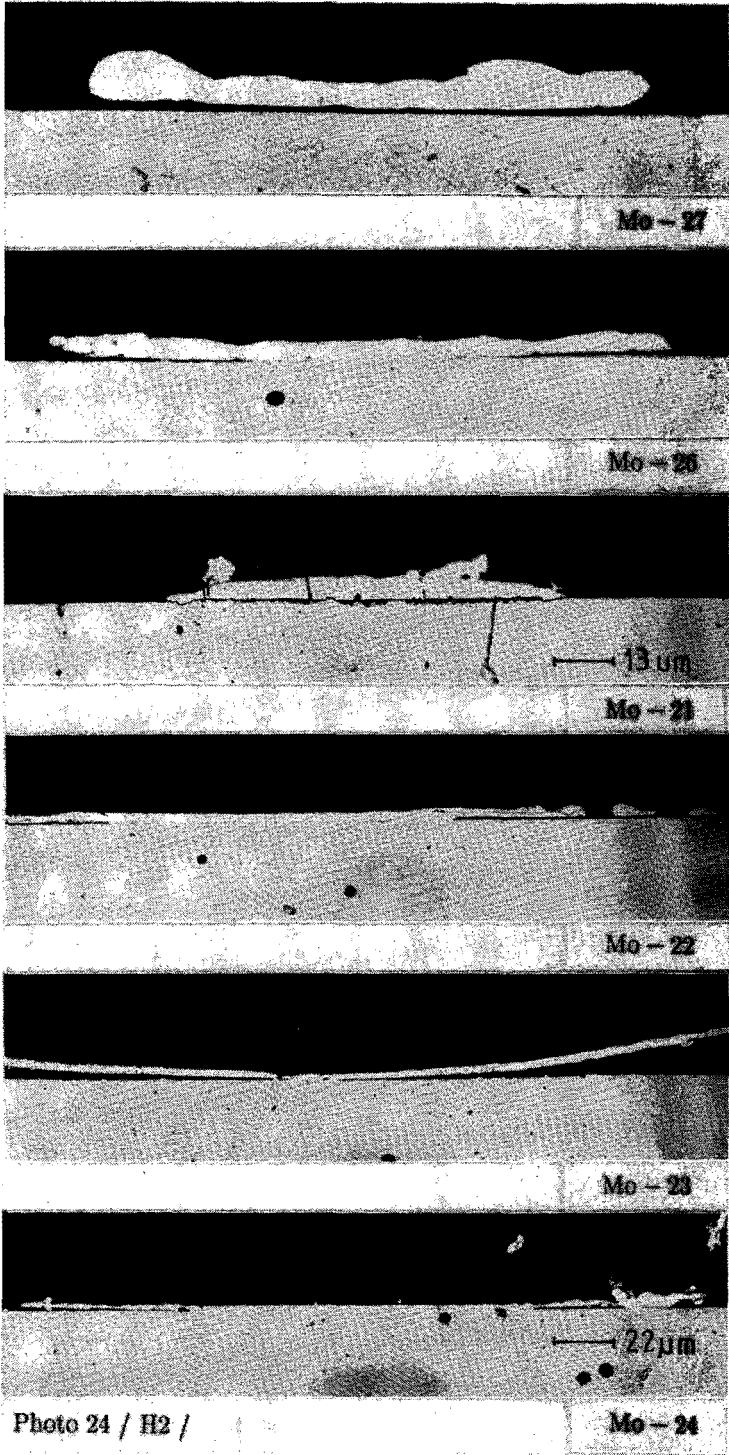
The central part exhibits an excellent contact to the surface while the edge is not in contact at all. Some of the particles have the flower type appearance. Photo 25 shows a very remarkable structure detail of photo 24 (Mo − 22).

The edge is built up as a two layer body. The lower layer is probably due to lateral flow of the compressed material in the contact zone, while the upper layer is formed by lateral movement of the particle's surface material. The flower type deposits, as shown in Mo − 21 and Mo − 23 have typical cross sections as shown in the previous section, see photo 26. Photos 27 and 28 describe a splashed super heated Mo particle, experiment code Mo − 41 according to table 18. This picture completely confirms the structure of previously depicted flower type deposits. However, not until now, this typical morphology can be ascribed to the super heated state of the spray material. Photo 29 is an arrangement of three pictures, taken from spread Mo with the successive heat content H1, H2 and H3 and with an unavoidable slight variation of the velocity from 73 ms^{-1} to 79 ms^{-1}, see table 18. This grouping shows quite clearly the strong influence of the heat content on the spreading of a particle. The shapes are successively pancakes, pancakes mixed up with flowers without distinct corona and flowers with chaplet corona.

Photo 25: Detail of the edge structure of Mo – 22, see also fig. 3.15
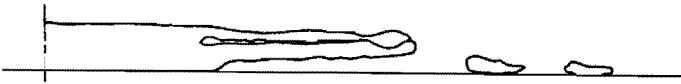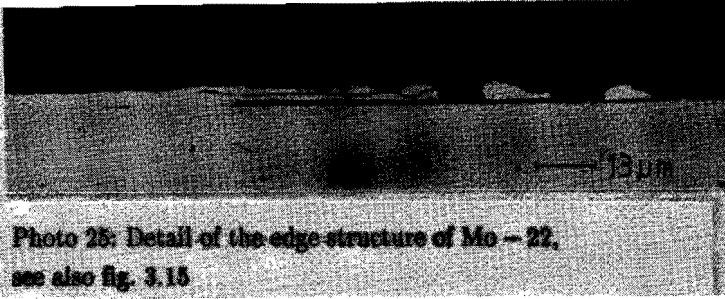
Fig 3.15: Detail of the edge of photo 25.

Photo 26: Cross section through a flower type deposit occuring in the upper velocity domain of the Mo – H2 series.
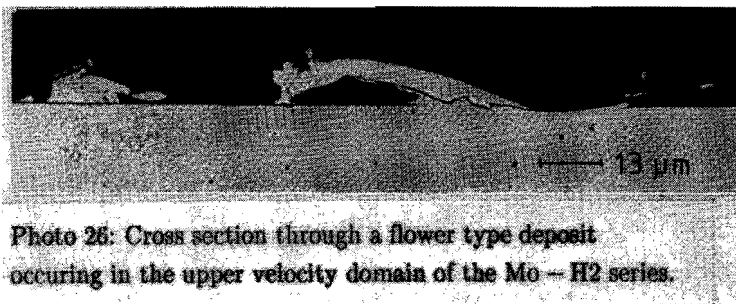
Photo 27: Flower type Mo deposit as typical for splashed super heated particles, heat content H3, experiment Mo 41.
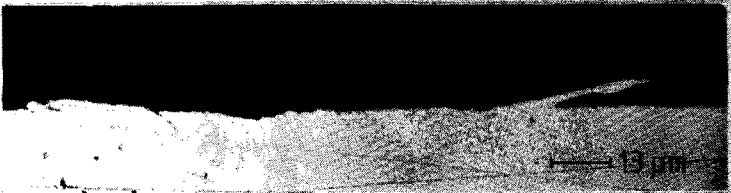
Photo 28: Cross section of the deposit of photo 27.

154

Mo – 1

H1

Mo – 21

H2

Mo – 41

H3
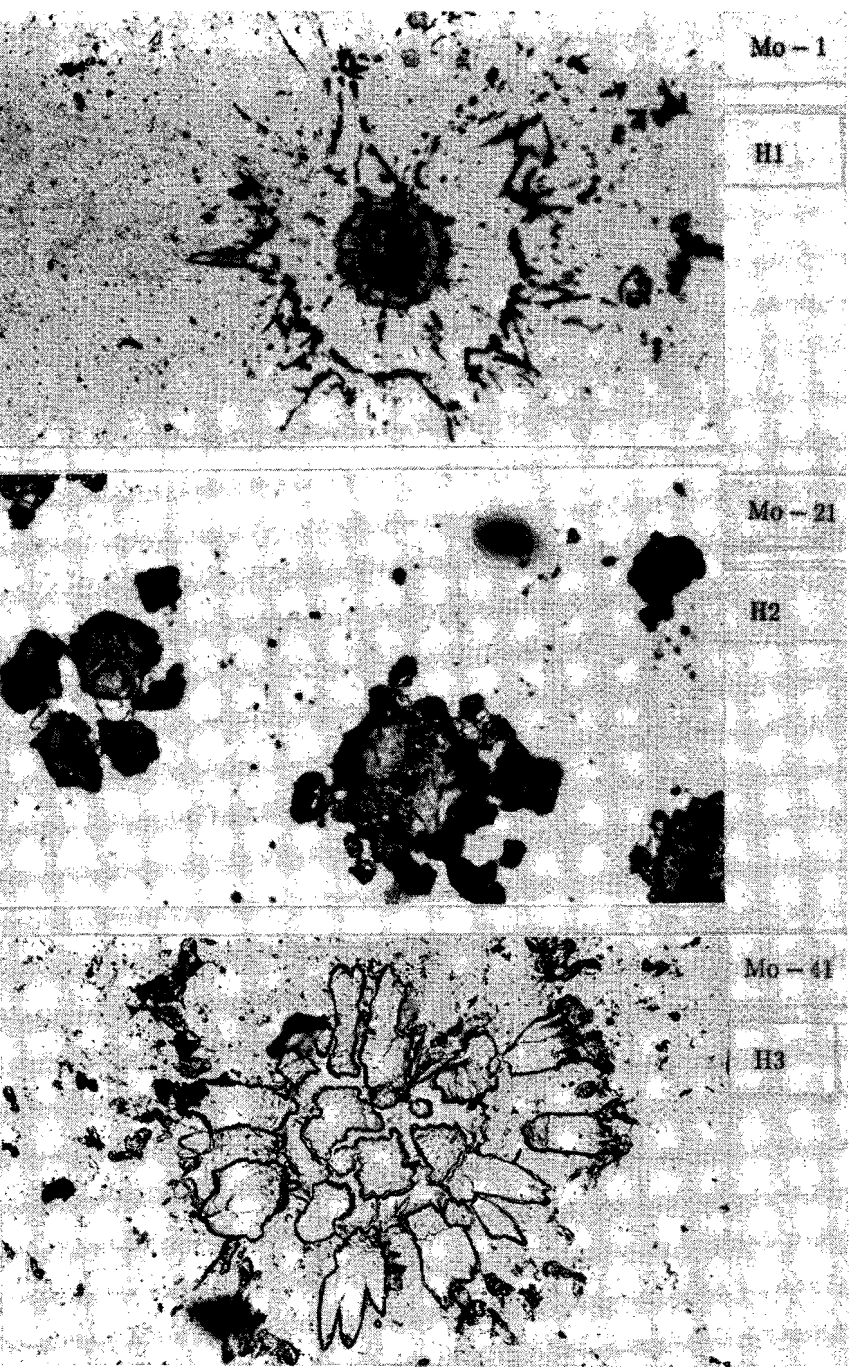
├──┤ 34 µm   Photo 29: Mo morphology as a function of H.

155

SECOND MATERIAL: AISI – 316 stainless steel.

Photo 30 arranges an overview of spread material with the fixed heat content H1
(just below melting point) as a function of the impact velocity, see table 18. The
typical shape is that of a pancake over the whole velocity range. In photo 31 the
cross sections of this series are presented. Mind the bad bond between the
moderately spread particle and the substrate. With this heat content it is
impossible to build up a coating; it loosens from the surface while being sprayed.
The detail picture of A 316 – 7 shows once again the lateral out flow of the
material from the contact zone.

Photos 32a and 32b arrange the H2 heat content series as a function of the impact
velocity. The shape can be characterized as a pancake without corona for the low
velocities ending up with a distinct radial string at elevated velocity level.
Photo 32b exposes clearly how the string type corona develops from the radial
flow of particle surface material.

Figures 3.16, 3.17 and 3.18 show the schematic development of the string via the
intermediate radial corona. The same phenomena can be observed microscopically
with Mo.

In photo 33 the cross sections through particles of the H2 series are arranged. In
the central part, the typical pancake has a good contact with the substrate.
Diffusion like bonding seems to be present. The edge of the spread particle is
detached from the substrate.

Photo 34 shows the morphology of A316 – 41 particles with a heat content of
level H3. At this level, most of the particles spread according to the flower type,
photo 34a, with its cross section in photo 34b. Note that the material on the right
hand side of photo 34a is closely in contact with the substrate. The wave pattern
in the interface indicates the probability of a friction weld due to the lateral

Photo 30 / H1 / A316 — 7

45 µm

A316 — 1
A316 — 6
A316 — 2
A316 — 4
A316 — 3

157
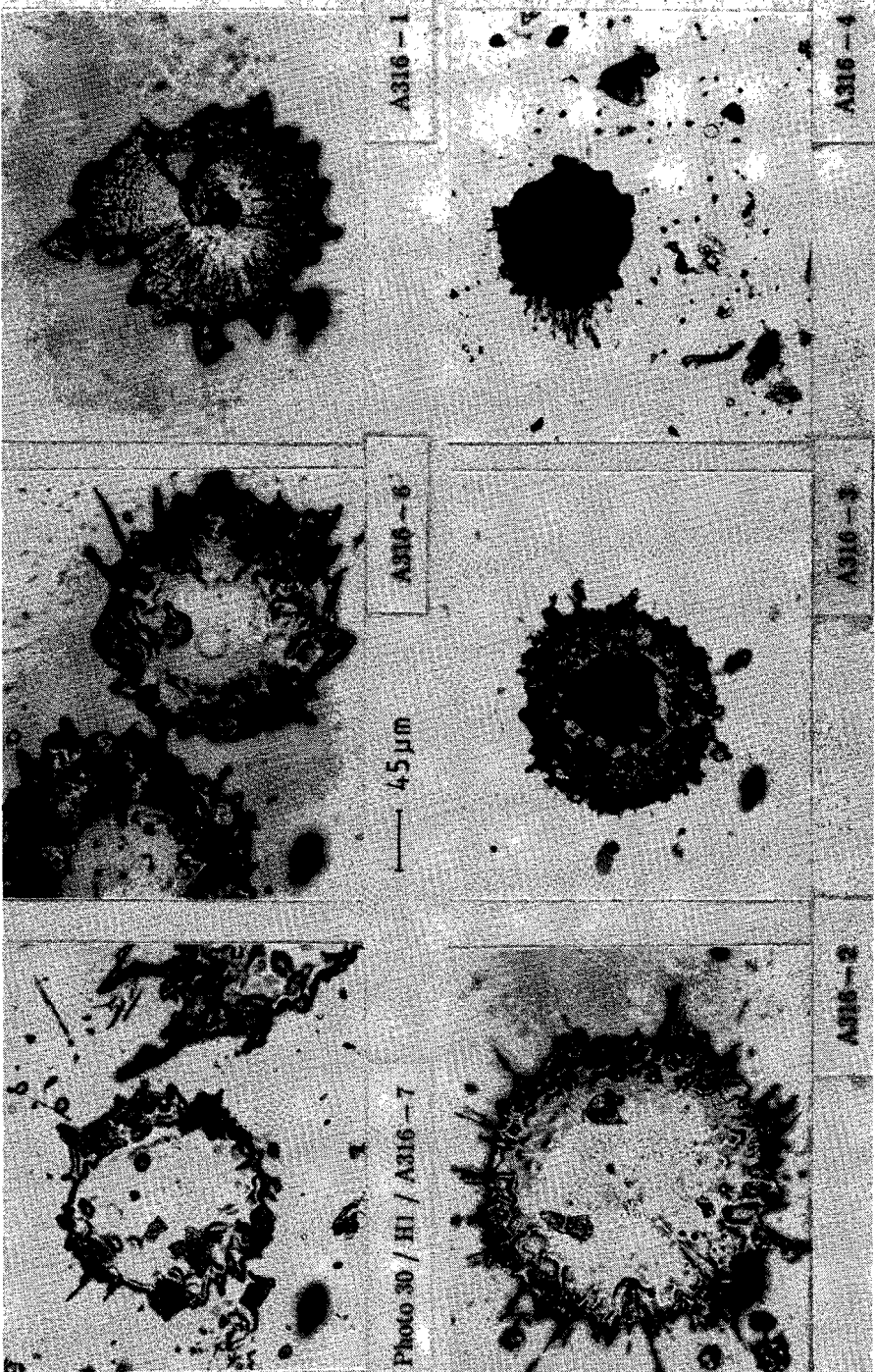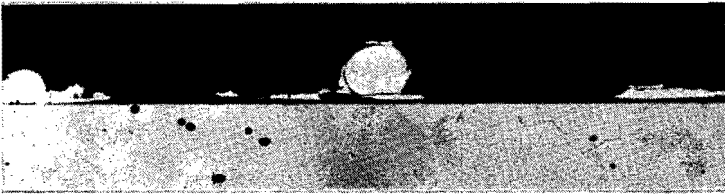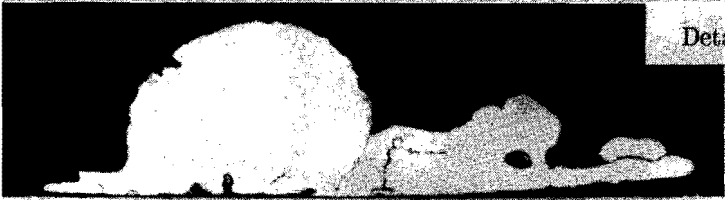
A316 – 7

Detail of A316 – 7
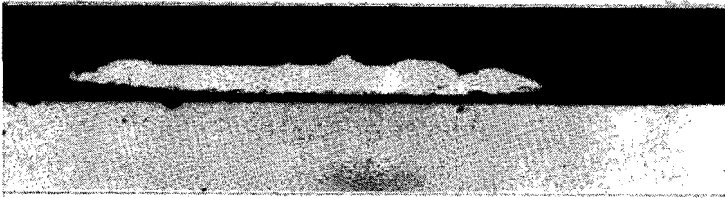
A316 – 6
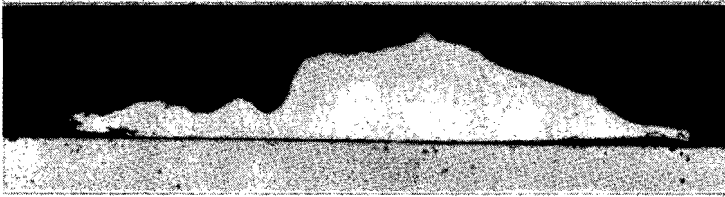
A316 – 2
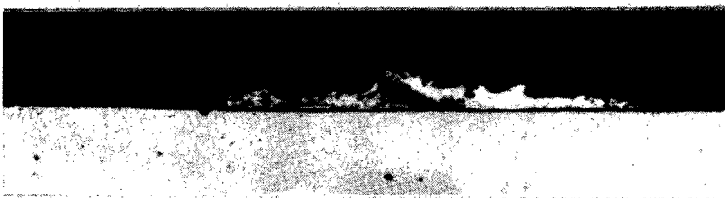
A316 – 3
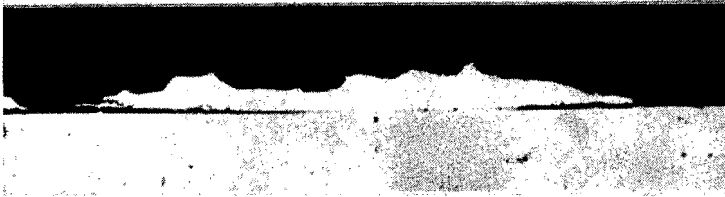
A316 – 4

├──┤ 13 µm   Photo 31 / H1 /

158

A316 – 27

A316 – 25

A316 – 23

━━► 35μm

Photo 32a / H2

159
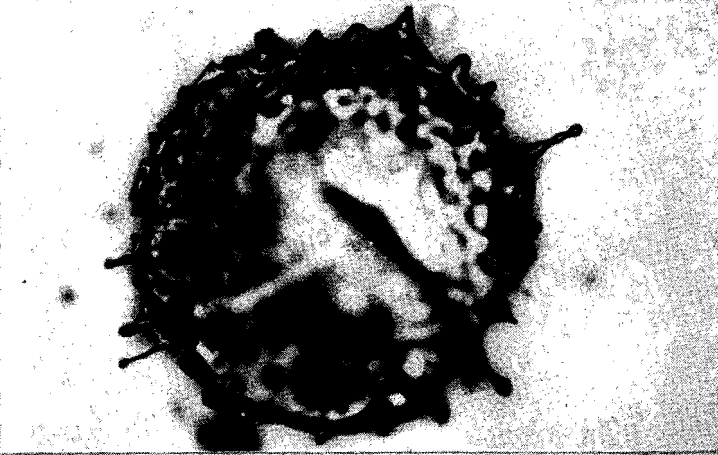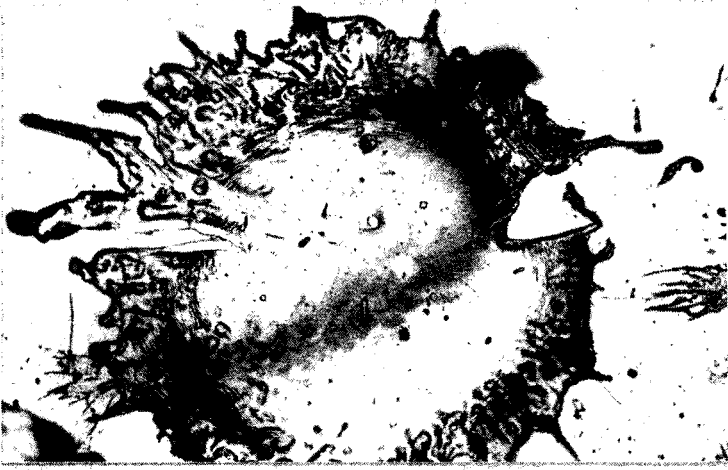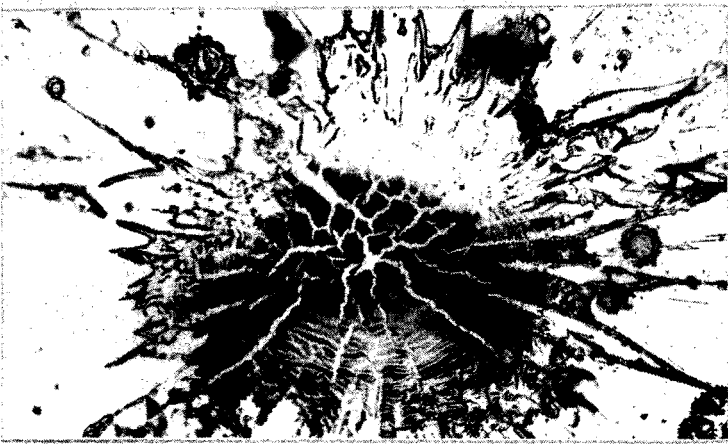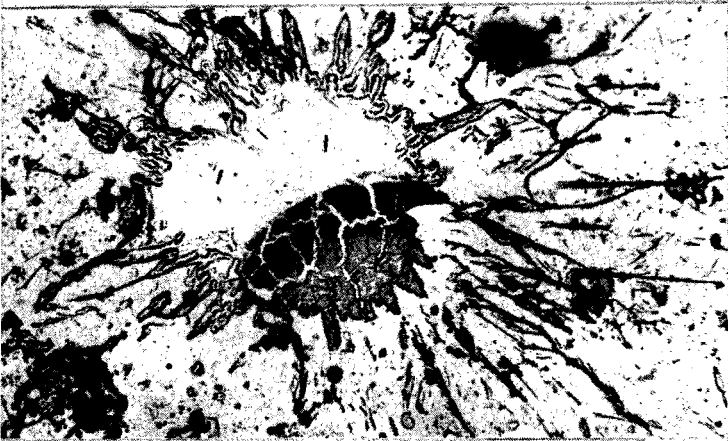
A316 – 22

A316 – 23

A316 – 24

├──┤ 35um   Photo 32b / H2

160
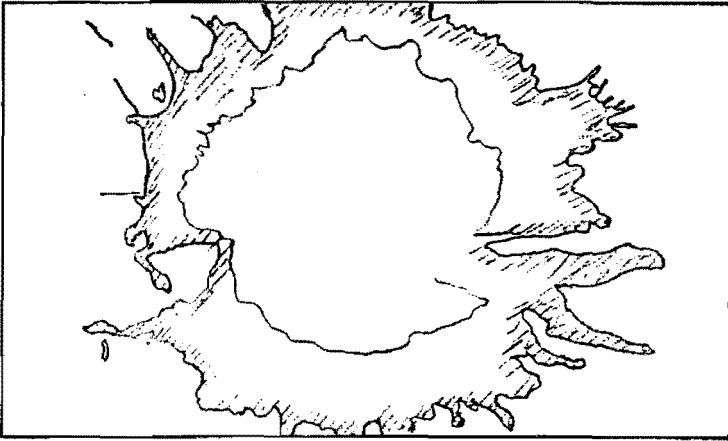
A316–22

Fig. 3.16

A316–23

Fig. 3.17

A316–24

Fig. 3.18

161
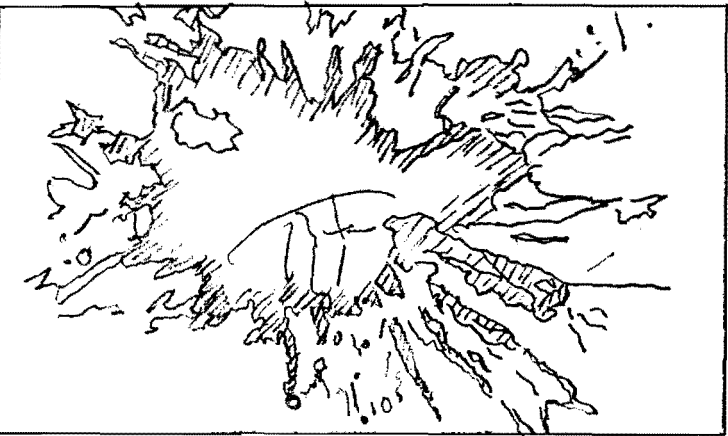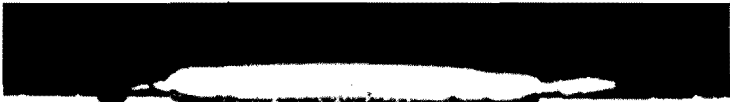
A316 – 27

A316 – 26

A316 – 21

A316 – 22

A316 – 23

A316 – 24

$\longmapsto$ 13 µm   Photo 33 / H2

34a   H3   A316 – 41   ⊢———⊣ 34 µm

34b   H3   Cross section A316 – 41   ⊢———⊣ 13 µm

34c   H3   Cross section A316 – 41
pancake type.   ⊢———⊣ 13 µm

Photo 34 / H3

163
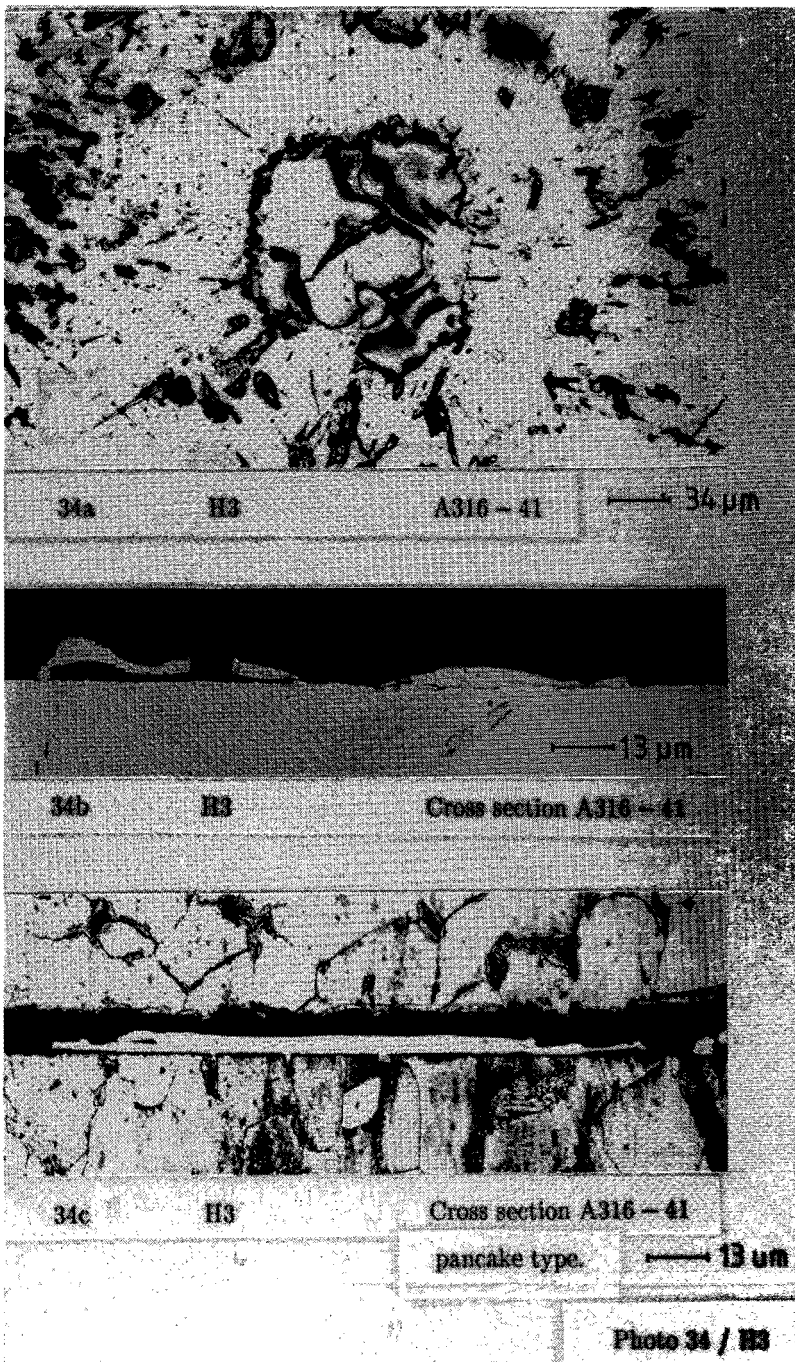
movement. The left hand side material is detached from the surface. The centre of impact can be recognized but the typical relatively deep crater as occurs with Mo, is absent. Also pancakes occur and their cross section is represented by photo 34c. The central part seems to be diffusion bonded to the substrate especially at the substrate grain boundaries. The specimen has been etched to make this effect visible. Photo 34c shows a double layer structure at the edges as is reported previously with Mo.

The edge is detached from the surface. The last arrangement of stainless steel splashes is presented in photo 35. With increasing heat content the splash expands from a pancake without corona to a flower type deposit with chaplet corona. As is the case with Mo, the influence of the heat content is apparently dominant over the influence of the velocity, at least within the experimental velocity variation which is applied in the course of this work.

A316 – 1

H1

35a

A316 – 21

H2

35b

A316 – 41

H3

35c
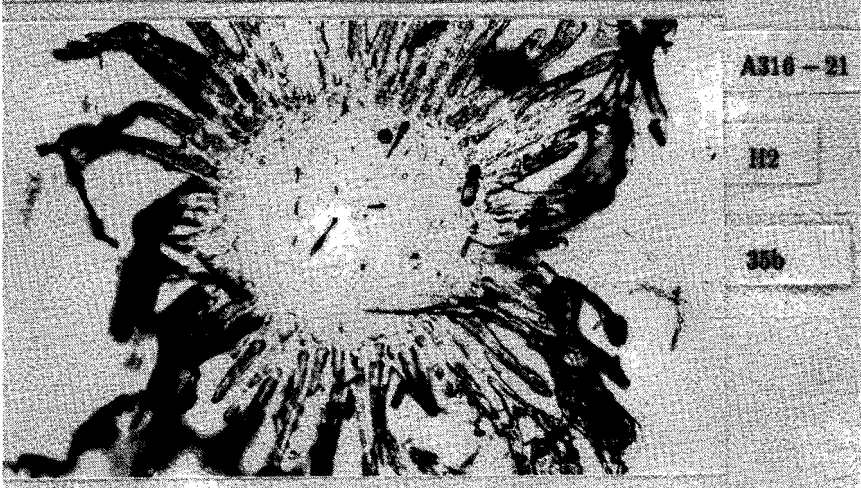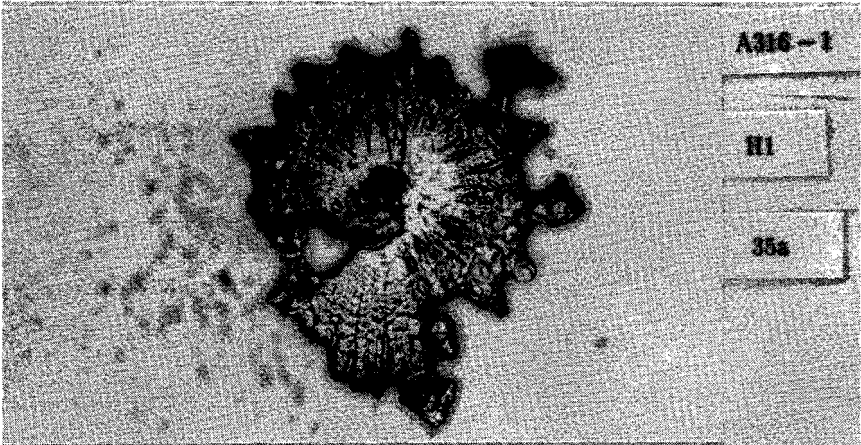
|—— 34 µm

Photo 35

THIRD MATERIAL: ALUMINIUM

Photo 36 gives an overview of aluminium splashes, all deposited in the liquid
state. The material spreads stronger with increasing temperature. The appearance
of the H4 example is like a solidified liquid which did not wet the substrate and
therefore was contracted by it's own surface tension prior to the solidification.
Photo 37 gives an overview of relevant cross sections through Al particles; 37a
and 37b demonstrate clearly a zone of good and bad contact with the substrate.
The last one shows once morethat spreading can take place by a ground flow out
of the contact area and a top flow from the surface area of the particle. Photos
37c and 37d demonstrate the increasing splash diameter with increasing heat
content. The one, sprayed at level H4, has no material left in it's center. An
impact crater is absent, the substrate remains flat. Fig. 3.19 compiles the
experimentally found geometries of spread particles for three materials; the main
types are given in fig. 3.20.
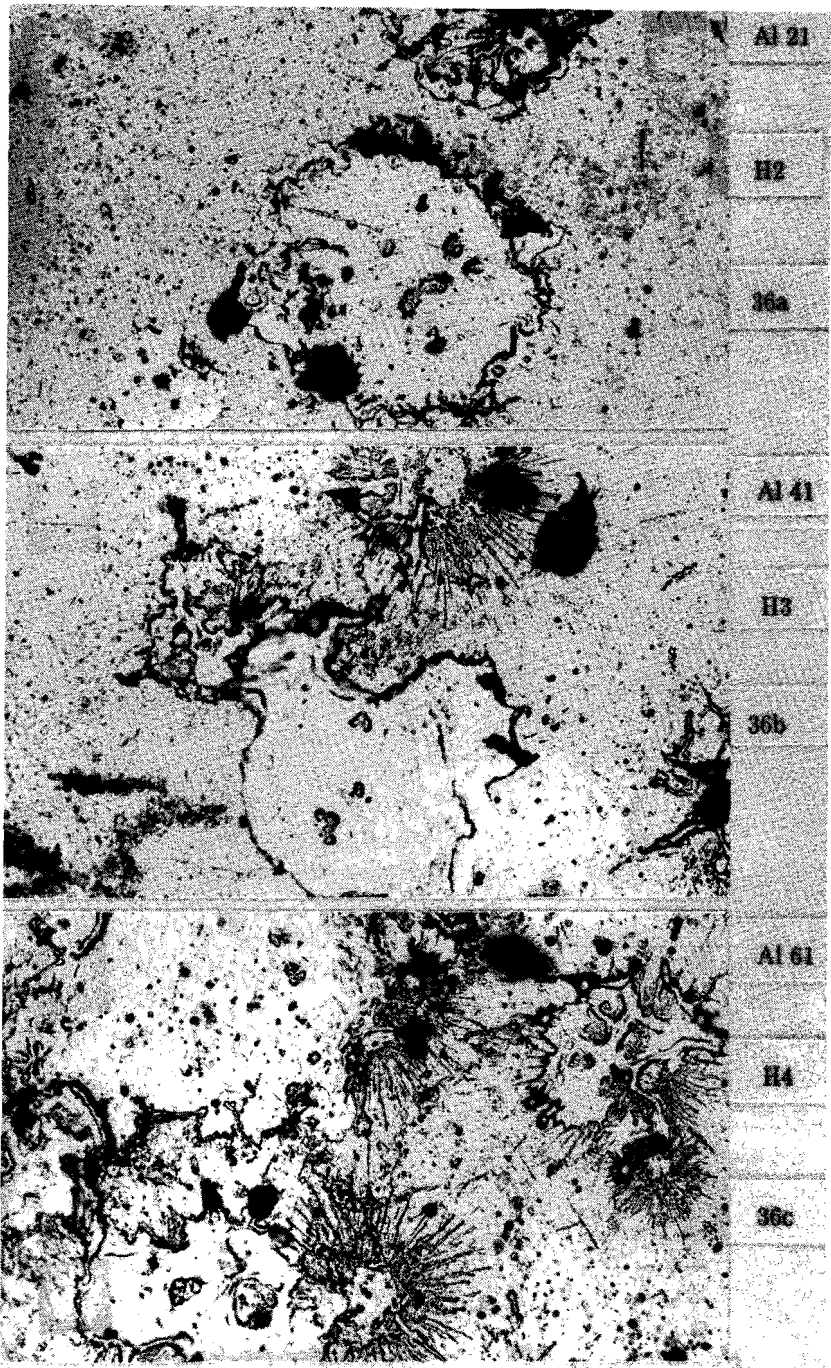
Al 21

H2

36a

Al 41

H3

36b

Al 61

H4

36c

├─────┤ 34 μm

Photo 36

Al – 21   H2   37a

Al – 21   H2   37b

Al – 41   H3   37c
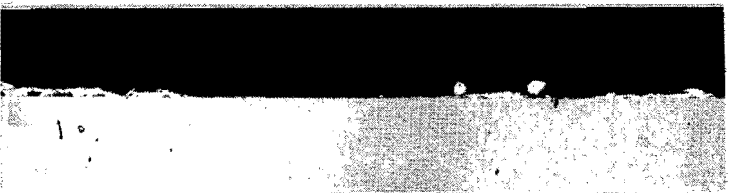
Al – 61   H4   37d   Photo 37

⊢——┤ 2 2 μm

168
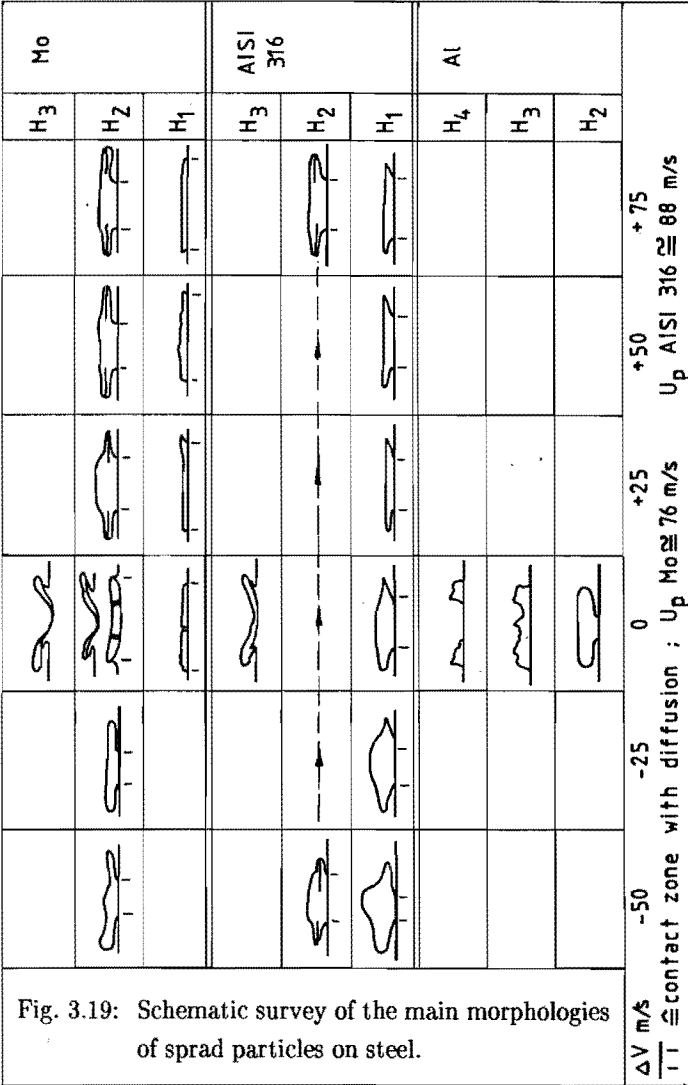
Fig. 3.19: Schematic survey of the main morphologies of sprad particles on steel.

Mo

AISI 316

Al

H_3 H_2 H_1 H_3 H_2 H_1 H_4 H_3 H_2

$+75$ $+50$ $+25$ 0 -25 -50

U_p AISI 316 ≅ 88 m/s

U_p Mo ≅ 76 m/s

$\triangle$ contact zone with diffusion ; U_p

ΔV m/s

169

Type 1	Solid material
	AlSl – 316

contact

Rather underformed pancake with and without R + S corona.

Type 2	Solid and slightly superheated Mo

diffusion

pancake with and without R + S corona.

Type 3	superheated liquid Mo and AlSl – 316.

diffusion

pancake with R + S corona.

Type 4	superheated liquid Mo and AlSl – 316.

friction weld | crater | friction weld

flower type deposit with chaplet corona.

Fig. 3.20:   Main type morphologies.

170

3.3.5 Concluding remarks regarding the morphology

Some concluding remarks to this section are given as a basis for discussion:

1 — The formation of a flower type deposit is mostly connected with
  - a chaplet corona
  - an impact crater
  - friction welds
  - an elevated velocity level or
  - an elevated heat content level of liquid material

2 — The formation of a pancake type deposit is connected with
  - a moderate velocity of liquid material
  - a moderate heat content of the liquid
    and leads to diffusion bonding or partial friction welds

3 — The formation of pancakes of high melting solid material is connected with a firm bond to the substrate. The particles do not flatten completely at low velocity levels.

4 — A slightly superheated liquid material forms pancakes with detached, double layered edges. The material is diffusion bonded in the contact zone. A high velocity level creates the more distinct detached rim.

5 — The double layer structure of the rim may be attributed to the combination of a ground flow and a top flow of the spreading material.

6   − The material spreads by lateral flow.

7   − The string corona emanates from the radial corona. Both come from
       radial flow of spray material which is located on the surface of the
       particle.

8   − The chaplet corona comes into being in combination with flower leave
       formation due to a liquid solid transformation vice−versa during the
       impact.

9   − Low melting point materials like Al do not form craters in the substrate
       High melting point materials benefit crater forming due to the softening
       of the substrate.

3.4   Mechanical testing of sprayed coatings.

Mo is sprayed with the heat content levels H1, H2, H3 according to the
experimental scheme of table 18.
To trace the influence of the particle size on the adhesion strength, one series of
fine Mo−powder $(5 - 15 \ \mu m)$ has been sprayed at the heat content level H3.
Shortage of time did not allow the determination of the related spray velocity.
However the found morphologies of small particles (always a pancake) made this
rather undefined experiment interesting enough to add it to the foregoing series.
The first coatings were made with a stationairy substrate. Subsequently the
rotating support is applied to increase and decrease the standard flight velocity at
the successive heat content levels with an amount of 50 ms $^{-1}$.

Molybdenum 53 – 63 µm

Heat content level	ΔV ms^{-1}	U_p ms^{-1}	Code table 19+16	Tensile strength σ Nmm^{-2}	$\bar{\sigma}$	Remark
H1	–50	23	Mo–17	64,9–63,4–52,4–42,3	55,7	E.F.[*]
	0	73	Mo–11	73,3–70,1–67,6	70,3	E.F.
	+50	123	Mo–13	62,0–58,8–41,3–61,2	55,8	E.F.
H2	–50	27	Mo–37			
	0	77	Mo–31	42,8–34,5–35,8	37,7	C.F.[*]
	+50	127	Mo–33			
H3	–50	29	Mo–57	41,6–60–63,5–42,8	51,9	E.F./C.F.
	0	79	Mo–51	51,5–39,2–47,1	45,9	C.F.
	+50	129	Mo–53	37,2–52,2–54,8–50,0	48,5	E.F./C.F.

Molybdenum 5–15 µm

Heat content level	ΔV ms^{-1}	U_p ms^{-1}	Code table 19+16	Tensile strength σ Nmm^{-2}	$\bar{\sigma}$	Remark
H3	–50	**	Mo–117	9,7–10,3–10,5–24,5	13,7	E.F./C.F.
	0		Mo–111	19,1–28,8–27,6	25,1	C.F.
	+50		Mo–113	8,1–9,7–17,7–8,1	10,9	C.F.

Stainless steel AISI – 316 63–75 µm

Heat content level	ΔV ms^{-1}	U_p ms^{-1}	Code table 19+16	Tensile strength σ Nmm^{-2}	$\bar{\sigma}$	Remark
H3	0	~90	A316–51	45,6–45,9–45,9	45,8	A.F.[*] see photo 38

E.F. = Epoxy Fracture
C.F. = Coating Fracture
A.F. = Adhesion Fracture

** = unidentified

Table 19: Survey of performed tensile tests.

173

The production of stainless steel coatings on a polished steel substrate is not possible for heat contents lower than H3. A survey of the tensile tests is given in table 19

3.4.1   Test method.

A common electronically controlled tensile machine is used to apply a tensile force F to the test specimen. The set up is sketched in fig. 3.21.
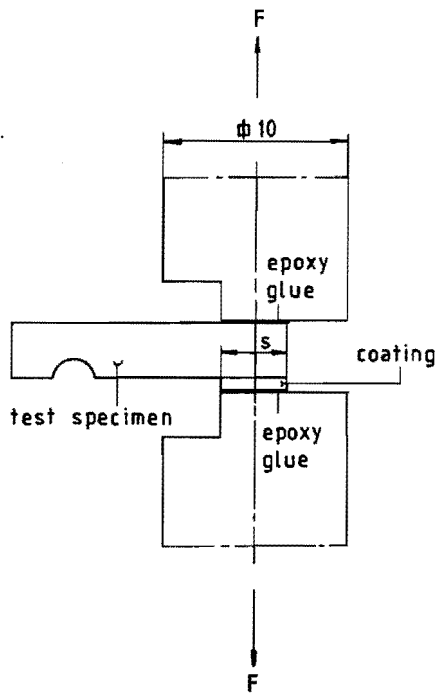
Fig. 3.21:   Tensile test set up.

The force F is divided by the fracture surface A_f which is determined after the fracture. The quotient $\sigma = F/A_f$ is taken as a measure for the tensile strength of the coating.

174

3.4.2   Test results.

The test results are listed in table 19 and visualized in fig. 3.22 and 3.23.
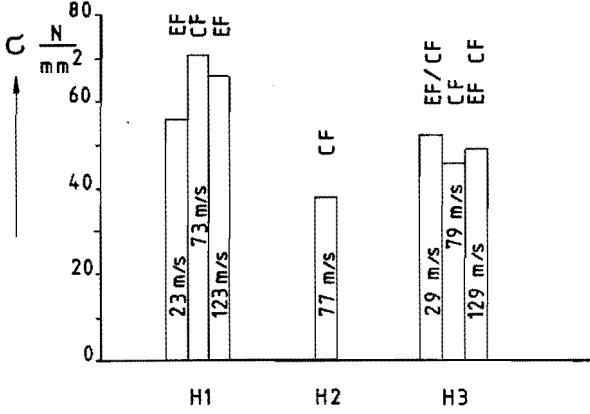
Fig. 3.22:   Tensile strength of Mo 53 − 63 μm as a function of heat content and velocity.
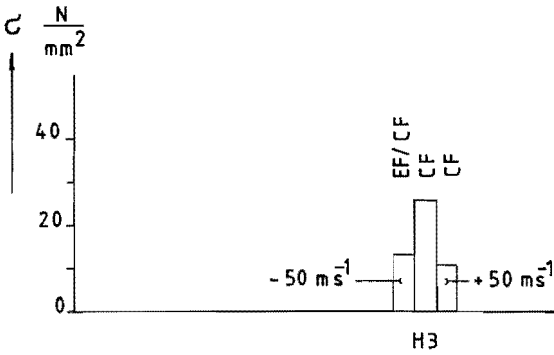
Fig. 3.23:   Tensile strength of Mo 5 − 15 μm.

Photo 38 demonstrates the typical failure mechanism for stainless steel particles.

The fracture occurs at the polished surface. Mind the heavily deformed rim.

The Mo (53 − 63 μm) specimen break within the coating with one exception: the

175
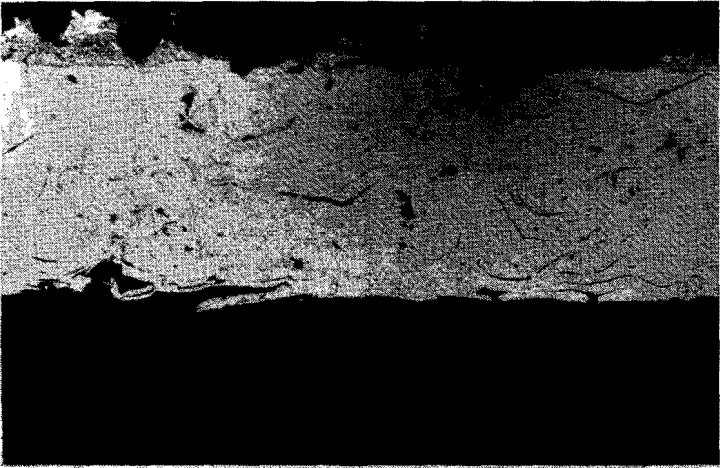
Photo 38a: Fracture on the coating side of testpiece A316 – 5 (heat content H3) ⊢——⊣ 42 μm

Photo 38b: Fracture on the substrate side of testpiece A 316 – 5. ⊢——⊣ 42 μm

coating sprayed at a heat content H1. The test specimen rupture in the epoxy film at the standard epoxy strength of approximately 70 Nmm^{-2}. The apparent strength of this coating and the adhesion to steel must be attributed to the pancake shaped deposits without a distinct loose rim. Pancakes with a loose rim or flower leaves with a free gap between the spray material and the surface, obviously suffer from high stress concentrations causing low fracture toughnesses and low nominal tensile strengths.

The measured tensile strengths for Mo $5 - 15$ μm are low compared to the values for the middle coarse particles. The fracture occurs in the coating.

For all tested specimens holds that the impact velocity is apparently not the determining factor regarding the strength. The coatings sprayed with a rotating substrate may be influenced in a negative way by the pick up of particles which first hit the rotating disk perimeter.

4.   DISCUSSION

4.1   On the relation between the determined morphologies and the theoretical
       model.

Two model features have been emphasized in the theory chapter:
   — The lateral flow out of the contact zone
   — a possible phase tranformation of initially liquid spray material into an
     amorphous solid during the compression.

The first model feature is confirmed by a great deal of the shown cross sections of
spread particles. The lateral flow occurs both with liquid and with solid material.
The double layered rim, which occurs for instance in all cross section of A316— H2
deposits, has turned up experimentally and was not foreseen with the theoretical
model

The second model feature is hard to detect directly. The shape of the flower type
deposits of Mo, including the existence of the chaplet corona, can be explained
fully on the basis of the liquid—solid transformation during the compression.
The same flower forming has been observed with relatively highly superheated
stainless steel. The Hugoniot pressure — temperature relation for this material
have not been determined. Therefore, the experiments with AISI—316 are not the
major ones to confirm the theory. For Al however, a complete theoretical picture
has been sketched and with Al no flower deposits occur within the applied
experimental range of size, velocity and heat content. This does not mean that
the concept of liquid — solid transformation only can be backed up by the Mo —
experiments, on the contrary, as may be clear from the following reasoning.

178

The specific heat at a constant pressure nearby the melting point is for Al: 1243 $Jkg^{-1}K^{-1}$ and for Mo: 500 $Jkg^{-1}K^{-1}$. This large difference in C_p implies that a certain increase in the heat content of liquid Al is related to a smaller temperature rise of the liquid phase than is the case with Mo.

Let the heat content level H2 be characteristic for a just molten state of both Al and Mo.

Let the heat content level H3, at which experiments are carried out for both Al and Mo, represent a superheated state of the liquid.

The numerical values for H2 and H3 are given in table 16.

For Al: H3 − H2 = 1483 − 1114,2 = 368,8 kJ kg^{-1}

For Mo: H3 − H2 = 1327,5 − 1225,2 = 102,3 kJ kg^{-1}

The successive temperature rises above the melting points then are:

For Al: $\Delta T = \dfrac{H3 - H2}{C_{p_{Al}}} = \dfrac{36880}{1243} = 297$ K

For Mo: $\Delta T = \dfrac{H3 - H2}{C_{p_{Mo}}} = \dfrac{102300}{500} = 205$ K

The superheated liquids then have the temperatures:

For Al: $T = T_M + \Delta T = 933 + 297 = 1230$ K

For Mo: $T = T_M + \Delta T = 2883 + 205 = 3088$ K

The nearest by Hugoniot pressure–temperature curves which have been determined by computation are (see fig 2.10 and 2.11) the curves where:

$T_0 = 1200$ K for Al and

$T_0 = 3000$ K for Mo

These curves, together with the Clapeyron lines for Al and Mo are given in fig. 4.1 where the Clapeyron lines coincide for $T = T_M$. So, the curves of fig 4.1 are basically the same as those presented in fig 2.10 and 1.11; only a horizontal

179
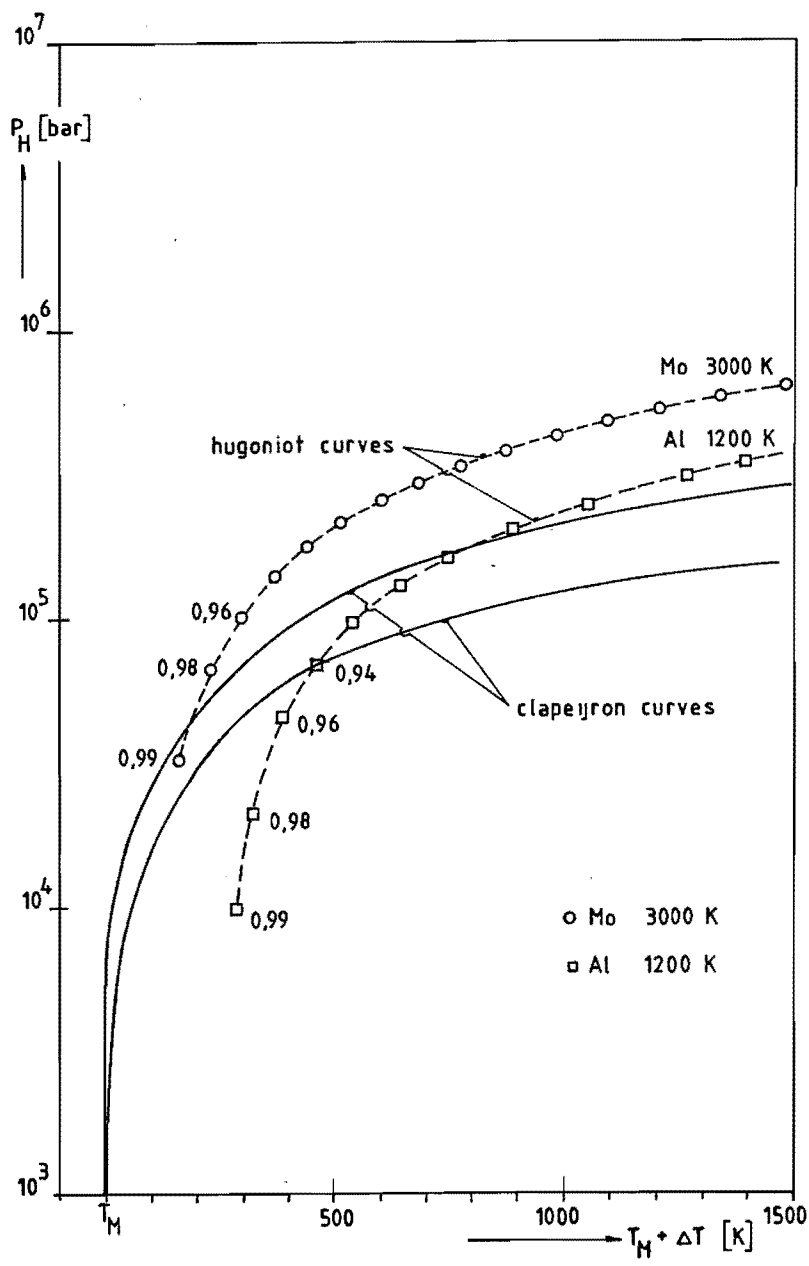
Fig. 4.1   Hugoniot pressure and Claperyron curves as function of $(T_M + \Delta T)$ for Al and Mo.

translation is applied. Now it turns out that the applied superheating level H3 implies for Mo a liquid–solid transformation at compression degrees between 0,99 and 0,98 and that a compression degree of 0,94 is required for Al, to make it undergo the same transformation.

In table 11c can be read that a compression degree for Al of $\rho_0/\rho_1 = 0,94$ is reached for an impact velocity $U_p = 387$ ms^{-1}. Table 13 gives the necessary impact velocity for Mo to reach an compression rate between 0,99 and 0,98: $U_p = 56,8 \to 114$ ms^{-1}. In table 18 can be read that the applied and measured impact velocity for Mo at the H3 level is 79 ms^{-1}, for Al however the impact velocity is unknown but certainly not at the required level of 387 ms^{-1} in order to create a phase transformation.

The conclusion is that the absence of flower type deposits for Al is completely coherent with the theory. The available experimental equipment does not allow a quick prove on the concept at an impact velocity exceeding 387 ms^{-1}. This experiment certainly will be carried out in next future.

4.2   On the relation between the potential energy, or for weak shocks, the
          kinetic energy of a particle and the final surface energy of a spread particle

Let a 60 μm Mo particle have a temperature of 3000 K at the moment of impact and let the compression degree be $\rho_0/\rho_1 = 0,98$. The specific potential energy of such a particle amounts 6489 J kg^{-1} (appendix 7.2). The mass of a 60 μm Mo particle is $1,15 \cdot 10^{-9}$ kg, so the total available potential energy to create the spread geometry is: $1,15 \cdot 10^{-9} \cdot 6489 = 7,5 \cdot 10^{-6}$ J.

Assume that the particle takes a spread shape like a disk of 2 μm thickness and diameter D. The volume of the spherical particle and the disk must be the same:
$$\frac{4}{3} \pi r^3 = \frac{\pi}{4} D^2 h \quad (r = 30 \ \mu m, \ h = 2 \ \mu m)$$

181

from which follows that D = 268 μm.

The total surface energy of such a liquid Mo disk is:

$$E_{surface} \cong 2 * \frac{\pi}{4} D^2 * \sigma$$

where σ = surface energy of liquid Mo = 2 Nm/m^2 [21]

$$E_{surface} = 2 * \frac{\pi}{4} (268 \cdot 10^{-6})^2 * 2 = 0{,}2 \cdot 10^{-6} \text{ J.}$$

The total surface enrgy amounts only $\dfrac{0{,}2 \cdot 10^{-6}}{7{,}5 \cdot 10^{-6}} \cdot 100\% = 2{,}7\%$ of the total

available potential energy at the moment of impact.

The conclusion must be that energy consuming processes different from spreading in a liquid phase must be active during the collision. Such processes are: vibration and deformation of the substrate, heat extraction by the substrate and deformation of the particle in a solid state.

In this thesis, the substrate is assumed to be rigid. This model feature certainly is not true for high melting materials like Mo. An advanced analysis should have to take into account the energy interaction with the substrate as a fourth input parameter of the system.

CONCLUSIONS.

The subject of this work describes a theory and experiments which relate the morphology of spread thermal spray particles to the input parameters velocity and heat content for a fixed narrow particle size range.
Both, the theory and the experiments, give insight in adhesion determining phenomena such as friction welding, diffusion and mechanically mixing.
The application of a rotating substrate support has turned out to be a powerfull new method for the determination of the relation between the morphology of spread particles and the input parameters velocity and heat content.
The spreading of a spray particle basically starts in the highly compressed initial contact zone with the substrate. It results from the lateral flow of the spray material which developes during the flow a good contact with the substrate, culminating in atomic adhesion, friction welds, diffusion and mechanically mixing of substrate and spray material.
The lateral flow of spray material, out of the compressed contact zone, can be followed by a lateral flow of spray material which is located in the upper part of the colliding particle. Thus, a double layered loose rim in conjunction with pancake type deposits are formed.
The combination of a heat content, corresponding to a super heated liquid and a slightly elevated impact velocity, can be attended by a liquid – solid phase transformation. The spray material forms flower type deposits if the phase transformation occurs. Flower type deposits are related with mechanically mixing of the spray material and the substrate over a depth of several tens of micrometers.

— Adhesion generally appears in a combination of a high heat content with a wide range of impact velocities. High impact velocities advance the formation of loose rims of the pancake deposits which deteriorates the nominal adhesion strength.

APPENDIX 1: Temperature profiles in depot and substrate right after the
solidification of one lamella with thickness X

PROFILE 1: Substrate temperature — Mo on Fe — X = 2 μm.

Equation: (1.44)

$$\frac{\theta_0 - T_{s0}}{T_m - T_{s0}} = \frac{B}{B + \text{erf } p}\left(1 + \text{erf}\frac{x}{X} - p\sqrt{\frac{a_1}{a_0}}\right)$$

$$= \frac{1,1826}{1,1826 + 0,5622}\left(1 + \text{erf}\frac{x}{2} \cdot 0,5487 \cdot 1,6463\right)$$

$$= 0,6778 \left(1 + \text{erf } 0,4517 \text{ x}\right)$$

MIND: — For the substrate holds that x is negative.

   — x to be inserted in μm.

   — x = 0 represents the contact interface.

Results:

x	0,4517 x	− erf 0,4517 x	$\dfrac{\theta_0 - T_{s0}}{T_m - T_{s0}}$	θ_0	
μm	[−]	[−]	[−]	K	C
0	0	0	0,6778	2048,5	1755,5
−0,5	−0,2259	0,250631	0,7494	1940,9	1667,9
−1,0	−0,4517	0,477047	0,5230	1647,6	1374,6
−1,5	−0,6776	0,662074	0,3379	1168,2	895,2
−2,0	−0,9034	0,798610	0,2014	814,6	538,6
−3,0	−1,3550	0,944668	0,0374	390,0	117,0
−4,0	−1,8069	0,989392	0,0072	311,6	38,6
−6,0	−2,7102	0,999873	0,0001	293,2	20,2

PROFILE 2: Substrate temperature – Mo on Fe – X = 12 μm.

Equation: (1.44)

$$\frac{\theta_0 - T_{s0}}{T_m - T_{s0}} = \frac{1,1826}{1,1826 + 0,5622}\left(1 + \text{erf}\,\frac{x}{12} \cdot 0,5487 \cdot 1,6463\right)$$

$$= 0,6778\,(1 + \text{erf}\,0,0753\,x)$$

Remarks: see profile 1.

x	0,0753x	$-\text{erf}\,0,0753\,x$	$\dfrac{\theta_0 - T_{s0}}{T_m - T_{s0}}$	θ_0	
μm	[–]	[–]	[–]	K	C
0	0	0	0,6778	2048,5	1775,5
−1	−0,0753	0,084807	0,6203	1899,6	1626,6
−2	−0,1506	0,168658	0,5635	1752,4	1479,4
−3	−0,2259	0,250631	0,5079	1608,5	1335,5
−4	−0,3012	0,329864	0,4542	1469,4	1196,4
−5	−0,3765	0,405587	0,4029	1336,4	1063,4
−6	−0,4518	0,477139	0,3544	1210,9	937,9
−8	−0,6024	0,605743	0,2672	985,1	712,1
−10	−0,7530	0,713080	0,1945	976,7	523,7
−12	−0,9036	0,798709	0,6778	646,3	373,3
−14	−1,0542	0,864003	0,0922	531,7	258,7
−16	−1,2048	0,911590	0,0599	448,2	175,2
−18	−1,3554	0,944740	0,0375	390,0	117,0
−20	−1,5060	0,966812	0,0225	351,3	78,3

<u>PROFILE 3</u>: Depot temperature — Mo on Fe — X = 2 μm.

Equation: (1.45)

$$\frac{\theta_1 - T_{s0}}{T_m - T_{s0}} = \frac{1}{B + \text{erf } p}(B + \text{erf } \frac{x}{X}p)$$

$$= \frac{1}{1,1826 + 0,5622}(1,1826 + \text{erf } \frac{x}{2} \cdot 0,5487)$$

$$= 0,5731 \ (1,1826 + \text{erf } 0,2744 \ x).$$

Results:

x	0,2774 x	erf 0,2744 x	$\dfrac{\theta_1 - T_{s0}}{T_m - T_{s0}}$	θ_1	
μm	[–]	[–]	[–]	K	C
0	0	0	0,6778	2048,5	1775,5
0,5	0,1372	0,153848	0,7657	2276,2	2003,2
1,0	0,2744	0,302029	0,8509	2496,8	2223,8
1,5	0,4115	0,439399	0,9296	2700,7	2427,7
2,0	0,5487	0,562239	1,0000	2883,0	2610,0

PROFILE 4: Depot temperature —Mo on Fe —X = 12 μm.

Equation: (1.45)

$$\frac{\theta_1 - T_{s0}}{T_m - T_{s0}} = \frac{1}{1,1826 + 0,5622}\left(1,1826 + \text{erf}\,\frac{x}{12} \cdot 0,5487\right)$$

$$= 0,5731\,(1,1826 + \text{erf}\,0,0457\,x)$$

Results:

x	0,0457 x	erf 0,0457 x	$\dfrac{\theta_1 - T_{s0}}{T_m - T_{s0}}$	θ_1	
μm	[–]	[–]	[–]	K	C
0	0	0	0,6778	2048,5	1775,5
2	0,0914	0,102847	0,7367	2201,0	1928,0
4	0,1829	0,204102	0,7948	2351,4	2078,4
6	0,2742	0,301819	0,8507	2496,4	2223,4
8	0,3658	0,395067	0,9042	2634,9	2361,9
12	0,5487	0,562239	1,0000	2883,0	2610,0

PROFILE 5: Substrate temperature − AlSl − 316 on Fe X = 2 μm.

Equation: (1.44)

$$\frac{\theta_0 - T_{s0}}{T_m - T_{s0}} = \frac{0,4987}{0,4987 + 0,6662}(1 + \mathrm{erf}\, \frac{x}{2} \cdot 0,6835 \cdot 0,4815)$$

$$= 0,4281\,(1 + \mathrm{erf}\, 0,1646\, x)$$

Results:

x	$0,1646\, x$	$-\mathrm{erf}\, 0,1646\, x$	$\dfrac{\theta_0 - T_{s0}}{T_m - T_{s0}}$	θ_0	
μm	[−]	[−]	[−]	K	C
0	0	0	0,4281	761,7	488,7
−0,5	−0,0823	0,092656	0,3884	718,3	445,3
−1,0	−0,1646	0,184067	0,3493	675,5	402,5
−1,5	−0,2469	0,273038	0,3066	628,7	355,7
−2,0	−0,3292	0,358469	0,2705	589,3	316,3
−3,0	−0,4938	0,515035	0,2046	517,0	244,0
−4,0	−0,6584	0,648208	0,1484	455,5	182,5
−6,0	−0,9876	0,837489	0,0685	368,0	95,0
−8,0	−1,3168	0,937430	0,0264	321,9	48,9
−10,0	−1,6460	0,980077	0,0085	302,3	29,3

PROFILE 6: Substrate temperature − AlSl − 316 on Fe X = 12 μm.

Equation: (1.44)

$$\frac{\theta_0 - T_{s0}}{T_m - T_{s0}} = \frac{0,4987}{0,4987 + 0,6662} \left(1 + \text{erf} \frac{x}{12} \cdot 0,6835 \cdot 0,4815\right)$$

$$= 0,4281 \ (1 + \text{erf} \ 0,0274 \ x)$$

Results:

x	0,0274 x	−erf 0,0274 x	$\dfrac{\theta_0 - T_{s0}}{T_m - T_{s0}}$	θ_0	
μm	[−]	[−]	[−]	K	C
0	0	0	0,4281	761,7	488,7
−1	−0,0274	0,030910	0,4149	747,3	474,3
−2	−0,0548	0,061773	0,4017	732,8	459,8
−4	−0,1096	0,123177	0,3754	704,0	431,0
−6	−0,1644	0,183848	0,3494	675,6	402,6
−8	−0,2192	0,243436	0,3239	647,6	374,6
−12	−0,3288	0,358064	0,2748	593,9	320,9
−16	−0,4384	0,464736	0,2291	543,9	270,9
−20	−0,5480	0,561654	0,1877	498,5	225,5
−24	−0,6576	0,647622	0,1509	458,2	185,2
−28	−0,7672	0,718928	0,1203	424,7	151,7
−30	−0,8220	0,754961	0,1049	497,8	134,8

190

PROFILE 7: Depot temperature $-AlSl - 316$ on Fe X $= 2$ μm.

Equation: (1.45)

$$\frac{\theta_1 - T_{s0}}{T_m - T_{s0}} = \frac{1}{0{,}4987 + 0{,}6662} \left(0{,}4987 + \text{erf} \frac{x}{2} - 0{,}6835\right)$$

$$= 0{,}8584 \left(0{,}4987 + \text{erf } 0{,}3418 \text{ x}\right)$$

Results:

x	0,3418 x	erf 0,3418 x	$\dfrac{\theta_1 - T_{s0}}{T_m - T_{s0}}$	θ_1	
μm	[–]	[–]	[–]	K	C
0	0	0	0,4281	761,7	488,7
0,5	0,1709	0,190979	0,5920	941,3	668,3
1,0	0,3418	0,371173	0,7467	1110,7	837,7
1,5	0,5126	0,531502	0,8844	1261,4	988,4
2,0	0,6835	0,666263	1,0001	1388,0	1115,0

PROFILE 8: Depot temperature $-\text{AlSl} - 316$ on Fe $X = 12 \ \mu m$.

Equation: (1.45)

$$\frac{\theta_1 - T_{s0}}{T_m - T_{s0}} = \frac{1}{0,4987 + 0,6662} \left(0,4987 + \text{erf} \frac{x}{12} \cdot 0,6835\right)$$

$$= 0,8584 \ (0,4987 + \text{erf} \ 0,0570 \ x)$$

Results:

x	0,0570 x	erf 0,0570 x	$\dfrac{\theta_1 - T_{s0}}{T_m - T_{s0}}$	θ_1	
μm	[-]	[-]	[-]	K	C
0	0	0	0,4281	761,7	488,7
2	0,1140	0,128080	0,5381	882,2	609,2
4	0,2280	0,252881	0,6452	999,5	726,5
8	0,4560	0,480996	0,8410	1231,9	940,9
12	0,6840	0,666617	1,0003	1388,3	1115,3

192

APPENDIX 2: Temperature profiles in the substrate <u>during</u> solidification of one lamella of Mo, see fig. 1.9. The equation to be used is (1.41a).

$$\frac{\theta_0 - T_{s0}}{T_m - T_{s0}} = \frac{B}{B + \text{erf } p}\left(1 + \text{erf }\frac{x}{\sqrt{4a_0 t}}\right)$$

The numerical values are taken from table 2.

$$\frac{\theta_0 - T_{s0}}{T_m - T_{s0}} = 0{,}6778\left(1 + \text{erf } 1{,}3351 \cdot 10^2 \frac{x}{\sqrt{t}}\right)$$

N.B: x to be inserted in [m]; x is negative.

Profile 1: $-x = 10$ Å

$-x=10$Å	$-1{,}3351.10^2\,\dfrac{x}{\sqrt{t}}$	$-\text{erf } 1{,}3351.10^2\,\dfrac{x}{\sqrt{t}}$	$\dfrac{\theta_0 - T_{s0}}{T_m - T_{s0}}$	θ_0	
				K	C
$t = 10^{-9}$[s]	0,0042	0,004739	0,6747	2040,2	1767,2
10^{-8}	0,0013	0,001467	0,6768	2045,9	1772,9
10^{-7}	0,0000	0	0,6778	2048,5	1775,5
10^{-6}	0,0000	0	0,6778	2048,5	1775,5
10^{-5}	0,0000	0	0,6778	2048,5	1775,5

Profile 2: $-x = 100$ Å

$t=$					
10^{-9} [s]	0,0422	0,047589	0,6455	1964,9	1691,9
10^{-8}	0,0133	0,015007	0,6676	2022,2	1749,2
10^{-7}	0,0000	0	0,6778	2048,5	1775,5
10^{-6}	0,0000	0	0,6778	2048,5	1775,5
10^{-5}	0,0000	0	0,6778	2048,5	1775,5

Profile 3: $-x = 500$ Å

$t=$					
10^{-9} [s]	0,2111	0,234709	0,5187	1636,5	1363,5
10^{-8}	0,0667	0,075151	0,6268	1916,5	1643,5
10^{-7}	0,0211	0,023805	0,6616	2006,7	1733,7
10^{-6}	0,0066	0,007447	0,6727	2035,4	1762,4
10^{-5}	0,0021	0,002370	0,6761	2044,3	1771,3

Profile 4: $-x = 1000$ Å

$t=$					
10^{-9} [s]	0,4222	0,449547	0,3730	1259,3	986,3
10^{-8}	0,1335	0,149748	0,5763	1785,6	1512,6
10^{-7}	0,0422	0,047589	0,6455	1964,9	1691,9
10^{-6}	0,0133	0,015007	0,6676	2022,1	1749,1
10^{-5}	0,0042	0,004739	0,6745	2040,2	1767,2

Profile 5: $-x = 5000$ Å

$t=$					
10^{-9}	2,1110	0,997168	0,0019	297,9	24,9
10^{-8}	0,6675	0,654824	0,2339	898,9	625,9
10^{-7}	0,2111	0,234709	0,5187	1636,4	1363,4
10^{-6}	0,0667	0,075151	0,6268	1916,5	1643,5
10^{-5}	0,0211	0,023805	0,6616	2006,7	1733,7

Profile 6: $\quad -x = 10.000$ Å $= 1\ \mu$m

$t=$					
10^{-9} [s]	4,2220	0,999999	0	293	20
10^{-8}	1,3351	0,940990	0,0399	396,6	123,6
10^{-7}	0,4222	0,449547	0,3730	1259,3	986,3
10^{-6}	0,1335	0,149748	0,5763	1785,6	1512,6
10^{-5}	0,0422	0,047589	0,6455	1964,9	1691,9

194

APPENDIX 3: Shock wave propagation velocity for longitudinal waves.

Zukas [11], pg. 2 table 1 states for an extended medium: (C_L = wave velocity)

$$C_L{}^2 = \frac{\lambda + 2\mu}{\rho} = \frac{E\ (1 - \nu)}{\rho\ (1 + \nu)\ (1 - 2\nu)} \qquad (A.3.1)$$

where   E   = Young's modulus

            ν = Poisson's ratio

            ρ = density

            λ,μ = Lamé parameters

According to Zwikker [12], pg. 85 and 90:

$\lambda = \mu = G$ = shearmodulus.

This implies for eq. (A.3.1.):

$$C_L{}^2 = \frac{3G}{\rho} = \frac{E\ (1 - \nu)}{\rho\ (1 + \nu)\ (1 - 2\nu)} \qquad (A.3.2)$$

The relation between E and G is:

$$G = \frac{E}{2\ (1 + \nu)} \qquad (A3.3)$$

Substitution of (A.3.3) into (A.3.2) reveals that eq. (A.3.2) holds for $\nu = 0,25$ only. For this reason, eq. (A.3.1) is restricted to:

$$C_L{}^2 = \frac{E\ (1 - \nu)}{\rho\ (1 + \nu)\ (1 - 2\nu)} \qquad (A.3.4 \equiv \text{eq. } 2.8)$$

which is in agreement with Zukas [11]. pg. 2 and Zwikker [12] pg. 190.

Eq. (A.3.4) can be transferred into a relation between G and the bulkmodulus

$$K \equiv -V_0 \left(\frac{\partial P}{\partial V}\right)_T = \frac{E}{3 (1 - 2\nu)} \qquad (A.3.5)$$

$$C_L^2 = \frac{1}{\rho} \cdot \frac{E (1 - \nu)}{(1 + \nu)(1 - 2\nu)} \qquad (A.3.1)$$

$$= \frac{1}{\rho}(K + \tfrac{4}{3} G) \qquad (A.3.6)$$

With $L = K + \tfrac{4}{3} G,$ $\qquad (A.3.7)$

the elastic modulus in a uniaxial strain situation as is considered in this thesis.

So, for an extended medium under uniaxial strain:

$$C_L^2 = \frac{L}{\rho} \qquad (A.3.8)$$

while for a bounded medium under uniaxial stress:

$$C_L^2 = \frac{E}{\rho} \qquad (A.3.9)$$

Eq. (2.7) can be worked out in terms of K and G or in terms of ν and E. Both

expressions for U_s will be derived here.

U_s in terms of K and G:

$$U_s = a + b U_p \qquad (2.7)$$

from (A.3.6) follows:

$$a = \left(\frac{K + \tfrac{4}{3} G}{\rho_0}\right)^{\tfrac{1}{2}} \qquad (A.3.10)$$

According to Zukas [11]

$$b = \frac{1 + \Gamma}{2} \qquad (A.3.11)$$

where $\qquad \Gamma \quad = \dfrac{3\beta K}{\rho_0 C_v}$ (A.3.12)

$\qquad\qquad\qquad$ = Grüneisenparameter

with: $\qquad \beta \quad$ = coefficient of linear thermal expansion = $\dfrac{\alpha}{3}$

$\qquad\qquad C_v \quad$ = specific heat capacity at constant volume.

C_v data are difficult to find in the literature. C_p data are readily available in many materials handbook. The relation between C_p and C_v is, ref. [19] –pg 23:

$$C_{p_m} = C_{v_m} + \dfrac{\alpha^2 V_m T}{\kappa}$$ (A.3.13)

where: $\qquad C_{p_m} \quad$ = molar heat capacity at constant pressure

$\qquad\qquad \alpha \quad$ = volume coefficient of thermal expansion

$\qquad\qquad V_m \quad$ = molar volume

$\qquad\qquad T \quad$ = Temperature

$\qquad\qquad \kappa \quad = -\dfrac{1}{V_0}\left(\dfrac{\partial_V}{\partial_P}\right)_T$ = compressibility

$\qquad\qquad\qquad = \dfrac{1}{K}$

Substitution of $\kappa = \dfrac{1}{K}$ into (A.3.13) yields for C_{v_m}:

$$C_{v_m} = C_{p_m} - \alpha^2 K V_m T_0$$ (A.3.14)

Substitution of $3\beta = \alpha$ into (A.3.12) yields for Γ:

$$\Gamma = \dfrac{\alpha K}{\rho_0 C_v}$$ (A.3.12a)

and the constant b = $\dfrac{1 + \Gamma}{2}$ can be written as:

$$b = \frac{1}{2} + \frac{\alpha \, K}{2 \, \rho_0 C_v} \tag{A.3.11a}$$

The shock propagation speed in terms of K and G is now determined by (2.7) (A.3.10) and (A.3.11a):

$$U_s = \left(\frac{K + \frac{4}{3} G}{\rho_0}\right)^{\frac{1}{2}} + \left(\frac{1}{2} + \frac{\alpha \, K}{2 \, \rho_0 C_v}\right) U_p \tag{2.7a}$$

<u>U_s in terms of E and ν:</u>

$$U_s = a + b \cdot U_p \tag{2.7}$$

with (A.3.1):

$$a = \left(\frac{E}{\rho_0}\right)^{\frac{1}{2}} \left(\frac{1 - \nu}{(1 + \nu) \, (1 - 2\nu)}\right)^{\frac{1}{2}} \tag{A.3.15}$$

Substitution of (A.3.5):

$$K = \frac{E}{3 \, (1 - 2\nu)} \qquad \text{into (A.3.12a) gives:}$$

$$\Gamma = \frac{\alpha E}{3 \, (1 - 2\nu) \, \rho_0 \, C_v} \tag{A.3.16}$$

and (eq. 2.7) can be written in terms of E and ν:

$$U_s = \left(\frac{E}{\rho_0}\right)^{\frac{1}{2}} \left(\frac{1 - \nu}{(1 + \nu) \, (1 - 2\nu)}\right)^{\frac{1}{2}} + \left(\frac{1}{2} + \frac{\alpha E}{6 \, (1 - 2\nu) \, \rho_0 C_v}\right) U_p \tag{2.7b}$$

where the value for the specific heat capacity C_v may be calculated from the molar heat capacity as given in (A.3.14):

$$C_v = \frac{1000}{\text{at wght}} \cdot C_{v_m} \tag{A3.14a}$$

198

: Defenition of Duvall's and Zwolinski's equation.

Duvall and Zwolinski [14] and Duvall [15] published a.o. two related reports on equations of state and on pressure − volume relations. In [14], 1955 D and Z give for the increase in internal energy of a shock front.

$$E = \int_0^T C_v \, dT \int_{V_0}^V \{T \, (\frac{\partial P}{\partial T})_V - P\} \, dV \qquad (A.4.1)$$

which may be converted into:

$$E_1 - E_0 = C_v \, (T_1 - T_0) + \int_{V_0}^{V_1} \{T \, (\frac{\partial P}{\partial T})_V - P\} \, dV$$

$$(A.4.2)$$

In [15], 1957, D gives for the increase in internal energy the equation:

$$E_1 - E_0 = C_v \, (T_1 - T_0) + \int_{V_0}^{V_1} f(V) \, dV \qquad (A.4.3)$$

In both reports use is made of the generalized form for the equation of state:

$$P = f(V) + T \cdot g(V) \qquad (A.4.4)$$

From this equation follows:

$$(\frac{\partial P}{\partial T})_V = g(V) \qquad (A.4.5)$$

So, f(V) can be written as:

$$f(V) = P - T \, (\frac{\partial P}{\partial T})_V \qquad (A.4.6)$$

and with (A.4.6) eq. (A.4.2) converts to

$$E_1 - E_0 = C_v \, (T_1 - T_0) + \int_{V_0}^{V_1} (-f(V)) \, dV,$$

rewritten:

$$E_1 - E_0 = C_v \, (T_1 - T_0) + \int_{V_1}^{V_0} f(V) \, dV \qquad (A.4.7)$$

A comparison of eq. (A.4.7) with (A.4.3) reveals that in the successive reports of

1955 and 1957 the integral boundaries are not consistent; V_0 and V_1 have exchanged their places. The question now is: what is the correct formula? The answer is as follows:

The internal energy can be written as a function of two state variables:

$$E = E\,(V,T) \qquad\qquad (A.4.8)$$

In differential form:

$$dE = (\frac{\partial E}{\partial T})_V\, dT + (\frac{\partial E}{\partial V})_T\, dV \qquad\qquad (A.4.9)$$

The first law of thermodynamics says:

$$(\frac{\partial E}{\partial T})_V \equiv C_v\, dT \qquad\qquad (A.4.10)$$

Assuming C_v = constant (A.4.9) can be written as:

$$dE = C_v\, dT + (\frac{\partial E}{\partial V})_T\, dV \qquad\qquad (A.4.11)$$

In integral form:

$$E_1 - E_0 = C_v\,(T_1 - T_0) + \int_{V_0}^{V_1} (\frac{\partial E}{\partial V})_T\, dV \qquad\qquad (A.4.12)$$

Atkins, ref [16] —pg. 153 inferred from the first law of thermodynamcis a so — called thermodynamic equation of state:

$$(\frac{\partial E}{\partial V})_T = T\,(\frac{\partial P}{\partial T})_V - P \qquad\qquad (A.4.13)$$

Using (A.4.13) eq. (A.4.12) can be converted into:

$$E_1 - E_0 = C_v\,(T_1 - T_0) + \int_{V_0}^{V_1} \{T(\frac{\partial P}{\partial T})_V - P\}\, dV$$

$$\qquad\qquad (A.4.14)$$

and this is exactly the same equation as (A.4.2) which Duvall produced in 1955. So, it must be concluded that the equation (A.4.2) —1955— is correct and equation A (4.3) is incorrect. In this thesis, use is made of (A.4.2) and the rewritten form of it: eq. (A.4.7).

So:

$$E_1 - E_0 = C_v \ (T_1 - T_0) + \int_{V_1}^{V_0} f(V) \ dV$$

which goes into the text of the thesis as eq. (2.9).

<u>APPENDIX 5:</u> Derivation of eq. (2.26).

For the entropy in locus B on the isotherm AB holds:

$$S = S\ (V,T) \tag{A.5.1}$$

in differential form:

$$dS = (\frac{\partial S}{\partial V})_T\ dV + (\frac{\partial S}{\partial T})_V\ dT \tag{A.5.2}$$

and for an isothermal change:

$$dS = (\frac{\partial S}{\partial V})_T\ dV \tag{A.5.3}$$

Substitution of the Maxwell relation

$$(\frac{\partial S}{\partial V})_T = (\frac{\partial P}{\partial T})_V \tag{A.5.4}$$

into eq. (A.5.3) yields for the integral from A to B:

$$\int_{S_A}^{S_B} dS = \int_{V_0}^{V_1} (\frac{\partial P}{\partial T})_V\ dV \tag{A.5.5}$$

$$\text{with } g(V) \equiv (\frac{\partial P}{\partial T})_V = \frac{\rho}{\rho_0}\ \alpha K \tag{2.19}$$

eq. (A.5.5) gives:

$$S_B - S_A = \int_{V_0}^{V_1} g(V)dV = \int_{V_0}^{V_1} \frac{\rho}{\rho_0}\ \alpha K dV \tag{2.26}$$

Aluminium — Appendix 6

P/P₁	8. -01	8.1-01	8.2-01	8.3-01	8.4-01
	5.5460071 05	4.7163596 05	3.9678719 05	3.2954638 05	2.6944288 05
	2.776769 10	2.5452055 10	2.3280215 10	2.1241573 10	1.9326429 10
	7.038525 06	6.9516296 06	6.8668537 06	6.7841205 06	6.7033571 06
	3.3407808 10	3.0303494 10	2.7459364 10	2.4845702 10	2.243702 10
	1.2373262 06	1.066234 06	9.1531214 05	7.821795 05	6.6480059 05
	8.01321 02	6.9788506 02	6.0859736 02	5.3125953 02	4.6403488 02
	1.401321 03	1.2978851 03	1.2085974 03	1.1312595 03	1.0640349 03
	7.865514 03	7.685775 03	7.516698 03	7.357314 03	7.2067709 03
	1.5731028 03	1.4602973 03	1.3530056 03	1.2507434 03	1.1530833 03
	-4.653634 02	-4.3945637 02	-4.1386723 02	-3.8858826 02	-3.6361205 02
	1.0360087 03	1.0049806 03	9.7524558 02	9.4673495 02	9.1938444 02
	2.5733793 02	2.1791419 02	1.8277653 02	1.5171372 02	1.2449046 02
	7.9860039 02	7.6437349 02	7.3510599 02	7.1016722 02	6.8900996 02
	3.9732799 02	3.9732799 02	3.9732799 02	3.9732799 02	3.9732799 02
	8.127535 02	8.127535 02	8.127535 02	8.127535 02	8.127535 02

	8.5-01	8.6-01	8.7-01	8.8-01	8.9-01
	2.1604029 05	1.689336 05	1.2774658 05	9.2129455 04	6.175678 04
	1.7525894 10	1.5831816 10	1.4236709 10	1.2733693 10	1.1316437 10
	6.6244941 06	6.5474651 06	6.4722069 06	6.3986591 06	6.326764 06
	2.0211349 10	1.8149657 10	1.6235385 10	1.445406 10	1.2792987 10
	5.6142636 05	4.7054667 05	3.9085185 05	3.2120133 05	2.6059788 05
	4.0538272 02	3.5400596 02	3.0880901 02	2.688637 02	2.3338157 02
	1.0053827 03	9.5400596 02	9.0880901 02	8.688637 02	8.3338157 02
	7.0643164 03	6.9292833 03	6.8010777 03	6.6791688 03	6.5630808 03
	1.0596475 03	9.7009966 02	8.8414009 02	8.0150025 02	7.2193888 02
	-3.3893142 02	-3.1453946 02	-2.9042949 02	-2.6659508 02	-2.4302998 02
	8.9513388 02	8.6792684 02	8.4371043 02	8.2043499 02	7.9805388 02
	1.0086578 03	8.0567243 01	6.3325429 01	4.8863554 01	3.69048 01
	6.7115677 02	6.5618897 02	6.4373763 02	6.3347624 02	6.251146 02
	3.9732799 02	3.9732799 02	3.9732799 02	3.9732799 02	3.9732799 02
	8.127535 02	8.127535 02	8.127535 02	8.127535 02	8.127535 02

	9. -01	9.1-01	9.2-01	9.3-01	9.4-01
	3.6325473 04	1.555307 04	-8.2388675 02	-1.3051318 04	-2.1358946 04
	9.9791114 09	8.7163437 09	7.5231759 09	6.39503 09	5.3276749 09
	6.2564667 06	6.1877142 06	6.1204565 06	6.0546452 06	5.990234 06
	1.1240986 10	9.7881781 09	8.425804 09	7.1460732 09	5.9420365 09
	2.0816641 05	1.631363 05	1.2482673 05	9.2634282 04	6.6022628 04
	2.0169124 02	1.7321973 02	1.4747724 02	1.2404413 02	1.0256053 02
	8.0169124 02	7.7321975 02	7.4747724 02	7.2404413 02	7.0256053 02
	6.4523857 03	6.3466974 03	6.2456666 03	6.1489764 03	6.0563386 03
	6.4523857 02	5.7120277 02	4.9965333 02	4.3042835 02	3.6338032 02
	-2.1972814 02	-1.9968387 02	-1.7389142 02	-1.5134537 02	-1.2904047 02
	7.7652325 02	7.5580138 02	7.3585094 02	7.1663387 02	6.9811623 02
	2.7176206 01	1.9411988 01	1.3356205 01	8.7647592 00	5.4067594 00
	6.1839373 02	6.130819 02	6.0897053 02	6.0587172 02	6.0361536 02
	3.9732799 02	3.9732799 02	3.9732799 02	3.9732799 02	3.9732799 02
	8.127535 02	8.127535 02	8.127535 02	8.127535 02	8.127535 02

	9.5-01	9.6-01	9.7-01	9.8-01	9.9-01
	-2.5961516 04	-2.7059924 04	-2.4842233 04	-1.9484619 04	-1.1152236 04
	4.3171967 09	3.3599718 09	2.4526429 09	1.5920965 09	7.754434 08
	5.9271789 06	5.8654375 06	5.8049691 06	5.7457347 06	5.687697 06
	4.8074773 09	3.7366198 09	2.7250499 09	1.7676481 09	8.6050362 08
	4.4513679 04	2.7680147 04	1.5139166 04	6.5468446 03	1.5935752 03
	8.2717365 01	6.4248909 01	4.6926524 01	3.0553361 01	1.4959872 01
	6.8271737 02	6.6424891 02	6.4692652 02	6.305533 02	6.1495987 02
	5.9674905 03	5.882192 03	5.8002234 03	5.721383 03	5.6454853 03
	2.9837453 02	2.3528768 02	1.740067 02	1.1442766 02	5.6454853 01
	-1.069716 02	-8.5133816 01	-6.3522339 01	-4.2132522 01	-2.0959864 01
	6.8026551 02	6.6305104 02	6.4644388 02	6.3041666 02	6.144352 02
	3.0653164 00	1.5378923 00	6.3587618-01	1.8472532-01	2.2648593-02
	6.0204703 02	6.010261 02	6.0042407 02	6.0012316 02	6.000151 02
	3.9732799 02	3.9732799 02	3.9732799 02	3.9732799 02	3.9732799 02
	8.127535 02	8.127535 02	8.127535 02	8.127535 02	8.127535 02

```
To= 800.
   2700.
   7.219 10
   4.2674 00
   7. 8-05
   3.87592 05
   9. 33 02
   9.    02
   8.52 02
```

8. -01	8. 1-01	8. 2-01	8. 3-01	8. 4-01
4.7118116 05	3.9238738 05	3.2170959 05	2.5863976 05	2.0270723 05
2.8049231 10	2.5716217 10	2.3527422 10	2.1472333 10	1.9540938 10
7.038525 06	6.9516296 06	6.8668537 06	6.7841205 06	6.7033571 06
3.4806428 10	3.1581013 10	2.8624765 10	2.5907002 10	2.3401407 10
1.289127 06	1.1111938 06	9.5415884 05	8.155908 05	6.9337503 05
9.6003028 02	8.4365777 02	7.4231133 02	6.5369841 02	5.7590117 02
1.7600303 03	1.6436578 03	1.5423113 03	1.4536984 03	1.3759012 03
8.0284711 03	7.8461092 03	7.6745484 03	7.5128071 03	7.360022 03
1.6056942 03	1.4907607 03	1.3814187 03	1.2771772 03	1.1776035 03
-4.653634 02	-4.3945637 02	-4.1386723 02	-3.8858826 02	-3.6361205 02
1.3813449 03	1.3399741 03	1.3003274 03	1.2623133 03	1.2253459 03
2.0641693 02	1.7404128 02	1.4540747 02	1.2027256 02	9.8337045 01
1.0062279 03	9.7067424 02	9.4027801 02	9.1438152 02	8.9241446 02
1.3841413 02	1.3841413 02	1.3841413 02	1.3841413 02	1.3841413 02
5.5383963 02	5.5383963 02	5.5383963 02	5.5383963 02	5.5383963 02

8. 5-01	8. 6-01	8. 7-01	8. 8-01	8. 9-01
1.5347562 05	1.1053991 05	7.3523865 04	4.2077722 04	1.5876025 04
1.7724629 10	1.6015145 10	1.4404986 10	1.288728 10	1.1455625 10
6.6244941 06	6.5474651 06	6.4722069 06	6.3986591 06	6.326764 06
2.108529) 10	1.8938996 10	1.6945413 10	1.5089589 10	1.3358404 10
5.8570253 05	4.9101101 05	4.0794513 05	3.3532421 05	2.7211564 05
5.0730858 02	4.4656232 02	3.9251322 02	3.4418602 02	3.0075072 02
1.3073086 03	1.2465623 03	1.1925132 03	1.144186 03	1.1007507 03
7.2154312 03	7.0783589 03	6.9482034 03	6.8244272 03	6.7065484 03
1.0823147 03	9.097024 02	9.0326644 02	8.1893126 02	7.3772033 02
-3.3893142 02	-3.1453946 02	-2.9042949 02	-2.6659508 02	-2.4302998 02
1.1908452 03	1.1572358 03	1.1249472 03	1.0939133 03	1.0640718 03
7.9497754 01	6.3350803 01	4.9694513 01	3.8282075 01	2.8873871 01
8.7387906 02	8.5834105 02	8.4541519 02	8.3476259 02	8.2608181 02
1.3841413 02	1.3841413 02	1.3841413 02	1.3841413 02	1.3841413 02
5.5383963 02	5.5383963 02	5.5383963 02	5.5383963 02	5.5383963 02

9. -01	9. 1-01	9. 2-01	9. 3-01	9. 4-01
-5.3843048 03	-2.198573 04	-3.4191709 04	-4.2248163 04	-4.6384812 04
1.0104241 10	8.8277226 09	7.6211032 09	6.479795 09	5.3995577 09
6.2564667 06	6.1877143 06	6.1204565 06	6.0546452 06	5.990234 06
1.1740302 10	1.0225068 10	8.8036449 09	7.4679761 09	6.2108724 09
2.1741299 05	1.7041779 05	1.3042437 05	9.6807097 04	6.9009693 04
2.6149918 02	2.2582573 02	1.9321136 02	1.632104 02	1.3543956 02
1.0614992 03	1.0258257 03	9.9321136 02	9.632104 02	9.3543956 02
6.5941337 03	6.4867918 03	6.3841691 03	6.2895447 03	6.1918267 03
6.5941337 02	5.8381126 02	5.1073353 02	4.4001613 02	3.715096 02
-2.1972818 02	-1.7389142 02	-1.7389142 02	-1.5134537 02	-1.2904047 02
1.0353643 03	1.0077358 03	9.8113458 02	9.5551183 02	9.3082164 02
2.1239377 01	1.5158627 01	1.0423243 01	8.6370685 00	4.2164304 00
8.1910398 02	8.1358845 02	8.0931896 02	8.0610054 02	8.0375673 02
1.3841413 02	1.3841413 02	1.3841413 02	1.3841413 02	1.3841413 02
5.5383963 02	5.5383963 02	5.5383963 02	5.5383963 02	5.5383963 02

9. 5-01	9. 6-01	9. 7-01	9. 8-01	9. 9-01
-4.6816405 04	-4.3743835 04	-3.7355166 04	-2.7826575 04	-1.5323214 04
4.3764685 09	2.4068953 09	2.4874727 09	1.6150795 09	7.8681879 08
5.9271789 06	5.8654375 06	5.8049691 06	5.7457347 06	5.687697 06
5.0259018 09	3.9072939 09	2.8498589 09	1.8439175 09	9.0024113 08
4.653e128 04	2.8942918 04	1.583255 04	6.847842e 03	1.6671132 03
1.095687 02	8.531309 01	6.2426986 01	4.0697673 01	1.9941698 01
9.095687 02	8.8531309 02	8.624269 02	8.4069767 02	8.199417 02
6.1015492 03	6.0148689 03	5.9315433 03	5.8514283 03	5.7742761 01
3.0507746 02	2.4059475 02	1.779469 02	1.1702657 02	5.7742761 01
-1.069716 02	-8.5133816 01	-6.3523339 01	-4.2132522 01	-2.0959864 01
9.0702067 02	8.0406806 02	8.6192518 02	8.4055555 02	8.199247 02
2.3901054 00	1.1990279 00	4.9579897-01	1.440448-01	1.7662977-02
8.0212736 02	8.0044083 02	8.0048083 02	8.0012805 02	8.000157 02
1.3841413 02	1.3841413 02	1.3841413 02	1.3841413 02	1.3841413 02
5.5383963 02	5.5383963 02	5.5383963 02	5.5383963 02	5.5383963 02

$T_0 = 933. = T_M$ Aluminium Appendix 6.3

```
2700.
7.219 10
4.2674 00
7.8-05
3.87592 05
9.33 02
9. 02
8.52 02
```

8.-01	8.1-01	8.2-01	8.3-01	8.4-01
4.1570715 05	3.3968708 05	2.7178299 05	2.1148685 05	1.5832803 05
2.8236455 10	2.5891885 10	2.3691814 10	2.1625622 10	1.9685583 10
7.038525 06	6.9516296 06	6.8668537 06	6.7841205 06	6.7033571 06
3.573651 10	3.2430564 10	2.9399757 10	2.6612767 10	2.4042725 10
1.3235745 06	1.1410754 06	9.7999189 05	8.3780932 05	7.1237703 05
1.0655719 03	9.4059662 02	8.3123111 02	7.3512026 02	6.5029225 02
1.9985719 03	1.8735966 03	1.7642311 03	1.6681203 03	1.5832922 03
8.1350306 03	7.9509417 03	7.7777456 03	7.6144523 03	7.4601914 03
1.6270061 03	1.5106789 03	1.3999942 03	1.2944569 03	1.1936306 03
-4.653634 02	-4.3945637 02	-4.1386723 02	-3.8658826 02	-3.6361205 02
1.6109935 03	1.5627448 03	1.5165069 03	1.4721728 03	1.4296428 03
1.836757 02	1.5456654 02	1.2891219 02	1.0646419 02	8.6973651 01
1.1442324 03	1.107816 03	1.0766837 03	1.050161 03	1.027663 03
0. 00	0. 00	0. 00	0. 00	0. 00
4.1542551 02	4.1542551 02	4.1542551 02	4.1542551 02	4.1542551 02

8.5-01	8.6-01	8.7-01	8.8-01	8.9-01
1.1187012 05	7.1708105 04	3.7465762 04	8.7933195 03	-1.4634678 04
1.7856787 10	1.6137059 10	1.4516891 10	1.2989383 10	1.1548186 10
6.6244941 06	6.5474651 06	6.4722069 06	6.3986591 06	6.326764 06
2.1666463 10	1.9463906 10	1.7417582 10	1.5512217 10	1.3734407 10
6.0184619 05	5.0461979 05	4.1931216 05	3.4471592 05	2.7977496 05
5.7508928 02	5.0811231 02	4.4817652 02	3.9427536 02	3.4555121 02
1.5080393 03	1.4411123 03	1.3811765 03	1.3272756 03	1.2785512 03
7.3141943 03	7.1757798 03	7.044341 03	6.9193361 03	6.800279 03
1.0971292 03	1.0046092 03	9.1576433 02	8.3032033 02	7.4803069 02
-3.3893142 02	-3.1453946 02	-2.9042949 02	-2.665950S 02	-2.4302998 02
1.3880232 03	1.3496262 03	1.3119697 03	1.2757764 03	1.2409738 03
7.0193483 01	5.5880599 01	4.3797977 01	3.716448 01	2.5416179 01
1.0086801 03	9.9276577 02	9.7952682 02	9.6861568 02	9.5972367 02
0. 00	0. 00	0. 00	0. 00	0. 00
4.1542551 02	4.1542551 02	4.1542551 02	4.1542551 02	4.1542551 02

9.-01	9.1-01	9.2-01	9.3-01	9.4-01
-3.3121307 04	-4.6949032 04	-5.6381311 04	-6.1664064 04	-6.3027014 04
1.0187452 10	8.9017895 09	7.6822249 09	6.5361638 09	5.4473598 09
6.2564667 06	6.1877143 06	6.1204565 06	6.0546452 06	5.990234 06
1.2072347 10	1.0515599 10	9.0549092 09	7.6820415 09	6.3896482 09
2.2356197 05	1.7525999 05	1.341468 05	9.958203 04	7.0996092 04
3.0127146 02	2.6080871 02	2.2362455 02	1.8925597 02	1.573041 02
1.2342715 03	1.1938087 03	1.1566245 03	1.122256 03	1.0903041 03
6.6867327 03	6.5783031 03	6.4746333 03	6.3753998 03	6.2803084 03
6.6867327 02	5.9204728 02	5.1797066 02	4.4627798 02	3.768185 02
-2.1972818 02	-1.9668387 02	-1.7389142 02	-1.5134537 02	-1.2904047 02
1.2074937 03	1.1752719 03	1.1442982 03	1.1143657 03	1.0855707 03
1.8687793 01	1.3333163 01	9.1658652 00	6.0113529 00	3.7068748 00
9.5257554 02	9.4692494 02	9.425505 02	9.3925263 02	9.3685072 02
0. 00	0. 00	0. 00	0. 00	0. 00
4.1542551 02	4.1542551 02	4.1542551 02	4.1542551 02	4.1542551 02

9.5-01	9.6-01	9.7-01	9.8-01	9.9-01
-6.0684906 04	-5.4838636 04	-4.5676266 04	-3.3373975 04	-1.8096914 04
4.4158842 09	3.4380995 09	2.5106346 09	1.6303631 09	7.9438343 08
5.9271789 06	5.8654375 06	5.8049691 06	5.7457347 06	5.687697 06
5.171154 09	4.0206592 09	2.9329569 09	1.9029617 09	9.2664862 08
4.7881056 04	2.9782661 04	1.6293649 04	7.0480063 03	1.716016 03
1.2742484 02	9.9320771 01	7.2734643 01	4.744364 01	3.3254612 01
1.0604248 03	1.0323208 03	1.0057346 03	9.804436 02	9.5625461 02
6.1890908 03	6.101502 03	6.0173175 03	5.9363315 03	5.8583547 03
3.0945454 02	2.4406008 02	1.8051959 02	1.1872663 02	5.8583547 01
-1.069716 02	-8.5133616 01	-6.3522339 01	-4.2132522 01	-2.0959864 01
1.0578129 03	1.0310444 03	1.0052202 03	9.8029791 02	9.5623718 02
2.1011862 00	1.0540961 00	4.3508754 -01	1.2664662 -01	1.5530854 -02
9.3518077 02	9.3409339 02	9.3345198 02	9.331313 02	9.330161 02
0. 00	0. 00	0. 00	0. 00	0. 00
4.1542551 02	4.1542551 02	4.1542551 02	4.1542551 02	4.1542551 02

$T = 1000.$
2700.
7.219 10
4.2674 00
7.8-05
3.87592 05
9.33 02
9. 02
8.52 02

8.-01	8.1-01	8.2-01	8.3-01	8.4-01
3.877616 05	3.131388 05	2.4663199 05	1.8773313 05	1.3597159 05
2.8330772 10	2.5980379 10	2.3774629 10	2.1702893 10	1.9755443 10
7.038525 06	6.9516296 06	6.8668537 06	6.7841205 06	6.7033571 06
3.6205048 10	3.2858533 10	2.9790166 10	2.6968302 10	2.4365794 10
1.3409277 06	1.1561336 06	9.3300554 05	8.490021 05	7.2194946 05
1.1187396 03	9.8943048 02	8.7602529 02	7.7613729 02	6.8776745 02
2.1187396 03	1.9894305 03	1.8760253 03	1.7761373 03	1.6877675 03
8.1881357 03	8.0032319 03	7.829217 03	7.6651465 03	7.5101466 03
1.6376371 03	1.5206141 03	1.4092591 03	1.3030749 03	1.2016235 03
-4.653634 02	-4.3945637 02	-4.1386723 02	-3.8858826 02	-3.6361205 02
1.7266812 03	1.6749477 03	1.6254093 03	1.5778916 03	1.5323074 03
1.743364 02	1.4659047 02	1.2217312 02	1.0083542 02	8.2330391 01
1.2137407 03	1.1768935 03	1.1453931 03	1.1185569 03	1.0957929 03
-6.241507 01	-6.241507 01	-6.241507 01	-6.241507 01	-6.241507 01
3.5301044 02	3.5301044 02	3.5301044 02	3.5301044 02	3.5301044 02

8.5-01	8.6-01	8.7-01	8.8-01	8.9-01
9.0910957 04	5.2146219 04	1.9301154 04	-7.9740112 03	-3.0004731 04
1.7923363 10	1.6198474 10	1.4573264 10	1.3040828 10	1.1594814 10
6.6244941 06	6.5474651 06	6.4722069 06	6.3986591 06	6.326764 06
2.1959233 10	1.9728335 10	1.7655441 10	1.5725119 10	1.3925822 10
6.099787 05	5.1147534 05	4.250384 05	3.4944709 05	2.8363341 05
6.0923444 02	5.3911869 02	4.7621743 02	4.1950833 02	3.6811988 02
1.6092344 03	1.5391187 03	1.4762174 03	1.4195083 03	1.3681199 03
7.3634455 03	7.2243589 03	7.0922777 03	6.9666576 03	6.8470106 03
1.1045168 03	1.0114102 03	9.219961 02	8.3599891 02	7.5317117 02
-3.3893142 02	-3.1453946 02	-2.9042949 02	-2.6659500 02	-2.4302998 02
1.4885565 03	1.4465447 03	1.406184 03	1.3673916 03	1.3300698 03
6.6414876 01	5.2851436 01	4.1410043 01	3.186952? 01	2.4018726 01
1.0765853 03	1.0604823 03	1.0470861 03	1.036045 03	1.0270468 03
-6.241507 01	-6.241507 01	-6.241507 01	-6.241507 01	-6.241507 01
3.5301044 02	3.5301044 02	3.5301044 02	3.5301044 02	3.5301044 02

9.-01	9.1-01	9.2-01	9.3-01	9.4-01
-4.7094083 04	-5.952453 04	-6.7559531 04	-7.1445007 04	-7.1410679 04
1.022937 10	8.9391014 09	7.7190305 09	6.5645601 09	5.4714405 09
6.2564667 06	6.1877143 06	6.1204565 06	6.0546452 06	5.990234 06
1.2239617 10	1.0661967 10	9.1814859 09	7.789879 09	6.4797083 09
2.2665958 05	1.7769929 05	1.3602201 05	1.0097991 05	7.1996759 04
3.2130712 02	2.7843171 02	2.3894547 02	2.0237667 02	1.6831859 03
1.3213071 03	1.2784317 03	1.2389455 03	1.2023767 03	1.1683186 03
6.732898 03	5.9615315 02	6.51973 03	6.4199915 03	6.324413 03
6.732898 02	5.215784 02	5.215784 02	4.4939941 02	3.7946478 02
-2.1972818 02	-1.9668387 02	-1.7389142 02	-1.5134537 02	-1.2904047 02
1.2942054 03	1.2596698 03	1.2264182 03	1.1943893 03	1.163527 03
1.7657321 01	1.259638 01	8.6586073 00	5.678357 00	3.5014339 00
1.019813 03	1.0140944 03	1.0096671 03	1.0063292 03	1.0038981 03
-6.241507 01	-6.241507 01	-6.241507 01	-6.241507 01	-6.241507 01
3.5301044 02	3.5301044 02	3.5301044 02	3.5301044 02	3.5301044 02

9.5-01	9.6-01	9.7-01	9.8-01	9.9-01
-6.7671294 04	-6.0427746 04	-4.9868099 04	-3.616853 04	-1.9494191 04
4.4357403 09	3.4538188 09	2.5223025 09	1.6380624 09	7.9819419 08
5.9271789 06	5.8654375 06	5.8049691 06	5.7457347 06	5.687697 06
5.2443262 09	4.0777681 09	9.9746679 09	1.930187 09	9.3995164 08
4.8558576 04	4.0205689 04	1.6525933 04	7.1488407 03	1.7406512 03
1.3642004 02	1.0637727 02	7.7927268 01	5.0641985 01	2.4923524 01
1.13642 03	1.1037773 03	1.0779273 03	1.050842 03	1.0249235 03
6.232725 03	6.1446816 03	6.0600574 03	5.9786456 03	5.9002562 03
3.1163625 02	2.4578726 02	1.8180172 02	1.1957291 02	5.9002562 02
-1.069716 02	-8.5133816 01	-6.3522339 01	-4.2132522 01	-2.0959864 01
1.1337758 03	1.1050851 03	1.0774065 03	1.0506944 03	1.0249059 03
1.9847219 00	9.568058-01	4.1174159-01	1.1963505-01	1.4671585-02
1.0022077 03	1.0011069 03	1.0004576 03	1.0001329 03	1.0000163 03
-6.241507 01	-6.241507 01	-6.241507 01	-6.241507 01	-6.241507 01
3.5301044 02	3.5301044 02	3.5301044 02	3.5301044 02	3.5301044 02

```
1200.
2700.
7.219 10
4.2674 00
7.8-05
3.87592 05
9.33 02
9.   02
8.52 02
```

8.1-01	8.-01	8.2-01	8.3-01	8.4-01
2.3389022 05	3.0434205 05	1.7155439 05	1.1682651 05	6.9235944 04
2.6244541 10	2.8612313 10	2.4021835 10	2.1933553 10	1.9969951 10
6.9516296 06	7.038525 06	6.8668537 06	6.7841205 06	6.7033571 06
3.4136053 10	3.7603668 10	3.0955567 10	2.8029602 10	2.5330181 10
1.2010833 06	1.3927285 06	1.0318522 06	8.3241341 05	7.5052389 05
1.1352032 03	1.2774488 03	1.0097393 03	8.9857617 02	7.9963374 02
2.3352032 03	2.4774488 03	2.2097393 03	2.0985762 03	1.9996337 03
8.1573288 03	8.3448441 03	7.9808886 03	7.8145167 03	7.6573285 03
1.5498925 03	1.6689688 03	1.4365599 03	1.3284678 03	1.2251726 03
-4.3945637 02	-4.653634 02	-4.1386723 02	-3.8858326 02	-3.6361205 02
2.0099612 03	2.0720174 03	1.9504912 03	1.8934699 03	1.8387689 03
1.2779593 02	1.5225803 02	1.063239 02	8.7626521 01	7.1455339 01
1.3830704 03	1.4211937 03	1.3504788 03	1.3227122 03	1.299158 03

8.5-01	8.6-01	8.7-01	8.8-01	8.9-01
2.834629 04	-6.2474699 03	-3.4921557 04	-5.8025745 04	-7.5885486 04
1.8122098 10	1.6381803 10	1.4741541 10	1.3194396 10	1.1734003 10
6.6244941 06	6.5474651 06	6.4722069 06	6.3986591 06	6.326764 06
2.2833175 10	2.0517673 10	1.836547 10	1.6360649 10	1.4489239 10
6.3425487 05	5.3193968 05	4.4213168 05	3.6356997 05	2.9515117 05
7.1116031 02	6.3167505 02	5.5992164 02	4.9483065 02	4.3548904 02
1.9111603 03	1.8316751 03	1.7599216 03	1.6948307 03	1.635489 03
7.5085425 03	7.3674662 03	7.2334829 03	7.1060417 03	6.9846487 03
1.1262814 03	1.0314453 03	9.4035278 02	8.5272501 02	7.6831136 02
-3.3893142 02	-3.1453946 02	-2.9042949 02	-2.6659508 02	-2.4302998 02
1.7862678 03	1.7358537 03	1.6874209 03	1.64087 03	1.5961078 03
5.758 01	4.5779281 01	3.5841969 01	2.7567524 01	2.0766523 01
1.2792824 03	1.2626181 03	1.2487536 03	1.2373254 03	1.2280106 03

9.-01	9.1-01	9.2-01	9.3-01	9.4-01
-8.880386 04	-9.706333 04	-1.0092735 05	-1.0064185 05	-9.6436546 04
1.0354499 10	9.0504803 09	7.8169578 09	6.6493251 09	5.5433233 09
6.2564667 06	6.1877143 06	6.1204565 06	6.0546452 06	5.990234 06
1.2738933 10	1.1098847 10	9.5593269 09	8.1117819 09	6.7485441 09
2.3590617 05	1.8498078 05	1.4161966 05	1.0515273 05	7.4983824 04
3.8111506 02	3.3103769 02	2.8467959 02	2.4154293 02	2.0119762 02
1.5811151 03	1.5310377 03	1.4846796 03	1.4415429 03	1.4011976 03
6.8688597 03	6.758274 03	6.6525291 03	6.5512961 03	6.4542761 03
6.8688597 02	6.0824466 02	5.3220232 02	4.5859073 02	3.8725657 02
-2.1972818 02	-1.9668387 02	-1.7389142 02	-1.5134537 02	-1.2904047 02
1.5530465 03	1.5116038 03	1.4717019 03	1.4332677 03	1.3962325 03
1.526089 01	1.0883925 01	7.4801496 00	4.9050063 00	3.024436 00
1.2205213 03	1.2146 03	1.2100151 03	1.2065579 03	1.2040394 03

9.5-01	9.6-01	9.7-01	9.8-01	9.9-01
-8.8526183 04	-7.7111657 04	-6.2381032 04	-4.4510486 04	-2.3665169 04
4.4950121 09	3.5007423 09	2.5571324 09	1.6610454 09	8.0956958 08
5.9271789 06	5.8654375 06	5.8049691 06	5.7457347 06	5.687697 06
5.462507 09	4.2482422 09	3.0994769 09	2.0114564 09	9.7966215 08
5.0581025 04	3.1468461 04	1.7219316 04	7.4498387 03	1.8141892 03
1.6327137 02	1.2744145 02	9.3427639 01	6.0986297 01	2.590535 01
1.3632714 03	1.3274415 03	1.2934276 03	1.2609663 03	1.2299054 03
6.3611964 03	6.271608 03	6.1858829 03	6.1032117 03	6.0236022 03
3.1805982 02	2.5087232 02	1.8557049 02	1.2206423 02	6.0236022 01
-1.069716 02	-8.5133816 01	-6.3522339 01	-4.2132522 01	-2.0959864 01
1.360531 03	1.3261021 03	1.2928878 03	1.2608333 03	1.229887 03
1.714359 00	8.6006874-01	3.5569873-01	1.033617-01	1.2677325-02
1.202288 03	1.2011473 03	1.2004744 03	1.2001378 03	1.2000169 03

Molybdeen

Appendix 7.1

Reference-state values (left column, strip 1):

- T_o = 3500.
- P_o = 10200.
- 2.7458 11
- 1.95-05
- 2.88 05
- 2.883 03
- C_p = 2.55 02
- C_v = 2.52 02
- 1.8555 00

0.82	0.85	0.88	0.91	0.94	0.97
195819.2381	77813.29694	-1613.540951	-46101.87547	-58843.27441	-42647.86069
6.9950414 10	5.5390401 10	4.2168395 10	3.0153199 10	1.919964 10	9183935896.
6529646.341	6299188.235	6084443.182	5883857.143	5696074.468	5519907.216
8.4157286 10	6.5480653 10	4.9194276 10	3.4815962 10	2.199173 10	1.0454887 10
742564.2882	481475.3689	289378.0942	153599.8823	64681.55765	15374.83434
2169.623215	1601.833698	1154.728711	792.4670943	490.177905	230.2487898
5669.623215	5101.833698	4654.728711	4292.467094	3990.177905	3730.24879
6770.325084	6542.003695	6339.668916	6158.399509	5994.51405	5845.194482
1218.658515	981.3005543	760.76027	554.2559558	359.670843	175.3558345
-104.1733182	-85.31144406	-67.10387249	-49.50672688	-32.48040126	-15.98902345
5291.750782	4910.130132	4567.875316	4259.783059	3981.479364	3729.26616
17.38132483	9.651493075	4.746534194	1.926140326	.5499567169	.0663911268
3746.885744	3635.010371	3565.758621	3526.537319	3507.556571	3500.911369
-49.45254521	-49.45254521	-49.45254521	-49.45254521	-49.45254521	-49.45254521
50.44339652	50.44339652	50.44339652	50.44339652	50.44339652	50.44339652
3746.885744	3635.010371	3565.758621	3526.537319	3507.556571	3500.911369
62955.8647	34427.64461	16768.4483	6767.016265	1926.925654	232.399195
742564.2882	481475.3889	289378.0942	153599.8823	64681.55765	15374.83434
679608.4235	447047.7443	272609.6459	146832.816	62754.63199	15142.43515

P_e/P_i = 8.-01

0.80	0.83	0.86	0.89	0.92	0.95	0.98
297958.2566	151951.7754	47240.97354	-20158.90001	-53730.40567	-56531.0963	-31256.83632
8.0588074 10	6.4958625 10	5.0839002 10	3.8036895 10	2.6390567 10	1.5762437 10	6034994158.
6692887.5	6450975.904	6225941.86	6016078.652	5819902.174	5636115.789	5463581.633
9.8259759 10	7.7629347 10	5.9813315 10	4.4209142 10	3.038321 10	1.8014284 10	6858451487.
963330.974	666911.2269	410483.5368	238382.6261	119149.8434	44152.65595	6723.972046
2640.367926	1964.124808	1441.438743	1025.958437	686.0327343	399.5387014	150.7174935
6140.367926	5464.124808	4941.438743	4525.958437	4186.032734	3899.538701	3650.717494
6940.212439	6690.555799	6471.94524	6277.108168	6101.993613	5943.24194	5798.263553
1388.042488	1137.463166	906.0723336	690.4818985	488.159489	297.162097	115.9652711
-117.1352694	-97.8104239	-79.17181439	-61.17237036	-43.76970417	-26.92550971	-10.60505469
5571.060698	5159.805041	4791.947165	4461.613491	4163.900565	3894.674976	3650.435658
24.51939762	14.44070692	7.741363711	3.608361292	1.335895637	.314504867	.0194551562
3853.252007	3703.925457	3607.883302	3549.878597	3518.383935	3504.319397	3500.267042
-49.45254521	-49.45254521	-49.45254521	-49.45254521	-49.45254521	-49.45254521	-49.45254521
50.44339652	50.44339652	50.44339652	50.44339652	50.44339652	50.44339652	50.44339652
3853.252007	3703.925457	3607.883302	3549.878597	3518.383935	3504.319397	3500.267042
90079.26183	52000.95164	27510.24212	12719.04229	4687.903518	1101.446128	68.0956437
963330.974	646911.2269	410483.5368	238382.6261	119149.8434	44152.65595	6723.972046
873251.7121	594910.2352	382973.2947	225663.5838	114461.9398	43051.20982	6655.876403

0.81	0.84	0.87	0.9	0.93	0.96	0.99
244431.6609	112667.8321	20810.19412	-34949.03487	-57942.92168	-51102.01735	-17013.7158
7.5197356 10	6.0094651 10	4.6433772 10	3.4033616 10	2.2740903 10	1.2425175 10	2974806961.
6610259.259	6374178.571	6154379.31	5949233.333	5757322.581	5577406.25	5408393.939
9.1025608 10	7.1412916 10	5.4390388 10	3.9420686 10	2.6111724 10	1.4171183 10	3375464980.
847768.9011	560094.242	346605.4158	193238.6584	89599.05241	27786.6332	1654.639696
2394.195399	1775.501627	1292.838181	905.5067193	585.4840242	313.0502606	74.08077576
5894.195399	5275.501627	4792.838181	4405.506719	4085.484024	3813.050201	3574.080776
6853.306221	6614.934819	6404.560282	6216.729983	6047.39559	5893.495694	5752.633651
1302.128182	1058.389571	832.5928366	621.6729983	423.3179713	235.7398278	57.52633651
-110.6142868	-91.52373370	-73.10316468	-55.30714339	-38.09470454	-21.42878564	-5.275746447
5428.748079	5032.678705	4677.926199	4358.969864	4071.178157	3810.642584	3574.046654
20.72939021	11.87456821	6.115502305	2.6761205	.8839601805	.1591668048	.0024058825
3796.405488	3666.838993	3584.952881	3536.92448	3512.15384	3502.185324	3500.033022
-49.45254521	-49.45254521	-49.45254521	-49.45254521	-49.45254521	-49.45254521	-49.45254521
50.44339652	50.44339652	50.44339652	50.44339652	50.44339652	50.44339652	50.44339652
3796.405488	3666.838993	3584.952881	3536.92448	3512.15384	3502.185324	3500.033022
75583.39938	42545.94317	21662.98455	9415.74251	3099.229283	557.2577138	0.420627595
847768.9011	560094.242	346605.4158	193238.6584	89599.05241	27786.6332	1654.639696
772185.5017	517550.2988	324942.4312	183822.9159	86499.82313	27229.37549	1646.219069

Molybdeen

Appendix 7.2

0.82
224165.5853
6.9637613 10
6529646.341
8.2747988 10
730129.3063
2007.792544
5207.792544
6713.397818
1208.411607
-104.1733182
4838.172144
18.55200738
3441.487463
-26.60144474
73.29449698
3441.487463
61579.39303
730129.3068
668550.0033

0.85
101435.2528
5.5106937 10
6299188.235
6.4409915 10
473602.3176
1476.853432
4676.853432
6488.295908
973.2443862
-85.31144406
4489.261835
10.31618798
3332.112373
-26.60144474
73.29449698
3332.112373
33688.65499
473602.3176
439913.6626

0.88
17284.02375
4.1949355 10
6084443.182
4.8407171 10
284748.067
1061.365251
4261.365251
6288.747303
754.6496765
-67.10387249
4176.343146
5.078700216
3264.371608
-26.60144474
73.29449698
3264.371608
16414.76015
284748.067
268333.3069

0.91
-31928.70194
2.9994335 10
5883857.143
3.4269527 10
151190.8552
726.6649094
3926.664909
6109.916151
549.8924536
-49.50672688
3894.658797
2.062460441
3225.986807
-26.60144474
73.29449698
3225.986807
6626.635665
151190.8552
144564.2196

0.94
-49394.49205
1.909711 10
5696074.468
2.1653115 10
63685.62801
448.7306352
3648.730635
5948.184971
356.8910983
-32.48040126
3640.209704
.5891873195
3207.402272
-26.60144474
73.29449698
3207.402272
1887.579243
63685.62801
61798.04877

0.97
-37923.46952
9134256231.
5519907.216
1.0296625 10
15142.09599
210.5776409
3410.577641
5800.784619
174.0235386
-15.98902345
3409.614775
0.071154098
3200.893039
-26.60144474
73.29449698
3200.893039
227.7248825
15142.09599
14914.3711

0.83
178723.3254
6.4629826 10
6450975.904
7.633996 10
636166.3319
1815.250026
5015.250026
6635.160261
1127.977244
-97.8104239
4717.539695
15.42135752
3399.494424
-26.6014447e
73.29449698
3399.494424
50871.07804
636166.3319
585295.2538

0.86
69288.13236
5.0577512 10
6225941.86
5.8842527 10
403821.2652
1327.512432
4527.512432
6419.209574
898.6693404
-79.17181439
4381.208837
8.277691023
3305.581301
-26.60144474
73.29449698
3305.581301
26923.23181
403821.2652
376898.0334

0.89
-2836.132359
3.7838364 10
6016078.652
4.3506625 10
234594.5453
942.1852286
4142.185229
6227.034438
684.9737882
-61.17237036
4079.189478
3.861942923
3248.832445
-26.60144474
73.29449698
3248.832445
12452.2734
234594.5453
222142.2719

0.92
-41132.0292
2.6250889 10
5819902.174
2.9909689 10
117292.8977
628.6703448
3828.670345
6054.257224
484.3405779
-43.76970417
3806.994802
1.430720519
3218.004602
-26.60144474
73.29449698
3218.004602
4591.173392
117292.8977
112701.7243

0.95
-48657.11151
1.5677896 10
5636115.789
1.7738519 10
43476.76288
365.6106126
3565.610613
5897.576647
294.6788323
-26.92550971
3560.845692
.3369866151
3204.231647
-26.60144474
73.29449698
3204.231647
1079.070015
43476.76288
42397.69286

0.98
-28107.2422
6002212668.
5463581.633
6755189106.
6622.734418
137.8173675
3337.817368
5754.448026
115.0889605
-10.60505469
3337.541173
.0208531135
3200.261697
-26.60144474
73.29449698
3200.261697
66.73269038
6622.734418
6556.001727

3200.
10200.
2.7458 11
1.95-05
2.88 05
2.883 03
2.55 02
2.52 02
1.8555 00

8. -01
329454.1978
8.0186501 10
6692887.5
9.6585817 10
946919.7697
2450.260206
5650.260206
6680.842135
1376.168427
-117.1352694
5093.541209
26.13952925
3545.42758
-26.60144474
73.29449698
3545.42758
88084.0329
946919.7697
858835.7368

0.81
274352.8047
7.4820571 10
-6610259.259
8.9486401 10
833641.776
2218.646711
5418.646711
6795.190478
1291.086191
-110.6142868
4963.426815
22.11292636
3489.882849
-26.60144474
73.29449698
3489.882849
73920.12653
833451.776
759531.6495

0.84
137864.585
5.978869 10
6374176.571
7.0235268 10
550864.8463
1638.869926
4836.869926
6560.207018
1049.633123
-91.5237357e
4601.306245
12.68666792
3363.236065
-26.60144474
73.29449698
3363.236065
41625.19667
550864.8463
509239.6497

0.87
41282.55588
4.6193751 10
6154379.31
5.3513994 10
341020.552
1189.436493
4389.436493
6352.752299
825.8577989
-73.10316468
4276.961096
6.541447275
3283.150712
-26.60144474
73.29449698
3283.150712
21203.43152
341020.552
319817.1205

0.9
-19201.06428
3.3855139 10
5949233.333
3.8798418 10
190188.3214
830.9102608
4030.910261
6167.468224
616.7468224
-55.30714339
3985.343876
2.664892386
3236.154305
-26.60144474
73.29449698
3236.154305
9219.347757
190186.3214
180968.9737

0.93
-46919.34227
2.262 10
5757322.581
2.5707262 10
88211.19281
536.2322821
3736.232282
6000.380696
420.0266487
-38.09470454
3722.220029
.9468698786
3211.904377
-26.60144474
73.29449698
3211.904377
3035.61607
88211.19281
85175.57674

0.96
-44802.82911
1.2358246 10
5577406.25
1.3955476 10
27363.67801
286.3750283
3486.375028
5848.469672
233.9387869
-21.42878564
3484.016077
.1705659813
3202.141152
-26.60144474
73.29449698
3202.141152
545.9937223
27363.67801
26817.68429

0.99
-15438.91874
2958581780.
5408303.939
3324909825.
1629.857757
67.73324006
3267.73324
5709.391837
57.09391837
-5.275746447
3267.699798
.0025790172
3200.032364
-26.60144474
73.29449698
3200.032364
8.252695735
1629.857757
1621.604861

Molybdeen

Appendix 7.3

Left-margin parameters:
```
3000.
10200.
2.7459 11
1.95-05
2.88 05
2.883 03
2.55 02
2.52 02
1.8555 00
```

0.82
```
242063.1499
6.9402746 10
6529646.341
8.1808456 10
721839.3184
1899.905431
4899.905431
6675.176598
1201.531788
-104.1733182
4535.786385
19.45879313
3237.888052
-10.14412185
89.75181987
3237.888052
10661.45314
721839.3184
661177.8652
```

0.85
```
117183.2234
5.4917962 10
6299188.235
6.369609 10
468353.6034
1393.533254
4393.533254
6452.242356
967.8363533
-85.31144406
4208.68297
10.8319629
3130.180199
-10.14412185
89.75181987
3130.180199
33195.9508
468353.6034
435157.6526
```

0.88
```
29882.40023
4.1803328 10
6084443.182
4.7882435 10
281661.3822
999.1229444
3999.122944
6254.569543
750.5483092
-67.10387249
3915.321699
5.336749204
3063.446891
-10.14412185
89.75181987
3063.446891
16178.95716
281661.3822
265482.4251
```

0.91
```
-22479.91959
2.9888425 10
5883857.143
3.3905904 10
149584.8705
682.7967862
3682.796786
6077.379035
546.9641131
-49.50672688
3651.242622
2.168436238
3025.619791
-10.14412185
89.75181987
3025.619791
6533.046787
149584.8705
143051.8237
```

0.94
```
-43095.30382
1.9028758 10
5696074.468
2.1427369 10
63021.67492
421.099122
3421.099122
5917.097399
355.0258439
-32.48040126
3412.696598
.6196957889
3007.299405
-10.14412185
89.75181987
3007.299405
1861.348155
63021.67492
61160.32677
```

0.97
```
-34773.8754
9101136788.
5519907.216
1.0191117 10
14986.93708
197.4635416
3197.463542
5770.968185
173.1296455
-15.98902345
3196.513851
.0748585686
3000.880818
-10.14412185
89.75181987
3000.880818
224.6086719
14986.93708
14762.32841
```

8.-01
```
350451.4919
7.9918765 10
6692887.5
9.5469855 10
935978.9669
2323.521726
5323.521726
6840.975687
1368.195137
-117.1352694
4775.194884
27.39246968
3340.210197
-10.14412185
89.75181987
3340.210197
86753.60036
935978.9669
849225.3666
```

0.83
```
196571.0254
6.4410492 10
6450975.904
7.5480568 10
629003.0685
1716.000171
4716.000171
6597.656996
1121.605727
-97.81042239
4422.693464
16.18145614
3196.540015
-10.14412185
89.75181987
3196.540015
50117.79374
629003.0685
578685.3648
```

0.86
```
83986.23825
5.0403186 10
6225941.86
5.8195335 10
399379.7508
1251.561558
4251.561558
6383.810445
893.7334623
-79.17181439
4107.383284
8.694046761
3104.046521
-10.14412185
89.75181987
3104.046521
26531.86289
399379.7508
372847.8879
```

0.89
```
8712.379406
3.7706011 10
6016078.652
4.303628 10
232069.158
886.3364232
3886.336423
6193.427042
681.2769746
-61.17237036
3824.240135
4.058996816
3048.134985
-10.14412185
89.75181987
3048.134985
12274.42116
232069.158
219794.7369
```

0.92
```
-32733.11155
2.6157771 10
5819902.174
2.9554008 10
116054.9339
590.4287518
3590.428752
6022.22275
481.77782
-43.76970417
3569.057627
1.504448543
3017.751709
-10.14412185
89.75181987
3017.751709
4526.685766
116054.9339
111528.2481
```

0.95
```
-43407.78798
1.5621534 10
5636115.789
1.7554676 10
43026.1675
342.9918868
3342.991887
5866.935656
293.3467828
-26.92550971
3338.292636
.3544710323
3004.173147
-10.14412185
89.75181987
3004.173147
1064.152555
43026.1675
41962.01494
```

0.98
```
-26007.51279
5960358342.
5463581.633
6686347519.
6555.242666
129.2172836
3129.217284
5725.051382
114.5010276
-10.60505469
3128.94485
.0219404079
3000.258134
-10.14412185
89.75181987
3000.258134
65.82405474
6555.242665
6489.418611
```

0.81
```
294305.2341
7.4569381 10
6610259.259
8.8461596 10
823907.025
2101.614253
5101.614253
6756.16893
1263.672097
-110.6142868
4653.213639
23.18378297
3265.533635
-10.14412185
89.75181987
3285.533635
72811.07685
823907.026
751095.9491
```

0.84
```
154662.4203
5.9584717 10
6374170.571
6.9457069 10
544711.9159
1547.815459
4547.815459
6523.456749
1043.75468
-91.52373376
4313.724705
13.3170131
3160.833851
-10.14412185
89.75181987
3160.833851
41012.62202
544711.9159
503699.2839
```

0.87
```
54930.79706
4.6033737 10
6154379.31
5.2929322 10
337297.3095
1120.502034
4120.502034
6317.977632
821.3370922
-73.10316468
4009.651028
6.872240775
3081.949195
-10.14412185
89.75181987
3081.949195
20697.04485
337297.3095
316400.2647
```

0.9
```
-8702.41722
3.3736154 10
5949233.333
3.8383572 10
186154.7635
781.1792865
2781.179288
6134.407282
613.4407282
-55.30714339
3736.259883
3.011617262
3035.640841
-10.14412185
89.75181987
3035.640841
9088.414433
188154.7635
179066.349
```

0.93
```
-39570.26933
2.2539397 10
5757322.581
2.5437621 10
87285.95308
503.3977873
3503.397787
5968.228097
417.8180299
-38.09470454
3489.581277
.9957687878
3011.738066
-10.14412185
89.75181987
3011.738066
2993.206875
87285.95308
84292.7462
```

0.96
```
-40603.37029
1.2313627 10
5577406.25
1.3811671 10
27081.70788
268.59158
3268.59158
5818.258747
232.7303499
-21.42878564
3266.265072
.1794316511
3002.111703
-10.14412185
89.75181987
3002.111703
538.4843828
27081.70788
26543.2235
```

0.99
```
-14389.05403
2947764992.
5408393.939
3291206388.
1613.336465
63.50154958
3063.50155
5680.381087
56.80381087
-5.275746447
3063.46856
.0027136774
3000.031926
-10.14412185
89.75181987
3000.031926
8.14107492
1613.336465
1605.19539
```

Molybdenum
Appendix 14

	0.82	0.85	0.88	0.91	0.94	0.97
	254118.2252	126395.7862	37252.45046	-16952.38191	-32410.2787	-32931.36284
	6.9265231 10	5.4807411 10	4.1717903 10	2.9826468 10	1.8983771 10	9081761914.
	6529646.341	6299138.235	6084443.132	5883857.143	5636074.463	5519907.216
r+ 2833.	8.125883 10	6.3278502 10	4.7575464 10	3.369295 10	2.1295209 10	1.0129395 10
r- 10200.	716989.6755	465283.1056	279855.6716	148645.3695	62533.26237	14896.16912
K 2.7458 11	1836.791469	1344.79095	962.711195	657.1339341	404.9346863	189.7917935
α 1.95-05	4719.791469	4227.79095	3845.711195	3540.133934	3287.95468	3072.791794
E 2.88 05	6652.715381	6431.057322	6234.438213	6058.263803	5293.835213	5753.485731
TM 2.883 03	1197.489769	964.6585983	748.1385856	545.2437427	353.9301123	172.6045719
Cp 2.55 02	-104.1733182	-85.31144406	-67.10387249	-49.50672598	-32.430-0126	-15.98902345
Cv 2.52 02	4359.890716	4044.544334	3762.624153	3508.84416	3273.60143	3071.849811
S 1.8555 00	20.04584812	11.16630334	5.504165124	2.23722497	0.639503631	.0772639395
	3118.782146	3012.0493	2945.905912	2908.405084	2890.239227	2883.873669
	0.	0.	0.	0.	0.	0.
	99.89594173	99.89594173	99.89594173	99.89594173	99.39594173	99.89594173
	20.06672921	11.17793491	5.50989863	2.239555412	-5491698307	.0773444229
	57792.18013	32192.45253	15868.50805	6449.919587	1343.689112	222.7513977
	716989.6755	465283.1056	279855.6716	148645.3695	62533.26237	14896.16912
	659197.4953	433090.6531	263987.1636	142195.4499	60733.57325	14673.41719

	8.-01	0.83	0.86	0.89	0.92	0.95	0.98
ΔA	362734.909	207011.9299	92584.63019	15468.25879	-27819.74472	-40336.93371	-24779.17109
ΔH	7.9762172 10	6.4282183 10	5.0301205 10	3.7628584 10	2.6103296 10	1.5538563 10	5967573561.
Pi	6692887.5	6450975.904	6225941.86	6016078.652	5819902.174	5636115.789	5463581.633
	9.4817507 10	7.4977507 10	5.7816728 10	4.2764299 10	2.9409335 10	1.7447128 10	5646075190.
ΔG	929578.5373	624812.5595	396781.4649	230591.8065	115330.7251	42762.5692	6515.75399
ΔT	2249.379715	1657.939006	1207.130297	853.664872	568.0574199	329.7599322	124.1862344
Tu	5132.379715	4540.939006	4090.130297	3736.664872	3451.05742	3212.759932	3007.186234
	6817.545736	6575.68426	6363.010654	6173.681899	6003.403334	5348.936259	5707.784154
	1363.509147	1117.866324	890.8214916	679.1050089	480.2722667	292.4468129	114.1556831
	-117.1352694	-97.8104239	-79.17237036	-61.17237036	-43.76970417	-26.93550971	-10.60505469
	4588.962283	4250.208419	3947.195336	3675.09477	3429.86438	3203.099416	3006.916001
	28.20271037	16.6737813	8.964028488	4.186866103	1.552310344	.3658234283	.0226464117
Te	3220.157537	3077.911512	2986.148624	2930.72696	2900.603765	2897.138925	2883.256949
	0.	0.	0.	0.	0.	0.	0.
	99.89594173	99.39594173	99.39594173	99.89594173	99.89594173	99.89594173	99.89594173
	28.23208819	16.69114983	8.973366019	4.191227422	1.553927334	.3662044944	.0226700017
	81308.41399	48070.5115	25843.29413	12070.73497	4475.310721	1054.868944	65.28960479
	929578.5373	624812.5595	396781.4649	230591.8065	115330.7251	42762.5692	6515.75399
	848270.1833	576742.048	370938.1708	218521.0716	110855.4144	41707.90025	6450.470386

	0.81	0.84	0.87	0.9	0.93	0.96	0.99
	305969.4803	164489.154	62915.01315	-2560.70869	-35271.09336	-38146.68689	-13774.88318
	7.4422435 10	5.9465393 10	4.5940129 10	3.3666548 10	2.2492245 10	1.2297524 10	2941437171.
	6610259.259	6374178.571	6154379.31	5949233.333	5757322.581	5577406.25	5408393.939
	8.7862086 10	6.8991838 10	5.2587998 10	3.8140887 10	2.527988 10	1.3727545 10	3271489877.
	818323.3472	541112.4516	335119.2126	186965.1321	86744.68783	26916.75535	1603.671508
	2033.150265	1494.536895	1080.175375	752.0866697	484.1896079	258.1382629	61.02601066
	4916.150265	4377.536895	3963.175375	3635.08667	3367.189608	3141.138263	2944.026011
	6733.236482	6501.877443	6297.545428	6114.983762	5950.293693	5800.512409	5663.340902
	1279.314932	1040.300391	818.6809056	611.4983762	416.5205585	232.0204963	56.63340902
	-110.6142868	-91.52373376	-73.10316463	-55.30714339	-38.09470454	-21.42878564	-5.275746447
	4471.737346	4145.489345	3853.274698	3590.545748	3353.487607	3138.380734	2943.993286
	23.87668668	13.72527455	7.086800527	3.106843466	1.027547908	.1851881728	.0028011151
	3165.98899	3042.428438	2964.246277	2918.340458	2894.840774	2885.094476	2883.031669
	0.	0.	0.	0.	0.	0.	0.
	99.89594173	99.89594173	99.89594173	99.89594173	99.89594173	99.89594173	99.89594173
	23.90155823	13.73957171	7.094182611	3.110079761	1.02861827	.1853810771	0.002804033
	68806.48771	39569.96654	20431.24592	8957.029711	2962.420618	533.8975021	8.075614898
	818323.3472	541112.4516	335119.2126	186965.1321	86744.68783	26916.75535	1603.671508
	749486.8595	501542.4851	314667.9667	178008.1024	83782.26721	26382.85785	1595.595893

LIST OF SYMBOLS

η	energy efficiency; factor
q''	heat flow density
m	mass flow rate
d_p	diameter of a spray particle
ρ	density
N	number of particles
N_1	number of injected particles per second
v	velocity; traverse velocity of the torch
w, w_*	spray width
D	lamella diameter
A_p	surface per second, produced by N_1 spray particles
N_2	average number of lamellae on top of each other after one pass of the torch.
A_s	substrate area covered per second by the spray particles.
t_{dep}	deposition time
n	intensity of the particle bombardment
$\acute{N}_2$	number of particles per unit area of the substrate
t_w	waiting time in between two collisions of particles in the same trajectory
t_{sol}	solidification time
X	lamella thickness
p	Neumann and Schwartz parameter, constant.
a	thermal diffusivity
U_p	flight velocity of a spray particle
S	flight distance
	Index V: virtual
	Index L: liquid
A	area
λ	thermal conductivity
c	specific heat
x	coördinate

L	latent heat
T_{s0}	substrate temperature prior to the deposition of a particle
t	time
T_M	melting temperature
θ	temperature
	Index 0: substrate
	1: solidified depot
	2: molten spray material
x_α	penetration depth of α–solid solution of Mo in Fe
k	penetration constant
U_s	shock wave propagation velocity
P	pressure
V	specific volume
E	specific internal energy
α	volume coëfficient of thermal expansion; $\alpha = 3\beta$
β	linear coëfficient of thermal expansion
K	Bulk modulus
κ	Compressibility $\equiv 1/K$
E	Young's modulus
C_v	specific heat at constant volume
ν	Poissons's ration
G	shear modulus
f(V)	function of V
g(V)	function of V
T	temperature
T_0	temperature of a spray particle at the moment of impact
T_1	temperature of compressed material
V_1	specific volume of compressed material
V_0	specific volume of spray material prior to the shock compression
$P_1 = P_H$	Hugoniot pressure
P_i	isothermal pressure
P_a	adiabatic pressure
s	Bridgeman parameter

ρ, ρ_1 density of the spray material in the compressed state

ρ_0 initial density

S_1 entropy in the compressed state

S_0 entropy in the initial state

$\Delta H_{melt,m}$ molar enthalpy of fusion

T_f melting point of pressurized material

$\Delta V_{melt,m}$ molar volume change on melting

ϕ melting degree

C_p specific heat at constant pressure

ΔE_{th} part of the kinetic energy $\frac{1}{2} U_p{}^2$ that is transformed into thermal energy

ΔE_{pot} part of the kinetic energy $\frac{1}{2} U_p{}^2$ that is transformed into potential energy

$a(t)$ contact face radius as function of time

$\dot{a}(t)$ contact face perimeter velocity as a function of time

a_c critical radius of the contact face

$\dot{a}_c$ contact face perimeter velocity at the critical radius

t_c critical time

V Volume

M Mach number $= U_p / U_s$

σ surface tension

adhesion strength

214

REFERENCES

[1]   J.M. Houben. Thermisch Spuiten, een techniek met perspektief,

        Polytechnisch Tijdschrift, Procestechniek 35 (1980) nr. 4 pg. 203 – 213.

[2a]   W.G.J. 't Hart. Inleidend onderzoek van opgespoten lagen met

        betrekking tot de mechanische eigenschappen, porositeit en spanningen.

        Master's thesis, Eindhoven University of Technology, 1972.

[2b]   T.W. Kuijpers, J.H. Zaat. Influence of oxygen and cooling rate on the

        microstructure and microhardness of plasma – sprayed molybdenum,

        Metals Technology March 1974 pg. 142 – 150.

[2c]   J.M. Houben. Remarks concerning a rational plasma for thermal

        spraying, Proc. 9th. Int. Thermal Spraying Conf. The Hague 1980, pg.

        143 – 154.

[3]   H.S. Carslaw and J.C. Jaeger, Conduction of Heat in solids, 2nd

        Edition, Oxford University Press, Oxford.

[4]   C.P. Heijwegen, Diffusion in the binary systems of molybdenum with

        nickel, iron and cobalt, doctor thesis Eindhoven University of

        Technologie, 1973.

[5]   F.J.J. van Loo, Faculty for Chemical Engineering, Eindhoven

        University, Private communication.

215

[6]   M. Hansen e.a., Constitution of Binary Alloys, Mc Graw — Hill, 1958.

[7]   R.T. Allsop, T.J. Pitt and J.V. Hardy, The Adhesion of Sprayed
        Molybdenum, Metallurgia, March 1961, pg. 125 — 131.

[8]   J.M. Houben, G.G. van Liempd, Metallurgical interactions of Mo and
        steel during plasma spraying, Proc. 10th Int. Thermal Spray Conf.
        Essen 1983, pg. 66 — 71.

[9]   H.D. Steffens, K.N. Müller, H. Kayser, Oberflächenschutz durch
        thermisches Spritzen, Blech Rohre. Profile 2/1971, pg. 39 — 44.

[10]   J.M. Houben, Future developments in thermal spraying. Proc. Second
        National Conference on thermal spray, Long Beach, 1984, pg. 1 — 19.

[11]   Jonas A. Zukas e.a., Impact Dynamics, John Wiley and sons, New York
        1982.

[12]   C. Zwikker, Fysische materiaalkunde, part 2, Wetenschappelijke
        Uitgevery N.V. Amsterdam, 1967.

[13]   H. Steubel, Werkstoff — Handbuch Nichteisenmetalle, VDI Verlag,
        Düsseldorf 1960.

[14] G.E. Duvall, B.J. Zwolinski, Entropic equations of state and their
      application to shock wave phenomena in solids, The Journal of the
      Acoustic Society of America, Volume 27, Number 6, Nov. 1955,
      pg. 1054 – 1058.

[15] G.E. Duvall, Pressure – Volume Relations in Solids, Am. J. Physics, 26,
      (1958), pg. 235 – 238)

[16] P.W. Atkins, Physical Chemistry, W.H. Freeman and Company,
      San Francisco, 1978.

[17] P.W. Bridgman, Phys. Rev. 60, 351 (1941);
      Proc. Am. Acad. Arts Sci 77, 187 (1949);
      Proc. Am. Acad. Arts Sci 76, 55 (1948);

[18] M.H. Rice, R.G. Mc Queen, J.M. Walsch, Compression of solids by
      strong shock Waves, Solid state Physics, editors F. Seitz and
      D. Turnbull, Academic Press Inc. New York, 1958.

[19] R.A. Swalin, Thermodynamics of solids John Wiley and Sons, New
      York, 1962.

[20] B. Chalmers, R. King, Progress in Metal Physics 5, Pergamom Press,
      Oxford 1961.

[20a] C.J. Smithells, Metals reference book, vol. II, third edition,
      Butterworths, London, 1962, pg. 618.

[21]   R.C. Weast, Handbook of Chemistry and Physics 55th edition, CRC
         Press, Cleveland, 1974.

[22]   F.P. Bowden, J.E. Field, Proc. of the Royal Society, A, volume 282, pp
         331 – 352, 1964.

[23]   S. Safai and H. Herman, Plasma sprayed coatings: their
         ultramicrostructure. Advances in Surface coating technology London pg.
         1 – 14, The Welding Institute, Cambridge, 1978.

[24]   F.J. Heymann, On the shock wave velocity and impact pressure in
         high – speed liquid – solid impact. Transactions of the ASME, Journal
         of Basic Engineering, Sept. 1968, pg. 400 – 402.

[25]   F.E. Erdmann – Jesnitzer, R. Laschimke, Archiv für das
         Eisenhüttenwesen, 37. Jahrgang, Heft 12 – Dez. 1966. pg. 997 – 1012.

[26]   J.M. Houben, Problems encountered in the development of locally
         shielded plasma spray devices, Proc. 9th Int. Thermal Spraying
         Conference, the Hague, 1980, pg. 197 – 206, editor Nederlands Instituut
         voor Lastechniek.

[27]   J.M. Houben, Progress Report 1–10–'83 – 1–1–'84, BEOP project on
         coatings for high temperature coal conversion.

[28]   Y.S. Touloukian, E.H. Buyco, Thermophysical properties of matter,
         IFI/Plenum, New York 1970.

218

[29]   H.L.M. Van der Heiden, Master's thesis Eindhoven University of
        Technology, to be published Nov. 1988.

[30]   Berentzen, Grüters, Ermittlung der Solidus — und Liquidus —
        temperaturen von chemisch beständigen Werkstoffen, Internal report
        Thyssen Edelstahlwerke AG, Krefeld, Private communcation with Mr.
        D. Drees, 1988.

SUMMARY

This thesis is concerning with the process of plasma spraying of which some
particular features are described as an introduction. Then the heat exchange of a
spray particle with the substrate during the solidification is specified on the basis
of commonly known heat conduction theory. For Mo on steel, the heat exchange
is brought into relation with possible material transport across the contact
interface.

In this thesis a theory is developed on the mechanical and thermodynamical
collision phenomena which spray particles undergo during the deceleration at the
substrate surface.The theory is based on the application of the Murnaghan
equation of state and the entropic equations and the pressure – volume relations,
developed by Duvall and Zwolinski.

The theory permits the determination of the relationship between the Hugoniot
pressure and the temperature during the impact compression of the spray particle
material.

From a comparison of the Hugoniot – temperature curves with the Clapeyron
curve, which is the line that indicates the melting point of a material under
increased pressure, it turns out that during the deceleration of a particle, a liquid
solid transformation can take place. This transformation has a strong influence on
the morphology of the spread particle and it's adhesion to the substrate.

The morphology of spread particles has been determined experimentally as a
function of their velocity and the heat content, while the size range has been
restricted to a certain sieve fraction. Impact velocity and heat content are varied
independently from each other by the operation of a rotating substrate support.
Four different types of spread particles are identified: incompletely deformed
pancakes with a loose rim, flat firmly bound pancakes, pancakes with a loose

double layered rim and a flower type deposit. Mostly miscellaneous forms occur due to the random variation of the mentioned input parameter. The flower type deposits as the most complicated ones, are specifically observed to occur in relation with high thermal energy contents. The formation of these flowers can be explained on the basis of the produced theory.

The intrinsic strengths of the found morphologies have been measured. Diffusion bound pancakes appear to be superior to other geometries. They occur when high melting materials, such as Mo, are sprayed with a heat content corresponding to a state just below the melting point. This is not the case for materials such as stainless steel or Al. Stainless steel needs a high degree of super heating to reach a diffusion bond with the substrate.

The new method for the independent variation of impact velocity, heat content and particle size has been proven to be very elucidating.

ACKNOWLEDGEMENTS

SAMENVATTING

Dit proefschrift handelt over het plasma spuitproces waarvan karakteristieke bijzonderheden beschreven worden als inleiding tot de daarna volgende studie. Dan wordt de warmteuitwisseling van een spuitdeeltje met het substraat gedurende het stollen numeriek uitgewerkt voor de spuitmaterialen Mo en roestvrijstaal AISI – 316, op een stalen substraat. Hierbij wordt gebruik gemaakt van de algemeen gangbare theorie omtrent warmtegeleiding. Voor de kombinatie van Mo op staal is nagegaan welke konsekwenties de warmteuitwisseling heeft met betrekking tot een eventueel materietransport door diffusie over het contactvlak heen. In dit proefschrift wordt verder een theorie ontwikkeld die handelt over de mechanische en thermodynamische aspekten van de botsing die een spuitdeeltje ondergaat bij het treffen van het substraat. De theorie is gebaseerd op het gebruik van de Murnaghan toestandsvergelijking en de entropie en druk – volume relaties zoals ontwikkeld door Duvall en Zwolinski. De theorie leidt ertoe dat de relatie tussen de Hugoniot druk en de compressietemperatuur vastgesteld kan worden door berekening. Deze druk – temperatuur curven blijken snijpunten te vertonen met de Clapeyron curve, welke aangeeft hoe het smeltpunt verloopt bij stijgende druk. Het zich snijden van deze curven houdt in, dat er tijdens de compressiefase van de botsing een fasenovergang van vloeistof naar amorf vaste stof zal plaats hebben. Deze fasenovergang heeft een grote invloed op de vorm van de gedeformeerde spuitdeeltjes na de botsing en op hun adhesie met het substraat. De morfologie van uiteengespatte deeltjes is experimenteel bepaald als funktie van hun snelheid en hun warmte inhoud. Daarbij is gebruik gemaakt van een nauw begrensde zeeffraktie van het poeder om de derde belangrijke ingangs parameter, de afmeting van de poederkorrel, zo goed mogelijk vast te leggen. De botssnelheid en de warmte inhoud van de spuitdeeltjes zijn

onafhankelijk van elkaar gevarieerd door gebruik te maken van een roterende proefstukhouder. Vier verschillende typen van gespreide spuitmaterie kunnen worden onderscheiden: onvolledig gedeformeerde pannekoeken met een los zittende rand, stevig aan het substraat gebonden pannekoeken, pannekoeken met een los zittende, uit een dubbellaag bestaande rand en een depot in de vorm van bloembladen. Meestal komen mengvormen voor die toe te schrijven zijn aan de onvermijdelijke variatie in de ingangs parameters. Het depot van het bloembladtype is het meest gecompliceerde. Het treedt op in relatie met een hoge warmte inhoud. De formatie van deze bloembladstruktuur kan met behulp van de ontwikkelde model theorie verklaard en voorspeld worden. De intrinsieke hechtsterkten van de verschillende morfologieën zijn gemeten. Het blijkt dat de diffusie gebonden pannekoeken superieur zijn. Zij treden op bij hoog smeltende materialen zoals Mo, als deze verspoten worden met een warmte inhoud die correspondeert met een temperatuur juist beneden het smeltpunt. Bij materialen met een laag tot gemiddeld hoog smeltpunt ten opzichte van het stalen substraat, treedt deze pannekoek binding niet op. Deze materialen moeten hoog oververhit worden om hechting op staal tot stand te brengen. De nieuwe methode voor de onafhankelijke variatie van botssnelheid en warmte inhoud bij een nagenoeg vastgelegde korreldiameter, levert een goed inzicht op in de invloed van de parameters op het botsgedrag en derhalve in het tot stand komen van een plasma gespoten coating.

CURRICULUM VITAE.

De schrijver van dit proefschrift is geboren op 4 september 1940 te Oirsbeek.

1958	HBS – b te Hoensbroek
1961	HTS – W te Heerlen
1962	School voor reserve officieren van de Technische Troepen te Utrecht.
1971	THE – W met lof, te Eindhoven.

Zijn eerste civiele werkkring lag bij Philips Bedrijfsapparatuur Nederland te Eindhoven. Hij werkte bij dit bedrijf van juli 1961 tot en met maart 1962, vervolgens van april 1964 tot september 1964. Daarna trad hij als werkstudent in dienst bij de toenmalige Technische Hogeschool Eindhoven, waar hij in 1971 afstudeerde als werktuigkundig ingenieur met materiaalkunde als specialisatie. Het deelprojekt thermisch spuiten kwam toen onder zijn leiding te staan. In 1975 werd hij bevorderd tot de rang van wetenschappelijk hoofdmedewerker. Deze rang heeft hij tot op heden behouden.

DANKWOORD

Tot slot een dankwoord aan allen die hebben bijgedragen aan het tot stand komen van dit proefschrift, zoals daar zijn:

– de promotoren Prof. Klostermann en Prof. Metselaar. Zij hebben mij gedurende enige jaren steeds weer voorgehouden het nu maar 'ns op te schrijven. Ondanks een lange aanloop periode, waarin ze van de promovendus niet zo erg veel hoorden omtrent de voortgang, zijn zij bereid geweest om in de laatste fase een grote hoeveelheid werk te verzetten om de promotie op de geplande datum te laten doorgaan. Hun aanwijzingen hebben de inhoud en het uiterlijk van dit proefschrift verbeterd.

– de leden van de kerncommissie, Prof. Schouten en Prof. Doorschot. Hen dank ik eveneens voor de coulante wijze waarop zij het handgeschreven manuscript in gedeelten verwerkt hebben.

– de Centrale Technische Dienst, voor de vervaardiging van hulp– en proefstukken.

– de vakgroep Fysische Chemie, o.a. voor de uitvoering van micro analyses.

– de medewerksters van de studie bibliotheek werktuigkunde, Mevr. J. Bognetteau – Janssen en Mevr. Carola Tak.

- de voormalige studenten binnen het thermische spuitgroepje,
  ir. Jaques Brouwer en ir. Ad Verbeek. Jaques, bedankt voor de fantastische
  REM foto's, Ad, bedankt voor de vanzelfsprekendheid waarmee je als
  huidige medewerker van de groep, in de laatste fase van het typewerk
  ingesprongen bent.

- de huidige (nog) student Hendrik van der Heiden, voor zijn jeugdig
  optimisme, zijn experimenten, zijn snelheidsmeting, zijn fotografische
  voorstudie en zijn prepareerwerk, maar vooral voor zijn enthousiaste,
  bekwame en belangeloze manier van tekstverwerken.

- de part – time medewerkster Mevr. Helma Scheerens, die in een
  ongelooflijk korte tijd het T3 – tekstverwerken van vervelende formules
  onder de knie gekregen heeft en dit op een uitermate efficiënte wijze heeft
  toegepast. Zonder Hendrik en Helma had de promotiedatum verschoven
  moeten worden. Ik dank ze van harte voor hun inspanningen.

- tot slot, de twee medewerkers, veeleer collega's, Gijs van Liempd en
  Piet de Waal. Zij hebben nagenoeg alle experimenten met een grote
  zelfstandigheid uitgevoerd, alle preparaten, alle figuren, alle foto's
  gemaakt. Bij het samenstellen van de lay – out hebben zij overgewerkt als
  ware het hun eigen promotie. Voor deze akties, maar nog veel meer, voor
  de morele steun die ik van hen mocht ondervinden, ben ik ze zeer
  erkentelijk.

227

Stellingen

1 Een diffuse stroomdoorgang van een atmosferische boogontlading in argon
wordt bevorderd door koeling van het anode materiaal.
E.R.G. Eckert en E. Pfender, Welding Research Supplement,
October 1967.

2 Vloeibare metaaldeeltjes die met een voldoende snelheid op een substraat
botsen vertonen lokaal een kortstondige transformatie van de vloeibare
naar een amorf vaste toestand.
Dit proefschrift.

3 De mechanische opmenging van deklaag– en substraatmateriaal die
ontstaat bij thermisch spuiten wordt veelal aangeduid als een door diffusie
bepaald verschijnsel.
H.D. Steffens, K.N. Müller, H. Kayser, Blech Rohre, Profile 2/1971.

4 Hechting van thermische spuitdeeltjes komt primair tot stand door laterale
deformatie van het spuitmateriaal tijdens de botsing.
Dit proefschrift.

5 Indien effektief rendement van ontwikkelingshulp gewenst is, dient
overwogen te worden deze vooral op die landen te richten, die intellectueel
in staat zijn om de geboden hulp te verwerken tot structurele
verbeteringen van hun economische situatie. Een voorbeeld van een
dergelijk land zou India kunnen zijn.

6 De doorstroming van HBO afgestudeerden naar het universitaire onderwijs
wordt door de beperking van de studieduur tot 6 jaar ernstig belemmerd.
De harmonisatiewet die deze beperking regelt, is economisch schadelijk
omdat zij verhindert dat de kombinatie van praktische en theoretische
talenten van jonge mensen in een vroeg stadium tot ontwikkeling gebracht
wordt.

7   Het kiezen of benoemen van politici die niet of nauwelijks een professionele
     beroepsuitoefening achter de rug hebben, is afkeurenswaardig omdat het
     hen ontbreekt aan ervaring en voorstellingsvermogen. In dit verband dient
     het passieve kiesrecht verschoven te worden naar een leeftijd van 30 jaar.

8   Evenmin als het aan te bevelen is om huisartsen te laten opleiden door
     docenten die nooit patiënten behandeld hebben, dient men ingenieurs niet
     uitsluitend te laten opleiden door docenten die het synthetiserend karakter
     van het ingenieursberoep niet enige tijd ervaren hebben.
     A.D. Kerr, Mechanical Engineering, July 1986, 35.

9   Catastrofale management beslissingen kunnen voorkomen worden door de
     informatie van ondergeschikten serieus te betrekken bij de besluitvorming.
     E. Magnuson, J. Branegan, J. Hannifin, Time, March 10, 1986.

10   Hiërarchisch management van wetenschappelijke werkverbanden zonder
     optimale, horizontale kommunikatie tussen de personeelsleden, leidt tot
     een vermindering van kreativiteit, werklust en produktie en is in strijd met
     algemeen aanvaarde management methoden van succesvolle
     ondernemingen.
     T.J. Peters, R.H. Waterman, Excellente ondernemingen,
     Veen Utrecht/Antwerpen, 1985.

                              J.M. Houben   17–11–1988